Development of Novel Computational Simulation Tools to Capture the Hysteretic Response and Failure of Reinforced Concrete Structures under Seismic Loads

Mohammadreza Moharrami Gargari

Dissertation submitted to the faculty of the Virginia Polytechnic Institute and State University in partial fulfillment of the requirements for the degree of

Doctor of Philosophy
In
Civil Engineering

Ioannis Koutromanos, Chair
Finley A. Charney
Roberto T. Leon
Cristopher D. Moen

June 27, 2016
Blacksburg, VA

Keywords:
Nonlinear analysis, Reinforced concrete structures, Reinforced masonry structures, Columns, Walls, Beam-column joint, Bridge pier, Flexure-dominated, Shear-dominated, Triaxial constitutive model, Elastoplastic model, Smeared cracking, Confinement effect, Collapse, Nonlinear truss model, Aggregate interlock, Cyclic loading, Seismic loading.

Development of Novel Computational Simulation Tools to Capture the Hysteretic Response and Failure of Reinforced Concrete Structures under Seismic Loads

Mohammadreza Moharrami Gargari

ABSTRACT

Reinforced concrete (RC) structures constitute a significant portion of the building inventory in earthquake-prone regions of the United States. Accurate analysis tools are necessary to allow the quantitative assessment of the performance and safety offered by RC structures. Currently available analytical approaches are not deemed adequate, because they either rely on overly simplified models or are restricted to monotonic loading. The present study is aimed to establish analytical tools for the accurate simulation of RC structures under earthquake loads. The tools are also applicable to the simulation of reinforced masonry (RM) structures.

A new material model is formulated for concrete under multiaxial, cyclic loading conditions. An elastoplastic formulation, with a non-associative flow rule to capture compression-dominated response, is combined with a rotating smeared-crack model to capture the damage associated with tensile cracking. The proposed model resolves issues which characterize existing concrete material laws. Specifically, the newly proposed formulation accurately describes the crack opening/closing behavior and the effect of confinement on the strength and ductility under compressive stress states. The model formulation is validated with analyses both at the material level and at the component level. Parametric analyses on RC columns subjected to quasi-static cyclic loading are presented to demonstrate the need to regularize the softening laws due to the spurious mesh size effect and the importance of accounting for the increased ductility in confined concrete. The impact of the shape of the yield surface on the results is also investigated.

Subsequently, a three-dimensional analysis framework, based on the explicit finite element method, is presented for the simulation of RC and RM components under cyclic static and dynamic loading. The triaxial constitutive model for concrete is combined with a material model for reinforcing steel which can account for the material hysteretic response and for rupture due to low-cycle fatigue. The reinforcing steel bars are represented with geometrically nonlinear beam elements to explicitly account for buckling of the reinforcement. The strain penetration effect is also accounted for in the models. The modeling scheme is validated with the results of experimental static and dynamic tests on RC columns and RC/RM walls. The analyses are supplemented with a sensitivity study and with calibration guidelines for the proposed modeling scheme.

Given the computational cost and complexity of three-dimensional finite element models in the simulation of shear-dominated structures, the development of a conceptually simpler and computationally more efficient method is also pursued. Specifically, the nonlinear truss analogy is employed to capture the response of shear-dominated RC columns and RM walls subjected to cyclic loading. A step-by-step procedure to establish the truss geometry is described. The uniaxial material laws for the concrete and masonry are calibrated to account for the contribution of aggregate interlock resistance across inclined shear cracks. Validation analyses are presented, for quasi-static and dynamic tests on RC columns and RM walls.

To My Parents

Acknowledgements

I wish to express my gratitude to the Civil and Environmental Engineering department of Virginia Tech for fully supporting my research through a graduate research assistantship.

I would like to thank the members of my committee, namely, Professor Finley Charney, Professor Roberto Leon, and Professor Cristopher Moen for teaching me courses that prepared me for my research and for providing useful feedback for the content of my dissertation.

I would also like to thank Professor Mazdak Tootkaboni from the University of Massachusetts, Dartmouth, for being my research advisor during my Master's degree and for supporting and encouraging my application for doctoral studies at Virginia Tech.

I wish to thank personnel of the Livermore Software and Technology Corporation (LSTC) for support in the implementation of the constitutive models in LS-DYNA. Furthermore, the support of the Advanced Research Computing (ARC) division of Virginia Tech for conducting the simulations in the cluster Blueridge is greatly appreciated.

I would like to thank Dr. Yuan Lu of Computers and Structures, Inc, and Dr. Marios Panagiotou of Nabih Youssef Structural Engineers for providing a custom version of OpenSees that allowed me early uses of truss modeling capability. I would also like to thank Dr. Marios Mavros of Simpson Gumpertz & Heger and Professor Benson Shing of UC San Diego for providing experimental test data and detailed drawings of experimental tests simulated using the nonlinear truss analogy. I also wish to acknowledge Professor R. Sause (Lehigh University), Professor K. Beyer (EPFL) and Professor J. Restrepo (UC San Diego) and Dr. M. Schoettler (PEER) for providing the recorded data from the experimental tests on RC walls and a bridge pier, respectively.

I am most grateful to my advisor, Ioannis Koutromanos, for his guidance, support, and patience throughout all these years. I wish to thank him for giving me the opportunity to work with a person with his expertise and high moral standards.

Finally, I wish to thank my parents, my wife, and my siblings, for their support throughout the duration of my undergraduate and graduate studies. It is to them that I dedicate this dissertation.

Chapters 3 and 4, in part, are a reprint of material as it appears in Moharrami, M., Koutromanos, I. (2016). “Triaxial constitutive model for concrete under cyclic loading.” *ASCE Journal of Structural Engineering*, 04016039. The dissertation author was the primary investigator and author of this paper.

Chapters 7 and 8, in part, are a reprint of material that appears in Moharrami, M., Koutromanos, I., Panagiotou, M., and Girgin, S. C. (2015). “Analysis of shear-dominated RC columns using the nonlinear truss analogy.” *Earthquake Engineering and Structural Dynamics*, *44*(5), 677-694. The dissertation author was the primary investigator and author of this paper.

Chapters 7 and 8, in part, are a reprint of material as it appears in Moharrami, M., Koutromanos, I., and Williams, S. A. (2015). “Analysis of shear-dominated reinforced masonry walls using truss models.” *The Masonry Society Journal*, 33(1), 27-48. The dissertation author was the primary investigator and author of this paper.

Table of Content

List of Figures

List of Tables

List of Abbreviations

1D: One-Dimensional

2D: Two-Dimensional

3D: Three-Dimensional

ACI: American Concrete Institute

ASCE: American Society of Civil Engineers

BTM: Beam-Truss Model

DEM: Discrete Element Method

ERC: Equivalent Reinforced Concrete model

FE: Finite Element

GMP: Giuffre-Menegotto-Pinto material

GSA: General Service Administration

K&C: Karagozian and Case

MCFT: Modified Compression Field Theory

MSJC: Masonry Standards Joint Committee

MVLEM: Multi-Vertical-Line-Element Model

PEER: Pacific Earthquake Engineering Research

PGA: Peak Ground Acceleration

RA-STM: Rotating Angle Softened Truss Model

RC: Reinforced Concrete

RM: Reinforced Masonry

SPH: Smoothed Particle Hydrodynamics

URI: Uniform Reduced Integration

List of Symbols

Chapter 2:

f_c : Concrete compressive strength

f_{conf} : Confined concrete compressive strength

f_y : Yield stress of steel reinforcement

f_u : Ultimate stress of steel reinforcement

M_c : Capping moment

M_{cr} : The moment at tensile cracking

M_r : Assumed residual moment capacity for a member

M_y : The moment at longitudinal reinforcement yielding

M_u : Ultimate moment capacity of a structural member

ε_0 : Strain at peak compressive strength

ε_{c0} : Strain at peak confined compressive strength

ε_{cu} : Ultimate principal compressive strain

θ_{cap} : Capping rotation

θ_{pc} : Post-capping rotation

θ_y : Rotation at yielding

φ_{cr} : Cracking curvature

φ_r : Curvature at residual moment

φ_u : Curvature at ultimate moment

φ_y : Curvature at longitudinal reinforcement yielding

Chapter 3:

a : Auxiliary material parameter

b : Auxiliary material parameter

c_c : Uniaxial strength parameter in compressive regime

c_t : Uniaxial strength parameter in tensile regime

d : A parameter increasing the ductility due to confinement

d_a : Maximum aggregate size

$\left[D\right]$: Material tangent stiffness matrix

$\left[\hat{D}\right]$: Material elastic isotropic stiffness matrix in principal coordinate

e : Eccentricity

E : Elastic modulus

f : Yield function

f_b : Biaxial compressive strength

f_o : Compressive strength of material at first yielding

f_c : Uniaxial compressive strength

f_{res} : Residual compressive strength

f_t : Tensile strength

g : Plastic potential function

g_c : Total area under hardening-softening curve

g_{c0} : Area under hardening portion of strength curve

g_{c1} : Area under softening portion of strength curve

G : Shear modulus

G_c : Compressive fracture energy

G_t : Mode-I fracture energy

h : Finite element mesh size

I_1 : First invariant of stress tensor

$I_1^{(tr)}$: First invariant of trial stress tensor

J_2 : Second deviatoric invariant of stress tensor

$J_2^{(tr)}$: Second deviatoric invariant of trial stress tensor

J_3 : Third deviatoric invariant of stress tensor

(k) : Iteration number to enforce consistency conditions

K : Bulk modulus

(l) : Iteration number for elastoplastic material

m_{ij} : ij-component of the direction of plastic flow

$\left[m\right]$: The direction of plastic flow in tensor form

M : Fraction of residual tensile strength

n : Index defining the time step “n”

$n+1$: Index defining the time step “$n+1$”

p : Pressure

$\left[Q\right]$: Eigenvector

r : Weight factor

$r(\theta,e)$: Radial distance

s_{ij} : ij-component of the deviatoric stress tensor

$\hat{s}_i$: i-component of deviatoric principal stress

w/c : Water/cement ratio

X : A material parameter to exclude confinement effect for uniaxial loading

α : Material parameter increasing the strength due to confinement

α_0 : Aggregate type parameter

α_p : Dilatancy parameter

β : Material parameter for Lubliner yield criterion

γ : Material parameter for Lubliner yield criterion

δ_{ij} : Kronecker delta

Δ : Delta operator (defines increment)

ε_o : The value of strain at peak compressive strength

ε_o^{pl} : The value of plastic strain at peak compressive strength

ε_{ij} : ij-component of strain tensor

$\hat{\varepsilon}^{cr}$: Principal cracking strain value

$\hat{\varepsilon}_i$: i-component of principal strain vector

$\hat{\varepsilon}_i^{pl}$: i-component of principal plastic strain vector

$\hat{\varepsilon}_{ini}$: Strain at onset of tensile softening

$\left\{\varepsilon\right\}$: Strain vector (6×1)

$\left\{\hat{\varepsilon}\right\}$: Principal strain vector (3×1)

$\left\{\hat{\varepsilon}^{cr}\right\}$: Principal cracking strain vector

$\left\{\varepsilon^{el}\right\}$: Elastic strain vector

$\left\{\hat{\varepsilon}^{el}\right\}$: Principal elastic strain vector

$\left\{\varepsilon^{pl}\right\}$: Plastic strain vector

$\left\{\hat{\varepsilon}^{pl}\right\}$: Principal plastic strain vector

$\left\{\hat{\varepsilon}^{uc(tr)}\right\}$: Principal trial uncracked strain vector

$\left[\varepsilon\right]$: Strain tensor

$\left[\varepsilon^{el}\right]$: Elastic strain tensor

$\left[\hat{\varepsilon}^{el}\right]$: Principal elastic strain tensor

$\left[\varepsilon^{pl}\right]$: Plastic strain tensor

$\left[\hat{\varepsilon}^{pl}\right]$: Principal plastic strain tensor

$\left[\hat{\varepsilon}^{uc}\right]$: Principal continuum (uncracked) strain tensor

$\left[\hat{\varepsilon}^{uc(tr)}\right]$: Principal trial uncracked strain tensor

θ : Lode angle

κ : Hardening variable

κ_o : Value of hardening variable at peak compressive strength

λ : Plastic multiplier

λ_t : A parameter controlling the rate of tensile softening

v : Poisson's ratio

σ_{ij} : ij-component of stress tensor

$\hat{\sigma}_1$: First principal stress value

$\hat{\sigma}_2$: Second principal stress value

$\hat{\sigma}_3$: Third principal stress value

$\hat{\sigma}_i$: i-component of principal stress vector

$\hat{\sigma}_{\min}$: Minimum principal stress

$\hat{\sigma}_i^{+}$: i-component of principal stress vector that contains only tensile (positive) values

$\hat{\sigma}_i^{+(cr)}$: i-component of tensile (positive) stress vector obtained from cracking law

$\hat{\sigma}_i^{(tr)}$: i-component of principal stress vector calculated based on trial elastic strain

$\hat{\sigma}_i^{(uc)}$: i-component of principal stress vector obtained from elastoplastic law

$\hat{\sigma}_i^{(uc,tr)}$: i-component of trial principal stress vector obtained from elastoplastic law

$\hat{\sigma}_i^{+(uc)}$: i-component of tensile (positive) stress vector obtained from elastoplastic law

$\hat{\sigma}_{\max}$: Principal stress with the maximum algebraic value.

$\{\sigma\}$: Stress vector

$\{\hat{\sigma}\}$: Stress vector in principal space

$\left\{\hat{\sigma}^{+(cr)}\right\}$: Tensile stress vector obtained from cracking law

$\left\{\hat{\sigma}^{(tr)}\right\}$: Principal stress vector calculated based on trial elastic strain

$\left\{\hat{\sigma}^{+(uc)}\right\}$: Tensile stress vector obtained from elastoplastic material law (uncracked)

$\left\{\hat{\sigma}^{(uc,tr)}\right\}$: Principal stress vector calculated from trial elastic strain of elastoplastic model

$[\sigma]$: Stress tensor

$\left[\hat{\sigma}^{(uc)}\right]$: Principal stress tensor calculated from elastoplastic law

$\left[\hat{\sigma}^{(uc,tr)}\right]$: Principal stress tensor calculated from trial elastic strain of elastoplastic model

φ : An increasing function affecting the uniaxial compressive strength value

^ : Indication of principal space

Chapter 4:

c_c : Uniaxial strength parameter in compressive regime

c_t : Uniaxial strength parameter in tensile regime

d : A parameter increasing the ductility due to confinement

e : Eccentricity

E_c : Elastic modulus of concrete material

E_s : Elastic modulus of steel material

f_c : Uniaxial compressive strength

f_{res} : Residual compressive strength

f_t : Tensile strength

f_y : Yield strength of steel reinforcement

f_u : Ultimate strength of steel reinforcement

g_c : Total area under hardening-softening curve

g_{c0} : Area under hardening portion of strength curve

g_{c1} : Area under softening portion of strength curve

G_c : Compressive fracture energy

h : Finite element mesh size

I_1 : First invariant of stress tensor

M : Fraction of residual tensile strength

r : Radial distance

α : Material parameter increasing the strength due to confinement

α_p : Dilatancy parameter

γ : Material parameter for Lubliner yield criterion

ε_o : The value of strain at peak compressive strength

ε_{sh} : Steel strain at the onset of strain hardening

λ_t : A parameter controlling the rate of tensile softening

v : Poisson's ratio

$\hat{\sigma}_1$: First principal stress value

$\hat{\sigma}_2$: Second principal stress value

$\hat{\sigma}_3$: Third principal stress value

Chapter 5:

a_h : Hourglass coefficient

c : Speed of wave in the material

d : A parameter increasing the ductility due to confinement

D : Damage index in steel material

D_{cr} : Critical damage parameter for steel material under cyclic loading

$D_{cr}^{(mon)}$: Critical damage parameter for steel material under monotonic loading

E_c : Elastic modulus of concrete material

E_s : Elastic modulus of steel material

E_u : Elastic unloading modulus of steel

f : Stress in steel material

f_o : Yield strength of concrete material

$f_{i\alpha}^{k}$: Anti-hourglassing force

f_c : Uniaxial compressive strength

f_r : Reversal stress in steel material

f_{res} : Residual compressive strength

f_{sh1} : Steel stress at an intermediate point on strain hardening curve

f_t : Tensile strength

f_{target} : Target stress in steel material

f_y : Yield strength of steel reinforcement

f_u : Ultimate strength of steel reinforcement

$g_{i\alpha}$: Projection of the nodal response

G_c : Compressive fracture energy

G_t : Mode-I fracture energy

h : Finite element mesh size

M : Fraction of residual tensile strength

Q_{HG} : User-defined hourglass coefficient

S_{peak} : The amount of slip at maximum bond strength

t : Steel material parameter that affects the rate of damage accumulation

T_{max} : Maximum bond strength

α : Material parameter increasing the strength due to confinement

α_p : Dilatancy parameter

ε_o : The value of strain at peak compressive strength

ε_p : True plastic strain in steel material

ε_r : Reversal strain in steel material

ε_{sh} : Steel strain at the onset of strain hardening

ε_{sh1} : Steel strain at an intermediate point on strain hardening curve

$\varepsilon_{\mathrm{target}}$: Target strain in steel material

ε_u : Strain at ultimate strength of steel

$\gamma_{\alpha k}$: Hourglass shape vector

κ : Hardening variable

λ_t : A parameter controlling the rate of tensile softening

ρ : Material density

v : Poisson’s ratio

v_e : Element volume

Chapter 6:

d : A parameter increasing the ductility due to confinement

E_c : Elastic modulus of concrete material

E_s : Elastic modulus of steel material

f_o : Yield strength of concrete material

f_c : Uniaxial compressive strength

f_{res} : Residual compressive strength

f_{sh1} : Steel stress at an intermediate point on strain hardening curve

f_t : Tensile strength

f_y : Yield strength of steel reinforcement

f_u : Ultimate strength of steel reinforcement

G_c : Compressive fracture energy

G_t : Mode-I fracture energy

h : Smoothing length

I : Particle index

J : Particle index

M : Fraction of residual tensile strength

m : Particle mass

S_{peak} : The amount of slip at maximum bond strength

t : Steel material parameter that affects the rate of damage accumulation

T_{max} : Maximum bond strength

$\vec{v}$: Particle velocity vector

$A(\vec{x})$: Field function

$\vec{x}$: Particle position vector

$\|\vec{x}\|$: Magnitude of vector $\vec{x}$

α : Material parameter increasing the strength due to confinement

α_p : Dilatancy parameter

ΔV : Particle volume

ε_o : The value of strain at peak compressive strength

ε_{sh} : Steel strain at the onset of strain hardening

ε_{sh1} : Steel strain at an intermediate point on strain hardening curve

ε_u : Strain at ultimate strength of steel

κ : Hardening variable

Λ : The region for which the kernel function is nonzero

λ_t : A parameter controlling the rate of tensile softening

v : Poisson’s ratio

ρ : Particle density

$[\sigma]$: Stress tensor

Φ : Kernel function

Ω : Analysis domain

Chapter 7:

a : Ratio of the applied shear stress at cracking over the compressive strength

$A_{c,h}$: Sectional area of the horizontal concrete elements

$A_{m,h}$: Sectional area of the horizontal masonry elements

$A_{s,h}$: Sectional area of the horizontal steel elements

$A_{s,h,tot}$: Total sectional area of the horizontal steel elements

$A_{s,v1}$: Sectional area of the left outermost vertical steel elements

$A_{s,v2}$: Sectional area of the intermediate vertical steel elements

$A_{s,v3}$: Sectional area of the right outermost vertical steel elements

$A_{s,v2,tot}$: Total Sectional area of the intermediate vertical steel elements
b : Spacing of vertical truss elements
b_d : Cross-sectional depth of diagonal element
c_1 : Cover of vertical rebar at left end of wall section
c_2 : Cover of vertical rebar at right end of wall section
E_c : Initial tangent stiffness of concrete material
E_m : Initial tangent stiffness of masonry material
E_s : Young’s modulus of steel
E_u : Unloading and reloading tangent stiffness of concrete/masonry material
d_b : Rebar diameter
D_{max} : Maximum size of aggregate
$F_{a,h}$: Horizontal component of total inclined shear force at crack interface due to aggregate interlock
f_c : Compressive strength of concrete
f_{cc} : Cube compressive strength of concrete
f_{conf} : confined compressive strength of concrete
f_m : Compressive strength of masonry
f_t : Tensile strength of concrete/masonry
f_{tint} : Stress value of the intermediate point in the trilinear tensile regime of the uniaxial stress-strain curve of concrete/masonry
f_u: : Ultimate stress of steel reinforcement
f_y : Yield strength of steel
H : Member height
h : Cross-sectional depth of horizontal element (distance between two successive horizontal element)
L_b : Length of the slip elements
L_d : Inclined crack length
L_h : Overall length of the member (horizontal direction)
L_g : Strain gage element length
L_R : Reference length (600 mm)
N : Axial load on wall
s : Crack parallel displacement

S_F : Aggregate interlock resistance scale factor

s_y Total slip at yielding of reinforcement

t : Out-of-plane thickness of a member (out-of-plane width of the crack plane)

T : Total aggregate resistance obtained from theoretical approach for maximum aggregate size of 10 mm

T_{ref} : Total aggregate resistance obtained from theoretical approach for maximum aggregate size of 24 mm

$u_{cr,h}$: Crack displacement magnitude (horizontal crack displacement)

V : Lateral shear force

V_c : The contribution of concrete to the shear resistance

V_m : The contribution of masonry to the shear resistance

V_s : The contribution of transverse reinforcement in the shear capacity

w : Crack normal displacement (crack opening)

α : Reloading from tension to compression (masonry material parameter)

β : Concrete strength reduction coefficient

β_{int} : Concrete/masonry strength reduction coefficient at an intermediate point

β_h : Steel material strain hardening ratio

β_{res} : Concrete/masonry residual strength reduction coefficient

ε_0 : Strain value corresponding to the peak compressive strength of concrete/masonry (for a reference length of 600mm)

ε_{12} : Axial strain of diagonal truss element

ε_{34} : Axial strain of fictitious gage element

ε_{c0} : Strain value corresponding to the peak confined compressive strength of concrete

ε_{cr} : Cracking strain of concrete/masonry

ε_{cs} : Strain value of the intermediate point in the softening portion of compressive stress-strain curve of confined concrete

ε_{cu} : Ultimate compressive strain of confined concrete

ε_h : Total strain of the horizontal concrete/masonry elements

ε_{int} : Strain value corresponding to β_{int}

ε_n : Strain normal to the longitudinal axis of diagonal truss element

ε_{res} : Strain value corresponding to β_{res}

ε_s : Strain in reinforcing steel

ε_{tint} : Strain value of the intermediate point in the trilinear tensile regime of the uniaxial stress-strain curve of concrete/masonry

ε_{tres} : Strain at which the concrete/masonry completely loses tensile strength

ε_u : Ultimate compressive strain of concrete (for a reference length of 600mm)

ε_y : Yield strain of reinforcing steel

θ : Angle between diagonal element and fictitious gage element

θ_d : Angle of inclined crack with horizontal line (inclination angle)

θ_p : Direction angle of the maximum principal stress

μ : Frictional coefficient at crack interface

v : Ratio of the uniform compressive stress over the concrete compressive strength

σ : Uniform compressive stress on section

σ_1 : Maximum principal stress

σ_2 : Minimum principal stress

$\sigma_{a,h}$: Horizontal component of crack interface stress due to aggregate interlock

$\sum a_x$: Projections of the crack contact surfaces along the horizontal plane

$\sum a_y$: Projections of the crack contact surfaces along the vertical plane

σ_h : Total stress of the horizontal concrete/masonry elements

σ_{pu} : Ultimate plastic strength of cement matrix

σ_s : Stress in reinforcing steel

τ : Crack shear strength

$\tau_{10\text{mm}}$: Crack shear strength for a maximum aggregate size of 10 mm

Chapter 8:

$A_{c,d}$: Sectional area of the diagonal concrete elements

$A_{c,h}$: Sectional area of the horizontal concrete elements

$A_{c,v1}$: Sectional area of the outermost vertical concrete elements

$A_{c,v2}$: Sectional area of intermediate vertical concrete elements

$A_{m,d}$: Sectional area of the diagonal masonry elements

$A_{m,d1}$: Sectional area of the diagonal masonry elements for flanges W-5

$A_{m,d3}$: Sectional area of the diagonal masonry elements for flanges W-8

$A_{m,h}$: Sectional area of the horizontal masonry elements

$A_{m,h1}$: Sectional area of horizontal masonry elements for flanges W-5

$A_{m,h3}$: Sectional area of horizontal masonry elements for flanges W-8

$A_{m,v1}$: Sectional area of the (left) outermost vertical masonry elements

$A_{m,v2}$: Sectional area of intermediate vertical masonry elements

$A_{m,v3}$: Sectional area of the right outermost vertical masonry elements

$A_{s,h}$: Sectional area of the horizontal steel elements

$A_{s,v1}$: Sectional area of the (left) outermost vertical steel elements

$A_{s,v2}$: Sectional area of the intermediate vertical steel elements

$A_{s,v3}$: Sectional area of the right outermost vertical steel elements

E_c : Initial tangent stiffness of concrete material

E_m : Initial tangent stiffness of masonry material

E_s : Young's modulus of steel

D_{max} : Maximum size of aggregate

f_c : Compressive strength of concrete

f_{cint} : Strain values of an intermediate point in the compressive softening regime of the uniaxial stress-strain curve of concrete

f_m : Compressive strength of masonry

f_{mint} : Strain values of an intermediate point in the compressive softening regime of the uniaxial stress-strain curve of masonry

f_t : Tensile strength of concrete/masonry

f_{tint} : Stress value of the intermediate point in the trilinear tensile regime of the uniaxial stress-strain curve of concrete/masonry

f_{tres} : Residual tensile strength of concrete/masonry

f_y : Yield strength of steel

L_{sp} : Length of the slip elements

M : A parameter affecting the tensile strength degradation of reinforced concrete

β_h : Steel material strain hardening ratio

ε_0 : Strain value corresponding to the peak compressive strength of concrete/masonry (for a reference length of 600mm)

ε_{cint} : Strain values of an intermediate point in the compressive softening regime of the uniaxial stress-strain curve of concrete

ε_{cres} : Strain at which the concrete loses compressive strength

ε_{mint} : Strain values of an intermediate point in the compressive softening regime of the uniaxial stress-strain curve of masonry

ε_{mres} : Strain at which the masonry loses compressive strength

ε_{tint} : Strain value of the intermediate point in the trilinear tensile regime of the uniaxial stress-strain curve of concrete/masonry

ε_{tres} : Strain at which the concrete/masonry completely loses tensile strength

ε_{u} : Ultimate compressive strain of concrete/masonry (for a reference length of 600mm)

θ_{d} : Angle of inclined crack with horizontal line (inclination angle)

Chapter 1 : Introduction

Reinforced concrete (RC) is a popular construction material in many countries, including the United States, due to the availability of concrete constituents (aggregate, water, and cement) and due to the flexibility it provides in terms of the construction form. Reinforced concrete is used for various types of structural systems, such as buildings, bridges, dams, reservoirs, and offshore platforms (Wight MacGregor 2012). A reinforced concrete structure consists of a series of members, e.g. beams, columns, shear walls, and slabs, each contributing towards ensuring an appropriate path for various types of loading. In earthquake-prone areas, such as the western United States, RC structures include an appropriate lateral load-resisting system, which consists of moment frames, shear walls, or combinations thereof.

Reinforced masonry (RM) shear walls are also an attractive structural system, especially for residential and commercial low-to-medium rise buildings. Such structures are characterized by durability, fire resistance and soundproofing, and low maintenance cost (Lourenço et al. 1998). Reinforced masonry walls in the United States are typically constructed from hollow concrete units, with reinforcing steel placed in the unit voids which are subsequently filled with grout (Drysdale et al. 1999). For seismically active areas, it is common for all the voids in the units to be filled with grout, resulting in fully-grouted masonry which has a relatively homogeneous macroscopic behavior similar to that of concrete.

The intensity of earthquake ground motion that a structure may experience during its service life depends on geographical location (ASCE 2010). Structures located in areas with increased seismic activity must ensure adequate strength and ductility to satisfy the seismic design demands. In such areas, RC structures are usually designed as special moment-resisting frames or special shear walls according to the ACI 318-14 (ACI 2014), while RM wall structures are designed as special shear walls in accordance with the MSJC code (ACI 2011). The design of special moment-resisting frames and shear walls pursues the development of inelastic response mechanisms dominated by flexural yielding at appropriate locations, such as the base of shear walls. The response of such structures depends on the behavior of concrete and reinforcing bars at the material level. Under uniaxial compressive stress states, the concrete develops compressive strains in the direction of the applied stress, while it has a tendency to expand laterally due to the dilatation effect. By using closely spaced ties in locations where the majority of inelastic deformations would occur, the lateral expansion of concrete is restrained. The restraint of the ties leads to the development of confining pressure in the concrete, which is known to increase both the strength and deformability (ductility) of the material, and subsequently, improves the overall performance of a member. Consequently, a RC/RM structure with a well-detailed lateral load resisting system exhibits significant deformability before collapse, as depicted in Figure 1.1. The collapse of the specific structure was due to inadequate detailing of gravity load resisting system.

A flexure-dominated inelastic response may not be feasible for squat columns and walls. The response of such structures may be dominated by shear cracking, as observed in recent analytical (Koutromanos and Shing 2010) and experimental (Ahmadi et al. 2015a and 2015b) research.

Additionally, the design of older RC and RM construction has been dominated by gravity load considerations, without appropriate detailing to prevent the occurrence of shear failures under strong earthquakes (Beres et al. 1992, Hoffmann et al. 1992, Koutromanos et al. 2011). Furthermore, many RC frame buildings in the less seismically active Central and Eastern United States are designed as ordinary moment-resisting frames. These types of frames have not been detailed with capacity design principles which ensure that the occurrence of flexure-dominated inelastic modes precedes that of the less ductile, shear-dominated modes.

Figure 1.1: Ductile collapse of a 4-story parking garage at California State University (Northridge Earthquake 1994).

1.1 Damage patterns and failure modes of RC and RM construction

The response of RC and RM components designed for ductile response is dominated by damage and inelastic deformations at specific locations, which are typically located at the ends of members, such as beams, columns and walls. The damage in such cases can be manifested through loss of cover material, as shown in Figure 1.2a, and yielding of the member longitudinal reinforcement. For relatively large values of earthquake-induced deformations, severe damage can occur in the form of concrete crushing, rebar buckling and subsequent rebar rupture, as shown in

Figure 1.2b. Rebar rupture is typically the result of low-cycle fatigue and usually follows the occurrence of inelastic buckling (Kim and Koutromanos 2016).

(a) Cover spalling

(b) Rebar buckling, concrete crushing and subsequent rebar rupture

Figure 1.2: Damage at the base of a column, photograph from the work by Schoettler et al. (2012). Under fair use 2016.

A flexure-dominated inelastic response is not always bound to occur, especially for old RC and RM construction. For components not designed with modern standards, shear-induced failures are common, wherein damage is manifested through the occurrence of large inclined (diagonal) cracks. Shear-induced failures entail sudden member strength degradation, which is undesirable because it does not allow significant inelastic deformability in the structural system. Shear failures may even be inevitable for several types of structural configurations, such as low-rise coupled shear walls (e.g., Ahmadi et al. 2015a and 2015b).

An example case involving shear failure in an RC wall with occurrence of a large inclined crack is depicted in Figure 1.3a. Shear failure is not always associated with inclined cracks. For example, in very squat walls or walls with very low axial force, flexural cracks, originating from different corners of the wall panel, might intersect during successive cycles of loading and form a localized horizontal crack that runs over the entire length of the wall section. This eventually leads to an inelastic response mode dominated by sliding along the localized horizontal crack. Such localized sliding can also occur along horizontal construction joints as shown in Figure 1.3b. Shear-related damage patterns may even occur after the development of inelastic flexural deformations in members. For example, Figure 1.3c is taken from a post-tensioned RC wall tested by Pakiding et al. (2014) which lost its lateral load capacity due to extensive damage in the web concrete. The damage shown in the figure occurred after the wall developed significant inelastic deformations associated with flexure.

(a) Diagonal shear crack (2010 Chile earthquake)

(b) Sliding at construction joint (1985 Chile earthquake)

(c) Web crushing of a post-tensioned shear wall (Pakiding et al. 2014), Under fair use 2016.

Figure 1.3: Shear damage in reinforced concrete walls

For members such as columns carrying gravity loads, severe damage can eventually lead to axial failure, i.e. to inability of a structural component to carry its gravity loads. The specific type of failure usually follows the occurrence of severe shear damage and/or inelastic flexural deformations. For instance, the column presented in Figure 1.4a lost its axial capacity after the occurrence of severe shear-induced damage, the out-of-plane buckling of the wall presented in Figure 1.4b is due to excessive flexural deformation, and the column depicted in Figure 1.4c failed due to severe shear damage, tie rupture, concrete crushing, and finally buckling of longitudinal bars.

(a) Shear damage (2011 Christchurch earthquake). (b) Out-of-plane buckling (2011 Christchurch earthquake). (c) Hoop rupture (1979 Imperial Valley earthquake).

Figure 1.4: Axial failure in reinforced concrete structures

Experimental testing provides the most reliable means to investigate the damage patterns and evaluate the performance of RC and RM structures. Different types of experiments have been conducted on small- or full-scale RC and fully-grouted RM structures subjected to quasi-static or dynamic loading. The experimental results have been instrumental for the establishment of modern seismic design guidelines. However, experimental testing is mostly limited either to small-scale tests or to tests of single structural components. Additionally, due to the relatively high cost of experimentation, parametric experimental investigations are impractical, even if the focus is on a single type of structural component. It becomes clear that computational simulation may be the most appropriate means to systematically evaluate the performance and safety of RC and RM structures. The reliable determination of the seismic response of RC structures obviously requires computational simulation tools which can capture the inelastic behavior of concrete and reinforcing steel and its effect on the structural response. Despite the current availability of computational resources and parallel computing, the computational simulation of RC and RM structures greatly relies on tools such as phenomenological beam-based models. Such tools are overly simplified and may not accurately capture important features of the response, such as the axial-shear-flexure interaction in wall members. Based on the above, research for the improvement of simulation capabilities for RC and RM structures is much needed.

1.2 Objective and scope of dissertation

The present study focuses on the development of analytical tools for the analysis of RC and fully grouted RM structures. Two methods with different level of complexity are examined for the analysis of RC/RM structures. The accuracy of each modeling technique is evaluated through validation analyses, using experimental test results in the literature.

A three-dimensional (3D) finite element (FE) analysis scheme is developed for simulating the damage and failure in flexure- and shear-dominated RC and RM components subjected to cyclic lateral loads. An issue that has limited the use of three-dimensional, continuum-based, finite element models may be the lack of multiaxial constitutive laws for concrete that can capture the material response and ensure a robust stress update process. Many studies have identified and described limitations of existing triaxial models for concrete (Sasani and Kropelnicki 2008, Yu et al. 2010, Deaton 2013, Murcia-Delso 2013). To address this issue, a novel triaxial concrete model is proposed for concrete and masonry under cyclic multiaxial stress states. The model can accurately capture the crack opening/closing behavior and the increased strength and ductility of confined concrete, while ensuring numerical robustness and eliminating the possibility for convergence failure in the stress update algorithm. The model is validated, both at the material level and at the component level, through the simulation of RC columns and of a beam-to-column joint.

To account for important aspects of behavior, such as rebar buckling and rupture, the proposed triaxial constitutive model for concrete is combined with a uniaxial steel material law, developed by Kim and Koutromanos (2016), which accounts for Bauschinger effect precisely and can capture the rebar fracture due to low-cycle fatigue. The reinforcing steel bars are represented with nonlinear beam elements to explicitly account for buckling of the reinforcement. The strain penetration effect is also accounted for in the models. The modeling scheme is validated with the results of experimental tests on RC columns and RC/RM walls that experienced severe lateral strength degradation due to rebar buckling, rebar rupture, and shear damage. Specifically, two post-tensioned RC walls and two shear-dominated squat walls subjected to cyclic loading, a U-shaped wall under bi-directional cyclic loads, a bridge pier subjected to a sequence of ground motions, and a five-story wall system under a sequence of triaxial ground motions are analyzed. The very good agreement between analytically obtained and experimentally recorded data, in terms of both the hysteretic response and the damage pattern, indicates that the proposed three-dimensional analytical scheme has a potential to complement experimental testing programs with sufficient accuracy and can also be used for the validation of simpler methods.

Additional parametric studies are conducted to examine the effect of viscous damping, to evaluate the influence of not accounting for strain penetration, to emphasize the importance of accounting for the effect of increased ductility due to confinement in analysis of walls and columns, and to show the capability of the modeling scheme to capture full collapse of structures, without failure in the stress update process of the material laws. The analyses are supplemented with calibration guidelines for the proposed modeling scheme, and a set of sensitivity analyses to investigate the effect of mesh size and tensile fracture energy for the analysis of shear-dominated members. A comparison of the efficiency of implicit static solution algorithms and explicit dynamic algorithms is also conducted. A preliminary verification of the capability of the meshless, Smoothed Particle Hydrodynamics (SPH) method, to capture the response of shear-dominated RC walls is pursed.

Despite the accuracy of three-dimensional finite element models, the vast majority of researchers and practitioners will most probably prefer simplified analysis methods for performance assessment of RC and RM structures. A simplified analysis method, based on the nonlinear truss analogy, is developed and used for the efficient and accurate prediction of shear-induced failures in RC and RM structures. An algorithm is established to provide the truss geometry, and a methodology is presented to account for the effect of aggregate interlock over an inclined shear crack. The analysis technique is validated through nonlinear analyses on RC and RM components. The nonlinear truss analogy is conceptually simple and computationally efficient, because it relies on uniaxial material laws. Consequently, the method is well-suited for researchers and practicing engineers.

1.3 Outline of dissertation

Chapter 2 presents a review of previous methods for the analytical simulation of reinforced concrete and masonry structures. Issues associated with existing simplified and refined analysis methods are discussed.

Chapter 3 presents a numerically efficient and algorithmically robust triaxial constitutive model that can capture stiffness and strength degradation due to tensile cracking and compression-induced crushing. The material model also accounts for the increased strength and ductility of the concrete subjected to multiaxial compression due to confining pressure.

Chapter 4 presents the verification of the capability of the proposed triaxial concrete model to be used in simulations of structural components under cyclic loading. Two reinforced concrete columns and a reinforced concrete beam-to-column joint are analyzed under prescribed displacement histories, and the obtained hysteretic response is compared with corresponding experimental data. A parametric investigation is also provided to elucidate the effect of different yield surfaces on the obtained results, and the impact of confinement on the ductility.

Chapter 5 provides the results of three-dimensional finite element analyses for flexure-dominated RC structural components subjected to cyclic loads. The analyses combine the new material model for concrete with a uniaxial steel model that can account for rebar rupture due to low-cycle fatigue. The explicit integration scheme, which is more suitable for simulations of failure or collapse, is used to circumvent the need for iterations and preclude the probability of failure to satisfy the convergence criteria of the global solution algorithms that characterizes implicit solution schemes. The modeling approach is validated using the results of experimental tests on two post-tensioned RC walls subjected to quasi-static loading, a U-shaped RC wall under bi-directional cyclic loading, and a full-scale RC bridge pier subjected to a sequence of ground motions. Additional parametric studies are conducted to investigate the effects of the viscous damping, the impact of strain penetration effect, and the importance of accounting for the increased ductility due to confinement. The efficiency of explicit and implicit solvers is compared and the capability of the analytical models to capture full collapse of components is assessed.

Chapter 6 provides the results of numerical simulations on shear-dominated RC and RM walls with three-dimensional finite element models. Two single-story, shear-dominated walls under cyclic loading and a five-story shear-dominated wall system subjected to a sequence of triaxial ground motions are analyzed. A set of parametric studies are performed to investigate the effect of mesh refinement and to elucidate the impact of the tensile fracture energy on the analytical results. To address the potential difficulties of using continuum-based finite element models for analysis of shear failure, a preliminary verification is conducted for the capability of the meshless, Smoothed

Particle Hydrodynamics (SPH) method to capture the global response and damage pattern of shear-dominated RC members under cyclic loading.

Chapter 7 provides a methodology based on the nonlinear truss analogy for the analysis of shear-dominated RC/RM structures. A step-by-step procedure to determine the geometry of a truss model is described. The uniaxial constitutive laws used to represent the concrete and the reinforcing steel are also described. A procedure to account for the effect of aggregate interlock on an inclined shear crack and a simplified equation to calculate the inclination angle of the diagonal elements are also proposed.

Chapter 8 presents the verification of the capability of the nonlinear truss models for the analysis of shear-dominated RC and RM structural components. Several aspects of the modeling technique, such as the mesh size effect and the influence of the inclination angle of the diagonal elements on the analytical results, are investigated. Additional parametric studies are performed to elucidate the importance of accounting for the effect of aggregate interlock on the results.

Chapter 9 presents the concluding remarks and provides recommendations for future research.

Chapter 2 : Literature Survey

This chapter summarizes various existing analytical techniques to simulate the behavior of reinforced concrete (RC) and fully grouted reinforced masonry (RM) structures. Simulation tools with different levels of sophistication are described and the limitations associated with each analysis method are highlighted. Additionally, recent efforts for capturing the local and global failure of structural components in the context of failure simulation are reviewed.

The numerical analysis of RC/RM structures is typically conducted with one of the following analysis methods:

- Lumped plasticity (concentrated plastic hinge) beam-based models
- Fiber-section (layered-section) beam-based models
- Nonlinear truss models
- Refined finite element models
- Other analysis methods which cannot be classified in one of the above categories.

Each of the aforementioned methods with its applicability range is discussed briefly in the following sections, and some relevant studies on analysis of RC/RM structures are cited.

2.1 Lumped plasticity beam-based models

The simplest type of modeling uses beam elements to represent structural components, such as walls or columns, (Otani and Sozen 1972, Lybas and Sozen 1977). As shown in Figure 2.1a, the inelastic behavior is captured through the addition of elastoplastic components in parallel with elastic elements (Clough et al. 1965) or by using rotational springs to represent the plastic hinges at the ends of a beam element (Giberson 1967). A plastic hinge can be defined as the region of the element where the majority of inelastic flexural deformation occurs. The plastic hinge moment-rotation diagram is usually obtained from a moment-curvature diagram like the one shown in Figure 2.1b. Transition points on the moment-curvature diagram correspond to different stages of damage, e.g. cracking of the concrete, M_{cr}, yielding of reinforcement, M_y, ultimate strength, M_u, and the residual moment, M_r. The post-peak feature enables modeling of the strain-softening behavior associated with concrete crushing, rebar buckling and fracture, or bond failure (Ibarra et al. 2005, Haselton and Deierlein 2007).

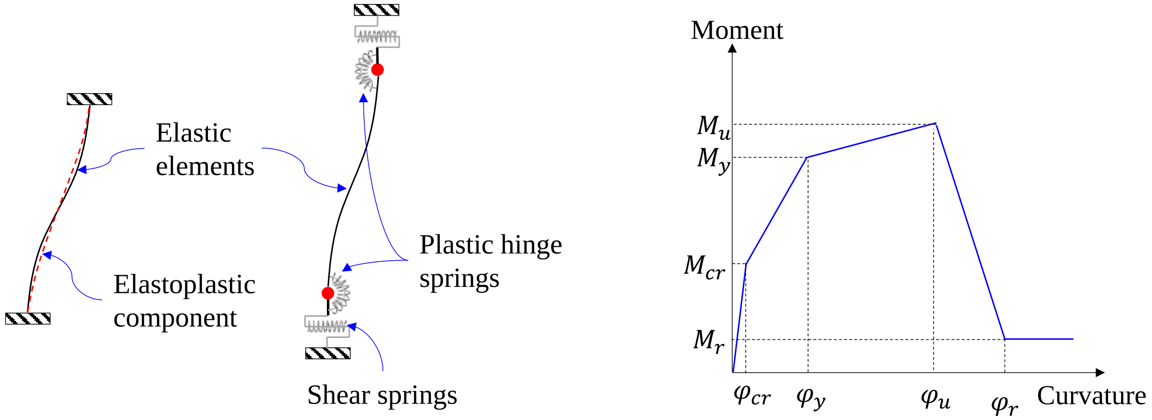

(a) Analytical model (b) Plastic hinge properties

Figure 2.1: Lumped plasticity beam models and a typical moment-curvature diagram

Lybas and Sozen (1977) used beam-based models to obtain the response of coupled walls with a multi-stage linear analysis. The different levels of damage in the beam elements were accounted for by moment-curvature diagrams which had been obtained from sectional analyses. Takayanagi and Schnobrich (1977) introduced a way to include the shear inelasticity in beam elements by multiplying the elastic shear stiffness of the beam with a reduction factor, calculated as the ratio of secant inelastic stiffness over elastic flexural stiffness. Enhancements have been gradually introduced to beam models to account for the stiffness degradation (Brancaleoni et al. 1983), axial load effects (Keshavarzian and Schnobrich 1985, Saatcioglu et al. 1987) and bond-slip (Roufaiel and Meyer 1987).

The lumped plasticity models are also used to simulate the progressive collapse of RC structures subjected to notional column removal. In this method, one or more gravity resisting members, e.g. a column or a wall, will be removed from the analysis, and the rest of the structure will be analyzed under amplified vertical forces. By such an approach, the capability of the damaged structure in providing alternative load path and redistributing the applied external forces can be examined.

Tsai and Lin (2008) utilized the commercial program SAP2000 (CSI 2000) to evaluate the vulnerability of an earthquake-resistant RC building against progressive collapse. They followed the procedure recommended by the US General Service Administration (GSA 2000) for collapse assessment based on linear static analysis, and compared the results with nonlinear analysis. Kokot et al. (2012) performed linear and nonlinear static and dynamic analysis on a flat-slab RC frame building which survived after intentional destruction of its two central columns during the experiment. In both works, the nonlinearity was introduced to the models by means of plastic hinges at both ends of beam elements, and a drop to a residual moment, M_r, was assumed in the moment-curvature diagram to represent the element failure.

Haselton and Deierlein (2007) used lumped plasticity beam-based models to assess the seismic collapse safety of modern designed RC structures. To account for the cyclic deterioration of components, the hysteretic model of Ibarra et al. (2005) was employed. The specific hysteretic model captures four basic modes of cyclic deterioration, including strength deterioration of the inelastic strain-hardening branch, strength deterioration of the post-peak strain-softening branch, accelerated reloading stiffness deterioration, and unloading stiffness deterioration. Figure 2.2 schematically presents the backbone curve and the hysteretic response of the model by Ibarra et al. (2005). Such models need to be calibrated from experimental data. Specifically, the hinge parameters are so determined that the analytical model can provide optimal fit to the results of experimental tests. Still, manual adjustments are required to obtain the best possible agreement with experimental results.

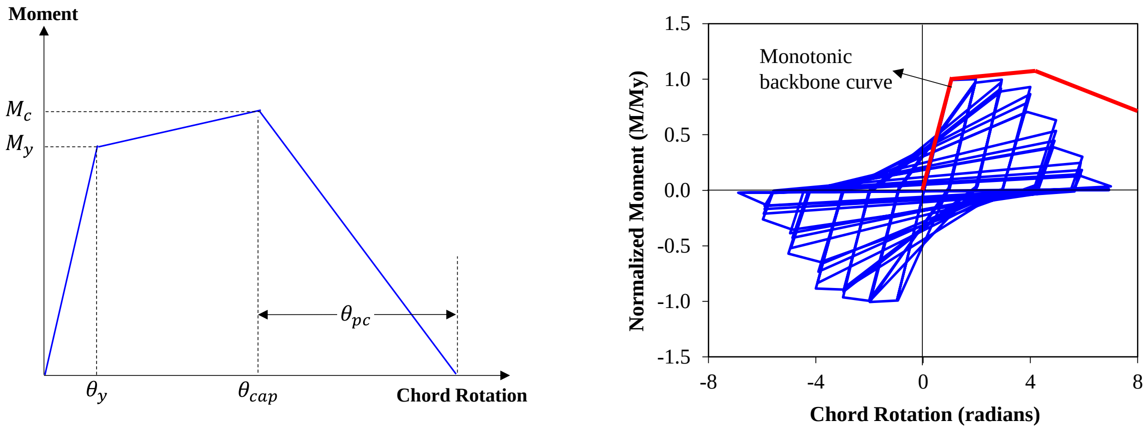

(a) Monotonic backbone curve (b) Cyclic response

Figure 2.2: Hysteretic law by Ibarra et al. (2005), used for the moment-rotation response of plastic hinges in beam models by Haselton and Deierlein (2007). Under fair use 2016.

Previous research on RC structures has mainly used phenomenological hinge models, where the axial-flexural interaction is not reliably and rigorously accounted for (Inel and Ozmen 2006). A fiber-section formulation (Mahin and Bertero 1975) can be used in the hinge regions, to capture the axial-flexural interaction and the inelasticity of a member at the sectional level. In this approach, the cross section of a beam element is discretized either in both directions (fiber-section) or in one direction (layered-section) as shown in Figure 2.3. Each fiber/layer is assigned an appropriate cross sectional area and a uniaxial constitutive law for the steel and concrete materials. The axial stress of each fiber/layer is calculated by evaluating the stress-strain relation at each gauss point along the beam longitudinal axis, and then multiplied by the fiber area and eccentricity to find the corresponding axial force and moment acting on each fiber. The total axial force and moment at the section is obtained by integrating the axial force and moment of all fibers/layers.

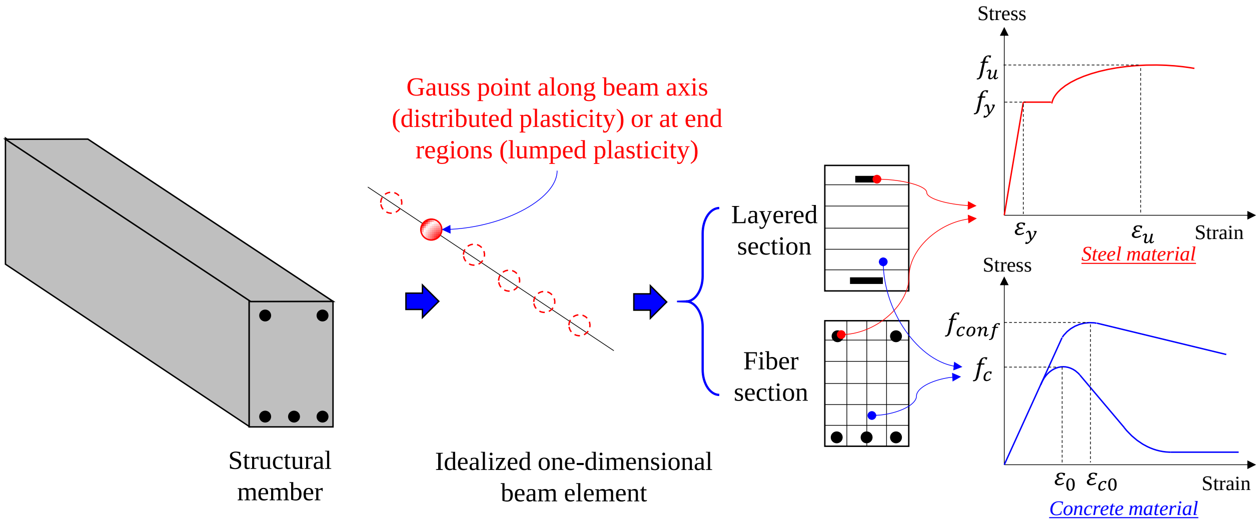

Figure 2.3: Typical fiber-section beam model for the analysis of RC/RM structures

A force-based beam element with end plastic hinges (Scott and Fenves 2006), which is currently available in the open-source, object-oriented, finite element program, OpenSees (McKenna et al. 2000), allows inelastic deformations to occur only at the element end regions and thus can be thought of as a lumped-plasticity element. The length of the inelastic regions in the element is defined by the user. The major disadvantage of the lumped plasticity beam-based models compared to the distributed plasticity beam-based models is that the length of the plastic hinge should be assumed before conducting any analysis.

2.2 Distributed plasticity beam-based models

Beam formulations with distributed plasticity, using a layer- or fiber-section model and either a displacement-based (e.g., Kaba and Mahin 1984) or force-based (Zeris and Mahin 1989, Neuenhofer and Filippou 1997) formulation have also been established. Force-based beam elements strongly satisfy the differential equations of equilibrium and are very popular in structural analysis involving earthquake loading. The advantage of distributed plasticity beam elements is that they eliminate the need to estimate a plastic hinge length for each member.

Several efforts (Guedes et al. 1994, Ranzo and Petrangeli 1998, Petrangeli et al. 1999, Martinelli 2008) have modified or enhanced distributed plasticity beam models to account for the effect of shear deformations, through the addition of appropriate springs or by using enhanced element formulations. More recently, Elwood (2004) presented a modeling approach for the analysis of shear failures in RC columns. Essentially, beam-based models were combined with nonlinear shear springs to capture the strength and stiffness degradation associated with shear damage and also the shear-flexure interaction, as shown in Figure 2.1a. The properties of such springs typically rely on empirical equations which provide estimates of the lateral deformations at which shear failure will occur (Elwood and Moehle 2005a). Expressions have also been proposed to capture the effect of shear damage on the occurrence of column axial failure (Elwood and Moehle 2005b), defined as the inability of a column to carry its gravity loads due to the shear damage and pertinent geometric nonlinearity effects.

The model by Elwood (2004) was used by Elwood and Moehle (2008) to capture the response of a three-column, shake-table RC frame specimen for which the middle column incurred shear failure. The analysis provided satisfactory estimates of the response of the specimen until the occurrence of shear failure, after which point the lateral displacements were underestimated. Leborgne and Ghannoum (2013) have shown that their model can capture the results of various quasi-static experimental tests on shear-dominated columns; despite the establishment of algorithms to calibrate the model from experimental data, manual adjustments may still be required to achieve the best possible agreement with experimental results (Leborgne 2012). Additionally, the physical meaning of several parameters in the model, affecting the hysteretic behavior and strength degradation with repeated loading, is somewhat obscure, since it cannot be directly related to the mechanical behavior. The same applies for the model formulated by Elwood and Moehle (2005a).

Mostafaei and Kabeyasawa (2007) added an axial-shear spring to a displacement-based beam element with fiber-section model. Several simplifying assumptions were made to establish coupling equations for the parts of the model describing the axial-shear and the flexure-shear interactions. First, the axial strain in the two springs was taken equal to the axial strain obtained from the interpolation functions of the beam element. Second, the shear coupling was introduced by stipulating that the shear stress is constant over a cross section and that the shear force satisfies equilibrium with the element end moments. The method was shown to provide good estimates of the envelope curve of cyclic tests on shear-dominated columns and has not been shown to provide accurate results for cyclic analyses.

Koutromanos and Shing (2010) used distributed plasticity beam elements with a fiber-section to assess the collapse probability of a set of prototype RM wall buildings designed according to modern standards. The shear deformability of the walls was captured through the addition of horizontal springs to the beam models. The study concluded that there is much room for improvement in the analytical modeling methods, especially for low-rise walls, in which a plane-section assumption may not be accurate. Furthermore, the modeling of walls with openings was identified as a major challenge.

Mullapudi and Ayoub (2010) used force-based beam elements and formulated a fiber-section model accounting for the biaxial stress-strain behavior of concrete and for the existence of transverse reinforcement. The transverse strain was an additional parameter in the analytical solution which was calculated at the sections of each element during the determination of the internal force vector. The plane-stress constitutive law used in the formulation was a coaxial rotating-crack model, which could also account for the biaxial compression and for the reduction of compressive strength due to transverse tension. The model was used for the simulation of a quasi-static and a dynamic shake-table test of shear-dominated column specimens. The validation analyses were conducted for the pre-peak response of shear-dominated columns and no results have been presented to demonstrate capability of the method to capture the strength degradation associated with shear failure.

The fiber-section beam-based models with simplified strain-based failure criteria are widely used in progressive collapse simulation of RC structures. In this method, failure of structural components is captured through definition of strain limits accounting for different types of damage, like rebar rupture/buckling and confined/unconfined concrete crushing. The failed fibers are then deactivated or assigned zero strength, and finally, the element is fully removed from the analysis if all of its fibers have been deactivated.

Talaat and Mosalam (2008) conducted a research on progressive collapse simulation of RC frame structures under different loading scenarios including quasi-static and dynamic excitations. The element removal technique was implemented in OpenSees (McKenna et al. 2000). They have modified previously established uniaxial constitutive laws for reinforcing steel and concrete materials, and defined a strain-based threshold to capture rebar buckling. Iribarren et al. (2011) investigated the behavior of a planar RC frame structure in the context of progressive collapse. Simplified bilinear uniaxial material laws were used to represent concrete and reinforcing steel, and a tensile strain threshold was defined to limit the stress in reinforcement and capture the rebar rupture.

Sagiroglu and Sasani (2013) evaluated the response of a seven-story RC frame building, subjected to a single column removal, to emphasize the importance of catenary action offered by the beams bridging the removed column. The fiber-section beam-based model, exists in the commercial finite element programs, SAP2000 (CSI 2000) and Perform-Collapse (CSI 2006a), was used. The core concrete was represented with a uniaxial material law that can account for confinement effect (Mander et al. 1988) and the reinforcing steel bars were assigned a material law capable of accounting for rebar buckling (Urmson and Mander 2012).

Lu et al. (2013) used the finite element analysis software, MARC (MSC 2005), to analyze a frame-core tube reinforced concrete, high-rise, building subjected earthquake loading. A fiber-section beam formulation, with uniaxial material laws for concrete (Légeron et al. 2005, Mander et al. 1988) and reinforcing steel (Jiang et al. 2005), was used to simulate the beams and columns, while simple layered-shell elements were employed to represent the shear walls. The material models were calibrated by conducting analysis for structural components, and the result were used to propose a set of simple strain-based criteria to include failure modes associated with rebar rupture, rebar buckling and concrete crushing. The methodology, which also accounted for the collision between different structural parts, by means of an appropriate contact algorithm, was then used to simulate the collapse of the building and to identify the critical members for collapse initiation.

Fiber-section beam-based models are a cost efficient computational tool to analyze the RC and RM structures, but they also have some limitations. The method relies on uniaxial material law, and therefore cannot capture the triaxial behavior of concrete material accurately. The increased ductility and strength, offered by modern RC structures, can only be estimated using simplified, design-oriented, equations in which the compressive strength of confined concrete is related only to the transverse reinforcement properties, amount, and configuration (e.g. Mander et al. 1988). In reality, the strength of the confined concrete depends on the level of confining pressure which changes across the section of a flexurally loaded member. Moreover, explicitly capturing failure modes such as tie rupture is not possible, and many damage mechanisms, such as longitudinal rebar buckling and rupture, can only be considered in a simplified fashion. Finally, modeling of shear damage is done using shear springs whose property and location require judgment and whose accuracy is inherently limited. Given the limitations of beam-based models in analysis of RC/RM structures, a number of alternative modeling approaches have been developed and used for analysis.

2.3 Nonlinear truss models

The nonlinear truss model idealizes a RC column or a RM wall as an assemblage of truss cells, each includes horizontal, vertical and diagonal truss elements. The vertical elements are mainly intended to capture the axial-flexural response of the wall, while the diagonal elements capture the inclined compressive field developed due to the combined effect of axial force, shear force and bending moment in the member (Vecchio and Collins 1986). A schematic view of the truss representation of a RC column is depicted in Figure 2.4.

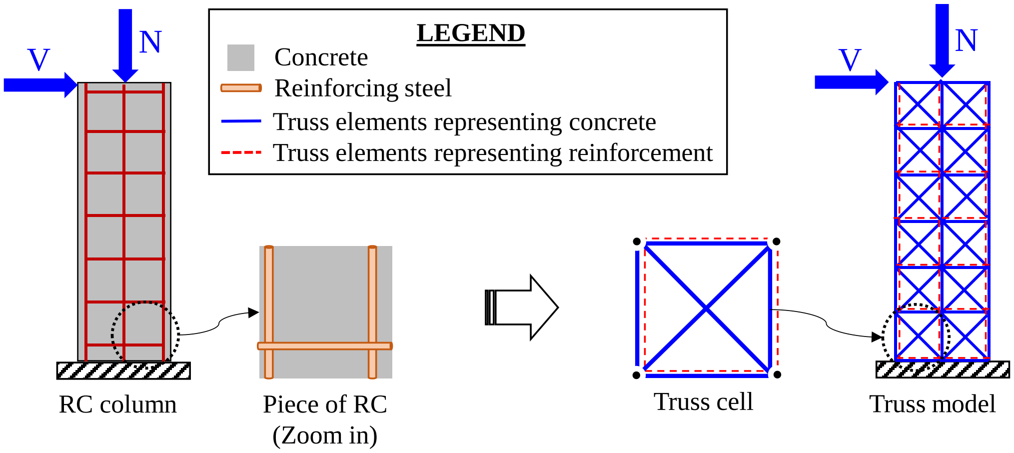

Figure 2.4: Truss representation of a RC column

The truss analogy for reinforced concrete has originated in the work of Ritter and later Mörsch in the early 1900s (Ramirez et al. 1998 and Mazars et al. 2002). They have postulated that a diagonally cracked beam can be simulated by a set of parallel chord truss elements connected with compressive diagonal members inclined at an angle of 45 degree with respect to the beam longitudinal axis. The methodology and geometry of the truss model was built upon by others and gradually became a well-known approach to estimate the shear strength of RC members.

Vallenas et al. (1979) have extended the truss modeling approach to a nonlinear analytical tool to investigate the shear deformation of a multi-story building under monotonic loading. Shear walls at each story were represented using a single truss cell, and the cross-sectional properties of each truss element was obtained using tributary area of each element. Hiraishi (1984) investigated the hysteretic behavior of flexure-dominated shear walls by means of nonlinear truss models. Similar to the work by Vallenas et al. (1979), single truss cells per story were used, and for the sake of simplicity, all elements except the tensile and diagonal chords of the first story were assumed to be perfectly rigid.

Schlaich et al. (1987) used the concept of truss models to develop design guidelines based on strut-and-tie models. Hsu (1996) distinguished the definition of the truss and strut-and-tie models, and integrated existing rotation theories to develop rotating angle softened truss model (RA-STM). Taghdi et al. (2000) employed strut-and-tie models to estimate the monotonic envelope curves of retrofitted masonry and concrete low-rise walls. The strut-and-tie models are a design tool, and are unable to capture hysteretic response of the structural member under cyclic loading. More works and the historical development of the truss models can be found in a report by the ASCE-ACI committee 445 (1998).

Mazars et al. (2002) introduced a truss-based method, termed the equivalent reinforced concrete (ERC) model, to examine the behavior of shear walls. The wall panels were modeled using multiple truss cells per story, each cell including horizontal, vertical, and diagonal elements, similar to the Figure 2.4. The model was, essentially, an adaptation of the framework by Hrennikoff (1941), where elastic properties of truss lattice elements were replaced by nonlinear constitutive laws. Later, Miki and Niwa (2004) proposed a three-dimensional lattice model to capture the torsional and biaxial response of reinforced concrete components. Truss members in conjunction with arch elements were used to represent shear resisting mechanism of RC columns.

Park and Eom (2007) used a truss-based modeling approach where the employed material laws could account for effects of confinement, rebar buckling and rupture. The truss elements geometry was updated by adding non-parallel diagonal elements, fan-type elements; and modified compression field theory (MCFT) by Vecchio and Collins (1986) was used to express the effect of transverse tension on the compressive strength of the diagonal elements. Different case studies, including a beam, a column, and a shear wall, were investigated and a good agreement was reported between the analytically obtained and experimentally recorded hysteretic response of the components. Additionally, a sensitivity analysis was conducted to demonstrate the effect of the configuration and angle of the diagonal elements on the accuracy of the obtained results. Although the approach of Park and Eom (2007) has been shown to be capable of predicting the behavior of structural components, the employed geometry is somehow complicated and cumbersome, potentially limiting the applicability and efficiency of this method.

Panagiotou et al. (2012) used nonlinear truss models to capture the hysteretic response and the failure modes of shear-dominated RC walls. Contrasting to the work by Park and Eom (2007), the truss model by Panagiotou et al. (2012) employed a parallel chord configuration, with identical material properties for all the horizontal elements, all the vertical elements and all the diagonal elements. A uniaxial material law was proposed for concrete and the constitutive law by Dodd and Restrepo (1995) was used for steel to account for yielding, strain hardening and the Bauschinger effect (Dodd and Restrepo 1995). The modified compression field theory was used to define a strength reduction factor, accounting for the effect of tensile transverse strain on compressive strength of diagonal elements. The tensile transverse strain of diagonal elements was measured using a fictitious strain gage element. The mesh-size sensitivity of the model was examined, and proper equations were proposed to regulariaze the softening response of the material law for concrete.

Lu and Panagiotou (2013) expanded the truss model of Panagiotou et al. (2012) to capture the triaxial response of a shear-wall structure. They used beam elements to model the out-of-plane flexural behavior of the walls, while the truss analogy by Panagiotou et al. (2012) was used to capture the in-plane response. The provided analytical results were closly matched the experimental observations, in terms of both the hysteretic response and the damage pattern. Later, Lu et al. (2014) used the beam-truss model (BTM) for the analysis of RC wall specimens under static and dynamic loadings. Equations were proposed to calculate the inclination angle of diagonal elements, and the computation of transverse strain was improved by using the strain-displacement relation of general four-node quadrilateral element. Using beam elements in the boundary regions of the models, i) prevents sliding type shear failure, ii) introduces additional complexity in terms of the definition of beam properties, and finally iii) increases the computational cost unnecessarily.

Compared to beam-based models, nonlinear truss models provide a powerful tool to capture shear damage and axial-shear-flexure interaction in analysis of RC/RM structural components. Additionally, the calibration of the material parameters is straightforward and only relies on material test data. However, the accuracy of the method to predict the flexural capacity of a member depends on the number of vertical elements used to represent an actual structural component. In fact, the vertical elements can be considered as the layers of the layered-section beam-based model.

2.4 Finite element models

The most refined analysis method to analyze the behavior of RC/RM structural components is based on nonlinear finite element (FE) models. In this approach, the actual structure is represented by discretizing its components into a mesh of elements, as depicted in Figure 2.5. Two-dimensional elements with plane-stress formulation or three-dimensional solid elements are commonly used to represent the concrete. The reinforcing steel bars are modeled either explicitly – i.e. with truss or beam elements, or as smeared reinforcement into concrete elements. Slip can also be modeled explicitly by means of springs or contact interface elements or implicitly, by modifying the constitutive law of reinforcing steel material.

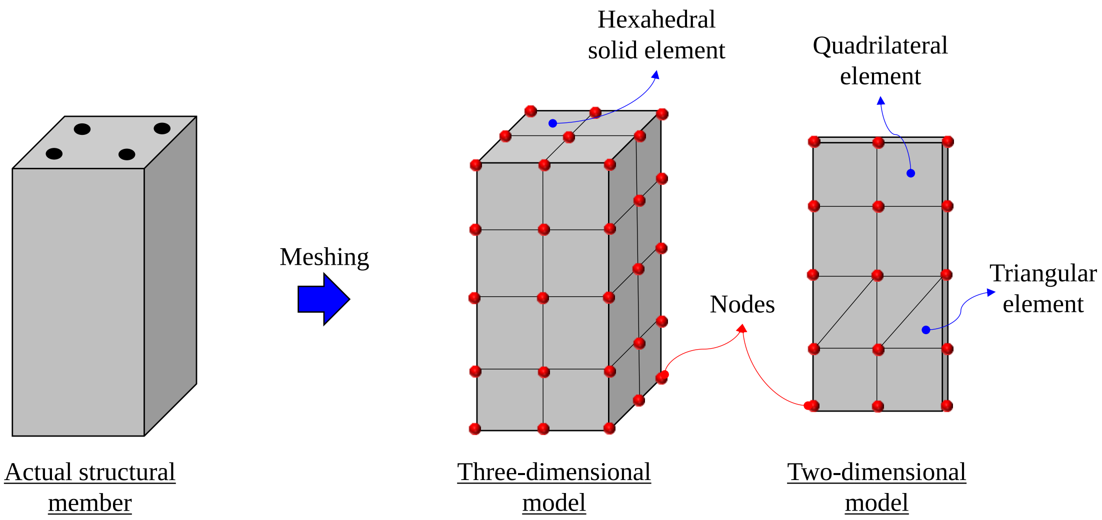

Figure 2.5: Finite element discretization

A major challenge for finite element analysis is the development of an appropriate constitutive law to capture the nonlinear behavior of concrete material accurately. Two main methods are used to account for the tensile cracking of the concrete, namely discrete- and smeared-crack models. In the discrete-crack model, the crack opens with separation of elements and, consequently, nodes. Remeshing techniques or using interface elements are necessary to analyze the cracked RC members. In smeared-crack models, cracking occurs within elements and the response would be handled by constitutive law. Damage-plasticity models can be considered as smeared-crack models.

Scordelis and Ngo (1967) used the discrete-crack models to analyze a RC deep beam. The cracks were initiated and propagated based on principal tensile stresses, and an automatic remeshing technique was used to update the mesh and account for crack propagation. Rashid (1968) used the smeared-crack model to simulate a pressure vessel discretized by triangular plane-stress elements. The steel material was assumed elastic-perfectly plastic, while a Von-Mises criterion with an associative flow rule was used to represent the concrete material.

Yuzugullu and Schnobrich (1972) used two-dimensional triangular elements with plane-stress formulation to analyze a reinforced concrete shear-wall panel, a deep beam and a wall-frame system. Later, Suidan and Schnobrich (1973) have used three-dimensional, twenty-node, hexahedral solid elements in the analysis of a RC beam subjected to monotonic loading. The reinforcing bars were smeared into concrete with elastic-perfectly plastic constitutive law, while the response of the concrete was represented by a Von-Mises yield criterion, and a strain-based threshold to account for crushing.

Bažant and Lin (1988) have proposed a nonlocal smeared-crack model to reflect the size effect observed in the failure of brittle materials. They used both fixed and rotating smeared-crack approaches and have shown that the proposed nonlocal model can precisely capture the size effect law established by Bažant and Oh (1984). Orthogonal and slanted meshes were used, and it was shown that they yield to a similar cracking zones and crack patterns.

Vecchio (1989) used the secant stiffness to establish a simple procedure where the linear elastic formulation can be modified to conduct a nonlinear finite element analysis for membrane RC components. Rebars were smeared into concrete and assigned an elastic-perfectly plastic constitutive law. Concrete was modeled using quadrilateral elements, with plane-stress formulation, and assigned a realistic material model employing the modified compression field theory by Vecchio and Collins (1986). Good agreement was obtained between analytical results and experimental observations and the method was identified as an efficient tool for the analysis of membrane RC structures, subjected to monotonic loadings. Additionally, it has been concluded that in formulation of nonlinear FE problems, the definition of concrete constitutive law is more critical than implementing complex element formulation or solution procedure.

Reinforced masonry structures have also been simulated with finite element models. Analyses have been conducted for structures subjected to both monotonic (Seible et al. 1990a) and cyclic (Seible et al. 1990b) lateral loads. Lotfi and Shing (1991) evaluated the capability of the smeared-crack models to predict the lateral strength of reinforced masonry wall panels subjected to in-plane axial and lateral loadings. The uncracked concrete was represented by J2 plasticity model, while the cracking was accounted for by including softening in the tensile response of concrete material. Good results were obtained for flexure-dominated RM wall specimens, while they have observed the stress lock-in phenomenon caused by continuum-based elements in the analysis of a shear-dominated RM wall. Later, Lotfi and Shing (1994) have proposed an interface element to describe the behavior of mortar joints and to capture the response of unreinforced masonry panels. The interface element formulation was further enhanced by decomposing interface displacement components into an elastic part, a plastic part to represent crack opening, sliding, and compaction, and a geometric part to simulate reversible shear dilatation (Mehrabi and Shing 1997).

Finite element models have also been used for analysis of RC structures subjected to cyclic loadings. Several studies have used two-dimensional models with plane-stress formulations to analyze RC members (Kwan and Billington 2001, Palermo and Vecchio 2004, Kim et al. 2005), and even a more complex system such as infilled RC frame (Koutromanos et al. 2011). Koutromanos and Shing (2012) have proposed a cohesive-crack interface element to capture the response of RC and RM structures under seismic loading. The model was formulated for plane-stress conditions with the hyperbolic yield criterion of Lotfi and Shing (1994) to represent the interface elements response. Truss elements with a uniaxial elastoplastic constitutive law were used to model the reinforcing bars. Very good results were obtained for shear-dominated structural components; however, since the model cannot account for concrete triaxiality, it is inappropriate for the simulation of RC structures with high level of confinement.

Ahmadi et al. (2015b) conducted nonlinear dynamic finite element analyses for two shear-dominated RM wall specimens. The models used simplified layered-shell elements with smeared reinforcement, available in the commercial program, PERFORM-3D (CSI 2006b). Each layer of the shell element was assigned a trilinear uniaxial constitutive law to represent masonry and reinforcing steel material. Although their analyses provided excellent estimates of the performance of the structure at early stages of damage, it did not capture the strength and stiffness degradation caused by severe shear cracking.

Recent studies have adopted three-dimensional, continuum-based FE models to investigate the behavior of RC components under impact (Murray et al. 2007, Lin et al. 2014) and monotonic loading (Grassl and Jirásek 2006a, Zheng et al. 2009). Murray et al. (2007) proposed a concrete constitutive law mainly for impact loading, and used the finite element program, LS-DYNA (LSTC 2007), to evaluate the applicability of the material model in simulation of vehicle that collides with roadside safety structure. The material model has been formulated with a single scalar damage parameter in tension and compression. Therefore, as explained in Section 3.1, such models can only be used for structures under monotonic and impact loadings.

Different structural components have been considered, including reinforced or fiber-reinforced concrete columns (Grassl and Jirásek 2006, Teng et al. 2015), frames (Bao et al. 2012, Sasani et al. 2011), precast beam-to-column connections (Kaya and Arslan 2009), slabs (Thiagarajan et al. 2015), post-tensioned bridge girders (Gangi 2015), composite bridge decks (Barth and Wu 2006, Chung and Sotelino 2006), and hybrid moment-resisting frame systems (Noguchi and Uchida 2004). These studies have validated the capability of FE models to capture the monotonic force-displacement response of RC components. However, less attention was paid for analysis of RC structures under cyclic loadings.

A few studies have also employed three-dimensional FE models for the analysis of shear walls (Faria et al. 2004, Spiliopoulos and Lykidis 2006) and beam-to-column connections (Eligehausen et al. 2006, Hawileh et al. 2010, and Deaton 2013) under cyclic loading. Faria et al. (2004) have used a simplified version of the material model by Faria et al. (1998) to investigate the seismic behavior of an arch dam and to reproduce the hysteric response of a small-scale six-story RC shear-wall subjected to base excitation. The analytical results satisfactorily matched the experimental observation; however, the fact that the material model does not allow any irreversible strain to form, may render the model inappropriate for cyclic loading.

Spiliopoulos and Lykidis (2006) modified the smeared-crack model by Kotsovos and Spiliopoulos (1998), and used it in relatively simple three-dimensional finite element models to capture the hysteretic response and damage patterns of RC structures under cyclic loading. The analysis was performed on a RC shear wall subjected to quasi-static cyclic loading and a two-story frame structure subjected to a sequence of ground motions. The analyses satisfactorily captured the peak lateral strength of the specimens, but they did not accurately capture the hysteretic response and energy dissipation. Additionally, all of the analyses permanently terminated due to failure to satisfy the convergence criteria.

Eligehausen et al. (2006) used the microplane model by Ožbolt and Kožar (2001) to simulate a RC beam-to-column joint subjected to quasi-static monotonic and cyclic loading. The reinforcement was modeled with truss elements with a simplified, trilinear, stress-strain curve. The bond-slip response of the reinforcement was explicitly accounted for using appropriate elements. It has been shown that the continuum model can potentially capture severe shear failure including the formation of a large diagonal shear cracks; however, the analytically obtained strength and stiffness degradation were more than those observed in the experimental tests.

Hawileh et al. (2010) developed a three-dimensional finite element model, using the commercial finite element program, ANSYS (CSC 2009), to study the response and predict the behavior of a precast beam-to-column connection which was experimentally tested under cyclic loads. In the analytical model, the longitudinal reinforcing bars and post-tensioning strands were modeled using hexahedral solid elements while other rebars were represented by link elements. The concrete was modeled by hexahedral solid elements assigned the yield criterion of Willam and Warnke (1975). Besides the fact that the experimental data were post-processed to better match the analytical results, i.e. to remove the effect of hydraulic jack relaxation during the load reversal from the experimental data, the methodology involved other simplifications. For example, the concrete crushing was turned off due to numerical difficulties and the rebar rupture was not accounted for, while the actual specimen failed due to rebar rupture.

Deaton (2013) developed three-dimensional finite element models in the commercial software, DIANA (TNO DIANA 2011), to numerically examine the nonlinear behavior of a set of beam-to-column joints representing old construction. The concrete was modeled using the triaxial material law by Selby and Vecchio (1997) and the behavior of the steel was described with the uniaxial law by Filippou et al. (1983). The model was validated using the results of experimental tests on beam-to-column connections. Good agreement between analytically obtained hysteretic response and experimentally recorded data was observed. However, similar to the work by Faria et al. (2004), the adopted concrete material model cannot account for the formation of plastic strain, and therefore, it may be inappropriate for capturing the hysteretic response and energy dissipation.

The issue associate with the triaxial material model by Selby and Vecchio (1997) is discussed in Section 3.1.

Finite element models have also been used in the context of progressive collapse simulations, where one or more gravity resisting members will be removed from the analysis, and the rest of the structure will be analyzed under amplified vertical forces. Sasani et al. (2011) used the commercial finite element program, DIANA (DIANA TNO 2011), to examine the effect of rebar fracture on overall response of a planar two-bay RC frame structure. The concrete and longitudinal reinforcement were modeled with twenty-node hexahedral solid elements, while the ties were modeled with truss elements embedded in the concrete. They attempted using a material law with Drucker-Prager type yield criterion for the concrete. This law encountered convergence problems for stress states in which a crack was open in one direction while the concrete was softening in the other direction (Sasani and Kropelnicki 2008, Yu et al. 2010). Accordingly, a simpler material model, based on the uniaxial constitutive law by Mander et al. (1988), was combined with a rotating smeared-crack model and used to describe the stress-strain relationship of the confined core concrete material. The use of such a simplified material law inherently limits the accuracy of the model for the analysis of more complicated structures or structures subjected to complex loading scenarios. Additionally, the methodology to consider rebar rupture was based on analysis repetition, which introduces additional unnecessary burden to the computational cost of FE simulation.

Kwasniewski (2010) simulated the progressive collapse of an eight-story, steel-frame, building, using the commercial software, LS-DYNA (LSTC 2007). The steel material was modeled based on Von-Mises yield criterion, while the Karagozian and Case (K&C) concrete model (Schwer and Malvar 2005) was used to represent the concrete slabs. As explained in Section 3.1, the specific material model is originally developed for blast simulation, therefor it is not appropriate for cases involving cyclic loads.

Given the issues pertaining to available multiaxial concrete models (as explained by Sasani and Kropelnicki 2008, Yu et al. 2010, Deaton 2013, Murcia-Delso 2013, Moharrami and Koutromanos 2016), and due to the lack of accounting for severe rebar damage, e.g. rebar buckling and rupture, the research community does not have the capability for reliable, three-dimensional finite element analysis of damage and failure in RC structures under earthquake loading. The present study is aimed to address this need through the formulation and validation of a finite element modeling scheme.

2.5 Other analysis methods

Several studies have also established and used models that rely on either phenomenological force-displacement relations assigned to discrete spring elements or use homogenization at the material level. Luccioni et al. (2004) used the program AUTODYN (CSC 2009) to simulate the impact of blast loading and subsequent collapse of a RC frame building. Hexahedral solid elements with homogenized material properties were used to model RC frames and infilled masonry walls. A set of simple tension cut-off criteria were defined to remove the element from the analysis accounting for the damage due to cracking. They claimed, without any supporting data, that the homogenized material parameters were obtained by comparing detailed and simplified modeling of a column located in the first story of the building. The work itself was a state-of-the-art in terms of modeling the actual event and visualizing the analytically obtained damage pattern and debris distribution. However, at least a displacement history record of a structural component is deemed necessary to judge the accuracy of such models.

Li and Li (2004) enhanced the multi-vertical-line-element model (MVLEM), previously established by Kabeyasawa et al. (1983) and gradually improved and used by others (Vulcano et al. 1988, Ghobarah and Youssef 1999, Linde 1993, Chen and Qian 2002). As depicted in Figure 2.6a, the method used five vertical springs to account for the flexural response and five shear springs to include the shear deformation. Two constitutive models for the concrete and reinforcing steel were coupled in parallel and used for the axial springs. The shear springs used an empirical constitutive law that was calibrated by means of experiments on nine reinforced concrete walls. In addition to the inherent inability of such modeling approach to predict the deformation and damage pattern of an actual structure, the analytical results were only provided for monotonic loading.

Lowes and Altoontash (2003) developed a 4-node, 12-degree-of-freedom macroelement aimed to capture the shear response of the joint panel and the bond-slip effect of the reinforcing steel. Improvements to the model were made by Mitra and Lowes (2007), while Anderson et al. (2008) developed a cyclic shear stress-strain law for joints with no transverse reinforcement which can be used in the macroelement by Lowes and Altoontash (2003) for simulations of non-ductile RC frame structures.

Bao et al. (2008) implemented the macromodel by Lowes and Altoontash (2003) in the finite element program, OpenSees (McKenna et al. 2000), to simulate the response of a beam-to-column connection subjected to a monotonic loading. Corotational forced-based beam elements with fiber discretization were used to model the beams and columns while the joint region was represented by the macromodel of Lowes and Altoontash (2003) that accounts for the shear deformation and bar pullout. As depicted in Figure 2.6b, the model combines three different types of springs: i) rotational springs to account for joint shear deformation, ii) shear springs to account for shear deformation and possible sliding at the beams-joint interface, and iii) a set of springs in series to account for flexural response and bond deterioration. Appropriate uniaxial material laws were used for the concrete and steel fibers, and a procedure was proposed to calibrate the properties of each spring. The model was calibrated based on the results obtained from three-dimensional nonlinear FE analysis on a beam-to-column joint, and then was used to simulate the progressive collapse of a multi-story RC building.

Caliò et al. (2012) proposed a discrete element model to capture the in-plane behavior of unreinforced masonry structures. The model was based on the concept of macro-element discretization in which the wall was idealized as an assemblage of macro-elements interacting with each other by means of boundary springs. As depicted in Figure 2.6c, the basic macro-element consists of four rigid edges, with hinged connections, forming a rectangle. Two diagonal springs govern the shear behavior while the flexural and sliding response and also the interaction between adjacent macro-elements are captured by adding distributed springs around the articulated quadrilateral element. Caliò et al. (2012) validated the proposed model for an unreinforced masonry wall system subjected to a cyclic loading. While the presented crack patterns fairly resembled the observed damage of the actual experiment, the provided hysteretic response did not capture the experimentally recorded force-displacement curve, especially in terms of energy dissipation.

Gu et al. (2014) proposed the use of discrete element method (DEM) to model RC frame structures subjected to earthquake or blast loading. In this approach, rigid cubic elements are connected with zero-length springs, as depicted in Figure 2.6d. Uniaxial, multilinear, hysteretic laws were assigned to springs representing concrete and steel materials, and a set of failure criteria were defined to account for the damage. The analytically obtained displacement histories and the damage patterns were compared with the test results. Although good agreement was reported in predicting the failure modes, the provided analytical displacement history matched the recorded data only at the initial stage of loading.

In the aforementioned modeling techniques, the material behavior is defined using simplified uniaxial relations that rely on empirical equations. Thus, the accuracy of such methods is inherently limited. The nonlinear truss analogy can capture the shear damage and the axial-shear-flexure interaction more accurately, while relying on conceptually simple uniaxial stress-strain laws for concrete and reinforcing steel.

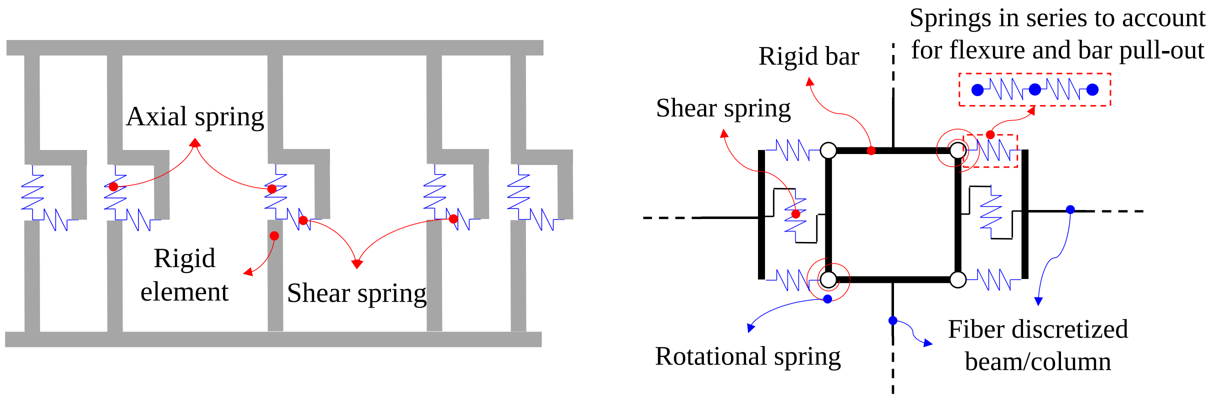

(a) Multi-vertical-line-element model for shear wall

(b) Macromodel for RC joint

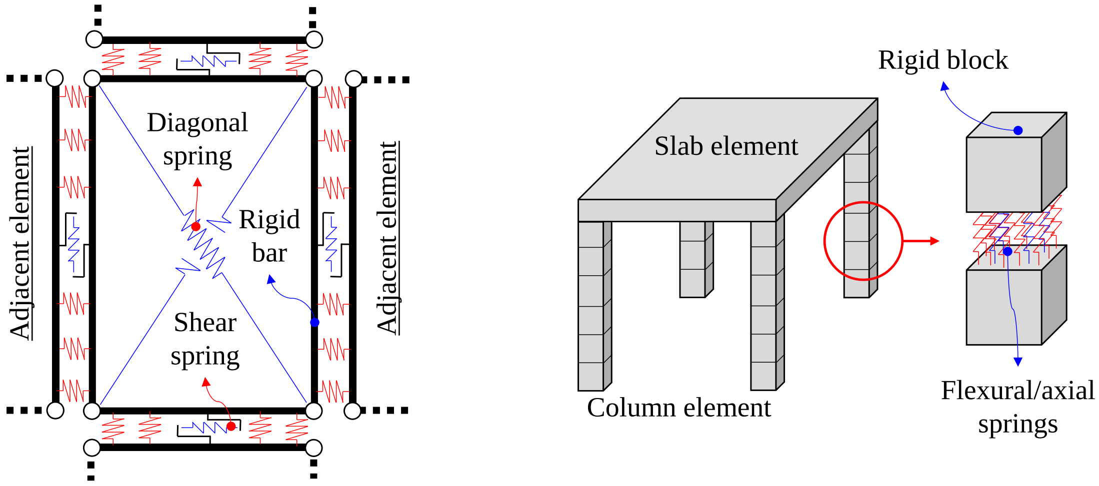

(c) Macro-element model for masonry panel

(d) Discrete element method for RC members

Figure 2.6: Discrete modeling techniques in the simulations of RC/RM structures

Chapter 3 : Triaxial Constitutive Model for Concrete under Cyclic Loading

This chapter provides the formulation of a new material model for the analysis of concrete under multiaxial, cyclic loading conditions. Essentially, an elastoplastic formulation, having a non-associative flow rule to capture compression-dominated behavior, is combined with a rotating smeared-crack model to capture the tension-dominated response. The proposed formulation resolves the issues which exist in many available concrete material models, related to properly capturing the crack opening and closing behavior and accounting for the effect of confinement on the strength and ductility under compression-dominated stress states. The accuracy of the model is validated at the material level by performing finite element analysis for simple models subjected to a variety of loading scenarios.

It is important to note that, despite many available triaxial concrete models which commonly require a large number of material parameters to be calibrated, the calibration of the proposed material model is straight forward and relies on monotonic test data.

3.1 Issues associated with existing triaxial concrete models

Reinforced concrete structures are common in earthquake-prone areas, where cyclic loading can lead to the opening and subsequent closing of cracks. Additionally, significant compressive strains are expected to occur in, e.g., the compression zone of the inelastic hinge regions in flexural members such as beams or columns. Modern design standards stipulate that, for structures located in regions with high seismicity, inelastic deformability of the concrete under compression must be ensured by means of transverse reinforcement which leads to the development of a confining pressure. This confinement effect has been found to lead to an increase in the compressive strength, ductility and strain capacity of concrete, and more importantly, it improves the deformability of RC components (Mander et al. 1988, Imran and Pantazopoulou 2001).

Typically, the analysis of RC structures such as frames and walls is conducted with models based on uniaxial stress-strain laws. Such models are numerically efficient and allow systematic parametric investigations, but they inherently lack the capability to accurately describe the behavior of regions like beam-to-column joints, shear keys etc., where multiaxial stress states may develop in the concrete. Additionally, the effect of confinement contributed by the transverse reinforcement is accounted for in these models by a prior adjustment of the parameters of the uniaxial material models using simplified equations (e.g., Mander et al. 1988). The only means to accurately determine the behavior of regions where multiaxial stress states develop is to use continuum-based finite element analysis with appropriate constitutive models which can capture the interaction of the various stress and strain components.

Early work by Willam and Warnke (1975), Ottosen (1977) and Hsieh et al. (1982) provided triaxial failure criteria for concrete. These studies were the first efforts to account for the salient features of concrete behavior, such as the different strength values of the compressive and tensile meridian and the impact of the third deviatoric invariant of the stress tensor on the failure state. Although the early failure criteria were primarily useful for simplified failure analyses, they were instrumental for the establishment of the yield surface in many multiaxial inelastic models which were subsequently developed.

The total-strain rotating-crack model by Selby and Vecchio (1997), which is essentially an orthotropic damage model, relies on the modified compressive field theory (Vecchio and Collins 1986) and establishes the stress as the product of the strain times a secant stiffness matrix. While this model is numerically robust and can account for the crack opening and closing behavior and the effect of confinement, the fact that no irreversible compressive strains develop, as depicted in Figure 3.1a, may render it inaccurate for simulations involving cyclic loading. Furthermore, the adjustment of the material law to account for the confinement effect is somewhat vague, because a modification for confinement is made only for the minimum principal compressive stress.

Damage-plasticity models based on a single scalar damage parameter, like the one by Murray (2007), are also available. Since they have been primarily developed for monotonic or impact loading, they cannot be used for analyses involving cyclic loading. An example case demonstrating potential issues with this type of models is demonstrated in Figure 3.1b for an analysis focusing on a cyclic uniaxial strain history. The figure shows that the tensile strength degradation due to cracking is accompanied by an identical degradation of compressive strength. This is not the case for concrete subjected to cyclic loading.

The Karagozian and Case (K&C) concrete model (Malvar et al. 1997, Schwer and Malvar 2005, Magallanes et al. 2011, Crawford et al. 2012) uses three independent strength surfaces – namely the yield strength surface, the maximum strength surface and the residual strength surface – to interpolate and obtain the failure surface of the material. Similar to the model by Murray (2007), the K&C model originally has been developed for impact and monotonic loading, and therefore, it is not accurate for the analysis involving cyclic loads. Essentially, the constitutive laws are established using a single internal damage parameter; hence, as depicted in Figure 3.1c, degradation in tension would be followed by same amount of strength reduction in compression, which is not the case for RC structures subjected to cyclic loading.

A damage-plasticity model which has been used for the analysis of components and systems is the one by Lee and Fenves (1998), which is the improved version of the model originally developed by Lubliner et al. (1989). This material law uses two scalar damage parameters to describe the effect of tensile cracking and inelastic compressive strains. While the model can give good accuracy for monotonic analysis, it has several issues which may not allow its use for simulations involving cyclic loading. One such issue is demonstrated in Figure 3.1d, for a single-element subjected to a uniaxial cyclic strain history. It can be seen that, after reaching tensile strains in the order of 0.1% – a value which is fairly low for reinforced concrete flexural members, since it would roughly correspond to a steel stress which is half of the yield stress – unloading does not lead to sufficient crack closure before compressive stresses develop. If the material parameters are modified to better capture the crack closing behavior, the stress update algorithm fails to converge. The specific issues of the model by Lee and Fenves (1998) have also been described in Murcia-Delso (2013). Issues also exist with models based on the smeared-crack model. Specifically, Deaton (2013) has reported that the models of De Borst and Nauta (1985) and Maekawa et al. (2003) lead to either numerical convergence failures in the stress update or to inaccurate results.

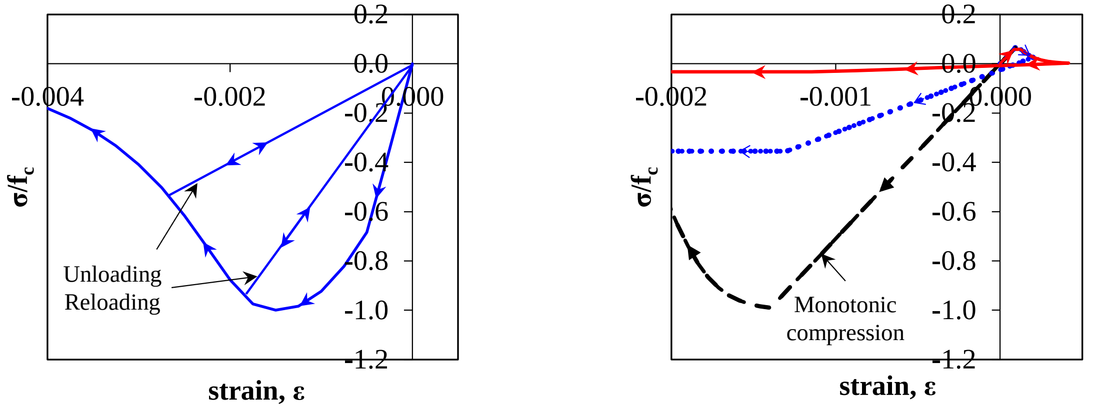

(a) Selby and Vecchio (1997)

(b) Murray (2007)

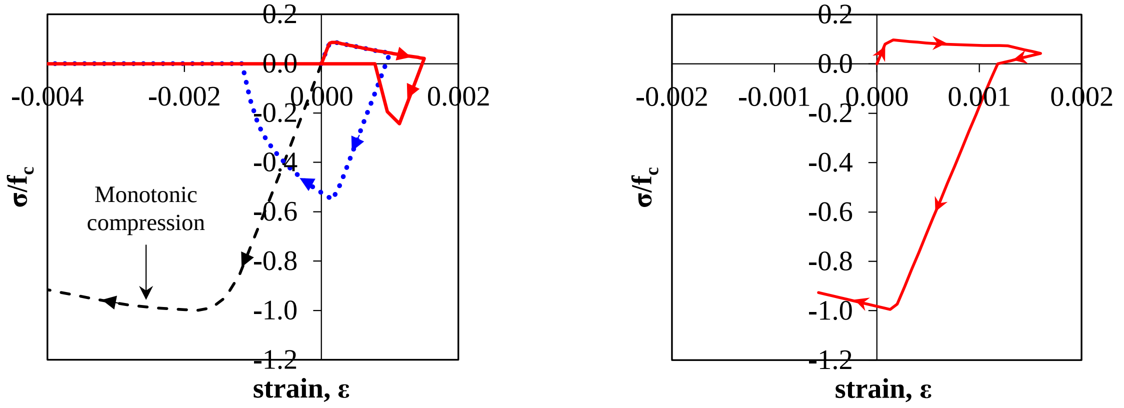

(c) Karagozian and Case (1998)

(d) Lee and Fenves (1998)

Figure 3.1: Issues of available damage-plasticity models pertaining to the behavior for a uniaxial strain history involving crack opening and subsequent crack closure and compressive loading.

Grassl and Jirásek (2006a) compared different aspects of plasticity and damage-plasticity models and proposed a damage-plasticity model for the analysis of RC structures. The model was used only for the analysis of a RC column subjected to axial force with and without eccentricity. Nguyen and Korsunsky (2008) presented the thermodynamic formulation for a non-local damage-plasticity model, and provided strategies for the calibration of the material parameters. The model was used for analysis of a RC beam subjected to three-point bending and uniaxial tension tests. Neither the model by Grassl and Jirásek (2006a) nor the one by Nguyen and Korsunsky (2008) were used for cyclic analysis of RC structural components.

Červenka and Papanikolaou (2008) used the idea of multi-surface plasticity model (Simo et al. 1988) to develop a fracture-plastic constitutive law for concrete material. Essentially, they combined the plasticity model by Menetrey and Willam (1995), for concrete under compression, with a Rankin type failure criterion, for material under tensile cracking. The methodology relies on solving two dependent nonlinear equations (yield functions) to find two distinct plastic multipliers for tensile and compressive yield criteria. Single-element analyses were performed to evaluate the behavior of the model in terms of crack opening/closing and compression-induced crushing. The model was also implemented in the commercial finite element program, ATENA (Červenka Counsulting *s.r.o* 2016), to investigate the numerical stability and the accuracy of the model in the analysis of a RC beam and RC columns subjected to monotonic loads. The provided results were in good agreement with the experimental records; however, no cyclic analysis was conducted to support the applicability of the model to simulate RC structures under seismic loading.

Valentini and Hofstetter (2013) reviewed the performance and the accuracy of two selective triaxial concrete models namely the extended Leon model, developed by Etse and Willam (1994) and improved by Pivonka (2001), and the damage-plasticity model by Grassl and Jirásek (2006a). Single-element analyses were performed to demonstrate the superiority of damage-plasticity constitutive laws over plasticity models. Subsequently, the enhanced version of the damage-plasticity model, which uses modified evolution law for the damage variable (Mohamad-Hussein and Shao 2007), was implemented in a finite element program to examine the performance of the material model in the analysis of a squat RC column. The model was subjected to cyclic load, only for the first three cycles of loading, and then pushed monotonically to calculate the envelope response curve. Valentini and Hofstetter (2013) reported that using a larger number of load cycles in the numerical simulation led to underestimation of stiffness and strength, because the material models by Grassl and Jirásek (2006a) and Mohamad-Hussein and Shao (2007) were developed for monotonic loading only.

Another family of material models for concrete is based on microplane concept originally proposed by Bažant and Oh (1983) and further developed by Bažant and Gambarova (1984). In this method, the strain tensor was projected on many special planes with arbitrary orientations, named microplane, to provide equivalent vector form representation. The one to one correspondence relation then was written between the components of strain and stress vectors, to circumvent the need for tensorial calculations. The tensorial properties, e.g. invariants, were preserved by means of kinematic constraint defined between the orientation of microplanes and the strain and stress tensors. The stress tensor then finally was obtained by integration over the calculated stress vectors (Bažant et al. 2000).

The recently developed M7 version of the microplane model (Caner and Bažant 2012a, 2012b) provides an algorithmically robust formulation since the stress update procedure is explicit. Still, the M7 model is somehow complicated, because it includes many parameters requiring calibration. Caner and Bažant (2012b) have provided recommended ranges for the values of the various parameters, but the impact of one parameter on the behavior of the model for various types of loading may be hard to predict. For example, changing the value of a parameter which primarily affects the behavior of the model for uniaxial compression may also affect the behavior for uniaxial tension. Furthermore, the M7 model may not be well-suited for simulations of large structural systems, since it requires a large number of history variables in each quadrature point of a finite element model.

A variety of similar material models, with different types of formulations, is available today. Several of them employ damage-plasticity formulations (Wu et al. 2006, Nguyen and Korsunsky

2008, Valentini and Hofstetter 2013) while others rely on plasticity formulation (Kang et al. 2000, Papanikolaou and Kappos 2007, Wolf 2008). All of these models have been used either for monotonic loadings, or for the simulations of cyclic loadings only at the material level.

Given the aforementioned issues pertaining to available multiaxial constitutive models for concrete, a sufficiently accurate and numerically efficient material model to allow the analysis of components such as beam-to-column joints under cyclic loading is much needed. The following section describes the formulation of a material model for the analysis of RC structures subjected to cyclic loading, with an emphasis to analysis under earthquake loading. The model can capture all the aspects of behavior, such as compressive crushing, strength and stiffness degradation due to cracking, and the effect of confinement on the material strength and ductility. The strain vector is essentially decomposed into three parts, namely an elastic part, a plastic part and a cracking part. The plastic part is to capture inelastic strains associated with compressive stresses, while the cracking part is to calculate the uniaxial tensile stress from crack opening strain. The model is validated by conducting various single-element analyses and comparing the analytically calculated stress-strain curves with either available experimental data or the empirical model by Maekawa et al. (2003).

3.2 Description of model

This section describes in detail the new triaxial constitutive law for concrete material (Moharrami and Koutromanos 2016). At first, the model is formulated for cracked and uncracked concrete materials separately, and then a set of compatibility criteria are proposed to combine the two material models and form a unified material constitutive law. Finally, an iterative stress update algorithm is established to satisfy the compatibility requirements.

3.2.1 Uncracked elastoplastic material

The behavior of the uncracked material is governed by an elastoplastic constitutive model. The formulation is established in total form, in accordance with the following equation.

$$\{\sigma\}=[D]\{\varepsilon^{el}\}=[D]\left(\{\varepsilon\}-\{\varepsilon^{pl}\}\right) \tag{3.1}$$

where $\{\sigma\}$ is the stress vector, $\{\varepsilon^{el}\}$ is the elastic strain vector, and $\{\varepsilon\}$, $\{\varepsilon^{pl}\}$ are the total and plastic strain vectors, respectively. The stress-strain law can also be formulated in the principal stress-strain space as follows.

$$\{\hat{\sigma}\}=\left[\hat{D}\right]\{\hat{\varepsilon}^{el}\} \tag{3.2}$$

where $\{\hat{\sigma}\}$ and $\{\hat{\varepsilon}^{el}\}$ are column vectors containing the principal stresses and principal elastic strains, respectively. Assuming that the elastic stiffness matrix, $\left[\hat{D}\right]$, is that of an isotropic material, its components can be expressed in terms of the elastic modulus, *E*, and Poisson's ratio, *v*, as follows.

$$\left[\hat{D}\right]=\frac{E}{(1+v)(1-2v)}\begin{bmatrix}1-v & v & v\\ v & 1-v & v\\ v & v & 1-v\end{bmatrix} \tag{3.3}$$

The yield surface in the principal stress space can be described, generally, by the following equation.

$$f\left(\{\hat{\sigma}\},\kappa\right)=\frac{1}{1-\alpha}\left[\alpha\cdot I_1+r(\theta,e)\sqrt{3J_2}+\beta\langle\hat{\sigma}_{\max}\rangle-\gamma\langle-\hat{\sigma}_{\max}\rangle\right]-c_c\left(\kappa\right)=0 \tag{3.4}$$

In Equation (3.4), the symbol $\langle\ \rangle$ denotes the Macaulay bracket, I_1 and J_2 are the first invariant and second deviatoric invariant, respectively, of the stress tensor, c_c is a compressive strength parameter which can be shown to be equal to the uniaxial compressive strength, κ is a hardening parameter expressing the cumulative effect of inelastic deformation, α, β and γ are dimensionless material parameters, $\hat{\sigma}_{\max}$ is the principal stress with the maximum algebraic value, and *r(θ,e)* is a dimensionless factor, termed the radial distance in Kang et al. (2000) and defined by the following equation.

$$r(\theta,e)=\frac{4(1-e^2)\cos^2\theta+(2e-1)^2}{2(1-e^2)\cos\theta+(2e-1)\sqrt{4(1-e^2)\cos^2\theta+5e^2-4e}} \tag{3.5}$$

Parameter *e*, termed the eccentricity, describes the deviation of the shape of the yield surface in the deviatoric plane from a circle, and it is a function of the first invariant, I_1, of the stress tensor, in accordance with Kang et al. (2000).

$$e=\frac{\sqrt{3}c_t-5.5c_c}{I_1/\sqrt{3}-5.5c_c} \tag{3.6}$$

where c_t is a tensile strength parameter. The radial distance, *r(θ,e)*, also depends on the Lode angle, *θ*, which is a polar angle in Haigh-Westergaard coordinate that ranges from 0 to π/3, and can be found from the following equation.

$$\theta=\frac{1}{3}cos^{-1}\left(\frac{3\sqrt{3}}{2}\frac{J_3}{\sqrt{J_2{}^3}}\right) \tag{3.7}$$

where J_3 is the third deviatoric invariant of stress tensor.

The general yield criterion presented in Equation (3.4) can be turned into the surface proposed by Lubliner et al. (1989) by setting the value of *r(θ,e)* equal to 1 or further to the yield surface used by Lee and Fenves (1998) with assuming zero value for parameter *γ*. These yield surfaces are schematically shown in Figure 3.2. Parameter *γ* expresses, for a given value of pressure, the ratio of the octahedral shear stress on the compressive meridian over the corresponding value on the tensile meridian, and it can be set equal to 3 for Lubliner et al. (1989) yield surface. Parameter *β* can be assigned a constant value (Lubliner et al. 1989) or can be defined as a function of the hardening variable (Lee and Fenves 1998).

By assigning zero values for both β and γ in the yield criterion by Lubliner et al. (1989), a Drucker-Prager yield surface will be attained, which is schematically presented in Figure 3.2. The specific yield criterion was also used by Lee and Fenves (1998) for compression-dominated state of stress. In Equation (3.4), parameter α accounts for increase in strength due to confinement and can be determined from the following expression (Lubliner et al. 1989).

$$\alpha = \frac{f_b - f_c}{2f_b - f_c} \tag{3.8}$$

where f_c is the uniaxial compressive strength of the material and f_b is the biaxial compressive strength. If the value of α assumed to be zero in the Drucker-Prager yield criterion, the simple Von-Mises yield surface would be obtained, which is pressure independent and, hence, appropriate for constitutive modeling of steel material.

Although the fairly simple Drucker-Prager surface has been characterized as inaccurate for capturing the multiaxial response of concrete, it can be used as a starting point to ensure a numerically efficient and robust material model which allows the simulation of RC components and systems. In this work, the Drucker-Prager yield surface is used for the validation analysis at the material level, presented in following sections, and for the verification analyses conducted for RC components in Chapter 4. In Section 4.3, the performance of the yield surface by Lubliner et al. (1989) is investigated and the issue pertaining to the overestimation of compressive strength of confined concrete and, consequently, structural member is demonstrated.

To have an accurate yield criterion while maintaining the numerical efficiency of the material model, a new yield surface is derived by setting the value of β and γ equal to zero in Equation (3.4). The modified yield surface can be expressed using the following expression.

$$f\left(\{\hat{\sigma}\},\kappa\right) = \frac{1}{1-\alpha}\left[\alpha \cdot I_1 + r(\theta,e)\sqrt{3J_2}\right] - c_c\left(\kappa\right) = 0 \tag{3.9}$$

For a given value of pressure and for stress states other than triaxial compression, the radial distance, $r(\theta,e)$, leads to decreased material strength compared to that predicted by the Drucker-Prager model. For this reason, the coefficient, α, which is determined to provide a target ratio of biaxial compressive strength f_b over f_c, should be increased compared to the value obtained from Equation (3.8) to attain correct biaxial compressive behavior. If the modified yield criterion and the Drucker-Prager criterion are to provide the same ratio of f_b over f_c, the value of α for the modified criterion must be 2.68 times greater than that of the Drucker-Prager criterion.

The Drucker-Prager yield surface is compared with the proposed criterion in two-dimensional (2D) plane in Figure 3.2c. For decreasing values of I_1 (i.e., for larger confinement effect), $r(\theta,e)$ assumes values close to 1 for the entire range of θ values. Thus, for large confining pressures, the modified surface tends to coincide with a Drucker-Prager surface as shown in Figure 3.2a.

The capability of the modified yield surface to capture the hysteretic response and behavior of RC members is validated in Section 4.3. Then the proposed yield surface is used for all simulations presented in Chapters 5 and 6.

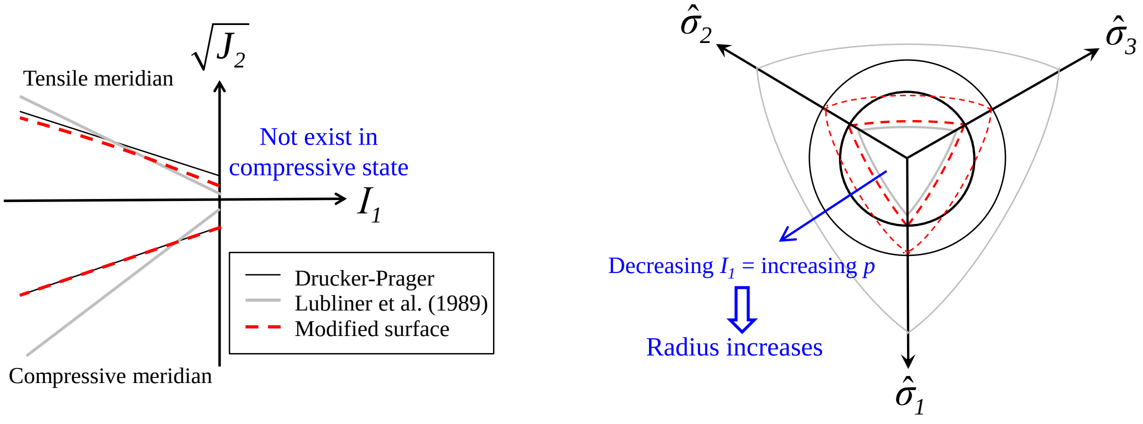

(a) Meridional plane

(b) π-plane

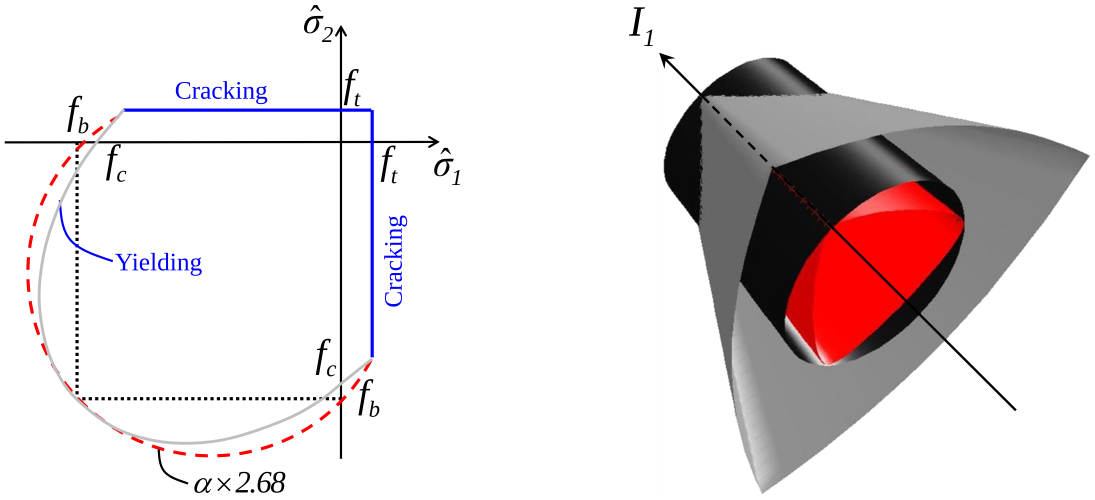

(c) 2D plane (d) 3D view

Figure 3.2: Different yield surfaces used for formulation of elastoplastic material model

The plastic potential function for the present model is described by the following equation.

$$g = \alpha_p \cdot I_1 + \sqrt{2J_2} \tag{3.10}$$

where α_p is a dilatancy parameter, controlling the volumetric expansion of the material due to inelastic behavior. Differentiating Equation (3.10) with respect to the stress components gives:

$$\frac{\partial g}{\partial \sigma_{ij}} = m_{ij} = \alpha_p \delta_{ij} + \frac{s_{ij}}{\sqrt{2J_2}} \tag{3.11}$$

where δ_{ij} is the Kronecker delta and s_{ij} is the ij-component of the deviatoric stress tensor. The plastic strain rate tensor and the total and deviatoric stress tensors can be proven to be coaxial, i.e. they have the same principal directions. This allows to establish a mathematical expression providing the rate of plastic strain in the three principal directions:

$$\dot{\hat{\varepsilon}}_i^{pl} = \dot{\lambda}\left(\alpha_p + \frac{\hat{s}_i}{\sqrt{2J_2}}\right), \ i = 1,2,3 \tag{3.12}$$

The strength of the material changes with the accumulation of inelastic strains in accordance with the following hardening-softening law (Lee and Fenves 1998).

$$c_c(\kappa)=\frac{f_o}{a}\left[(1+a)\sqrt{\varphi(\kappa)}-\varphi(\kappa)\right]\geq f_{res} \tag{3.13}$$

where f_{res} is the residual compressive strength in the material, κ is a non-negative hardening variable which is initially equal to zero, f_o and a are material constants, and $\varphi(\kappa)$ is an increasing function given by the following equation:

$$\varphi(\kappa)=1+a(2+a)\kappa \tag{3.14}$$

The evolution of κ is governed by the following rate equation.

$$\dot{\kappa}=(1-r).\frac{c_c}{g_c}\cdot\left.\frac{\partial g}{\partial\hat{\sigma}}\right|_{\hat{\sigma}_{\min}}\cdot e^{d.(1+X)\frac{p}{f_c}} \tag{3.15}$$

where r is a weight factor, g_c is a material parameter and $\left.\frac{\partial g}{\partial\hat{\sigma}}\right|_{\hat{\sigma}_{\min}}$ is the component of the rate of plastic strain vector in the direction of the minimum principal stress. The exponential term, for which factor d is a user-defined constant, expresses the effect of pressure on the evolution of the hardening variable. The pressure, p, is related to the first invariant of the stress tensor.

$$p=-\frac{I_1}{3} \tag{3.16}$$

The greater the pressure value, the greater the confinement effect on the material. The parameter X in Equation (3.15) is given from the following expression.

$$X=\frac{I_1}{\sqrt{3J_2}} \tag{3.17}$$

The exponential term in Equation (3.15) is equal to 1 for uniaxial compression and it decreases for multiaxial compressive states, meaning that the evolution of the hardening-softening variable becomes slower for the case of multiaxial compressive states. In this fashion, the exponential term, which was not present in the model by Lee and Fenves (1998), accounts for the increased ductility of confined concrete. In the limit, the value of X becomes minus infinity for isotropic compression, meaning that there is no evolution in the hardening variable. Of course, the case of isotropic compression cannot practically occur in the computation of X since isotropic compression stress states are always purely elastic states in the proposed model.

The variation of the strength parameter c_c with κ is presented in Figure 3.3a. The maximum value of $c_c = f_c$ is obtained for $\kappa = \kappa_o$, where κ_o is the value of κ which gives a zero first derivative of c_c. The values of κ_o, f_o and a can be found if the parameter g_c, the peak compressive strength, f_c and the strain, ε_o at the peak compressive strength are given, by solving the following system of nonlinear equations. The system includes an auxiliary parameter, b.

$$a = -1 + \sqrt{1 - \frac{3}{4\kappa_o - 1}} \tag{3.18a}$$

$$f_o = \frac{4a \cdot f_c}{(1+a)^2} \tag{3.18b}$$

$$b = \frac{f_o}{g_c}\left(1 + \frac{a}{2}\right) \tag{3.18c}$$

$$\kappa_o = \frac{f_o}{g_c}\left[\frac{a}{2b}e^{-2b\cdot\varepsilon_o^{pl}} - \frac{a+1}{b}e^{-b\cdot\varepsilon_o^{pl}} + \frac{a+2}{2b}\right] \tag{3.18d}$$

where $\varepsilon_o^{pl} = \varepsilon_o - \frac{f_c}{E}$. The parameter g_c can be obtained by stipulating that the area under the hardening-softening curve is equal to the ratio G_c/h, where G_c is a compressive fracture energy of the material and h is a mesh size parameter for the finite element model.

An alternative and more meaningful approach is to establish g_c as a summation $g_{co} + g_{c1}$, where g_{co} corresponds to the hardening regime of the strength evolution and g_{c1} to the softening regime, as depicted in Figure 3.3b. Of these two quantities, only the one related to the softening stage, i.e., g_{c1}, should be adjusted with element size to provide objective results. In this approach, the g_c is unknown, hence, the value of f_o need to be assumed first, e.g. $f_o = {}^{f_c}\!/_{1.5}$, and then the κ_o should be calculated using Equations (3.18a) and (3.18b). The area under hardening portion of the strength evolution curve, g_{co}, can be found using the following expression.

$$g_{co} = f_o\left[\frac{a}{2b}e^{-2b\cdot\varepsilon_o^{pl}} - \frac{a+1}{b}e^{-b\cdot\varepsilon_o^{pl}} + \frac{a+2}{2b}\right] \tag{3.19}$$

The value of g_c then can be found by setting the g_{c1} equal to G_c/h. Lubliner et al. (1989) have argued that G_c cannot be identified with a particular physical energy. Despite such objections pertaining to the existence of compressive fracture energy, the value of G_c is established in the present study as follows. First, an empirical equation by Bažant (2002), providing the best fit to a large number of data sets, is used to calculate the tensile (mode-I) fracture energy, G_t, of the material:

$$G_t = 2.5\alpha_0\left(\frac{f_c}{0.051}\right)^{0.46}\left(1+\frac{d_a}{11.27}\right)^{0.22}\left(\frac{w}{c}\right)^{-0.30} \tag{3.20}$$

where f_c is the compressive strength of concrete expressed in MPa, d_a is the maximum aggregate size in mm, w/c is the water/cement ratio, and $\alpha_0 = 1$ for rounded aggregate while $\alpha_0 = 1.44$ for crushed or angular aggregates Then, G_c is obtained by multiplying G_t by 100.

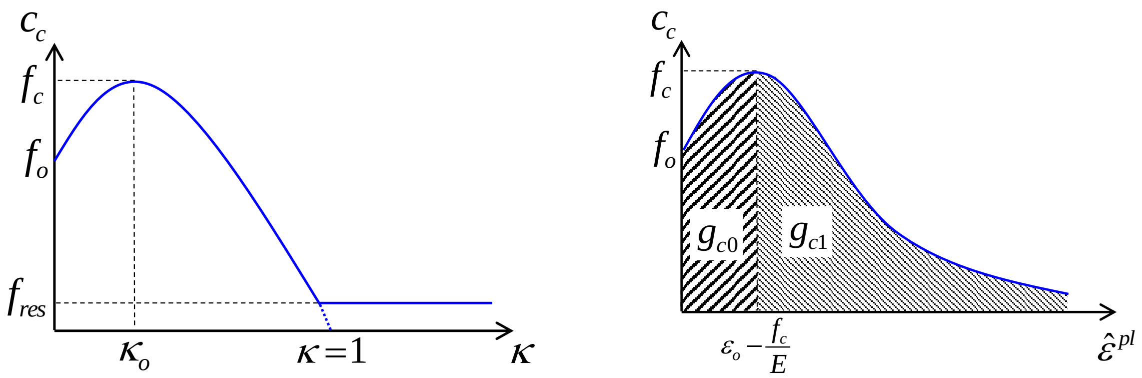

(a) Hardening-softening law (b) Area under hardening and softening portions

Figure 3.3: Hardening-softening law for elastoplastic model in compressive regime

3.2.2 Cracked material

If the cracking criterion is met in one of the principal directions – i.e., the stress in that direction is greater than the cracking strength of the material, then the stress must be corrected to account for the currently active crack. The principal stress of the cracked material is a function of the corresponding principal strain in accordance with the following equation.

$$\hat{\sigma}_i = c_t \cdot \left[(1-M) e^{-\lambda_t \frac{\hat{\varepsilon}_i - \hat{\varepsilon}_{ini}}{f_t}} + M \right],\ i = 1,2,3 \tag{3.21}$$

where M is the fraction of residual tensile strength, $\hat{\varepsilon}_{ini}$ is the strain at onset of softening and λ_t is a parameter controlling the rate of tensile softening. The value of material tensile strength, c_t, is obtained by the following expression.

$$\begin{aligned} c_t &= f_t,\ if\ \kappa \le \kappa_o \\ c_t &= \frac{c_c}{f_c} f_t,\ if\ \kappa > \kappa_o \end{aligned} \tag{3.22}$$

The softening law of the cracked material and the unloading-reloading behavior in the cracked regime are schematically presented in Figure 3.4a. Equation (3.22) implies that, if the material has reached the stage of compressive strength degradation, then the tensile strength will be subjected to a similar reduction. For unreinforced concrete, the value of parameter λ_t is obtained by stipulating that the area under the softening portion of the cracking stress-strain law is equal to the ratio G_t/h, where G_t is the tensile fracture energy, as depicted in Figure 3.4b.

$$\lambda_t = \frac{(1-M) f_t^2}{G_t} .h \tag{3.23}$$

For reinforced concrete, the values of M and λ_t can be found using, e.g., the approach given by Lu and Panagiotou (2013) which accounts for the tension stiffening effect of the reinforcement.

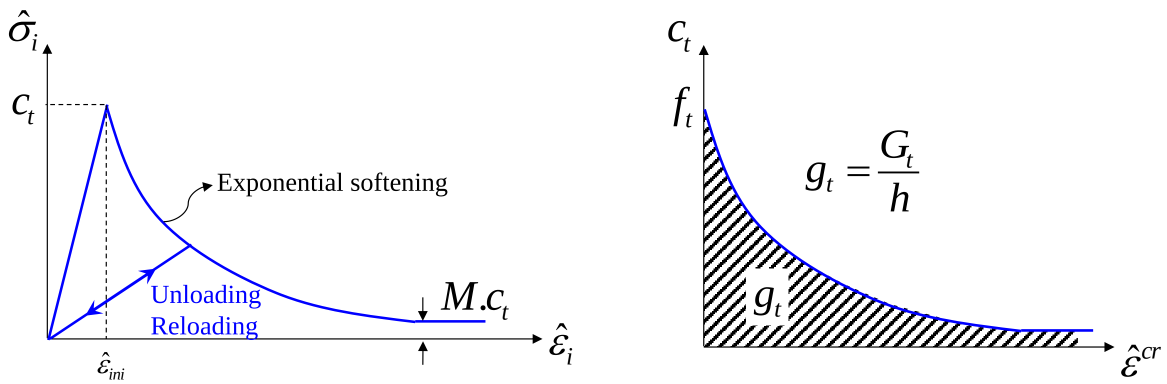

(a) Material response for uniaxial tension (b) Area under softening portion

Figure 3.4: Crack stress-strain model and definition of mode-I fracture in tensile regime

3.2.3 Compatibility between cracking law and elastoplastic material

The correction for cracking is made in the principal stress space. If one of the principal trial elastic stresses exceeds the corresponding cracking stress, then a cracking correction is conducted for the specific principal stress with a simultaneous development of a crack opening strain vector. Each principal direction is assigned the strength of the crack whose direction is closest to that principal direction. If not all three allowable cracks have already opened and a principal direction is not sufficiently close to a previously formed crack, then a new crack is initiated. A crack opens after the tensile strength is exceeded, closes once compression develops and then reopens once the stress becomes tensile. Consequently, the cracking strength is equal to c_t if a crack has never opened before and zero if the crack had been closed and now reopens.

The cracking correction is only made for the tensile stresses. If cracking has occurred, i.e., one or more cracks are open, then two stress vectors, $\left\{\hat{\sigma}^{+(uc)}\right\}$ and $\left\{\hat{\sigma}^{+(cr)}\right\}$ are defined. Each of these vectors has three terms, defined from the following equation.

$$\hat{\sigma}_i^+ = \begin{cases} \hat{\sigma}_i & \text{If a crack is open in principal direction "}i\text{"} \\ 0 & \text{Otherwise} \end{cases}, \; i = 1,2,3 \qquad (3.24)$$

If cracks are open in the material, then the stress in each cracked direction obtained from the elastoplastic constitutive model, $\left\{\hat{\sigma}^{+(uc)}\right\}$, must be equal to the stress obtained from the crack model, $\left\{\hat{\sigma}^{+(cr)}\right\}$. This condition can be mathematically expressed as:

$$\left\{\hat{\sigma}^{+(uc)}\right\}-\left\{\hat{\sigma}^{+(cr)}\right\}=\{0\} \tag{3.25}$$

Additionally, the total strain vector of the material must consist of three parts, namely, an elastic part, a plastic part and a cracking part.

$$\{\hat{\varepsilon}\}=\left\{\hat{\varepsilon}^{el}\right\}+\left\{\hat{\varepsilon}^{pl}\right\}+\left\{\hat{\varepsilon}^{cr}\right\} \tag{3.26}$$

Equations (3.25) and (3.26) must be enforced at each stage in the analysis, to satisfy the compatibility requirements between the uncracked and cracked components of the material model.

3.2.4 Numerical implementation-stress update algorithm

A discretized version of the constitutive model has been developed, in which the stress and internal variables are calculated at a set of discrete steps. The model is strain-driven, i.e., the strain is a given quantity at each step. Given the stress $[\sigma_n]$, total strain $[\varepsilon_n]$, plastic strain $\left[\varepsilon_n^{pl}\right]$ and hardening variable κ_n of a step *"n"*, as well as the total strain $[\varepsilon_{n+1}]$ of the new step *"n+1"*, calculate the new stresses $[\sigma_{n+1}]$, new plastic strains $\left[\varepsilon_{n+1}^{pl}\right]$ and new hardening variable, κ_{n+1}. The discrete stress update algorithm relies on an implicit Backward Euler scheme, where the direction of plastic flow is determined from the updated stress:

$$\left[\Delta\varepsilon_{n+1}^{pl}\right]=\Delta\lambda[m_{n+1}] \tag{3.27}$$

where $[m_{n+1}]$ is a tensor obtained by using the components of the updated stress tensor in Equation (3.11).

$$m_{n+1,ij} = \alpha_p \delta_{ij} + \frac{s_{n+1,ij}}{\sqrt{2J_{2,n+1}}} \tag{3.28}$$

The stress update is conducted using the well-established elastic prediction-plastic correction approach (e.g., Simo and Hughes 1998) which was also used by Lee and Fenves (2001). It can easily be proven that the trial elastic stress tensor, the updated stress tensor, and the trial elastic strain tensor are all collinear, i.e. they have the same eigenvectors (Lee and Fenves, 2001). This allows the cracking correction for the principal trial elastic stresses, before any necessary plastic correction step is conducted. Additionally, for the plastic potential adopted herein, the value of Lode angle, θ, in the modified yield surface is the same for the trial elastic stress and for the stress after the plastic correction. Thus, the angle θ can be calculated using the invariants of the deviatoric trial elastic stress tensor. However, additional iteration is required in the elastoplastic model, due to the dependence of eccentricity value, e, on the invariant I_1 and on c_c.

The following equations need to be enforced for the material, for the updated step "$n+1$" in an analysis, to retain consistency with the formulation of the model.

$$\left\{\hat{\varepsilon}_{n+1}\right\} = \left\{\hat{\varepsilon}^{el}_{n+1}\right\} + \left\{\hat{\varepsilon}^{pl}_{n+1}\right\} + \left\{\hat{\varepsilon}^{cr}_{n+1}\right\} \tag{3.29}$$

$$\left\{\hat{\sigma}^{+(uc)}_{n+1}\right\} = \left\{\hat{\sigma}^{+(cr)}_{n+1}\right\} \tag{3.30}$$

In other words, the total strain vector consists of an elastic part, a plastic part, and the cracking part. Also, if cracks are open, the stresses given by the elastoplastic part of the model for the cracked directions must equal the corresponding values obtained from the crack model. The stress update algorithm which is presented in Box 3.1 requires iterations for the calculation of the cracking part of the strains. Iterations are also required for the stress update of the elastoplastic component of the model, since it uses an implicit Backward Euler scheme. Despite the need for iterations at two levels during the stress update, the analyses conducted with the proposed model indicate that it is characterized by very good robustness and efficiency.

Box 3.1: Stress update algorithm

1. Initialize: $\left[\varepsilon^{pl}_{n+1(0)}\right]=\left[\varepsilon^{pl}_{n}\right]$, $\kappa_{n+1(0)}=\kappa_n$.
2. Calculate trial elastic strains, $\left[\varepsilon^{el}_{n+1(0)}\right]=\left[\varepsilon_{n+1}\right]-\left[\varepsilon^{pl}_{n}\right]$, and solve an eigenvalue problem and find principal trial elastic strain $\left[\hat{\varepsilon}^{el}_{n+1(0)}\right]$ and associated eigenvectors $\left[Q\right]$.

<u>*Iteration “k”*</u>*, k = 0,1,2,…*

3. Calculate the three components of the principal stress tensor corresponding to trial elastic strain for iteration *“k”*, $\left\{\hat{\sigma}^{(tr)}_{n+1(k)}\right\}=\left[\hat{D}\right]\left\{\hat{\varepsilon}^{el}_{n+1(k)}\right\}$
4. Calculate cracking stress and strain components in principal space: For each of the 3 principal directions *i =1,2,3*, if we have an active crack in that direction, replace $\hat{\sigma}^{(tr)}_{n+1(k),i}$ by $\hat{\sigma}^{+(cr)}_{n+1(k),i}$, then find the three components of the cracking strain in principal directions. $\left\{\hat{\varepsilon}^{cr}_{n+1(k)}\right\}=\left\{\hat{\varepsilon}^{el}_{n+1(k)}\right\}-\left[\hat{D}\right]^{-1}\left\{\hat{\sigma}^{(tr)}_{n+1(k)}\right\}$.
5. Calculate the trial continuum strain: $\left[\hat{\varepsilon}^{uc}_{n+1(k)}\right]=\left[\hat{\varepsilon}_{n+1}\right]-\left[\hat{\varepsilon}^{cr}_{n+1(k)}\right]$
6. Use the plasticity model for $\left[\hat{\varepsilon}^{uc}_{n+1(k)}\right]$ and obtain $\left[\hat{\sigma}^{(uc)}_{n+1(k)}\right]$, $\left[\Delta\varepsilon^{pl}_{(k)}\right]$, $\Delta\kappa_{(k)}$. Conduct the necessary coordinate transformation to the global coordinate system using $\left[Q\right]$.
    1. Calculate the trial elastic strain $\left[\hat{\varepsilon}^{uc(tr)}_{n+1(k)}\right]=\left[\hat{\varepsilon}_{n+1}\right]-\left[\hat{\varepsilon}^{pl}_{n}\right]$, and find the corresponding trial stress $\left\{\hat{\sigma}^{(uc,tr)}_{n+1(k)}\right\}=\left[\hat{D}\right]\left\{\hat{\varepsilon}^{uc(tr)}_{n+1(k)}\right\}$.
    2. Find the first invariant, $I^{(tr)}_1$, and second deviatoric invariant, $J^{(tr)}_2$, of the trial stress tensor, $\left[\hat{\sigma}^{(uc,tr)}_{n+1(k)}\right]$, and then check the yield function at Equation (3.4).
    3. **IF** $f<0$, **THEN** the step is purely elastic. Set $\left[\hat{\sigma}^{(uc)}_{n+1(k)}\right]=\left[\hat{\sigma}^{(uc,tr)}_{n+1(k)}\right]$, $\left[\Delta\varepsilon^{pl}_{(k)}\right]=\left[0\right]$, $\Delta\kappa_{(k)}=0$, and go to Step 7.

        ELSE do the iteration on *“l”*.

    <u>*Iteration “l”*</u>*, l=0,1,2,…*

        i. Assume $\kappa_{(l)}=\kappa_{n+1(k)}$, and calculate the plastic multiplier increment as:

        $$\Delta\lambda_{(l)}=\frac{\alpha I^{(tr)}_1+\sqrt{3J^{(tr)}_2}-(1-\alpha).C_c(\kappa_{(l)})}{9K\alpha_p\alpha+\sqrt{6}G}$$

        where *K* and *G* are the bulk and shear modulus respectively.

        ii. Find the components of corrected principal stress:

```
            $\hat{\sigma}_{i,(l)}^{(uc)} = \hat{\sigma}_{i,n+1(k)}^{(uc,tr)} - \Delta\lambda_{(l)} \left( \frac{2G}{\sqrt{2J_2^{(tr)}}} . \hat{\sigma}_{i,n+1(k)}^{(uc,tr)} - (\frac{2G}{3\sqrt{2J_2^{(tr)}}} - 3K\alpha_p) \right)$
        iii. Use the corrected stress tensor $\left[\hat{\sigma}_{(l)}^{(uc)}\right]$ to calculate the plastic strain increment, $\left[\Delta\hat{\varepsilon}_{(l)}^{pl}\right]$, from Equation (3.12).
        iv. Calculate the weight factor, if $\sum_{i=1}^{3}\left\|\hat{\sigma}_{i,(l)}^{(uc)}\right\| = 0$, $r = 0$ else $r = \sum_{i=1}^{3}\left\langle\hat{\sigma}_{i,(l)}^{(uc)}\right\rangle / \sum_{i=1}^{3}\left\|\hat{\sigma}_{i,(l)}^{(uc)}\right\|$
        v. Use Equation (3.15), and find the vale of $\Delta\kappa_{(l)}$.
        vi. IF $\Delta\kappa_{(l)} \leq tol$, THEN set $\Delta\kappa_{(k)} = \Delta\kappa_{(l)}$, $\left[\hat{\sigma}_{n+1(k)}^{(uc)}\right] = \left[\hat{\sigma}_{(l)}^{(uc)}\right]$, $\left[\Delta\varepsilon_{(k)}^{pl}\right] = \left[\Delta\varepsilon_{(l)}^{pl}\right]$.
            ELSE set $\kappa_{(l+1)} = \kappa_{(l)} + \Delta\kappa_{(l)}$ and $l \leftarrow l+1$, then go to Step i.
7. Set $\left[\varepsilon_{(k+1)}^{pl}\right] = \left[\varepsilon_{(k)}^{pl}\right] + \left[\Delta\varepsilon_{(k)}^{pl}\right]$, $\kappa_{(k+1)} = \kappa_{(k)} + \Delta\kappa_{(k)}$.
8. IF $\left\|\left\{\hat{\sigma}_{n+1(k)}^{+(uc)}\right\} - \left\{\hat{\sigma}_{n+1(k)}^{+(cr)}\right\}\right\| \leq tol$, THEN set $\left[\sigma_{n+1}\right] = \left[\sigma_{n+1(k)}^{(uc)}\right]$, $\left[\varepsilon_{n+1}^{pl}\right] = \left[\varepsilon_{n+1(k+1)}^{pl}\right]$, $\kappa_{n+1} = \kappa_{n+1(k+1)}$.
   Also, update history variables for cracks (if necessary) and RETURN.
   ELSE find improved guess for principal elastic strain: $\left[\varepsilon_{n+1(k+1)}^{el}\right] = \left[\varepsilon_{n+1}\right] - \left[\varepsilon_{n+1(k+1)}^{pl}\right]$
   Set $k \leftarrow k+1$ and go to Step 3.
```

3.3 Validation of material response

The proposed constitutive model is implemented in two finite element programs to conduct nonlinear analysis for various RC structures. The material model first has been implemented in FEAP (Taylor 2013) which is an open source finite element program appropriate for debugging. FEAP uses an implicit integration scheme and, therefore, has been selected to investigate the numerical efficiency and assess the convergence capability of the constitutive driver. Later, the constitutive model has been implemented in the commercial finite element program, LS-DYNA, to conduct more refined nonlinear simulations.

This section describes the validation analyses conducted at material level, e.g. by single-element analysis, to evaluate the behavior of the model under different loading scenarios. In all of the analyses presented here, a nonlinear iterative procedure using the initial stiffness matrix has been employed. The initial material stiffness matrix of the proposed model is that of an isotropic, linearly elastic material.

3.3.1 Crack opening/closing behavior

In this section, the cracking behavior of the material model is validated through conducting analysis for a single element subjected to three different load cases:

Case 1: Uniaxial compression beyond the maximum compressive strength (crushing), then unloading into tension (cracking), and then reloading again into compression. The stress-strain response of a single-element analysis is depicted in Figure 3.5. As can be seen from the figure, a crack forms and opens during unloading from compressive to tensile regime. The concrete tensile strength is reduced due to previous crushing as described in Equation (3.22).

The model resolves the issue that characterizes the material law by Lee and Fenves (1998). Specifically, if crack opening and closing occur, compressive stresses can only develop upon full crack closure. The occurrence of tensile strength degradation due to cracking does not affect the compressive strength after crack closure. Thus, the model is not characterized by the inaccuracies of models such as the one by Murray (2007). Figure 3.5 also indicates that irreversible (plastic) compressive strains can occur, contrary to the model by Selby and Vecchio (1997).

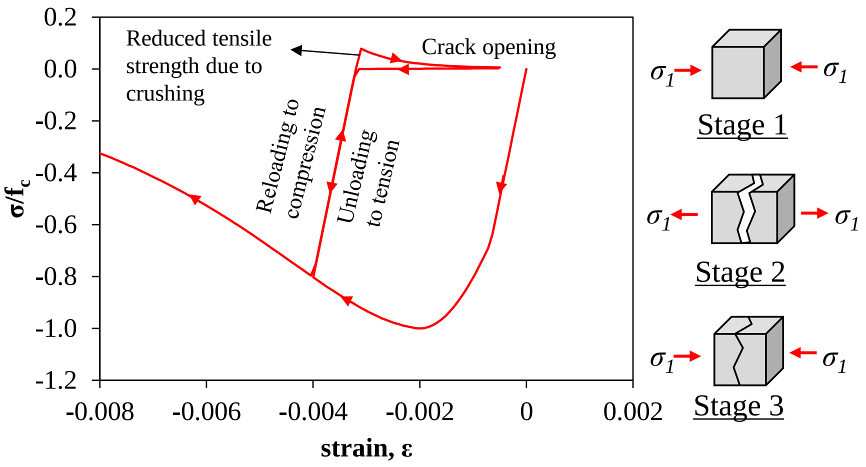

Figure 3.5: Crack opening/closing behavior for uniaxial compressive/tensile loading

Case 2: Biaxial loading where crack closes due to the concrete crushing in another direction. As depicted in Figure 3.6, at first a crack forms and opens in direction 1. Then nodal displacements are constraint in the same direction, and compressive strain is applied in direction 2. The opened crack in direction 1 gradually closes due to crushing of concrete in direction 3. By full closure of the crack, biaxial stress state forms and material starts to gain strength in compressive regime until it reaches to a second crushing (softening branch).

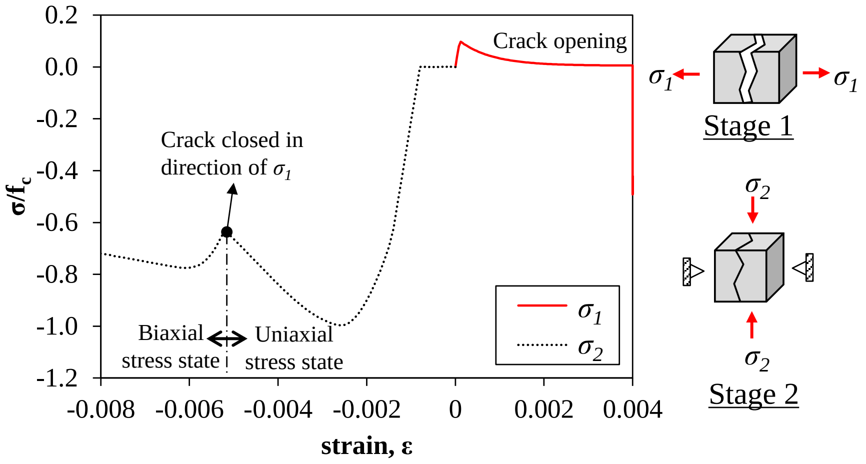

Figure 3.6: Crack opening/closing behavior for biaxial compressive/tensile loading

<u>Case 3:</u> Biaxial loading where two cracks are formed successively. At first, a crack forms and opens in direction 1. Then nodal displacements are constraint in the same direction, and tensile strain is applied in direction 2. As depicted in Figure 3.7, the concrete reaches to the same tensile strength in both directions; additionally by further loading the element in direction 2, the crack opens more in direction 1, and consequently, the tensile strength reduces.

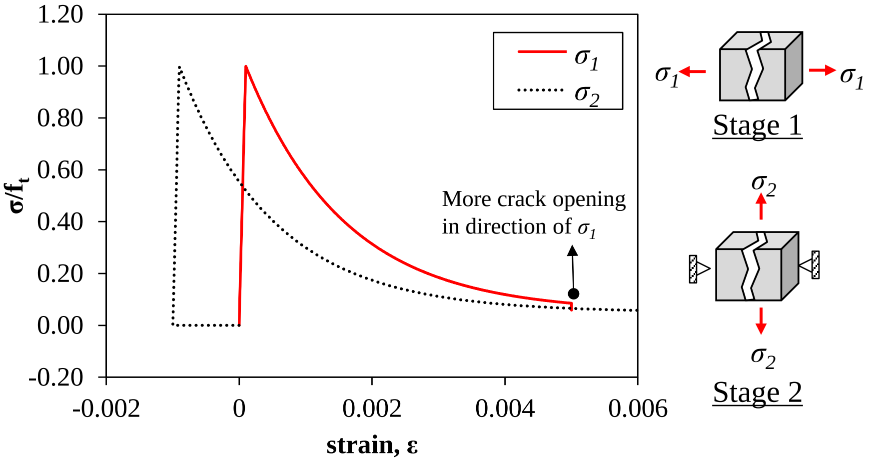

Figure 3.7: Crack opening/closing behavior for a biaxial tensile loading

3.3.2 Uniaxial cyclic behavior

The behavior of the model for uniaxial cyclic loading is validated in this section. Specifically, a single-element analysis is used to determine the performance of the model for cyclic loading in the compressive and tensile regimes. To this end, the results of the experimental tests by Gopalaratnam and Shah (1985) and Karsan and Jirsa (1969) are compared to the corresponding results obtained with the proposed model in Figures 3.8a and 3.8b. The model has been calibrated to capture well the envelope of the cyclic stress-strain curves. It can be seen that there is a discrepancy in the analytical and experimental results, in terms of the unloading-reloading behavior. This discrepancy is not considered significant for the performance of RC components and systems. Better agreement in terms of the unloading-reloading behavior has been obtained for damage-plasticity models (e.g., Lee and Fenves 1998, Grassl and Jirásek 2006b). However, the good agreement in these references had been obtained for a calibration which either did not accurately capture the envelope curve of the stress-strain response in tensile region or with the unloading strains that did not match the experimental unloading points.

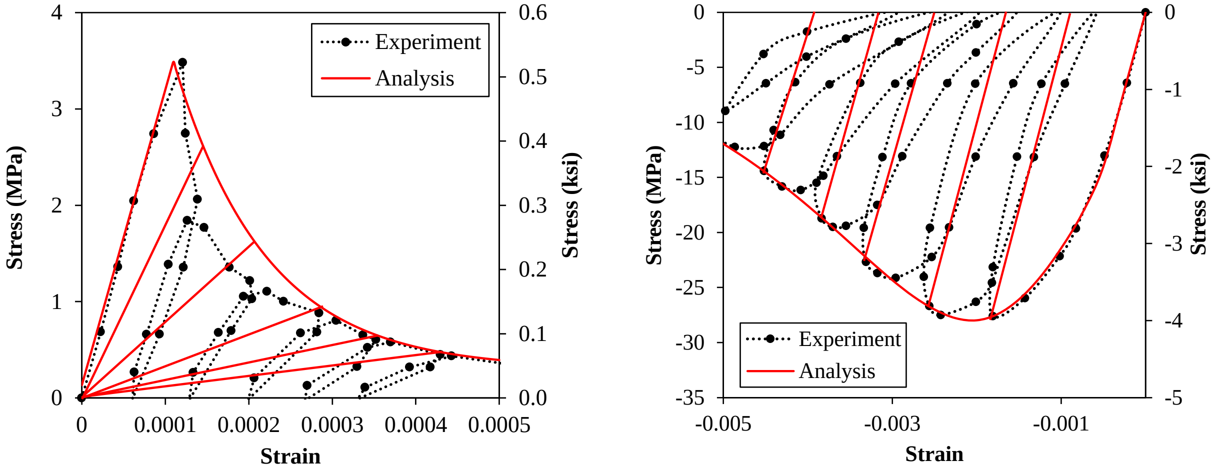

(a) Cyclic tensile loading (experiment by Gopalaratnam and Shah 1985)

(b) Cyclic compressive loading (experiment by Karsan and Jirsa 1969)

Figure 3.8: Validation for a single element subjected to uniaxial cyclic loading

3.3.3 Response for confined compression

Additional single-element analyses are conducted to demonstrate the behavior of the material under confined compression. Single-element analyses are performed for monotonically increasing compression under different levels of confining pressure, and the results are presented in Figure 3.9. To allow the calibration of the dimensionless parameter *d*, which expresses the effect of confinement on material ductility, the analyses have also been conducted using another model, namely, the one by Maekawa et al. (2003). This other model has been shown to be capable of capturing the lateral expansion due to dilatation and the increased material strength and ductility due to confinement, but - as mentioned in Section 3.1 - may be inappropriate for analysis of components and systems, because it has been found to lead to numerical convergence failures in the stress update process. The results shown in Figure 3.9 have been obtained for *d=3.2*. Thus, this value has been used for *d* in all the analyses presented in Chapter 4. In Chapters 5 and 6, the value of *d* is set equal to the compressive strength of concrete in ksi unit. This assumption is found to be valid in the analysis of different RC components.

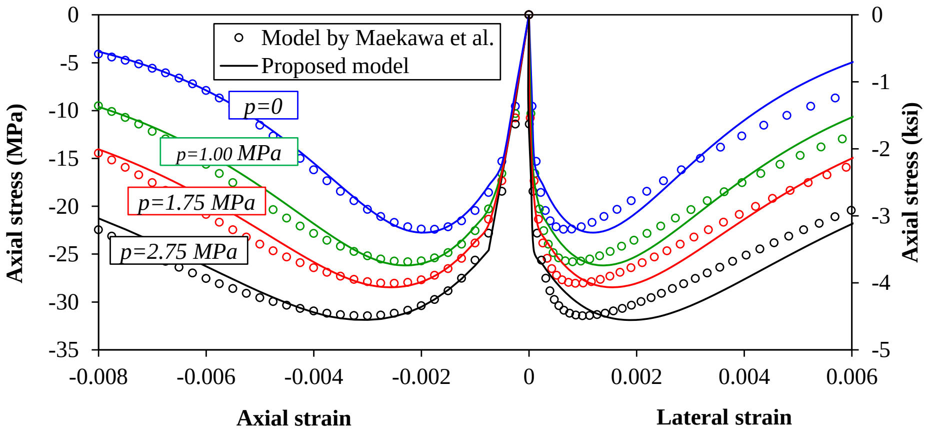

Figure 3.9: Behavior for confined compression with constant α_p, f_c = 22.4 MPa, ε_0 = 0.002.

As shown in Figure 3.9, the lateral expansion predicted by the proposed model for various levels of confining pressure is in satisfactory agreement with the corresponding values obtained from the model by Maekawa et al. (2003), which has been shown to be capable of capturing the lateral expansion due to dilatation and the increased material strength and ductility due to confinement. The only disagreement is in the pre-peak regime, where the proposed model overestimates the lateral expansion. This is due to the fact that, contrary to the present model, the dilatancy parameter in the model by Maekawa et al. (2003) is not constant. Specifically, it is negative at initial stage of inelastic response and continuously increases with accumulation of inelastic deformations.

Similar to the model by Maekawa et al. (2003), the dilatancy parameter of the proposed constitutive model, α_p, can be defined as a function of damage variable, κ.

$$\alpha_p = \sqrt{\kappa}\left(\alpha_{p1} - \alpha_{p0}\right) + \alpha_{p0} \le \alpha_{p1} \qquad (3.31a)$$

$$\alpha_{p0} = -\frac{1-2\nu}{\sqrt{3}(1+\nu)} \tag{3.31b}$$

where ν is the Poisson's ratio and α_{p1} is a user-defined constant indicating the maximum allowed dilatancy parameter. The value of α_{p1} has been set equal to 0.45, and the single-element analysis has been repeated. As can be seen in Figure 3.10, using Equation (3.31a) to define the dilatancy parameter, as a function of damage variable, leads to a closer match between the monotonic envelop curves predicted by the proposed model and the corresponding data obtained from the model by Maekawa et al. (2003). However, such an equation introduces more parameters to be calibrated, and increases computation cost of the stress update algorithm.

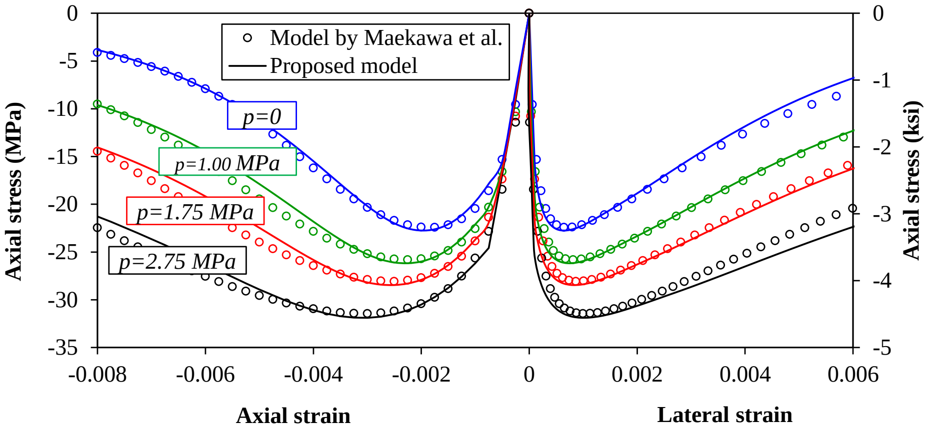

Figure 3.10: Behavior for confined compression with varying α_p, f_c = 22.4 MPa, ε_0 = 0.002.

Additionally, since it has been found that the discrepancy in terms of predicting the lateral expansion of the concrete material, shown in Figure 3.9, would not affect the analysis of RC components noticeably, the analyses provided in proceeding chapters use a constant dilatancy parameter.

Chapter 4 : Verification of the Capability of Novel Material Model for Concrete to Allow Simulations of Structural Components and Systems

A three-dimensional finite element modeling is the most reliable way to simulate the behavior of reinforced concrete (RC) structural components, especially for those that exhibit increased strength and ductility offered by transverse reinforcement. The precision of the analytical solutions for RC members with high level of triaxiality, e.g. beam-to-column joints, critically hinges on the capability of the material model to describe the concrete behavior sufficiently accurate. In this regard, the proposed triaxial concrete material model, described in Chapter 3, is implemented in the nonlinear finite element program, FEAP (Taylor 2013), and validated at the component level by conducting nonlinear finite element (FE) analysis for several RC structural components. Specifically, two column specimens and a beam-to-column joint are analyzed under quasi-static cyclic loadings. A very good agreement is obtained between analytically obtained and experimentally recorded hysteretic response. Parametric analyses are also pursued to provide information on the effect of mesh size, the need for adjusting (regularizing) the compressive softening law with element size, and to elucidate the effect of using different yield surfaces, namely, Drucker-Prager yield criterion, the yield surface by Lubliner et al. (1989), and the modified yield criterion that has been explained in Chapter 3.

4.1 Validation of the proposed material model for the analysis of structural components

The proposed concrete material model is validated with analyses of structural components. The effect of confinement in these components is important, due to the relatively high compressive axial forces and significant amounts of transverse reinforcement. In all the analyses, the concrete members have been modeled with hexahedral, eight-node, fully integrated solid elements. In all the analyses presented herein, the Poisson's ratio, v, is set equal to 0.2. The strain at the peak compressive strength, ε_o, is assumed to be 0.002. The value of the tensile strength, f_t, is set equal to 10% of the corresponding compressive strength. The modulus of elasticity of concrete, E_c, is set equal to $2f_c/\varepsilon_o$. The residual compressive strength, f_{res}, is assumed to be 5% of the compressive strength. Finally, the parameters M and λ_t in the cracking stress-strain law is calibrated in accordance with Lu and Panagiotou (2013). The remaining values of material parameters for the concrete model are presented in Table 4.1 for all the validation analyses. The reinforcing steel is modeled with truss elements which use the constitutive model by Dodd and Restrepo (1995). The values used for the material parameters of the reinforcing steel in the analyses are presented in Table 4.2. Perfect bond is assumed between the truss elements and the surrounding hexahedral continuum elements. Finally, the P-Delta effects (i.e., the geometric nonlinearity) have been accounted for in the analyses in a simplified fashion. Specifically, the obtained hysteretic plots have been post-processed to account for the impact of the second-order moment, which is equal to the product of the column horizontal displacement at the top and the column axial force.

Table 4.1: Concrete material model parameters

Specimen	f_c (MPa)	a_p	a	d	g_c (MPa)	λ_t	M
Gill (1979)	21.4	0.2	0.15	3.2	0.085	706.7	0.056
Ang (1981)	23.6	0.2	0.15	3.2	0.071	697.1	0.070
Beckingsale (1980)	31.4	0.2	0.15	3.2	0.240	678^1,760^2	0.07^1,0.06^2

[1]: For column

[2]: For beam

Note: f_c is concrete compressive strength, a_p is dilatancy parameter, a is a parameter affecting the increase in strength due to confinement, d is a parameter affecting the increase in ductility due to confinement, g_c is the area under stress-strain curve, λ_t is a parameter controlling the exponential softening in tensile regime, M is a ratio of residual tensile strength over tensile strength.

Table 4.2: Steel material parameters

Specimen	Bar Type	E_s (MPa)	f_y (MPa)	ε_{sh}	f_u (MPa)
Gill (1979)	DH24	187500	375	0.009	635.6
	R10	212000	297	0.012	416.8
Ang (1981)	DH16	213000	427	0.01	670.0
	R12	228000	320	0.016	434.0
	R10	200000	280	0.016	408.0
Beckingsale (1980)	D22.2H	196500^1	398	0.010	655.0
	D19.05	196500^1	298	0.019	461.0
	R12.7	196500^1	336	0.018	448.0
	R9.5	196500^1	332	0.016	469.0
	R6.35	196500^1	329	0.016	430.0

[1]: Estimated values from the experimental stress-strain curves for rebars tested by Beckingsale (1980). Exact value of E_s was not reported in the specific reference.

Note: E_s is Young's modulus, f_y is rebar yield stress, ε_{sh} is strain at onset of strain hardening, f_u is ultimate strength.

4.1.1 Analysis of columns under cyclic lateral loading

The first set of verification analysis is conducted for two flexure-dominated RC columns subjected to cyclic horizontal forces. In the finite element models, the constant axial force is applied as downward vertical forces at the top, and the horizontal cyclic force is applied by controlling the horizontal displacements at the top. The prescribed displacements vary in accordance with the experimentally recorded cyclic displacement histories.

The first analysis is conducted for a column which was referred as specimen 3 in Gill (1979). The specific specimen has a length-to-depth ratio of two, and can be characterized as a short column, based on the definition by Moretti and Tassios (2006). The amount of transverse reinforcement was so determined to ensure the occurrence of flexure-dominated response. The dimensions and reinforcement configuration of the column are shown in Figure 4.1a, and the corresponding finite element model is presented in Figure 4.1b. The axial load was equal to 2719 kN (611kip) which corresponds to an axial load ratio of 0.41, since the concrete compressive strength was 21.4 MPa (3.1 ksi). The longitudinal reinforcement consisted of 12 DH24, equally spaced bars, providing a reinforcement ratio of 0.018. The transverse reinforcement consisted of R10 triple-ties with a spacing of 75 mm (3 in) in the inelastic hinge region and 105 mm (4.1 in) in the remainder of the column. The yield and ultimate strength of reinforcement were equal to 375 MPa (54.4 ksi) and 635.6 MPa (92.2 ksi), respectively, for the longitudinal reinforcement, and 297 MPa (43 ksi) and 416.8 MPa (60.5 ksi), respectively, for the transverse ties. The clear cover of the longitudinal reinforcement was equal to 50 mm (2 in).

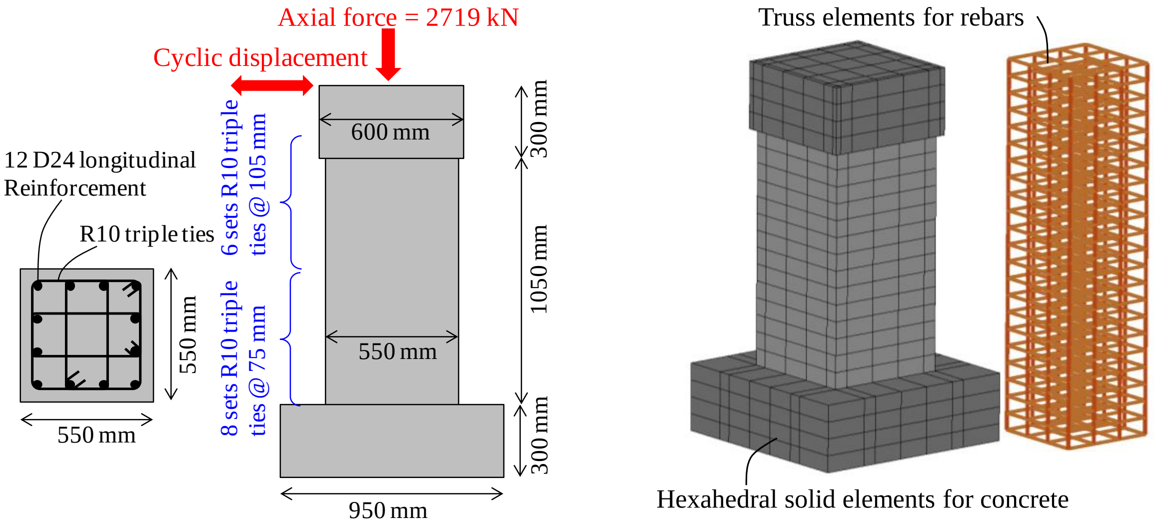

(a) Dimensions and reinforcing details

(b) Finite element model

Figure 4.1: Configuration and analytical model for the column tested by Gill (1979).

In accordance with Section 3.2.1, the value of g_c is set equal to G_c/h, where h is the element size and G_c has been obtained based on empirical expressions by Bažant (2002). However, there are many sources of uncertainty in the value of G_c (e.g. water-cement ratio, maximum aggregate size and aggregate type). Bažant (2002) has reported a coefficient of variation of 17.8% in his empirical formula. Using the aforementioned empirical equation gives a value of G_c equal to 6.4 kN/m. The value of g_c is then obtained for $h = 75\ mm$, which is used in the specific model. An apparently more meaningful approach is to establish g_c as a summation $\mathrm{g}_{\mathrm{co}}+g_{c1}$, where g_{co} corresponds to the hardening regime of the strength evolution and g_{c1} to the softening regime. Of these two quantities, only the one related to the softening stage, i.e., g_{c1}, should be adjusted with element size to provide objective results.

The analysis is performed and the hysteretic plot is depicted in Figure 4.2a. As can be seen from the force-drift plot, the analysis overestimates the column capacity by 7%. Moreover, the analysis predicts a more pronounced strength and stiffness degradation during the last loading cycles. The discrepancy between analytical results and experimental observations can be reduced if

g_c is set equal to $g_{co} + g_{c1}$, and g_{c1} is then set equal to G_c/h. Using this approach and a slightly modified value for parameter α improves the accuracy of the analytical results, as shown in Figure 4.2b. In this case, the discrepancy in terms of the column capacity is reduced to 3%.

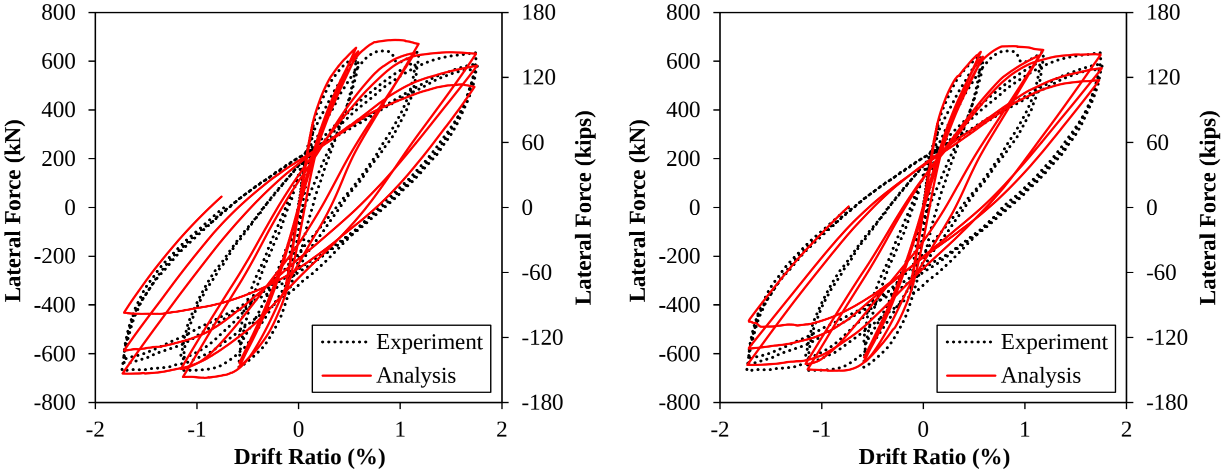

(a) $\alpha = 0.15$, $g_c = 0.085$ MPa

(b) $\alpha = 0.12$, $g_c = 0.12$ MPa

Figure 4.2: Hysteretic response of column specimen tested by Gill (1979).

The second analyses is performed for a column specimen tested by Ang (1981) and termed Unit 3. The specific column had a length-to-depth ratio of more than 4, and it was pushed up to drift ratios of 3.1%. The applied axial load was equal to 1435 kN (322 kips). The column dimensions and reinforcing steel details are presented in Figure 4.3a. In the analytical model, which is depicted in Figure 4.3b, the loadings were applied in the same fashion as for the column tested by Gill (1979).

The concrete compressive strength was 23.6 MPa (3.4 ksi), and the axial load ratio was equal to 0.38. The longitudinal reinforcement consisted of twelve DH16 bars, corresponding to a reinforcement ratio of 0.015 and having a 35 mm concrete cover. The transverse reinforcement consisted of triple ties, made of R12 bars with a spacing of 100 mm (4 in) in the inelastic hinge region, and R10 bars with a spacing of 180 mm (7.1 in) in the remainder of the column. The value of

g_c is calculated using a compressive fracture energy G_c=7.1 kN/m, in accordance with the equation by Bažant (2002). The mesh size parameter, h, is equal to 100 mm.

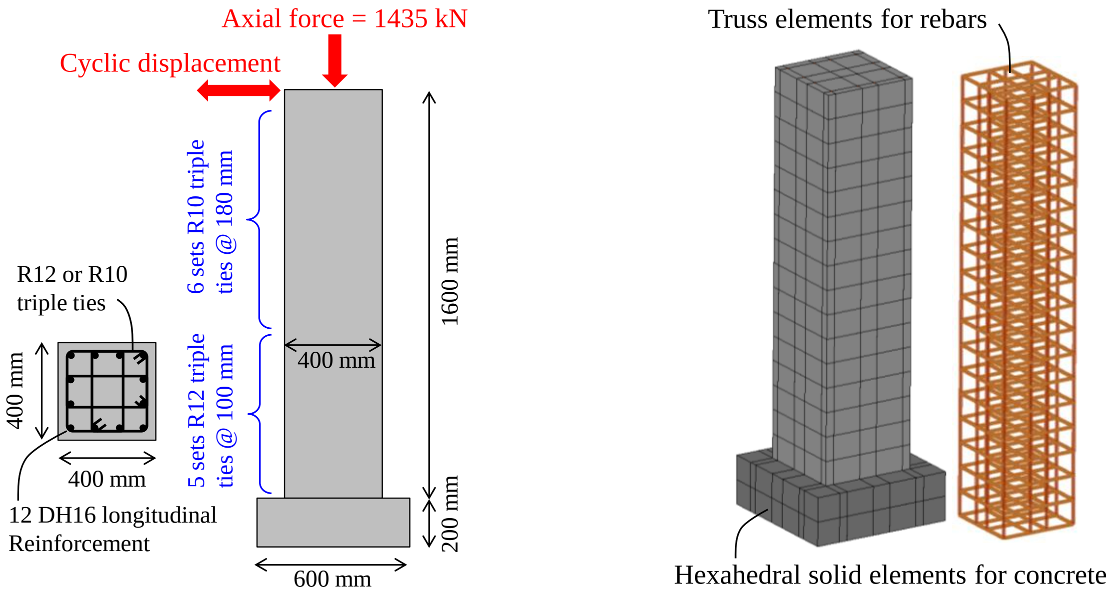

(a) Dimensions and reinforcement details

(b) Finite element model

Figure 4.3: Configuration and analytical model for the column tested by Ang (1981).

The analytically obtained hysteretic plot is compared to the experimental results in Figure 4.4a. The column lateral load capacity is underestimated by 8%, and the analytically predicted lateral strength degradation is more severe. Just like for the analysis of the column tested by Gill (1979), separation of g_c into two parts, g_{co} and g_{c1}, and calculation of g_{c1} as the ratio of G_c over h leads to significantly improved analytical results, as shown in Figure 4.4b where the observed discrepancy in the peak strength is only 2%. This verifies the assertion that, for a given material, only the softening portion of the evolution law for the compressive strength should be adjusted based on element size. This approach is adopted for the analyses presented below.

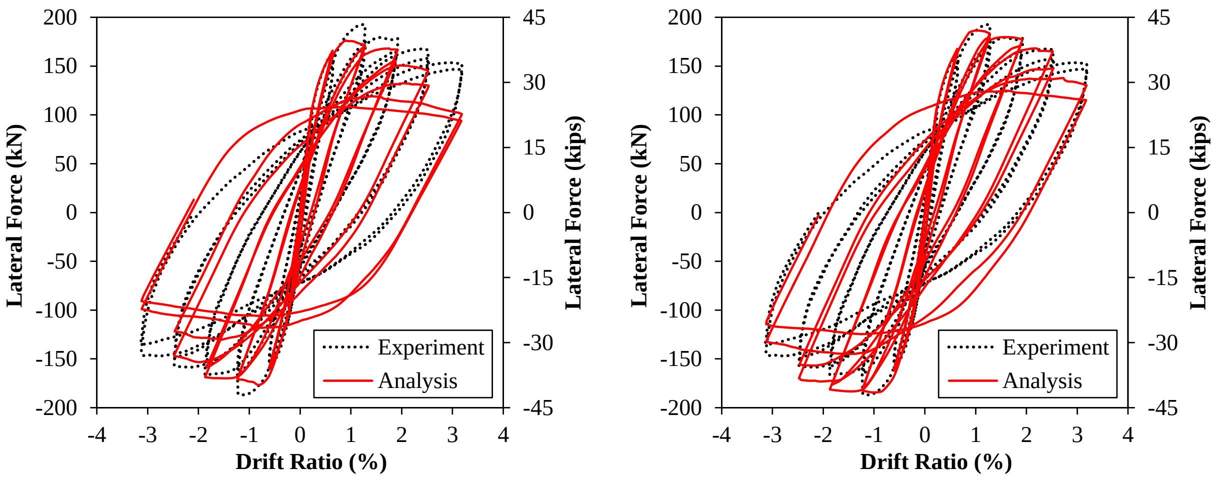

(a) g_c = 0.071 MPa (b) g_c = 0.106 MPa

Figure 4.4: Hysteretic response of column specimen tested by Ang (1981).

To evaluate the effect of mesh size on the obtained results, the analysis for the column tested by Ang (1981) was repeated, using a finer mesh. Specifically, the element height in the new mesh is exactly half the corresponding value in the original mesh. Accordingly, the value of g_{c1} needs to be multiplied by factor of 2, to remain consistent with the requirement that g_{c1} is equal to G_c/h. The force-drift plot is demonstrated in Figure 4.5a, which is consistent with the one with original mesh size plotted in Figure 4.4b. If no adjustment had been made to the hardening-softening law for the refined mesh, the analysis would predict premature strength degradation, as shown in Figure 4.5b. This observation indicates that a spurious mesh size effect exists for localization associated with compressive inelastic strains, and that the adjustment of g_{c1} so that it is equal to the ratio of G_c over element size, h, is necessary to ensure the mesh objectivity of the results, i.e. to preclude spurious mesh size effects associated with softening in the material laws.

The deformed mesh and strain contour obtained at the end of the analysis is depicted in Figure 4.5c. The same figure shows compressive strain localization, accompanied by concrete bulging (dilatation), in a band which is located at a distance of 5 to 12 cm (2 to 5 in) above the base.

Localization does not occur at the bottom row of elements, due to the confinement contributed by the base of the specimen.

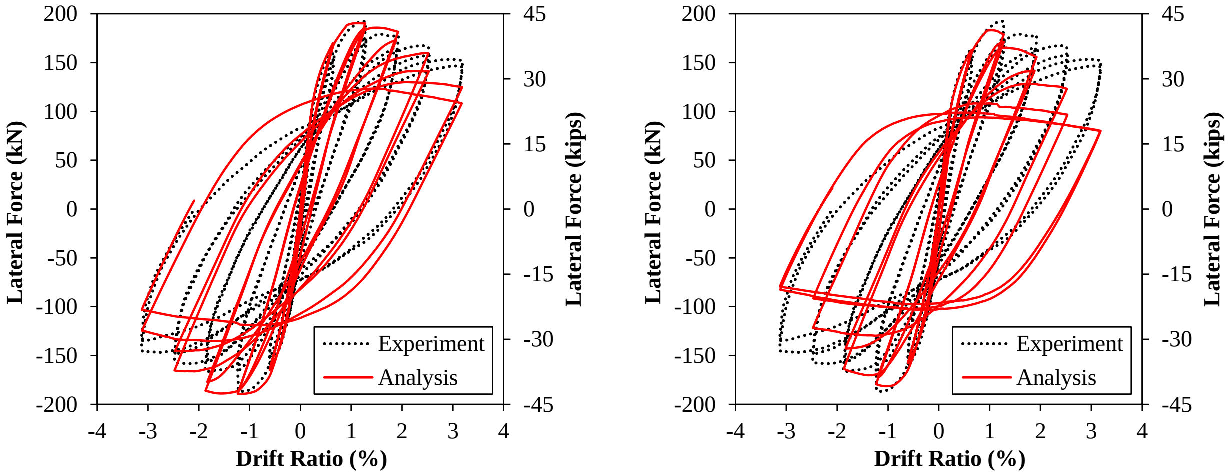

(a) Hysteretic response

(b) Hysteretic response without adjusting g_{c1} due to mesh size

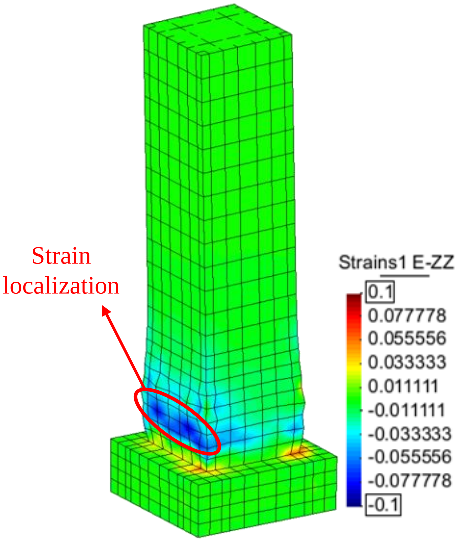

(c) Strain contours at the end of analysis

Figure 4.5: Results for Analysis of beam-to-column joint under cyclic loading

4.1.2 Analysis of Beam-to-Column Joint under Cyclic Loading

An additional verification analysis is conducted for the beam-to-column joint specimen tested by Beckingsale (1980) and termed B13A. The specific specimen was subjected to constant axial load in the column and to cyclic vertical displacement histories at the beams ends. The measured concrete compressive strength at test day was 31.4 MPa (4.55 ksi). The column axial load was equal to 2890 kN (650 kips) and corresponded to an axial load ratio of 0.44. The specimen configuration and reinforcing details are presented in Figure 4.6a, and the corresponding finite element model is depicted in Figure 4.6b. Using the equation by Bažant (2002) gives G_c = 6.9 kN/m for the compressive fracture energy, while the mesh size parameter h is equal to 35 mm.

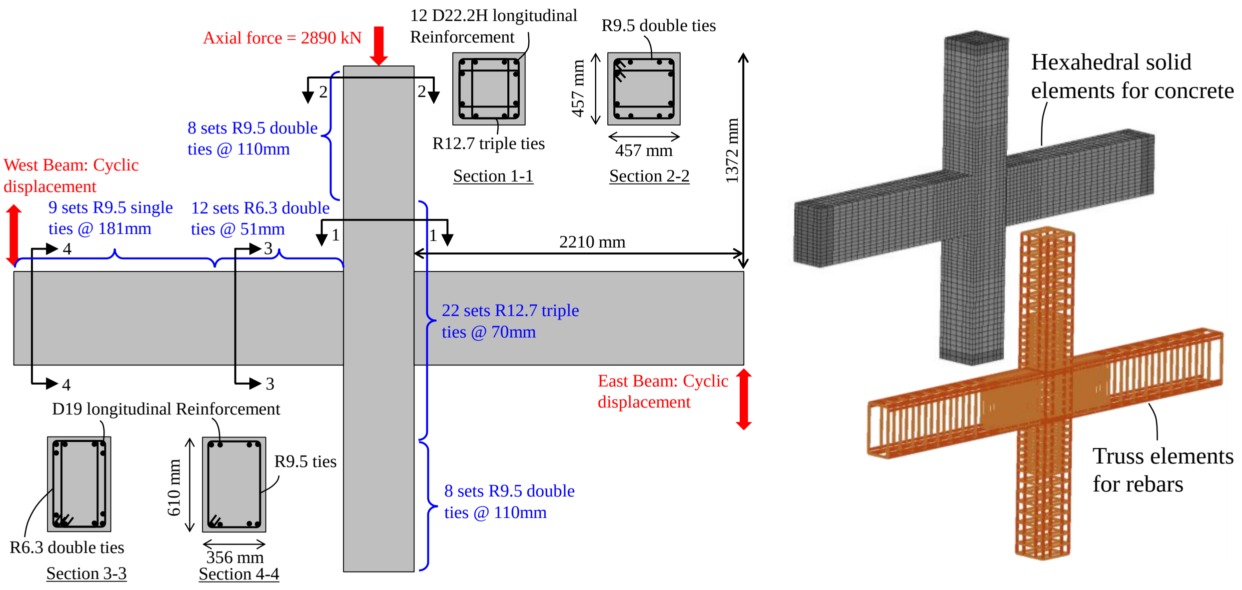

(a) Dimensions and reinforcement details (b) Finite element model

Figure 4.6: Configuration and the analytical model for beam-to-column joint tested by Beckingsale (1980).

The analytically obtained hysteretic response of the beams and column are compared to the experimental observations in Figure 4.7. As can be seen, the capacity of the beams and of the column is overestimated by 5% and 10%, respectively. Still, the agreement in terms of the strength is deemed satisfactory. The discrepancy in the shape of the unloading-reloading regime of the hysteretic curves is more significant than that obtained for the column specimens. This is attributed to the fact that the bond-slip effect of the reinforcing steel, which is not accounted for in the finite element model, has been significant. According to Beckingsale (1980), 30% of the end rotation of the beams was due to rebar slip.

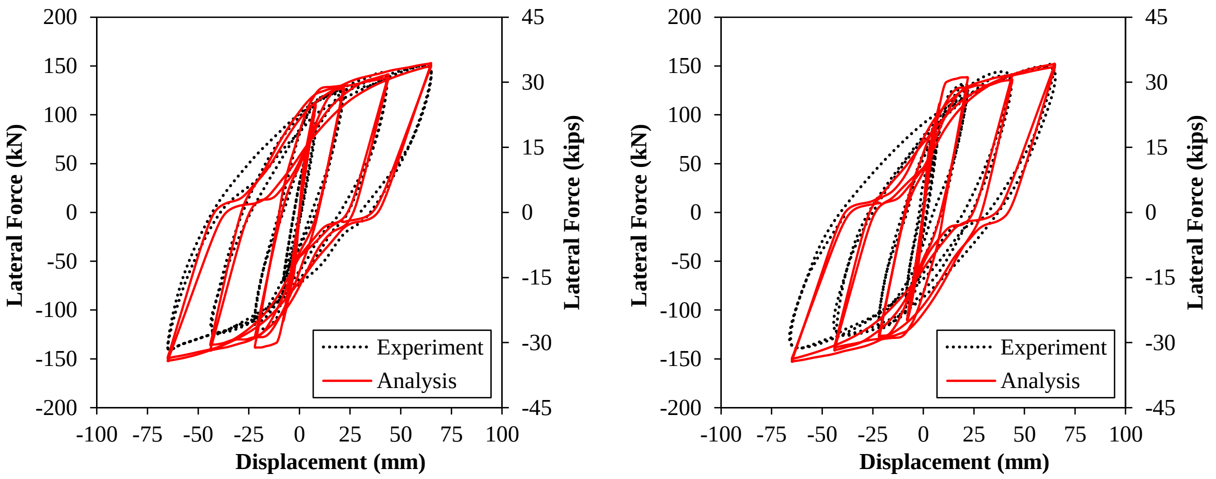

(a) West beam

(b) East beam

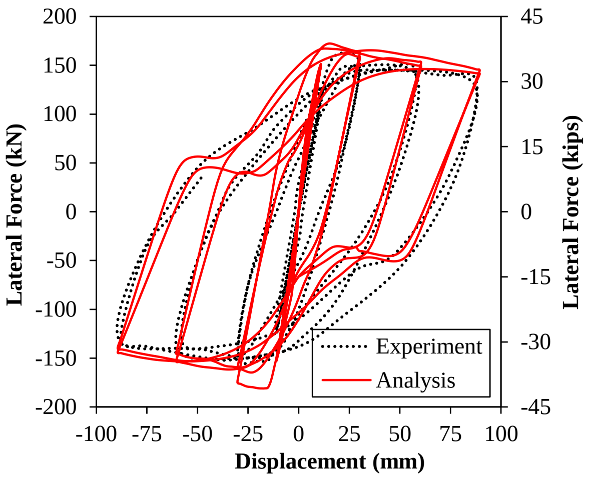

(c) Column

Figure 4.7: Hysteretic plots for beam-to-column joint tested by Beckingsale (1980).

The analytically obtained cracking pattern and its evolution are compared with the experimental observations in Figure 4.8. The maximum principal strain contours clearly shows the propagation of the cracks by increasing the applied displacement history. For instance the joint region is completely cracked in Figure 4.8c, which consistent with the presented experimental observation.

Note: White regions in the joint panel correspond to strains greater than 0.0002.

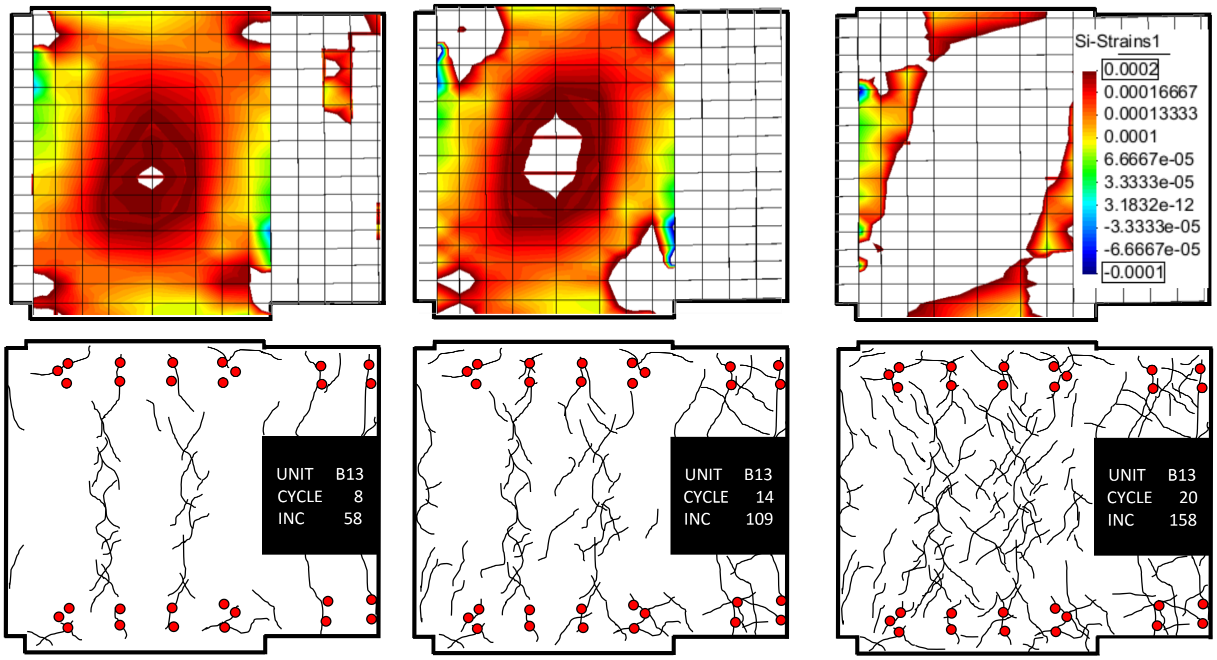

(a) 2nd peak (load run 8) (b) 3rd peak (load run 14) (c) 4th peak (load run 20)

Figure 4.8: Cracking propagation at joint region in different displacement peaks of beam-to-column joint tested by Beckingsale (1980).

4.2 Effect of confinement on ductility

An additional parametric investigation was conducted to demonstrate the effect of the increased ductility due to confinement on the nonlinear performance of the columns which were simulated using the proposed model. The effect of confinement on the strength is still captured through the pressure-dependence of the strength of the material. The hysteretic response obtained without including the increased ductility due to confinement is presented in Figure 4.9. The figure shows that neglecting the effect of confinement on the material ductility leads to significant underestimation of the column ductility. Quantitatively, the capacities of the columns at last loading cycles are underestimated by 65% and 57% for columns tested by Gill (1979) and Ang (1981) respectively. Thus, models such as the one by Lee and Fenves (1998), which do not account for increased material ductility due to confinement, would predict premature lateral strength degradation for the columns.

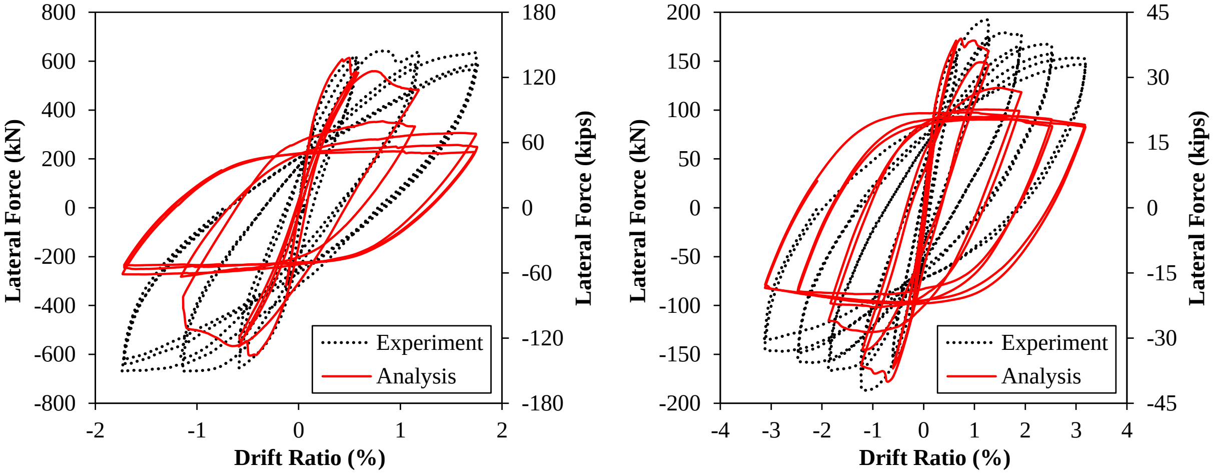

(a) Specimen by Gill (1979)

(b) Specimen by Ang (1981)

Figure 4.9: Analysis results for the two columns, neglecting the effect of confinement on the material ductility.

4.3 Effect of yield criterion on structural response

To investigate the effect of using more accurate yield criterion in the elastoplastic constitutive equation, the modified yield surface and the surface by Lubliner et al. (1989) are implemented in the FEAP (Taylor 2013), and the analyses for the two columns are repeated.

The results of the analyses using the modified yield surface for the two columns are presented in Figure 4.10. As can be seen in the figure, good agreement is obtained for both columns in terms of the overall response; however, still the analysis overestimates the lateral capacity of the column tested by Gill (1979) by 6% and underestimates the lateral capacity of the column tested by Ang (1981) by 1%.

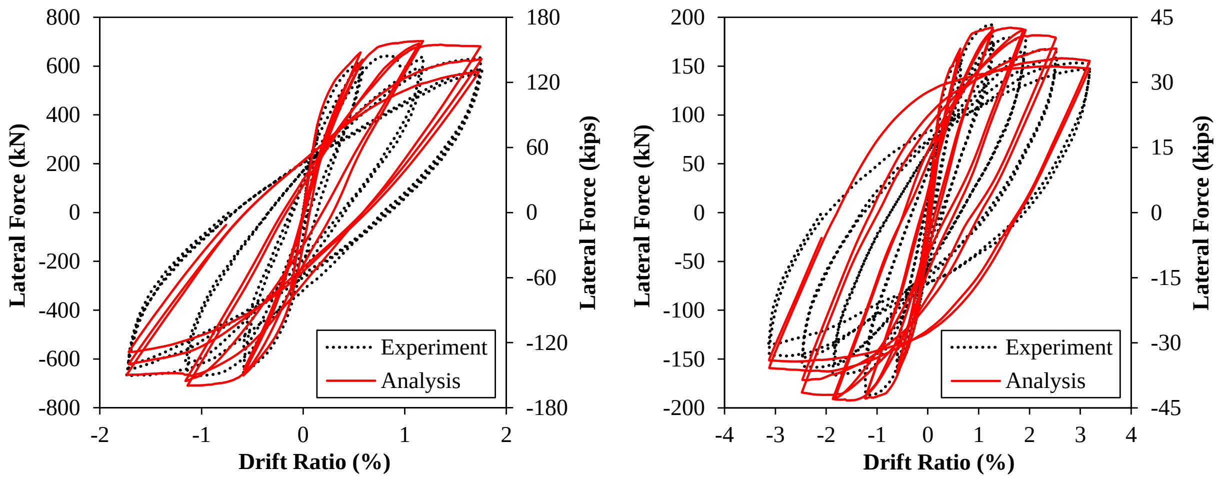

(a) Specimen by Gill (1979), α = 0.3 (b) Specimen by Ang (1981), α = 0.37

Figure 4.10: Results for columns using modified yield surface

The results of the analyses using the surface by Lubliner et al. (1989) for the two columns are presented in Figure 4.11. Parameters α and γ were assigned values of 0.08 and 3, respectively. As shown in Figure 4.11, the capacity of the column tested by Gill (1979) is overestimated by 20%, while the capacity overestimation for the column by Ang (1981) is less severe and equal to 8%. It is worth mentioning that the value of α was significantly lower than that used for the Drucker-Prager model. In fact, the value $\alpha=0.08$ corresponds to the minimum value of the range recommended by Lubliner et al. (1989) for α. If α had been assigned the same values as for the Drucker-Prager model, then the overestimation of the capacity for the model by Lubliner et al. (1989) would have been even greater.

To investigate why the modified surface gives satisfactory results while the surface by Lubliner et al. (1989) is apparently bound to overestimate the capacity, the relative magnitude of the three surfaces is compared in Figure 4.12 for different values of I_1/c_c. The figure shows that the modified surface, based on the introduction of the radial distance $r(\theta,e)$, is always inscribed on the Drucker-Prager surface. As the magnitude of the ratio I_1/c_c increases (i.e., for higher confinement), the modified surface gets closer to the Drucker-Prager surface. As shown in Figure 4.12a, the surface by Lubliner et al. (1989) is inside the other two surfaces for low values of I_1/c_c. As the confinement effect increases, the surface by Lubliner et al. (1989) practically coincides with the modified surface, as shown in Figure 4.12b. Further increasing the confinement effect, as indicated in Figures 4.12c, 4.12d and 4.12e, leads to the surface by Lubliner et al. (1989) predicting higher strength than the other two surfaces. Eventually, the increased strength predicted by the Lubliner et al. (1989) model becomes much higher than that predicted by the Drucker-Prager surface.

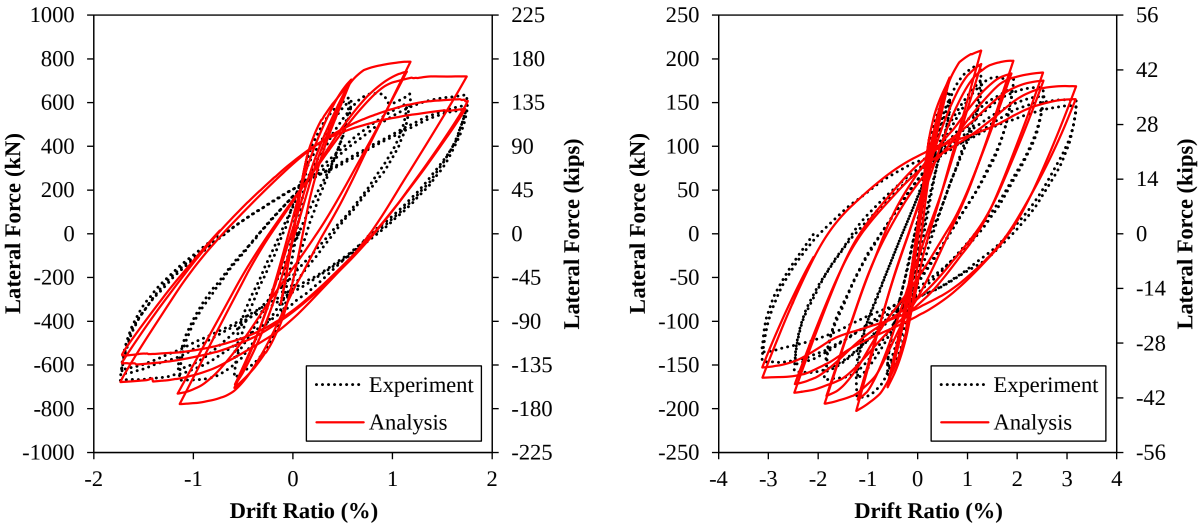

(a) Specimen by Gill (1979)

(b) Specimen by Ang (1981)

Figure 4.11: Results for analyses using the Lubliner et al (1989) yield surface.

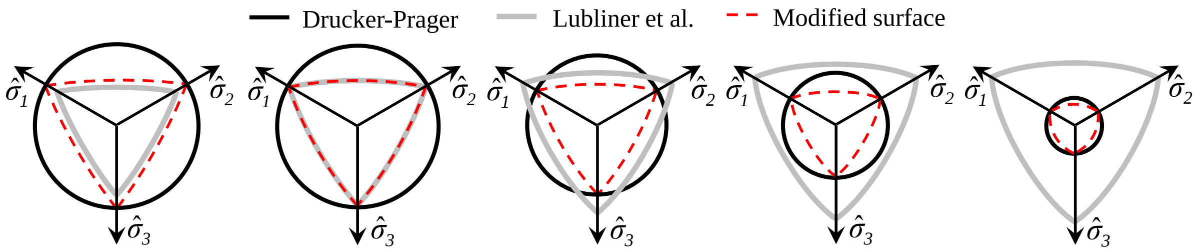

(a) I_1/c_c = -0.75

(b) I_1/c_c = -1.00

(c) I_1/c_c = -1.50

(d) I_1/c_c = -3.00

(e) I_1/c_c = -10.00

Figure 4.12: Comparison of different yield surfaces for various levels of confinement (note: the various figures are not using the same scale).

To provide further insight on the significance of the yield surface, the variation of the ratio I_1/f_c for an element at the core of the two column specimens is presented in Figure 4.13a. The fact that this ratio assumes values much less than -1 provides an explanation for the increased strength predicted for the surface by Lubliner et al. (1989). It is important to note that the ratio I_1/c_c may reach even higher magnitudes than the ratio I_1/f_c, due to the fact that f_c is the maximum value that c_c can acquire.

To remedy the issue of the strength overestimation when the surface by Lubliner et al. (1989) is used, the value of γ can be established as a function of the I_1/c_c ratio. If the ratio of I_1/c_c is greater than -1, then γ can have the value suggested by Lubliner et al. (1989). If I_1/c_c becomes lower than -1 due to either growth of confining pressure or reduction in c_c, the value of γ should decrease. Figure 4.13b shows the variation of the radial distance, $r(\theta,e)$, for the same elements at the core of the two columns. The figure indicates that the value of the radial distance significantly fluctuates throughout the analysis. The radial distance in excess of 1 indicates a discrepancy between the modified surface and the Drucker-Prager surface. Still, for the columns considered herein, the analyses using the two surfaces provided equally good estimates of the column hysteretic response. Thus, since the Drucker-Prager surface leads to increased conceptual simplicity and numerical efficiency, it would then appear as the most preferable surface to use for simulations of components similar to those examined in the present study.

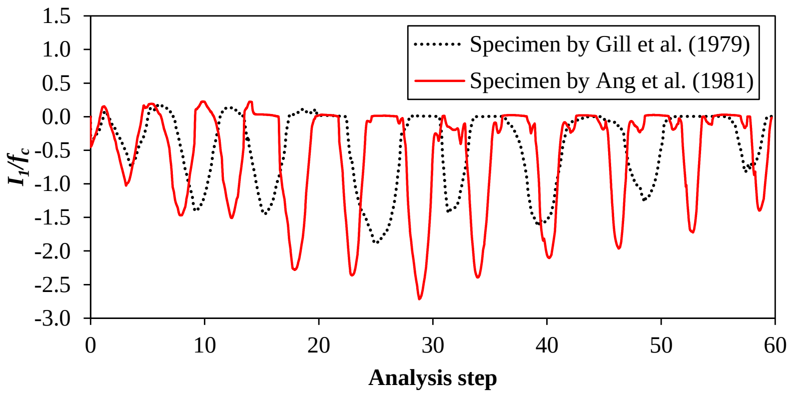

(a) Variation of I_1/c_c ratio at toe of columns

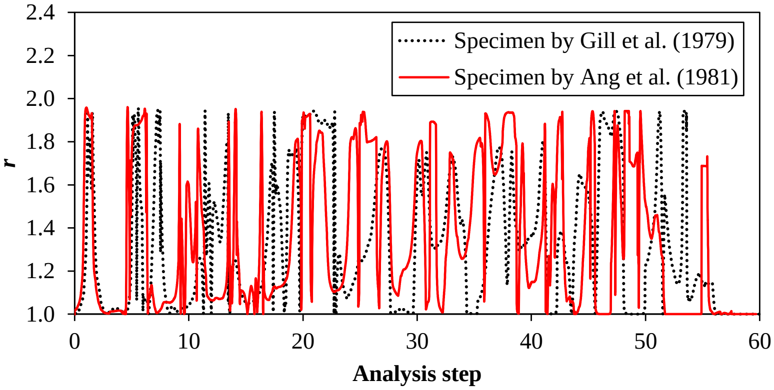

(b) Variation of *r* at toe of columns

Figure 4.13: Variation of quantities affecting the yield surface by Lubliner et al. (1989) and the modified yield surface.

4.4 Discussion

The proposed model uses a rotating-crack formulation to capture the effect of cracking on the material behavior. Several researchers (e.g., Leibengood et al. 1986, Maekawa et al. 2003) have argued that a fixed-crack approach is superior to a rotating-crack one, because the former has the capability to describe generic material states where the stresses and strains can be non-coaxial, i.e., the principal stress and principal strain orientations do not always coincide. This capability can be instrumental for cases where significant shear stress transfer occurs across a formed crack. Fixed-crack models allow the incorporation of different shear stress transfer laws to explicitly describe the shear transfer across cracks in concrete. Conversely, other studies (e.g., Rots and Blaauwendraad 1989) have concluded that the capability of having non-coaxial stresses and strains can lead to inaccuracy of the results. Although the use of a rotating-crack model could – in light of the above considerations – be considered as a limitation of the proposed model, the accuracy of the analyses presented herein was very good. To further enhance the applicability of the proposed model, it can be extended in the future to incorporate a fixed-crack approach for the cracking part of the strains.

The coupling between the elastoplastic and the fixed-crack parts of the model can be conceptually similar to the one described in De Borst and Nauta (1985).

The material model presented herein uses a smeared representation of cracking, so its accuracy for cases where strongly localized cracks may form is bound to be limited. Previous research (e.g., Rots and Blaauwendraad 1989, Lotfi and Shing 1991, Bažant and Planas 1998) has demonstrated that, in the case of strongly localized cracking, continuum-based, smeared-crack models suffer from the stress lock-in effect, which prevents the accurate description of the response. For this reason, if strongly localized cracks are expected to form, the proposed continuum-based model should be combined with a discrete-cohesive crack representation of localized fracture, in accordance with previous pertinent research (Rots and Blaauwendraad 1989, Lotfi and Shing 1991).

Chapter 5 : Analysis of Damage and Failure of Flexure-Dominated Reinforced Concrete Members under Earthquake Loading

Strong ground motions due to rare, extreme events can lead to opening of large cracks, cover spalling, rebar yielding, and crushing of the concrete. Inelastic deformations can lead to buckling and subsequent rupture of the longitudinal reinforcement due to low-cycle fatigue. The rupture of the longitudinal reinforcement is associated with significant degradation in the strength of a member and may lead to full or partial collapse of a structural system.

This chapter presents a three-dimensional (3D) analysis framework, based on the explicit finite element (FE) method, for the simulation of reinforced concrete (RC) components under cyclic static and dynamic loading. The proposed triaxial constitutive model for concrete, described in Chapter 3, is combined with a material model for reinforcing steel which can account for rebar rupture due to low-cycle fatigue. The reinforcing steel bars are represented with nonlinear beam elements to explicitly account for buckling of the reinforcement. The strain penetration effect is also explicitly accounted for in the models. The modeling scheme is employed in the commercial finite element program, LS-DYNA (LSTC 2007), and validated with the results of experimental static and dynamic tests on RC columns and walls. The analyses are supplemented with a sensitivity study and with calibration guidelines for the proposed modeling scheme.

5.1 Description of modeling scheme

This section describes the element types and the constitutive laws used for the analysis of RC structures subjected to cyclic loading. A detailed description of the concrete and steel material models is provided in Moharrami and Koutromanos (2016) and Kim and Koutromanos (2016), respectively.

5.1.1 Element formulation and constitutive model for concrete

In the proposed analysis scheme, the concrete is modeled using three-dimensional, hexahedral, eight-node solid elements with uniform reduced integration (URI), i.e. with a single quadrature point. While URI enhances the efficiency of finite element formulations by substantially reducing the computational cost with the stress update at the quadrature points of the mesh, it also entails the presence of spurious zero-energy modes (hourglass modes), for which URI-based elements cannot develop resistance. Figure 5.1 schematically demonstrates the hourglass modes of hexahedral element.

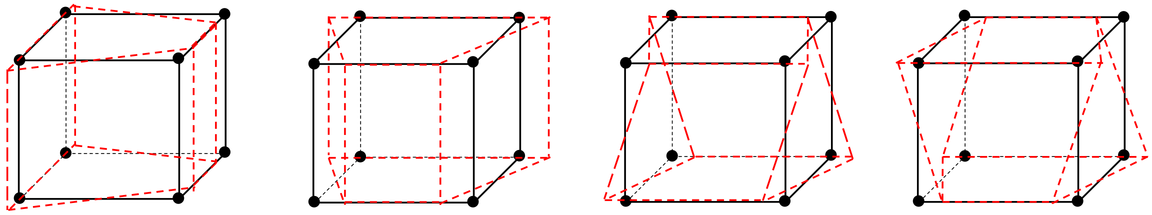

Figure 5.1: Hourglass modes of eight-node solid element (reprinted from Flanagan and Belytschko 1981)

An eight-node hexahedral element with URI has a total of twelve hourglass deformation modes. To prevent the hourglass modes from polluting the solution, hourglass-control methods must be employed to allow an element to develop hourglass-resisting forces. The hourglass-resisting force should be the summation of twelve vectors, each vector providing the resistance to one of the hourglass modes. For each node *k*, the *i*-th component of the force vector resisting the *a*-th hourglass mode is given by the following equation.

$$f_{i\alpha}^{k} = a_h . g_{i\alpha} . \gamma_{\alpha k} \qquad (5.1)$$

where $\gamma_{\alpha k}$ is the component corresponding to node *k* for the basis vector of the *a*-th hourglass mode, and $g_{i\alpha}$ is the projection of the nodal response on the *a*-th hourglass mode, for the *i*-th direction of the motion. The value of $g_{i\alpha}$ is non-zero only when the corresponding hourglass mode is present in the nodal response vector. The value of a_h in Equation (5.1) can be found from the following expression.

$$a_h = Q_{HG} . \rho v_e^{\frac{2}{3}} \frac{c}{4} \qquad (5.2)$$

where ρ is the material density, v_e is the volume of the element, c is the speed of sound in the material of the element, and Q_{HG} is a user-defined, hourglass coefficient. A value of 1 for Q_{HG} gives an optimal approximation of the bending stiffness for linearly elastic elements. The complete procedure for hourglass control, including the determination of the hourglass vectors and of the corresponding resistance forces, is described in Flanagan and Belytschko (1981).

Two different hourglass approaches can be established for hourglass control, depending on the nodal response quantity used to determine the hourglass component of the motion. Using the nodal displacements to obtain the hourglass part of the motion leads to stiffness-based hourglass control, while using the nodal velocities leads to viscous hourglass control. Both approaches are used in the present study. For elastic solid elements, e.g. the locations where no damage is expected to occur, and for the cover concrete, the hourglass-resisting force vector is stiffness-based. The hourglass coefficient is set equal to 1 for elastic elements, and 0.05 for the cover concrete. For cases involving quasi-static cyclic loading, and only for the core portion of the specimen, i.e. the location that are confined by stirrups or ties, the hourglass formulation developed by Belytschko and Bindeman (1993) is used.

The constitutive law for the concrete is the one formulated by Moharrami and Koutromanos (2016). The specific formulation accounts for the stiffness and strength degradation due to cracking and crushing, and for the increase in strength and ductility of the material under confined compression. A complete description of the model formulation and algorithmic implementation is provided in Chapter 3.

5.1.2 Element formulation and constitutive model for reinforcing steel

The reinforcing steel bars are modeled using continuum-based beam elements based on the formulation by Hughes and Liu (1981a, 1981b). Although beam elements are computationally more demanding compared to truss elements, they can naturally capture the effect of rebar buckling (Maekawa et al. 2003). The beam elements employed in the present study include a single quadrature location along the length, and a total of four quadrature points are used for the section of the specific location. To better capture the inelastic buckling in regions where inelastic deformations occur, nine sectional quadrature points are used for the beam elements of these regions.

The reinforcing steel material is described by the uniaxial constitutive law of Kim and Koutromanos (2016), which is essentially an enhanced version of the material model by Dodd and Restrepo (1995). The enhancements include the elimination of the need for iteration in the stress update algorithm and the capability to account for the material failure (rupture) due to low-cycle fatigue. The material model can be fully calibrated if the stress-strain curve of the material in monotonic tension, shown in Figure 5.2a, is given. As demonstrated in Kim and Koutromanos (2016), the constitutive law can capture the cyclic hysteretic response of reinforcing steel, as qualitatively shown in Figure 5.2b.

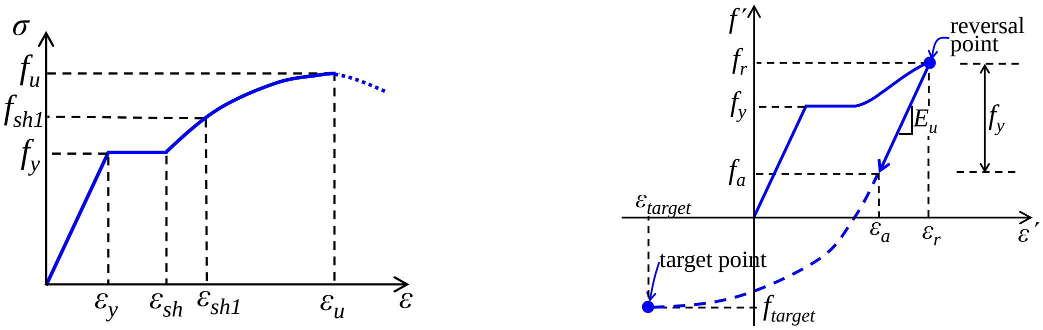

(a) Monotonic Tensile Response

(b) Cyclic Hysteretic Response

Figure 5.2: Behavior of reinforcing steel model (figures from Kim and Koutromanos 2016)

To account for the rebar rupture, a criterion based on the accumulation of a continuous quantity *D* (Huang and Mahin 2010) is adopted. Specifically, given the true material stress, f, and the plastic strain rate, $\dot{\varepsilon}_p$, the evolution of *D* is governed by the following rate equation.

$$\dot{D}=\begin{cases}\left(\dfrac{f}{f_y}\right)^{2t}\dot{\varepsilon}_p \text{ , if } f>0\\ 0 \text{ otherwise}\end{cases} \tag{5.3}$$

where *t* is a material constant. Rupture, i.e. material failure, occurs when the value of *D* becomes equal to D_{cr}, which is also a parameter of the material model.

5.1.3 Accounting for the strain penetration effect

The analysis methodology also accounts for the bond-slip effect associated with strain penetration at the base of the members considered. Specifically, one-dimensional contact elements are used to connect the nodes of the beam elements representing the rebars with the nodes of the surrounding solid elements representing the concrete. As shown in Figure 5.3a, the contact elements are essentially springs aligned with the axis of the beam elements, and can describe the coupling forces between the rebars and the surrounding concrete. The coupling forces are a function of the slip of the beam elements, i.e. the relative displacement of these elements with respect to the surrounding concrete. The displacements of the beam elements in directions other than the axial one are constrained to be equal to those of the surrounding solid elements. The relation between bond forces and slip is assumed to be elastoplastic, with a softening post-yield branch to account for local bond strength degradation, as depicted in Figure 5.3b. The curve describing the bond-slip law uses the peak bond strength, T_{max}, and the corresponding slip value, S_{peak}, obtained from the bond-slip law of Murcia-Delso and Shing (2014), to provide an approximation of the bond-slip curve obtained from the specific law. This approximation can be deemed adequately accurate, provided that the inelastic response in an analysis is not dominated by bond failure and pullout of reinforcing bars.

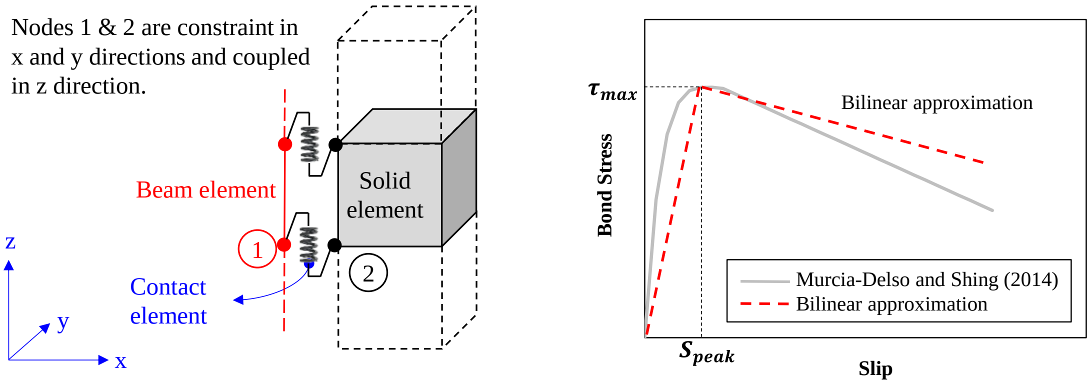

(a) Element types and connectivity

(b) Schematic comparison between approximate bond-slip law adopted in the present study and the model by Murcia-Delso and Shing (2014)

Figure 5.3: Methodology to account for strain-penetration

5.2 Validation of analysis methodology

The proposed modeling methodology is implemented in the commercial finite element program LS-DYNA (LSTC 2007) to allow the simulation of structural components under cyclic loading. An explicit transient integration scheme is employed for the solution of the global equations in the models. Specifically, the global equations are formulated as a dynamic problem, and a central-difference scheme is employed for integration of the global response in time.

The validation is based on the simulation of two post-tensioned walls subjected to cyclic loading (Pakiding et al. 2014), a U-shaped wall under bi-directional cyclic loading (Beyer et al. 2008), and a bridge pier subjected to a sequence of ten ground motions (Schoettler et al. 2012). Rayleigh damping is used in the analyses, with a prescribed damping ratio of 1% for the walls and 0.5% for the bridge pier, for the first and fourth elastic natural frequency of the models. Since all analyses use an explicit dynamic time-marching scheme, special care is taken to simulate the cases involving quasi-static loading. For these cases, the cyclic loads are applied at a sufficiently slow rate, thus ensuring that the analytical solution is not affected by dynamic effects.

The material parameters of the constitutive model for the concrete are calibrated in a consistent fashion. The uniaxial compressive strength, f_c, is obtained from material tests that accompanied the experiments of the structural components. In all analytical models, the Poisson's ratio, v, is set equal to 0.2. The values of parameters f_o and f_{res} in Equation (3.13) are taken equal to 2/3 of f_c, and 5% of f_c, respectively, while the value of the tensile strength, f_t, is set equal to 10% of f_c. The values of parameters ε_o, a_p and a are set equal to 0.0025, 0.15 and 0.375, respectively. The modulus of elasticity of the concrete is assigned a value of $2f_c/\varepsilon_o$. The parameter M in Equation (3.21) is calibrated in accordance with Lu and Panagiotou (2013), while the value of λ_t is found using the equation by Bažant (2002) for the mode-I fracture energy, G_t. Also, the compressive fracture energy, G_c, is set equal to $100G_t$. Finally, the dimensionless user-defined ductility factor, d, is assumed to be equal to the ratio of f_c over 6.89 MPa (1 ksi). The values of several material parameters for the concrete model are presented in Table 5.1.

Table 5.1: Concrete material model parameters

Specimen	f_c (MPa)	*d*	G_t (N/m)	G_c (N/m)	*M*
Pakiding et al. 2014, Wall #1	43.4	6.3	88.9	8890	0.053
Pakiding et al. 2014, Wall #2	47.6	6.9	92.7	9270	0.044
Beyer et al. 2008	77.9	11.0	108.9	10890	0.025
Schoettler et al. 2012	41.3	6.0	83.6	8360	0.036

Note: f_c is concrete compressive strength, *d* is a parameter affecting the increase in ductility due to confinement, G_t is mode-1 fracture energy, G_c is compressive fracture energy, *M* is a ratio of residual tensile strength over tensile strength.

The material failure of concrete associated with cover spalling and concrete crushing is accounted for through element removal. Specifically, solid elements are removed from the analysis whenever the hardening variable, κ, becomes equal to 1.

The material parameters of the uniaxial stress-strain model for reinforcing steel have been assigned the values presented in Table 5.2, based on the results of monotonic rebar tensile tests that accompanied each of the component tests. The value of the Poisson ratio, *v*, which is also required in the continuum-based beam elements, is set equal to 0.3 for all the analyses.

Table 5.2: Steel material parameters

Specimen	*Bar Type*	E_s (MPa)	f_y (MPa)	ε_{sh}	ε_{sh1}	f_{sh1} (MPa)	ε_u	f_u (MPa)
Pakiding et al. 2014, Wall #1	#3	200000	473.0	0.010	0.04	620.5	0.100	741.8
	#4	200000	441.2	0.010	0.04	531.0	0.130	683.3
	#7	200000	518.5	0.010	0.04	620.5	0.160	744.0
Pakiding et al. 2014, Wall #2	#3	200000	474.3	0.010	0.04	620.5	0.100	746.0
	#4	200000	441.2	0.010	0.04	531.0	0.130	683.3
	#5	200000	436.4	0.010	0.04	517.0	0.140	604.7
Beyer et al. 2008	D6	200000	518.0	0.004	0.04	650.0	0.084	681.0
	D12	200000	488.0	0.025	0.06	550.0	0.126	595.0
Schoettler et al. 2012	#11	195990	518.5	0.011	0.04	606.7	0.110	706.0
	#5	200000	377.8	0.002	0.04	517.0	0.125	592.2

Note: E_s is Young's modulus, f_y is yield stress, ε_{sh} is strain at onset of strain hardening, ε_{sh1} and f_{sh1} are the strain and stress of an intermediate point on hardening portion of the monotonic curve, f_u is ultimate strength and ε_u is the corresponding ultimate strain.

Calibration is also necessary for two parameters, t and D_{cr}, controlling the low-cycle fatigue criterion. The value of parameter t in Equation (5.3) is taken equal to 1. The value of parameter D_{cr} (i.e. the threshold value of the continuous quantity D that corresponds to material failure due to low-cycle fatigue) is set equal to $2.4D_{cr}^{(mon)}$, where $D_{cr}^{(mon)}$ is the value of D_{cr} required to capture the instant of rupture for monotonic tension. The value of D_{cr}, used for the various types of rebars in the analytical models is presented in Table 5.3. Longitudinal rebar rupture due to low-cycle fatigue is accounted for through element removal. A beam element is removed when the material failure criterion, $D = D_{cr}$, is satisfied for all sectional integration points of that element.

Table 5.3: Critical damage parameter for rupture in steel material model

Specimen	*Bar Type*	$D_{cr}^{(mon)}$	D_{cr}
Pakiding et al. 2014, Wall #1	#3	0.23	0.55
	#7	0.35	0.83
Pakiding et al. 2014, Wall #2	#3	0.2	0.48
	#5	0.28	0.65
Beyer et al. 2008	D12	0.18	0.44
	D6	0.13	0.31
Schoettler et al. 2012	#11	0.19	0.45

5.2.1 Post-tensioned reinforced concrete walls under quasi-static cyclic loading

The first set of analyses is conducted for two post-tensioned RC wall specimens tested by Pakiding et al. (2014). These were the first two specimens of the specific experimental study, termed Wall #1 and Wall #2, respectively. The configuration and reinforcing details of the wall specimens are depicted in Figure 5.4. Wall #1 represented a shear wall detailed in accordance with modern design standards, while Wall #2 included a higher amount of prestressing tendons to ensure a self-centering (rocking) capability. Two prestressing tendon bundles, each consisting of five strands, were used to provide a prestressing force of 1561 kN (351 kips) for Wall #1, and three bundles, one with five strands and two with seven strands each, were used to provide a prestressing force of 2907 kN (653.5 kips) for Wall #2. The cross-sectional dimensions were identical for the two specimens. The number and size of the reinforcing steel bars was the same, except for the vertical reinforcement in the boundary regions of the sections, where Wall #1 included eight #7 bars having a diameter of 22 mm and Wall #2 included eight #5 bars having a diameter of 16 mm. The walls included additional vertical #3 bars, with a diameter of 10 mm, in the web and boundary regions of the section, as shown in Figure 5.4a. The same figure shows the size and spacing of the transverse (horizontal) reinforcement for the two walls. Each wall specimen was subjected to a prescribed cyclic horizontal displacement history applied at a height of 3.81 m (150 in) from the foundation block until the occurrence of severe damage.

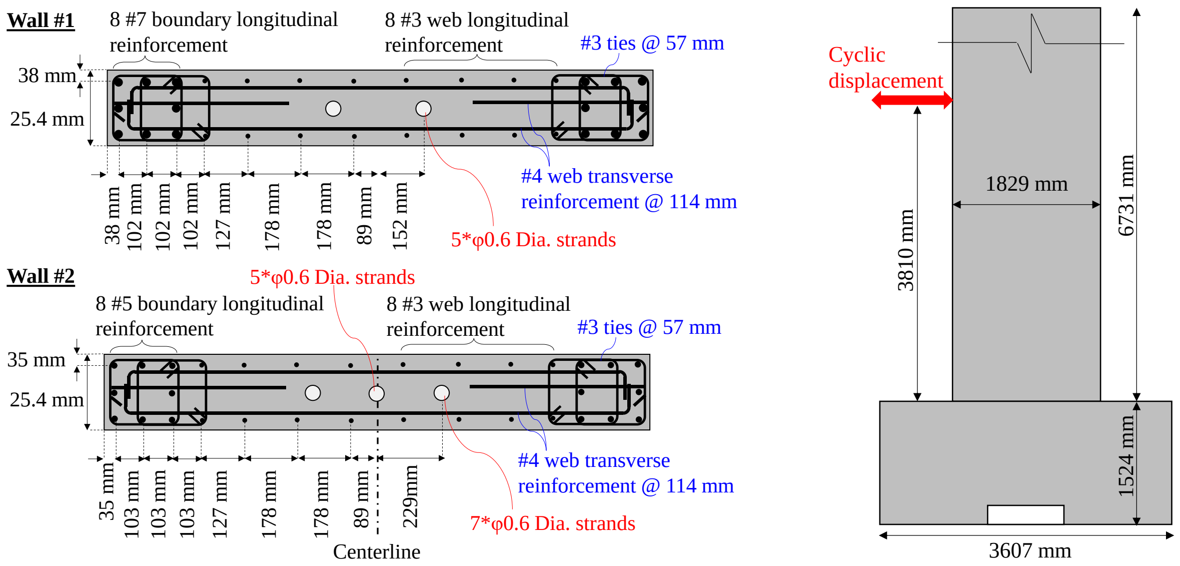

(a) Plan view (b) Elevation view

Figure 5.4: Reinforcement details and geometrical configuration of post-tensioned walls tested by Pakiding et al. (2014).

The finite element model of the walls is presented in Figure 5.5. An elastoplastic constitutive law with linear kinematic hardening is used to represent the material of the prestressing tendons in the model. The yield strength and the hardening slope of the material are set equal to 1675 MPa (243 ksi) and 2038 MPa (295 ksi), respectively, based on provided experimental data for the tendon stress-strain curve.

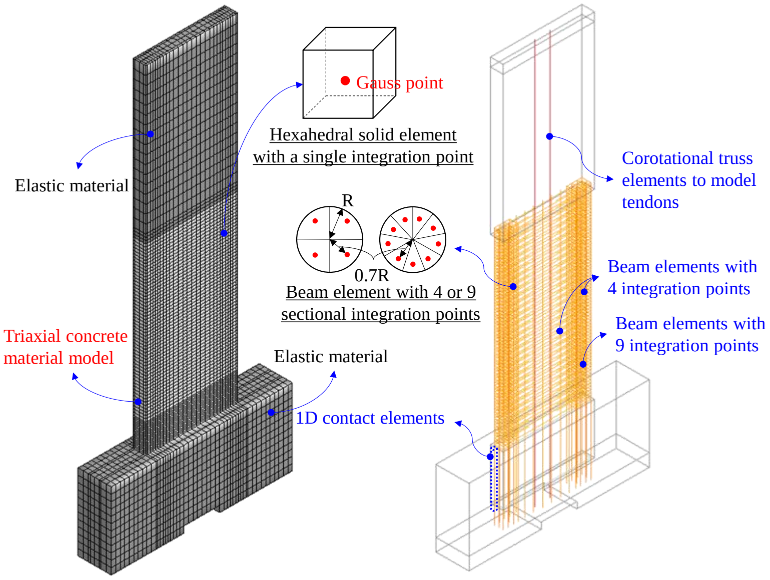

Figure 5.5: Analytical model of post-tensioned walls tested by Pakiding et al. (2014).

The analytically obtained hysteretic response for the two specimens is compared to the corresponding experimental observations in Figure 5.6. The points of the hysteretic curves corresponding to some key events in the analysis are also marked in the figure. The capacity of both specimens is well captured in the negative direction, and it is slightly underestimated in the positive direction. The analysis predicts the same peak strength for both positive and negative directions, while the experimentally obtained strength in the positive direction was higher than that in the negative direction. Pakiding et al. (2014) have not provided any discussion or explanation for this aspect of the experimentally recorded response.

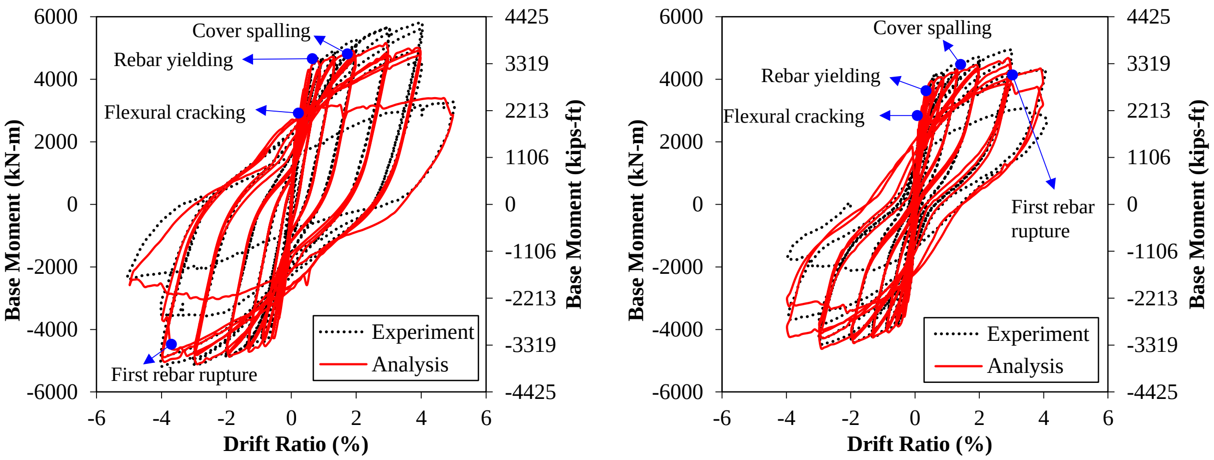

(a) Wall #1

(b) Wall #2

Figure 5.6: Hysteretic response of post-tensioned walls tested by Pakiding et al. (2014).

The sequence of damage accumulation obtained in the analysis of the two specimens is in good agreement with the experimental observations. For the analysis of Wall #1, the first flexural cracks are formed for the cycles with a drift ratio of 0.1%, as shown in Figure 5.7a. The longitudinal steel reinforcement first yields for the cycles with a drift ratio of 0.9%, as shown in Figure 5.7b. Spalling of the cover concrete, described in the models through element removal, first occurs for the cycles with a drift ratio of 1.35%, as shown in Figure 5.7c.

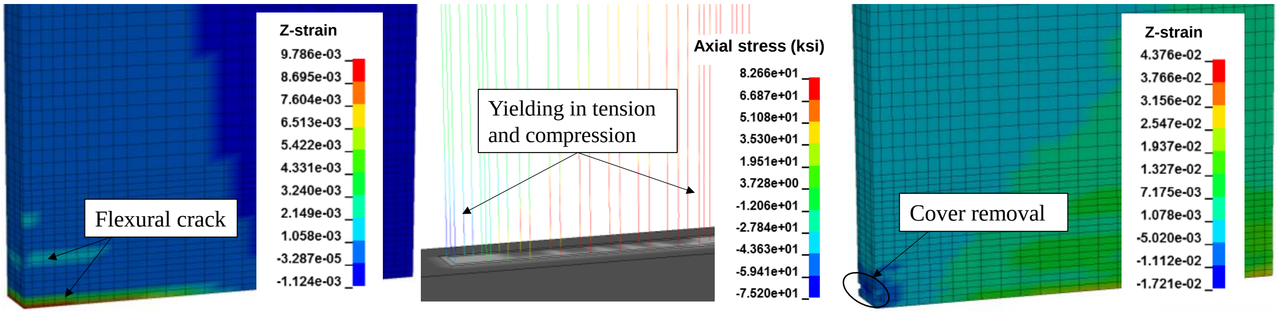

(a) Flexural cracking at 0.1% drift ratio

(b) Rebar yielding at 0.9% drift ratio

(c) Cover spalling at 1.35% drift ratio

Figure 5.7: Pre-peak damage sequence in Wall #1 tested by Pakiding et al. (2014).

The occurrence of tensile yielding of the vertical reinforcement is followed by the accumulation of inelastic tensile strains. During reversal of the applied lateral loads, the vertical rebars which have previously yielded in tension, begin carrying compressive stresses before the open crack fully closes. The vertical rebars also incur transverse deformations, due to the multiaxial stress and strain states developed in the surrounding concrete material. The combined effect of transverse deformations and of compressive stresses following the development of inelastic tensile strains leads to buckling of the vertical reinforcement. The specific process is schematically summarized for the analysis of Wall #1 in Figure 5.8. In the analytical models, buckling of reinforcement in the boundary regions of the specimens is visually detected, as depicted in Figure 5.9.

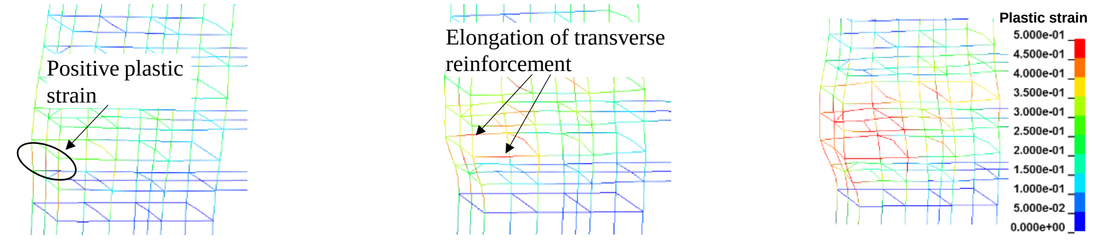

(a) Accumulation of positive plastic strain

(b) Lateral expansion of concrete

(c) Buckling of reinforcing bars

Figure 5.8: Contours of plastic strain at the west side of wall #1 tested by Pakiding et al. (2014).

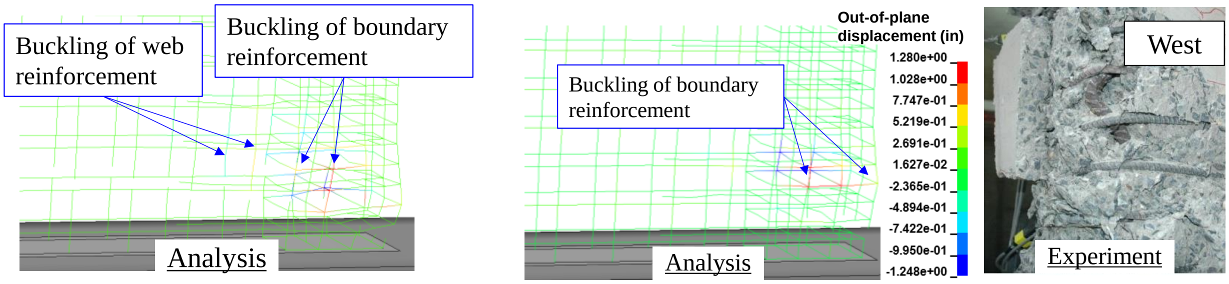

(a) Wall #1

(b) Wall #2

Figure 5.9: Reinforcement buckling in wall specimens tested by Pakiding et al. (2014).

Both wall specimens eventually incurred significant strength degradation due to rebar buckling and subsequent rupture (Pakiding et al. 2014). In the analytical models, the first rebar rupture for Wall #1 and Wall #2 occurs during the third and second cycle, respectively, with a drift ratio of 4%. The bars that rupture first for the analyses of the two wall specimens are presented in

Figure 5.10. Three vertical bars simultaneously rupture for Wall #1, while rupture of a single bar initially occurs for the analysis of Wall #2. In the experimental tests, rupture was obtained for Wall #1 at the same exact cycle as in the analysis. Rupture was observed in the test of Wall #2 during the last loading cycle with a drift ratio of 3%. Given the inherent variability in the yield strength, ultimate strength and fatigue resistance of rebars of the same material, the agreement between the analysis – where all bars are assumed to have identical material properties, calibrated from the monotonic tests – and the experimental observations is deemed satisfactory.

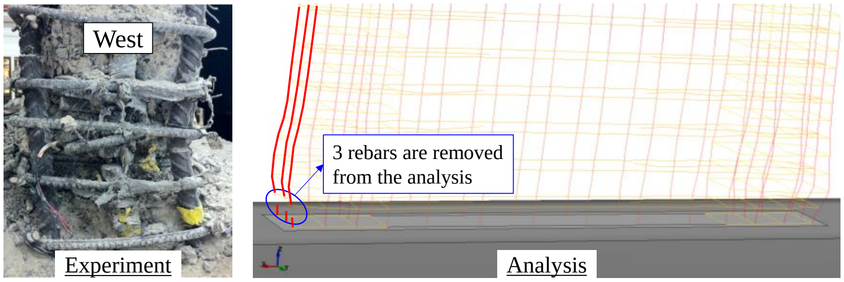

3 rebars are removed from the analysis

(a) Wall #1, third cycle of 4% drift ratio in both the analytical model and experiment

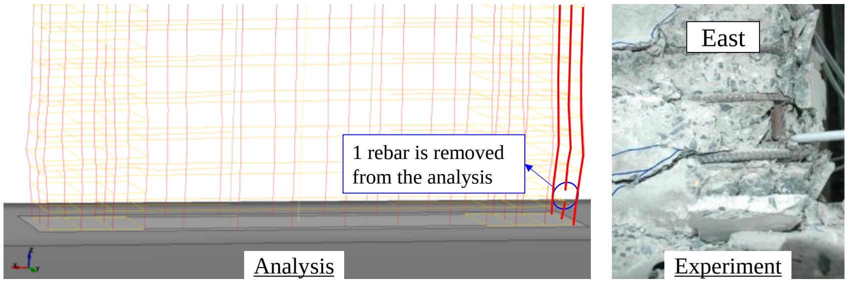

1 rebar is removed from the analysis

(b) Wall #2, second cycle of 4% drift ratio in the analytical model, and third cycle of 3% drift ratio during the experiment

Figure 5.10: Fracture initiation for post-tensioned walls tested by Pakiding et al. (2014).

Finally, Pakiding et al. (2014) described the damage pattern of Wall #1 as a shear failure due to extensive damage in the web of the wall, as shown in Figure 5.11. The specific damage pattern is satisfactorily captured by the analytical model, as depicted in the same figure.

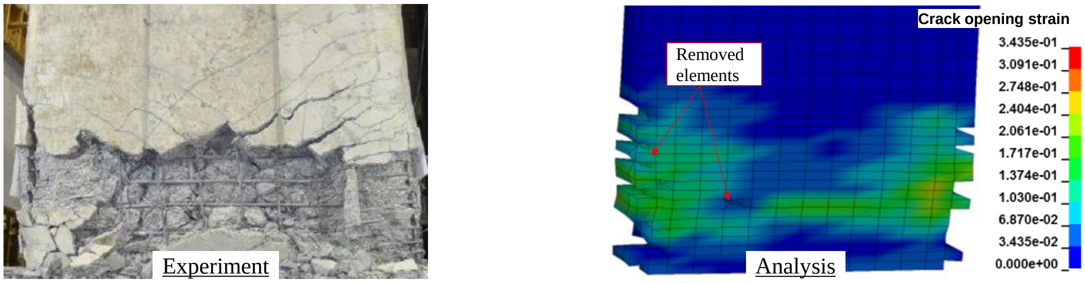

(a) Experimental damage pattern (b) Analytical crack opening strain contours

Figure 5.11: Experimental and analytical damage patterns of Wall #1 at the end of the analysis

5.2.2 U-shaped reinforced concrete wall under bi-directional quasi-static cyclic loading

The next validation analysis is conducted for a U-shaped RC wall specimen tested by Beyer et al. (2008) and referred to therein as specimen TUA. As shown in Figure 5.12a, the height of the specimen was 2.65 meters (104 in), and the thickness of the wall was 150 mm (5.9 in). The same figure defines a coordinate system to allow the efficient description of the bi-directional loading, which corresponded to forces applied along the X- and Y- directions. Figure 5.12b presents the cross-sectional dimensions and reinforcing details of the specimen. The boundary regions of the wall section included twenty-two longitudinal #4 bars with a diameter of 12 mm, while the web portion of the section included a total of twenty-eight #2 rebars with a diameter of 6 mm. The transverse reinforcement at the wall boundaries consisted of ties with a diameter of 6 mm and a spacing of 50 mm (2 in), while the diameter and spacing of the transverse reinforcement at the web regions of the wall section were equal to 6 mm and 125 mm (4.9 in), respectively. The specimen was subjected to a prescribed cyclic bi-directional displacement history until the occurrence of severe strength and stiffness degradation due to rebar rupture and concrete crushing. The displacement histories were applied at a height (above the base) of 2.95 m (116 in) and 3.35 m (132 in), for loading in the X- and Y- direction, respectively. The finite element model of the wall specimen is depicted in Figure 5.12c.

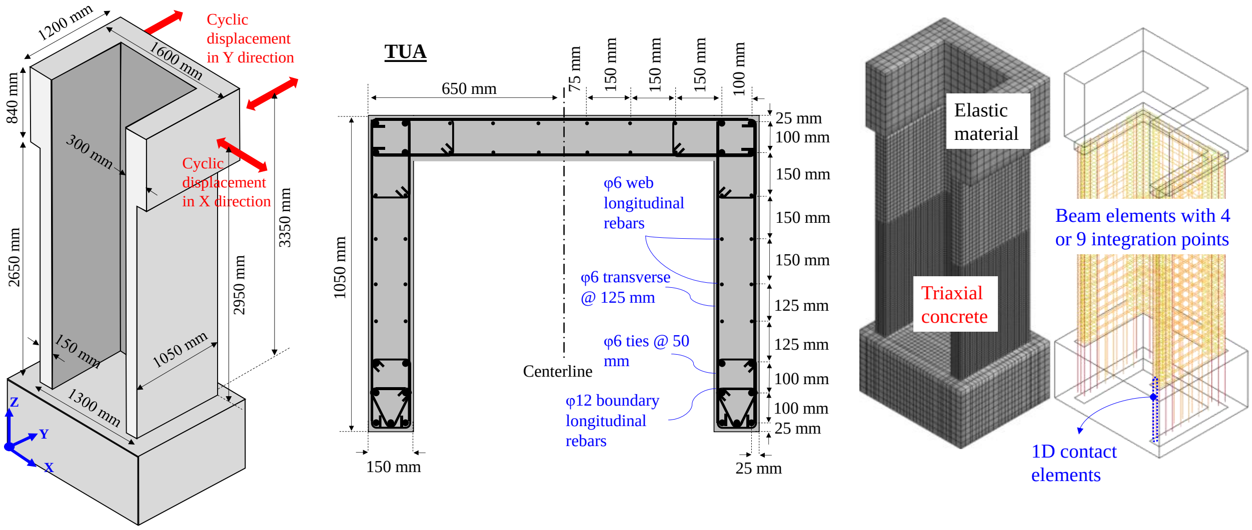

(a) Isometric view (b) Plan view (c) Finite element model

Figure 5.12: Configuration and computational model of the U-shaped wall tested by Beyer et al. (2008).

The analytically obtained hysteretic response of the specimen is compared to the corresponding experimental observations in Figure 5.13. The peak strength and the initial stiffness of the specimen are well captured by the analysis for the Y-direction, while they are slightly underestimated for the X-direction. The analysis also provides a satisfactory representation of the hysteretic response of the specimen.

In both the analytical model and the experimental test, severe damage occurred due to rebar fracture, as shown in Figure 5.14. Similar to the experiment, the first rebar rupture in the analysis occurs during the first loading cycle with a drift ratio of 2.5% along the X-direction. The analytical model successfully captures the damage associated with cover spalling and flexural and shear cracking in the specimen, as depicted in Figure 5.15.

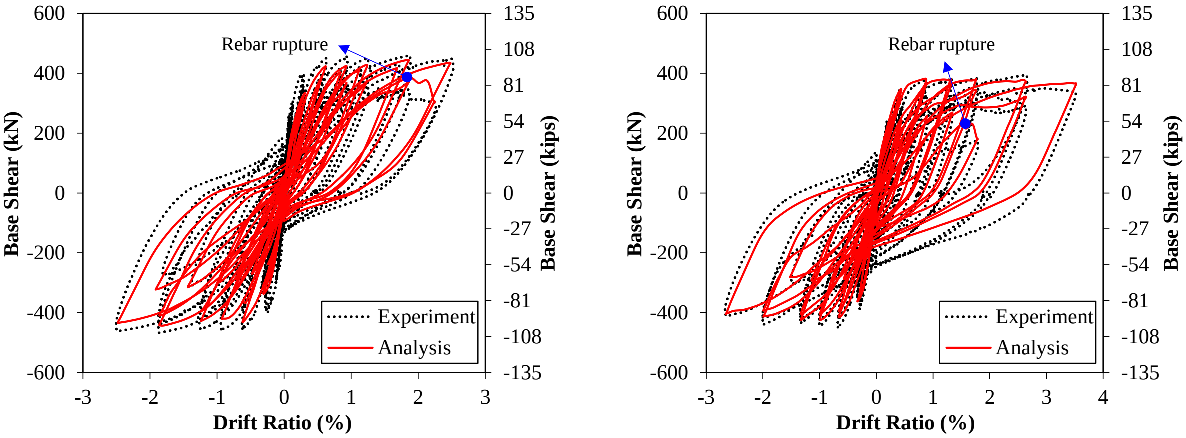

(a) X-direction

(b) Y-direction

Figure 5.13: Hysteretic response of U-shaped wall tested by Beyer et al. (2008).

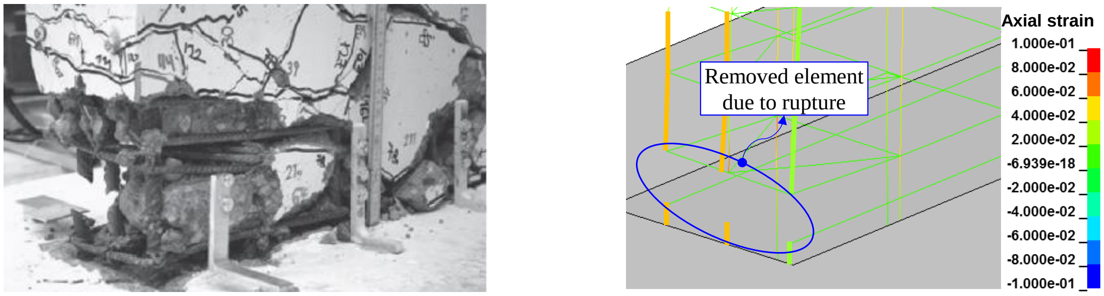

(a) Experiment

(b) Analysis

Figure 5.14: Rebar rupture in the U-shaped wall tested by Beyer et al. (2008).

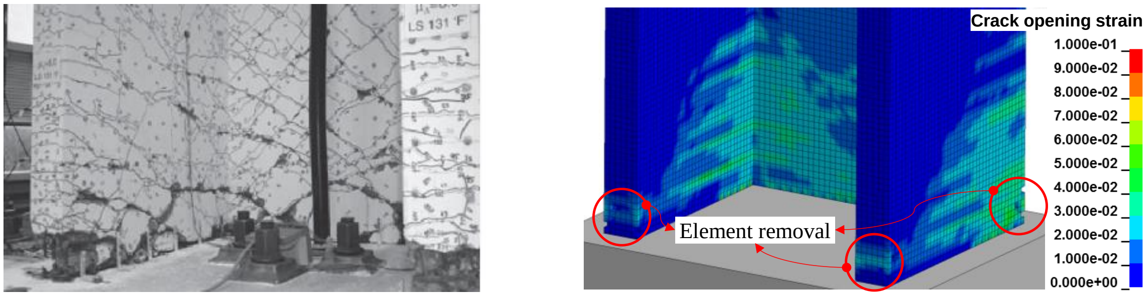

(a) Experiment

(b) Analysis

Figure 5.15: Damage at the base of the U-shaped wall tested by Beyer et al. (2008).

5.2.3 Full-scale reinforced concrete bridge pier subjected to seismic loading

Analysis is also conducted for a full-scale bridge column tested on a shake-table by Schoettler et al. (2012). The specimen was designed based on modern seismic provisions and subjected to a sequence of ten ground motions. As explained in Schoettler et al. (2012), the specimen was not based on a prototype structure, but it was meant to represent single-column bents commonly found in California. The column had a height of 7.31 m (288 in) and a circular cross-section with a diameter of 1.22 m (48 in) which was reinforced with eighteen #11 vertical bars, having a diameter of 36 mm. The transverse reinforcement consisted of double #5 ties at a spacing of 152 mm (6 in). The column configuration and reinforcing details are depicted in Figure 5.16a. The specimen included a concrete block at the top, with a total weight of 2.32 MN (521 kips), to represent the gravity loads and the seismic mass of the bridge column. The finite element model of the specimen is presented in Figure 5.16b and has been analyzed for the entire motion sequence of the specimen.

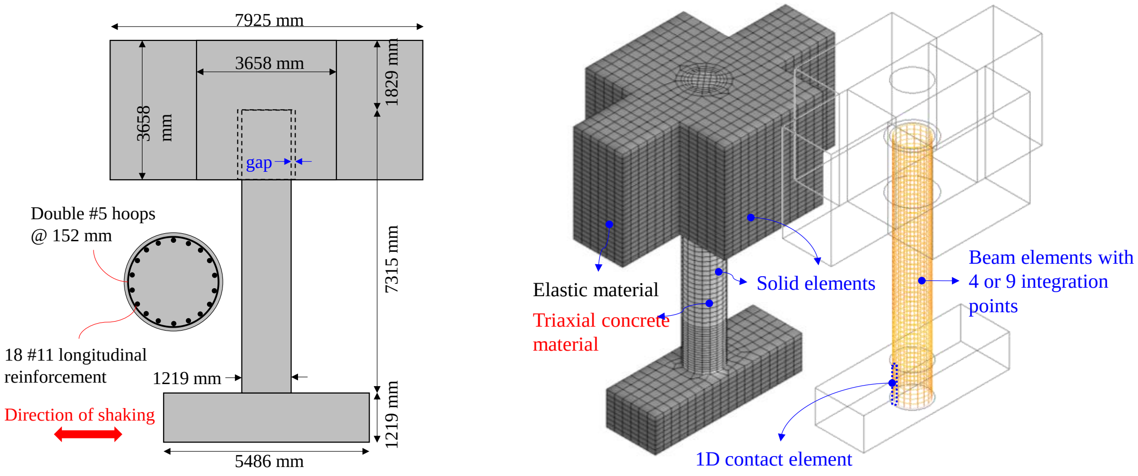

(a) Dimensions and reinforcement detail (b) Finite element model

Figure 5.16: Configuration and analytical model for the column tested by Schoettler et al. (2012).

The analytically obtained drift time histories for nine out of the ten motions of the sequence are compared to the corresponding experimental records in Figure 5.17. A very good agreement is obtained in terms of the peak displacements and drift histories, except for the last motion in the sequence. During the experimental test for that motion, the column came to contact with a safety support tower that was provided to prevent damage of the shake table from total collapse of the specimen. Since the effect of this support tower is not accounted for in the analytical model, the observed discrepancy between the analytically predicted and experimentally recorded drift time histories for this motion is expected.

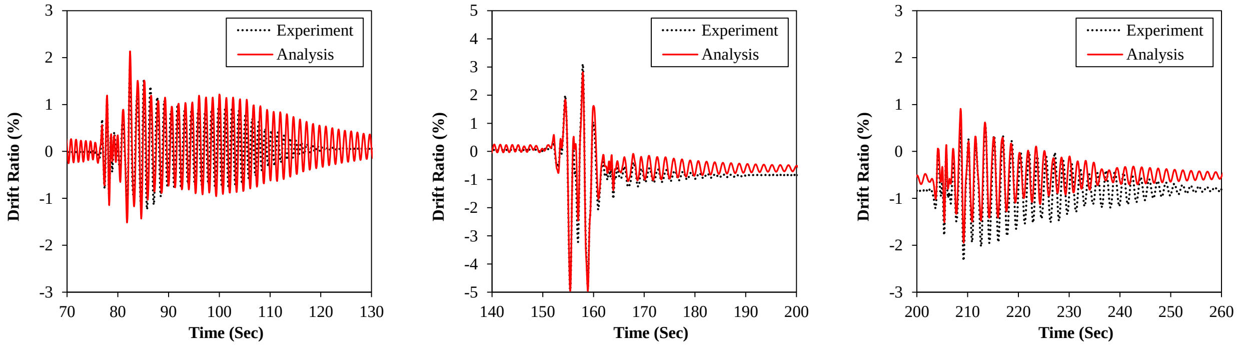

(c) EQ2: 100% Loma Prieta-90° (d) EQ3: 100% Loma Prieta (e) EQ4: 100% Loma Prieta-90°

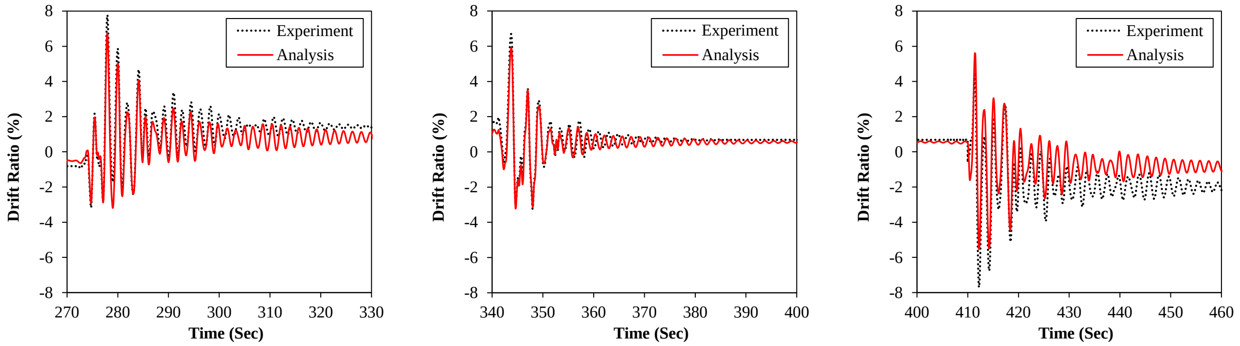

(f) EQ5: 100% Kobe (g) EQ6: 100% Loma Prieta (h) EQ7: 100% Kobe

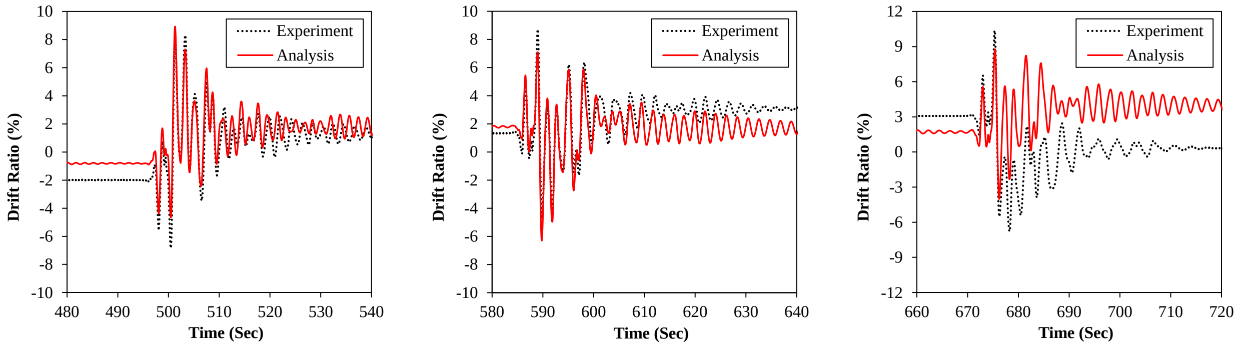

(i) EQ8: -120% Kobe (j) EQ9: 120% Kobe (k) EQ10: 120% Kobe

Figure 5.17: Comparison of analytically obtained and experimentally recorded drift histories for the column tested by Schoettler et al. (2012) for every motion.

Similar to the experimental observations, the analytical model predicts that yielding of the longitudinal reinforcement first occurs during the third ground motion. During the same motion, concrete cover spalling is observed for the first time in the analytical model, as depicted in Figure 5.18a. During the fifth and sixth motions, more extensive loss of cover material occurred in the test, and more cover elements are removed in the analysis, as shown in Figure 5.18b. At the end of the sixth motion, the core concrete in the vicinity of the base of the column was significantly damaged, as shown in Figure 5.19.

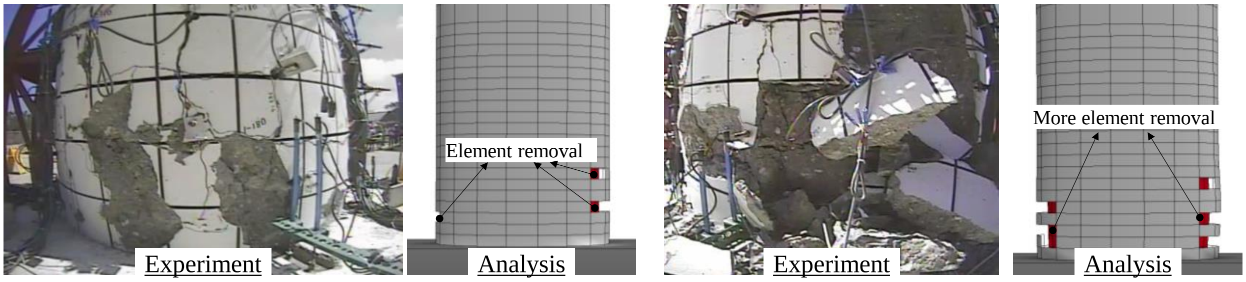

(a) After the third motion (b) After the fifth motion

Figure 5.18: Loss of cover during the test sequence, for the specimen by Schoettler et al. (2012).

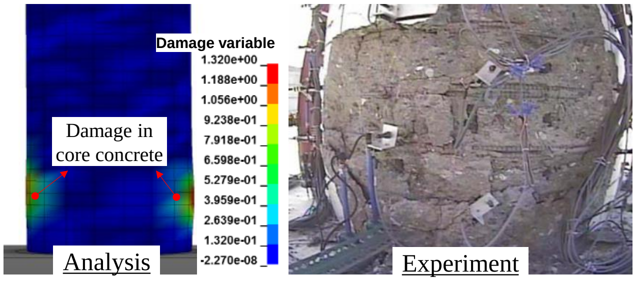

Figure 5.19: Damage at base of column specimen after the sixth motion for the specimen tested by Schoettler et al. (2012).

The experimental test specimen eventually incurred significant damage in the form of rebar buckling and subsequent rupture, as shown in Figure 5.20a. In the analytical model, the buckling of rebars is visually observed during the seventh motion, similar to the corresponding experimental observation, and it is significant during the eighth motion, as shown in Figure 5.20b. Additionally, as depicted in Figure 5.20c, the first rebar rupture is obtained during the eighth ground motion, which was also the case for the experimental test.

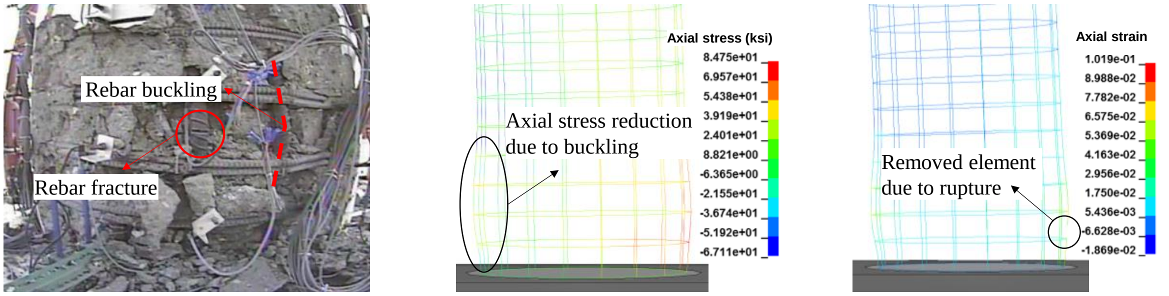

(a) Experimental photograph (b) Contours of axial stress (c) Contours of axial strain

Figure 5.20: Rebar buckling and first rebar fracture observed during the eighth motion for the specimen tested by Schoettler et al. (2012).

5.3 Parametric analyses

The analyses presented in the previous section all rely on a consistent calibration process for the material models. Despite the capability to fully calibrate the values of all parameters of the employed constitutive laws, there are still aspects of the analytical models – such as the amount of viscous damping – which can have implications for the accuracy of the obtained results. Furthermore, it is deemed necessary to assess the significance of several aspects of material behavior, such as accounting for the increased concrete material ductility due to confinement and accounting for the strain penetration effect. This section presents a set of parametric studies to investigate the effect of these aspects on the analytical results.

5.3.1 Effect of viscous damping for analysis of components under quasi-static loading

A first set of parametric analyses is conducted to determine the significance of viscous damping for analyses involving quasi-static loading. To this end, the analyses of the two specimens tested by Pakiding et al. (2014) are repeated, this time without any viscous damping in the models. The hysteretic response obtained for the two specimens is depicted in Figure 5.21. The overall response is similar to that presented in Figure 5.6, except for the initial cycles of loading, where high-frequency oscillations are observed in the hysteretic curves. Damping primarily affects the structural response in the elastic stage of behavior, and its effect becomes negligible after the occurrence of inelastic deformations.

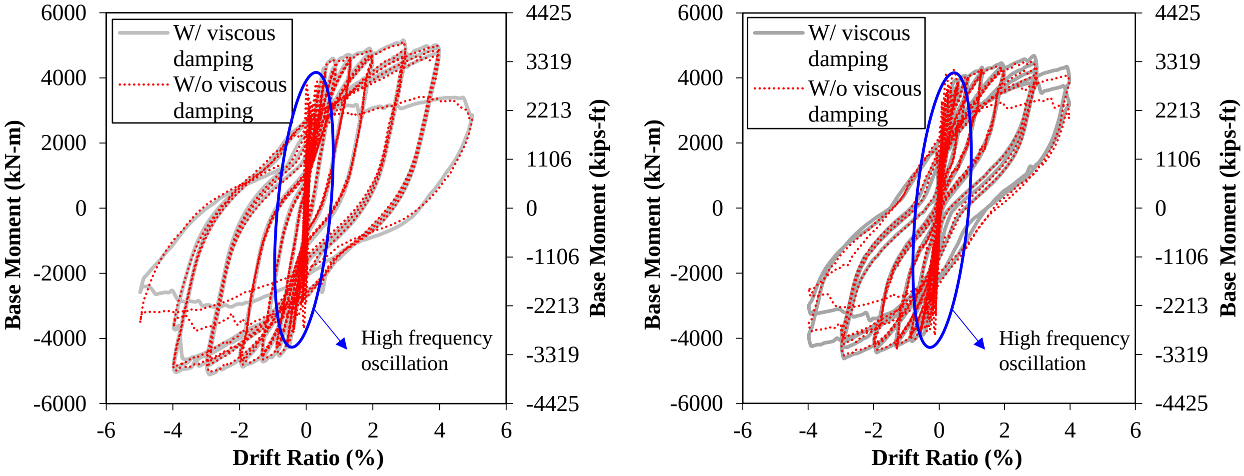

(a) Wall #1 (a) Wall #2

Figure 5.21: Analytically obtained hysteretic response of specimens by Pakiding et al. (2014) with and without viscous damping.

5.3.2 Effect of ductility parameter

To demonstrate the effect of the increased concrete ductility due to confinement on the nonlinear performance, the analysis of Wall #2 by Pakiding et al. (2014) is repeated by setting confinement parameter, *d*, of the concrete constitutive law to zero. This modified calibration neglects the effect of local confining pressure on the compressive ductility of the concrete. The analytically obtained hysteretic response is compared with the experimental data in Figure 5.22a. The figure shows that neglecting the effect of confinement on the material ductility leads to significant underestimation of the wall strength and ductility. Thus, the use of multiaxial material models for concrete which do not account for increased material ductility due to confinement, would entail predictions of premature lateral strength degradation for the walls.

5.3.3 Effects of not accounting for strain penetration

To elucidate the strain penetration effect on the response of the wall specimens, the analysis of Wall #2 by Pakiding et al. (2014) is repeated, this time without the one-dimensional contact elements accounting for rebar slip in the foundation block. The analytically obtained hysteretic response obtained with and without the strain penetration effect is compared to the experimental observations in Figure 5.22b. The figure indicates that ignoring the strain penetration effect has a minor impact, leading to a slight increase in the stiffness and peak strength.

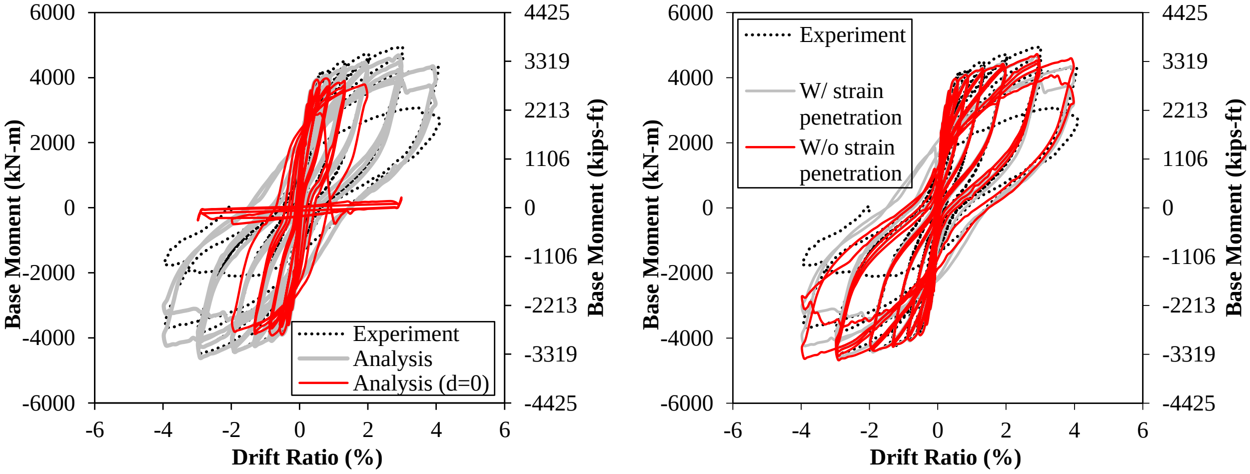

(a) Effect of confinement on ductility (b) Effect of strain penetration

Figure 5.22: Sensitivity analysis on Wall #2 tested by Pakiding et al. (2014).

5.4 Discussion

The proposed methodology has been shown to satisfactorily capture the global response and damage patterns of RC components under cyclic loads. The validation analyses have all been conducted with a consistent calibration scheme, without any effort to fine-tune material parameters to improve the agreement with the experimental tests. This fact shows the very good predictive capabilities of the proposed method.

The modeling scheme proposed herein may require several enhancements before it is applied to simulation of components such as beam-to-column joints. Specifically, it is well-established that the hysteretic response of such components is significantly affected by the bond-slip behavior of the reinforcing steel (e.g., Beckingsale 1980). For this reason, the implementation of a more refined bond-slip model that can account for cyclic deterioration of bond resistance, such as the one by Murcia-Delso and Shing (2014), is deemed necessary for the simulation of such components.

An important requirement for refined finite element models pertains to capturing full collapse of structural components. The present study has considered tests which were conducted up to the occurrence of severe damage, but full specimen collapse was not pursued, to avoid damaging the laboratory equipment. A preliminary assessment of the capability of the proposed scheme to capture component collapse is deemed necessary. To this end, an additional analysis of the shake-table specimen is conducted, wherein the parameters of the low-cycle fatigue model are so calibrated that collapse will occur in the analysis due to extensive, premature rebar rupture. The analysis does predict full collapse during the eighth motion of the sequence, as shown in the drift time history and the deformed configuration presented in Figure 5.23. The analysis has predicted the specimen collapse without any problem in the stress update process of the constitutive laws or in the global solution scheme.

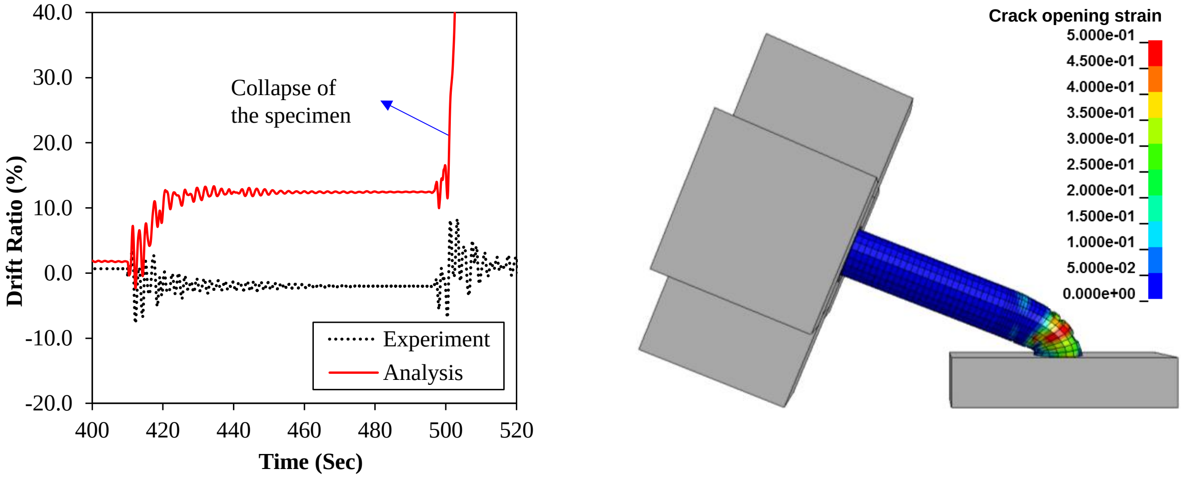

(a) Drift history (b) Crack opening strain contours

Figure 5.23: The full collapse of the bridge pier during 8th ground motion

The analyses presented herein rely on explicit transient integration. To verify that the inertial effects due to the use of the explicit solution scheme for quasi-static loading do not significantly affect the results obtained in the present study, the analysis of the wall specimen tested by Beyer et al. (2008) is repeated using an implicit static solution scheme. This analysis also allows the verification of the capability of the proposed modeling approach to be combined with an implicit static solution scheme. The analytically obtained hysteretic response is compared with the corresponding experimental data in Figure 5.24. As can be seen from the figure, the lateral strength of the wall is satisfactorily captured in both directions. Additionally, the analytical model can capture the strength degradation due to rebar rupture. The only significant disagreement with the hysteretic curve obtained for explicit analysis is in the initial stiffness, which is higher for implicit analysis. This discrepancy in initial stiffness is caused by the fact that the hourglass control in the implicit analysis is stiffness-based for all elements, while viscous-based hourglass control has been used for the solid elements representing the core concrete in the explicit analysis.

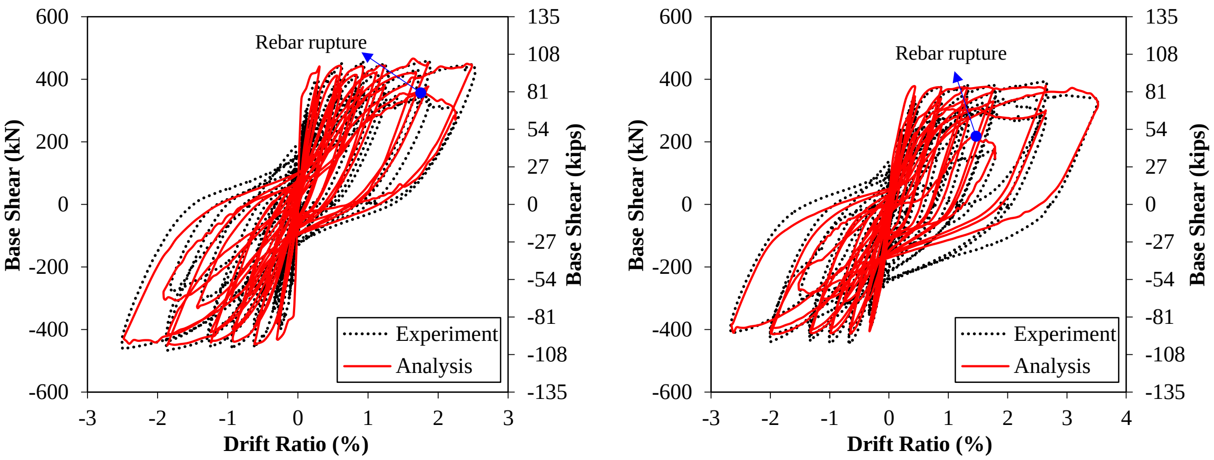

(a) X-direction (b) Y-direction

Figure 5.24: Hysteretic response of U-shaped wall by Beyer et al. (2008), obtained using implicit static global solution scheme.

For simulations focused on quasi-static loading, implicit static solution algorithms may be deemed preferable, because they eliminate the possibility for spurious inertial effects on the solution. Another issue which may affect the efficiency of explicit schemes is that they are conditionally stable, i.e. they require a sufficiently small time-step to preclude the occurrence of numerical instability. Still, implicit algorithms may not be well-suited for analyses of large models, because they typically entail large memory requirements, associated with the need to store a global tangent stiffness matrix. Furthermore, implicit schemes may not be appropriate for simulations of failure or collapse, due to the probability of failure to satisfy the convergence criteria of the global solution algorithms.

To comparatively assess the efficiency of parallel processing for explicit and implicit schemes, the analysis of the wall by Beyer et al. (2008) has been conducted for a varying number of processors. An insight in the effect of parallel processing is gained by examining the required analysis time as a function of the number of processors (CPUs) employed in the simulation. Such a plot is provided in Figure 5.25a for the explicit analysis, and in Figure 5.25b for the implicit analysis. For the range of number of processors examined here, an increase in the number of processors for the explicit analysis always leads to a decrease in the required computation time. On the other hand, the time required for a single global iteration in the implicit scheme is a decreasing function of the number of CPUs for relatively small number of CPUs. An increase to the number of CPUs beyond 16 has been found to lead to an increase in the computation time. This increase is probably caused by the increasing contribution of the operations involving communication between different processors to the computation time. This communication among processors is introduced by the need to solve linear systems of equations. While the exact dependence of the computation time on the number of CPUs depends on the specific iterative scheme employed and on the algorithm for the solution of the system of equations, the specific trend in behavior is expected to characterize all implicit solution schemes.

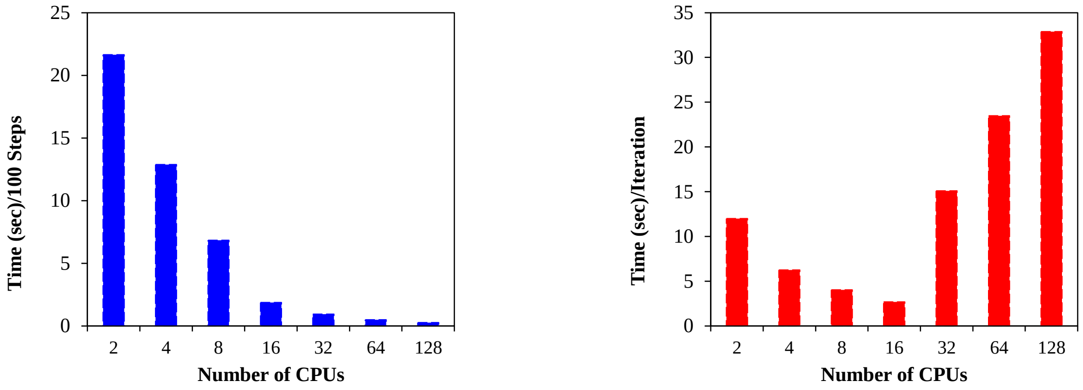

(a) Explicit integration scheme

(b) Implicit integration scheme

Figure 5.25: Effect of number of processors on the time required for the analysis of the U-shaped wall specimen tested by Beyer et al. (2008)

Chapter 6 : Analysis of Damage and Failure of Shear-Dominated Reinforced Concrete Members under Earthquake Loading

The modeling scheme presented in Chapter 5 has been found to be capable of reproducing the damage pattern and global hysteretic response of flexure-dominated reinforced concrete (RC) components, in which strength degradation typically occurs due to concrete crushing, rebar buckling and rebar fracture. Despite the fact that modern RC and reinforced masonry (RM) structures are designed to ensure a ductile, flexure-dominated response, there are cases where the occurrence of shear damage is inevitable (e.g., Ahmadi et al. 2015b). Furthermore, shear failures are probable for many existing RC and RM buildings which have not been designed to ensure a flexure-dominated inelastic response in accordance with modern design standards. Shear failures are manifested through the formation of large inclined cracks which are strongly localized, i.e. they mathematically correspond to a discontinuity of the displacement field. The formation of shear cracks in a RC or RM component is accompanied by a sudden degradation of the lateral resistance, which may even lead to full or partial collapse of the structural system.

While studies (Rots 1988, Lotfi and Shing 1991, Ožbolt and Kožar 2001, Palermo and Vecchio 2004) have attempted to capture the effect of strongly localized cracks with continuum-based finite element models, it is still questionable whether such models can provide accurate results. The major issue associated with the use of continuum finite element models for capturing strongly localized cracks is the propensity for stress lock-in (Rots and Blauuwendraad 1989, Lotfi and Shing 1994, Bažant and Planas 1998). Specifically, the cracks forming in neighboring continuum elements are not aligned to each other, which in turn leads to overestimation of the strength and ductility, and to unrealistic deformation patterns in the mesh. Stress lock-in has been found to primarily affect fixed smeared-crack elements, i.e. elements in which the orientation of the formed cracks remains fixed throughout the analysis. The study by Rots and Blaauwendraad (1989) has found that rotating-crack formulations – like that of the concrete constitutive model described in Chapter 4 – were capable of capturing the strength degradation associated with the occurrence of a localized crack in an unreinforced beam under monotonic loading.

The occurrence of stress lock-in has been attributed to the fact that a continuity of the displacement field is enforced in continuum-based finite element models, rendering them incapable of capturing strongly localized cracks which entail a discontinuity of the displacement field. This has led researchers in using discrete-cohesive-crack interface elements (Koutromanos and Shing 2012) or embedded crack formulations (Oliver 1996, Spencer and Shing 2002) to capture the effect of the displacement discontinuity on the structural response. Such elements require the establishment of separate formulations and stress update procedures to describe the traction-separation behavior of strongly localized cracks. An approach that could remove inaccuracies stemming from continuity of the solution, without requiring the formulation of separate traction-separation laws, is to use meshless particle methods (Li and Liu 2004). Such methods represent a solid body through an assemblage of particles, without enforcing continuity conditions on the displacement field. For this reason, it would appear that meshless methods are well-suited for simulations involving shear failures.

To address the aforementioned open issues regarding the simulation of shear-dominated RC/RM structures, the three-dimensional finite element modeling scheme described in Chapter 5, is adopted in this chapter to capture the hysteretic response and damage patterns of shear-dominated components. Analyses have been conducted for two single-story, shear-dominated, RC/RM walls under quasi-static cyclic loading, and for a five-story shear-dominated wall system under a sequence of earthquake motions. The provided analytical results match well with the experimental observations, and validate the capability of the modeling scheme for the analysis of shear-dominated structural components. Sensitivity analyses are also performed to investigate the effects of mesh refinement, selection of tensile fracture energy. Finally, the chapter pursues a preliminary verification of the capability of the meshless, Smoothed Particle Hydrodynamics (SPH) method, to capture the response of shear-dominated RC walls.

6.1 Finite element analysis of shear-dominated walls

A series of validation analyses have been conducted using the program LS-DYNA (LSTC 2007) with the element formulations and material models described in Section 5.1. The calibration procedure for the constitutive models is identical to that described in Section 5.2. Analyses have been conducted for two single-story, walls subjected to quasi-static loading (Massone 2006, Shing et al. 1991), and for an H-shaped, five-story, shear-dominated wall system with openings subjected to a sequence of earthquake motions (Kante 2005).

The values of material parameters used for the concrete and reinforcing steel in the analyses are presented in Tables 6.1 and 6.2, respectively. The uniaxial compressive strength of the concrete or masonry and the material parameters of the reinforcing steel have been obtained from material tests that accompanied the structural component tests.

Table 6.1: Concrete material model parameters

Specimen	f_c (MPa)	ε_o	*d*	G_t (N/m)	G_c (N/m)	*M*
Massone 2006, RC wall	32	0.0020	4.6	77.23	7723	0.025
Shing et al. 1991, RM wall	17.9	0.0020	2.6	59.17	5917	0.025
Kante 2005	34.8	0.0025	5.0	8.15	8150	0.120

Note: f_c is concrete compressive strength, ε_o is the strain at peak compressive strength, *d* is a parameter affecting the increase in ductility due to confinement, G_t is mode-I fracture energy, G_c is compressive fracture energy, *M* is a ratio of residual tensile strength over tensile strength.

Table 6.2: Steel material parameters

Specimen	*Bar Type*	E_s (MPa)	f_y (MPa)	ε_{sh}	ε_{sh1}	f_{sh1} (MPa)	ε_u	f_u (MPa)
Massone 2006, RC wall	#4	200000	424.0	0.012	0.04	517.0	0.130	630.8
Shing et al. 1991, RM wall	#7	200000	496.4	0.010	0.04	620.5	0.150	710.0
	#3	200000	386.1	0.010	0.04	496.0	0.100	558.5
Kante 2005	D6	200000	786.0	0.005	0.01	822.0	0.015	826.0
	D3	200000	483.0	0.004	0.04	597.0	0.088	631.0

Note: E_s is Young's modulus, f_y is yield stress, ε_{sh} is strain at onset of strain hardening, ε_{sh1} and f_{sh1} are the strain and stress of an intermediate point on hardening portion of the monotonic curve, f_u is ultimate strength and ε_u is the corresponding ultimate strain.

6.1.1 Analysis of single-story walls subjected to quasi-static loading

The first case considered is a reinforced concrete (RC) shear wall specimen tested by Massone (2006). The wall configuration and reinforcing details are depicted in Figure 6.1a. The thickness of the wall panel was 152 mm (6 in). The compressive strength of the concrete was equal to 32 MPa (4.64 ksi). The wall was reinforced vertically and horizontally with #4 bars, having a diameter of 13 mm and a yield strength of 424 MPa (61.5 ksi). A constant axial force of 334 kN (75 kips), corresponding to a compressive stress ratio of 5%, was applied over the top beam. The wall was restrained against rotation at both ends and the displacement history was applied at the top. The analytical model of the specimen is depicted in Figure 6.1b.

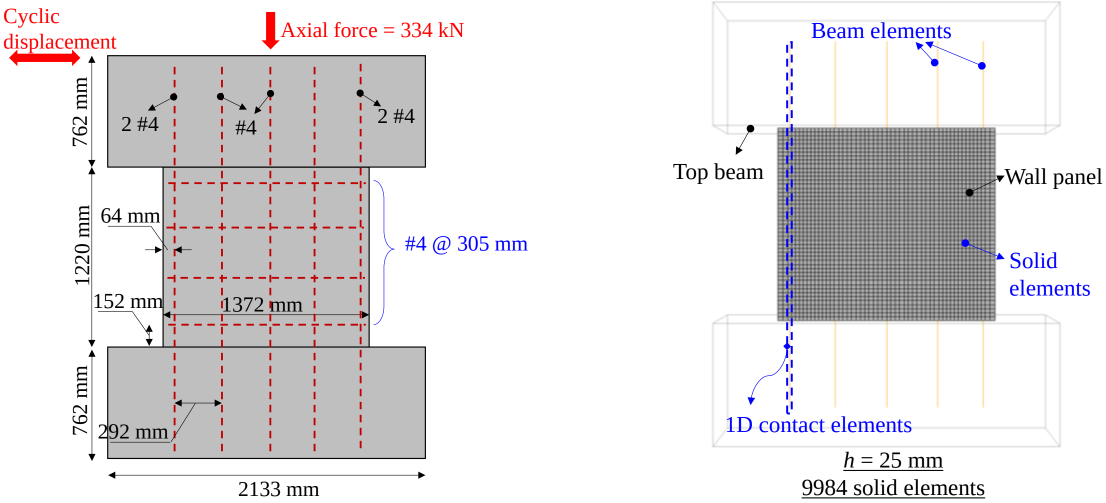

(a) Wall geometry and reinforcement detail

(b) Finite element model

Figure 6.1: Configuration and finite element representation of the RC shear-dominated wall tested by Massone (2006).

The analytically obtained hysteretic response is compared with the corresponding experimentally recorded data in Figure 6.2a. The initial stiffness and the capacity of the wall are captured well; however, the drift ratio at which the strength degradation occurs due to shear failure is underestimated. A potential reason for this underestimation of ductility is the fact that the finite element model does not accurately account for the dowel action of the reinforcing steel. Specifically, the formation of large, localized cracks will create concentrated flexural deformations of the rebars crossed by the crack. These flexural deformations will mobilize additional resistance from the bars which will contribute to the shear capacity of the specimen.

Figure 6.2b compares the analytically obtained crack opening strain at the onset of strength degradation with the experimentally observed damage pattern. The figure indicates that a localized shear crack has formed, similar to the experimental test damage pattern, shown in Figure 6.2c.

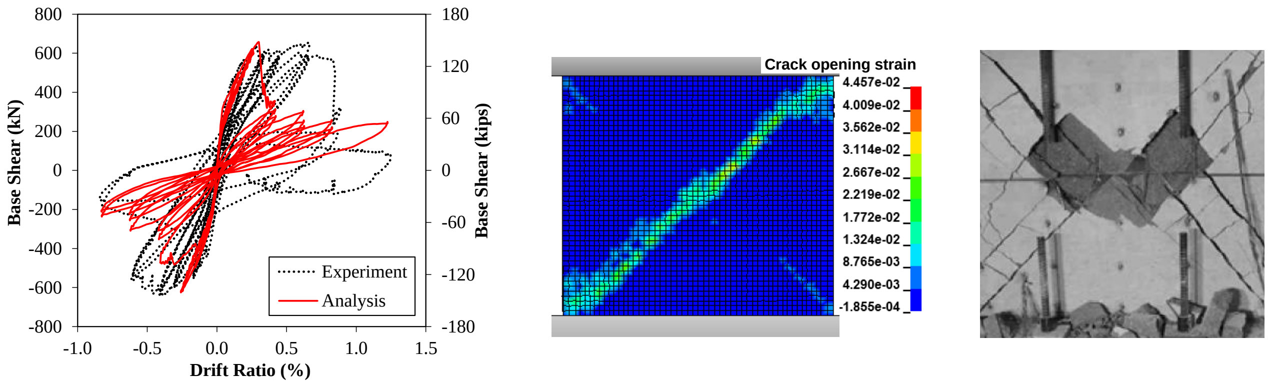

(a) Hysteretic response

(b) Crack opening strain contours at the onset of strength degradation

(c) Experimental damage pattern

Figure 6.2: Comparison of the analytically obtained and experimentally recorded hysteretic response and damage patterns of RC shear-dominated wall tested by Massone (2006).

Analysis is also conducted for a cantilever, reinforced masonry wall specimen tested by Shing et al. (1991). The configuration and cross-sectional reinforcement details of the specimen are shown in Figure 6.3a. The wall was made of masonry having a compressive strength of 17.9 MPa (2.6 ksi). The vertical reinforcement consisted of #7 bars with a diameter of 22 mm and a yield strength of 496 MPa (72 ksi). The transverse reinforcement was comprised of #3 bars with a diameter of 10 mm and a yield strength of 386 MPa (56 ksi). The longitudinal reinforcement ratio was equal to 0.74%, and the transverse reinforcement ratio was 0.14%. A constant axial load of 178 kN (40 kip), corresponding to an axial load ratio of 3.8%, was applied on top of the wall. The specimen was subjected to a cyclic displacement history at the top. Figure 6.3b presents the analytical model of the specimen.

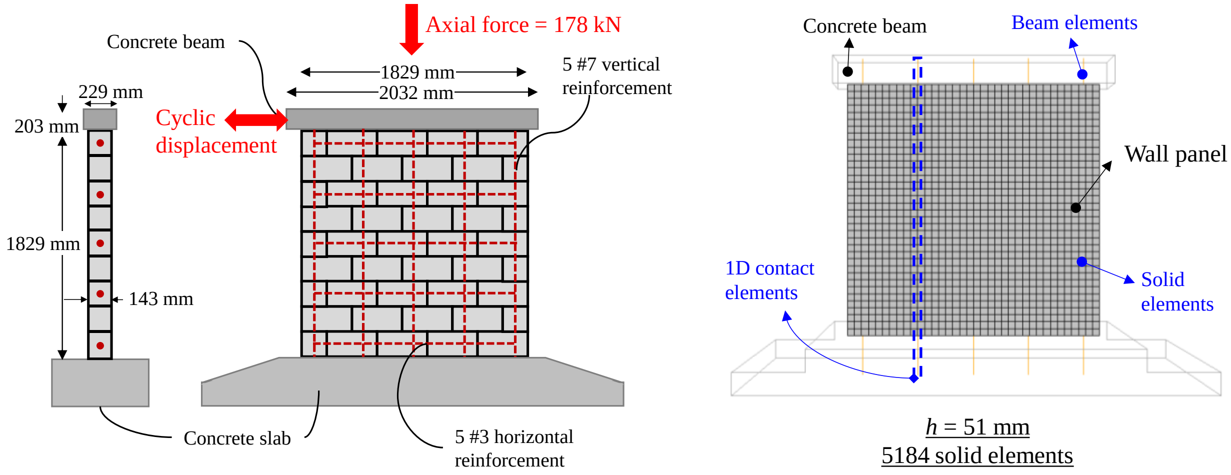

(a) Wall geometry and reinforcement detail (b) Finite element model

Figure 6.3: Configuration and finite element representation of the RM shear-dominated wall tested by Shing et al. (1991).

The analytically obtained hysteretic response and damage pattern are compared with the corresponding experimental observations in Figure 6.4. As can be seen from the figure, the analytical model slightly underestimates the lateral strength and the ductility of the wall, while it satisfactorily captures the cracking pattern of the wall.

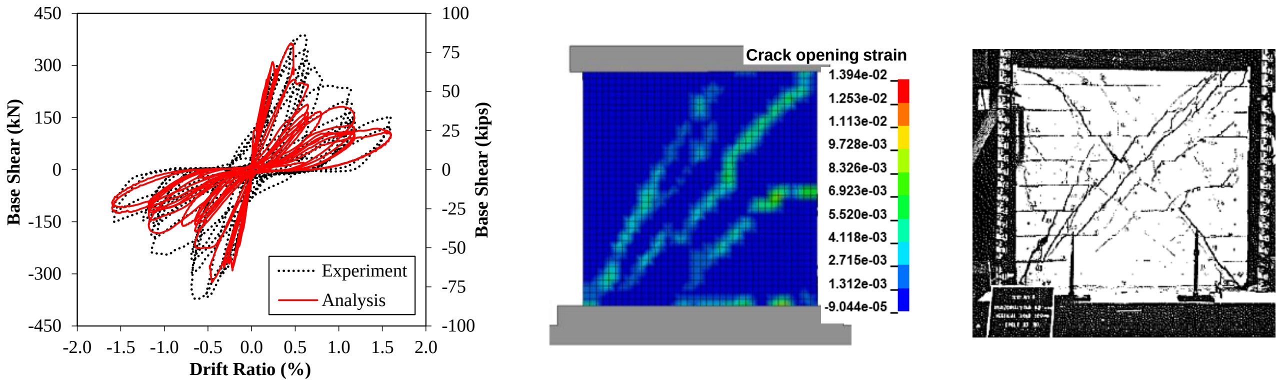

(a) Hysteretic response (b) Crack opening strain contours at the onset of strength degradation (c) Experimental damage pattern

Figure 6.4: Comparison of the analytically obtained and experimentally recorded hysteretic response and damage patterns of RC shear-dominated wall tested by Shing (1991).

6.1.1 Analysis of multi-story RC wall under earthquake loading

A validation analysis is also conducted for a five-story reinforced concrete wall building tested on a shake table by Kante (2005). As depicted in Figure 6.5, the five-story specimen consisted of two coupled T-shaped walls, joined by a coupling beam to form an H-shaped section. The height of each story was 0.9 m. The coupled wall segment parallel to the X-direction (termed the web wall) was 1.44 m long and 60 mm thick. It included an opening with a width of 0.27 , and a height of 0.67 m in the center; the two wall segments parallel to the Y-direction, termed the flange walls, had a length of 1.6 m and a thickness of 60 mm. Each floor had a 1.6 × 1.56 m slab that is 0.08 m thick.

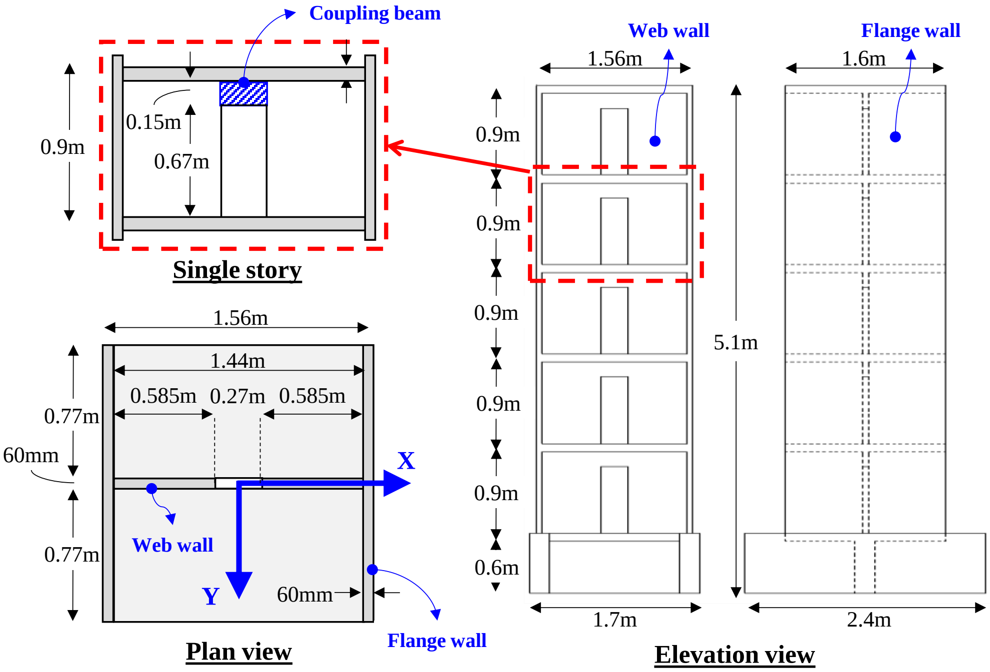

Figure 6.5: Geometry of the H-shaped wall specimen tested by Kante (2005)

Figure 6.6 shows the reinforcing details of the wall segments. The wall boundaries were reinforced with vertical rebars having a diameter of 6 mm and providing a reinforcement ratio of 0.42%. The concrete material at these sections was confined with 3 mm – diameter stirrups placed at every 100 mm. For regions other than boundaries, the wall was reinforced with vertical and horizontal wire having a diameter of 3 mm and a spacing of 100 mm. The floor slabs were reinforced in both directions with rebars having a diameter of 5 mm at top and bottom. There was a confined edge beam on each of the free edges of the slabs. The edge beams were reinforced with eight longitudinal bars having a diameter of 8 mm and with ties having a diameter of 4.5 mm.

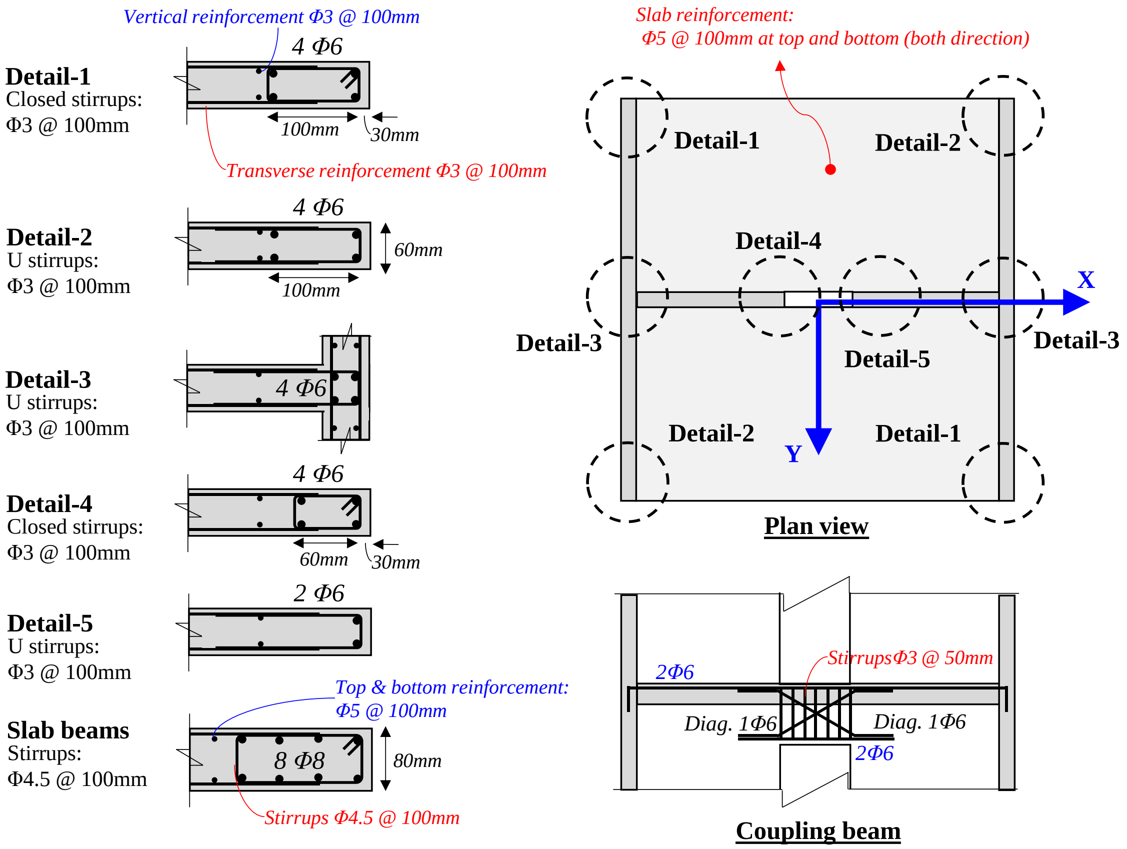

Figure 6.6: Reinforcement detail of the H-shaped wall specimen tested by Kante (2005)

The 3 mm – diameter reinforcing steel used in the wall was a steel wire with low ductility. Specifically, the yield strength was equal to 786 MPa, the ultimate strength was equal to 826 MPa, and the rupture strain was equal to 1.5%). The reinforcing bars with a diameter of 6 mm had a yield and ultimate strength of 483 MPa and 631 MPa, respectively, while their rupture strain was 8.8%. The average compressive strength, obtained with cubic specimens, was 38.8 MPa. Given that the cube compressive strength is usually higher than that obtained for cylinder specimens, a lower value of concrete compressive strength, equal to 34.8 MPa, is used for the analysis. This same value was used in the analysis of the specific specimen by Lu et al. (2014).

The weight per floor was equal to 58.1 kN. The majority of that amount, i.e. 48 kN, was applied through steel blocks attached to the slab of each floor, as shown in Figure 6.7. The axial load ratio of the specimen was 3.1%. The wall was subjected to a sequence of six triaxial base excitations, until the occurrence of severe shear damage.

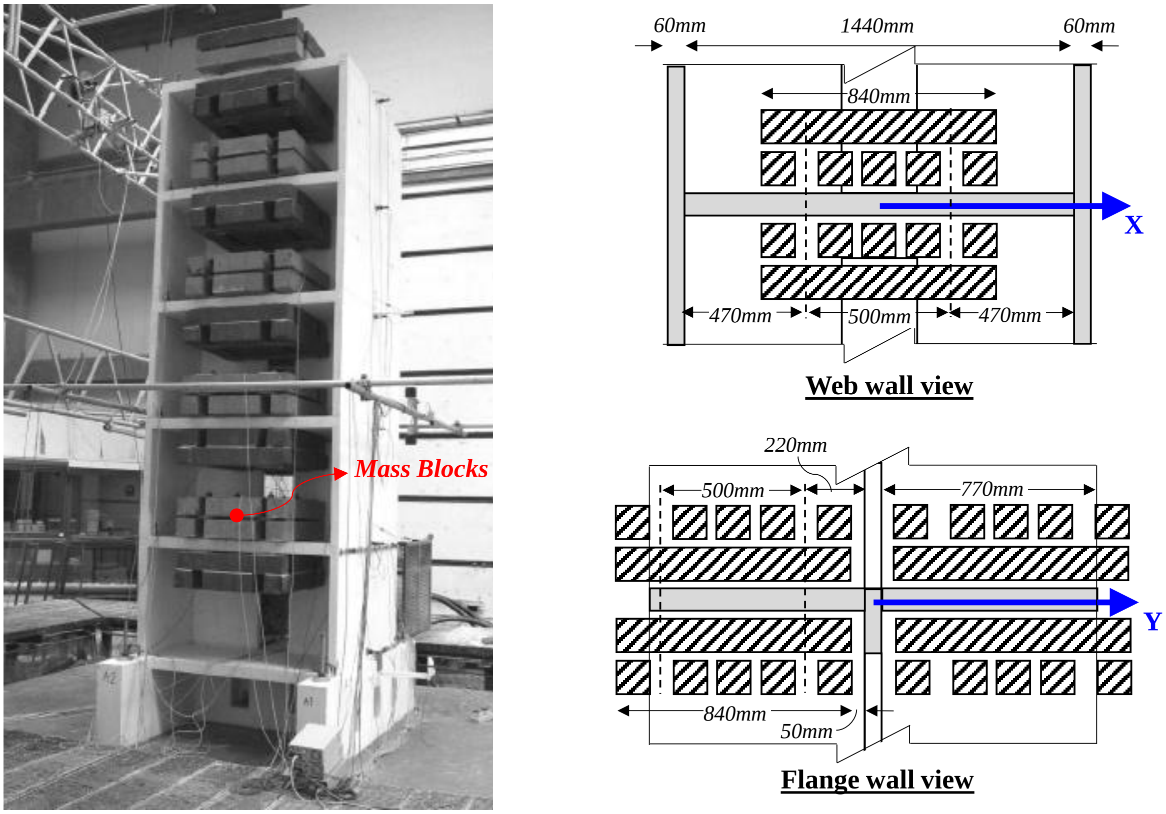

(a) Overall view (reprinted from Kante 2005)

(b) Location of mass blocks

Figure 6.7: Experimental setup and configuration of mass blocks (Kante 2005)

The finite element model used for the analysis of the shear-wall specimen is schematically shown in Figure 6.8. The model explicitly accounts for the floor slabs and for the mass blocks of the specimen. The modeling scheme described in Section 5.1 is used for the bottom two stories, where inelastic deformations are expected to occur. The top three stories and the base of the structure are modeled using elements with a linearly elastic material, having the same modulus of elasticity as that of the inelastic concrete.

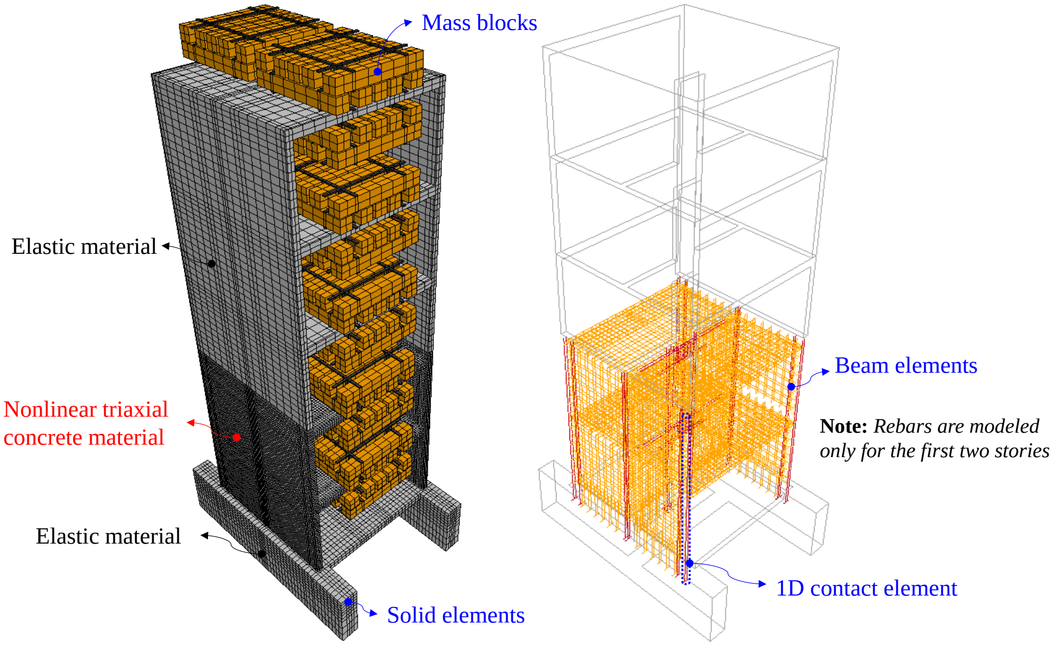

Figure 6.8: Finite element model of the wall specimen tested by Kante (2005)

The analytically obtained drift time histories are compared with the corresponding experimental data in Figure 6.9. The drift time histories and peak drift values for the various motions satisfactorily agree with the corresponding experimental observations.

The majority of damage occurred during the fifth and sixth ground motions. The first four motions only introduced minor cracking in the flanges. A similar damage pattern and sequence is obtained in the finite element analysis. As can be seen from Figure 6.10a, during the 4th motion, only flexural cracks are formed in the web and flanges of the analytical model.

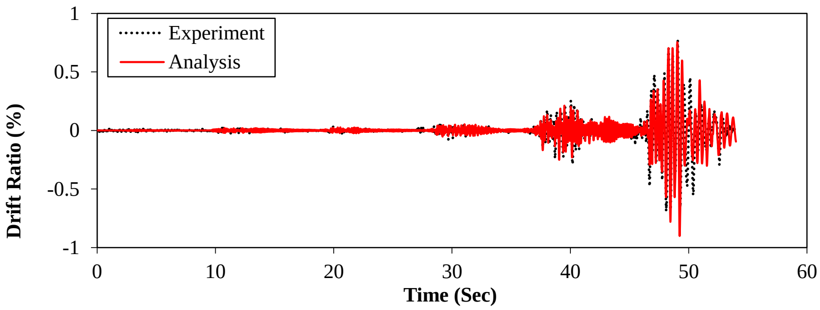

(a) X-direction (parallel to the web)

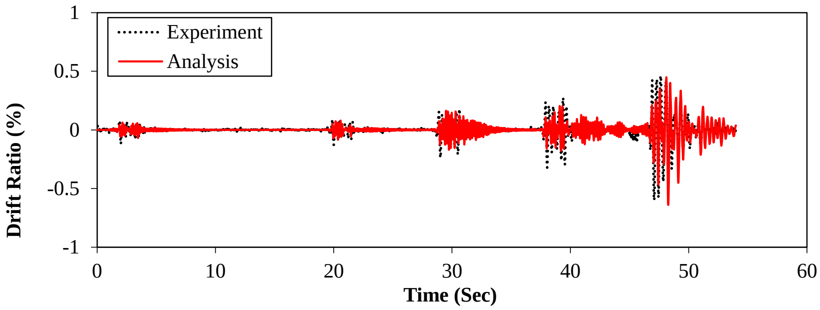

(b) Y-direction (parallel to the flanges)

Figure 6.9: Drift time histories of the wall specimen tested by Kante (2005)

The fifth ground motion had peak ground accelerations (PGA) equal to 0.73g and 0.42g, and resulted in a maximum roof drift ratio of 0.29% and 0.32%, for the X- and Y- directions, respectively. During this motion, shear cracks were formed in the web near the opening, and further cracking was observed in the flanges (Kante 2005). The analytically obtained crack opening contour plot is compared with the experimentally observed crack pattern for that motion in Figures 6.10b and 6.10c. As can be seen from the figures, the FE analysis has predicted the formation of inclined cracks in the web of the wall specimen well. A quantitative comparison of the drift ratio and base shear force histories is provided in Figure 6.11. The peak drift and base shear are well captured in the X-direction, while they are underestimated in the Y-direction. It is worth mentioning that the actual specimen was damaged by the crane during construction, as reported by Coelho et al. (2006). The fact that this damage is not accounted for in the analytical model might have contributed to the discrepancy between the analysis and the experimental test.

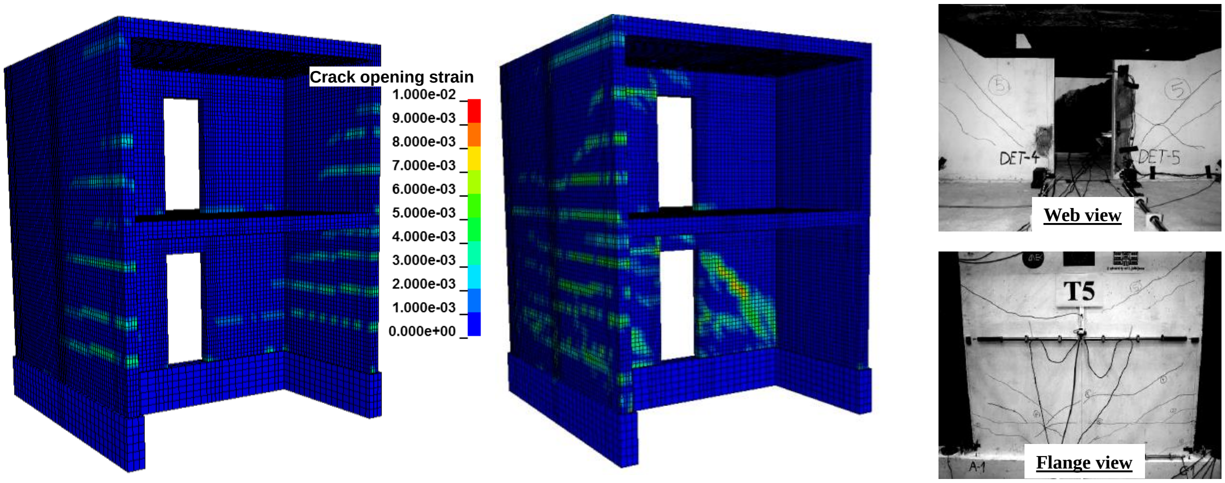

(a) Maximum crack opening strain contours during 4th motion

(b) Maximum crack opening strain contours during 5th motion

(c) Experimental cracking pattern after 5th motion

Figure 6.10: Analytical and experimental cracking patterns during 4th and 5th ground motion

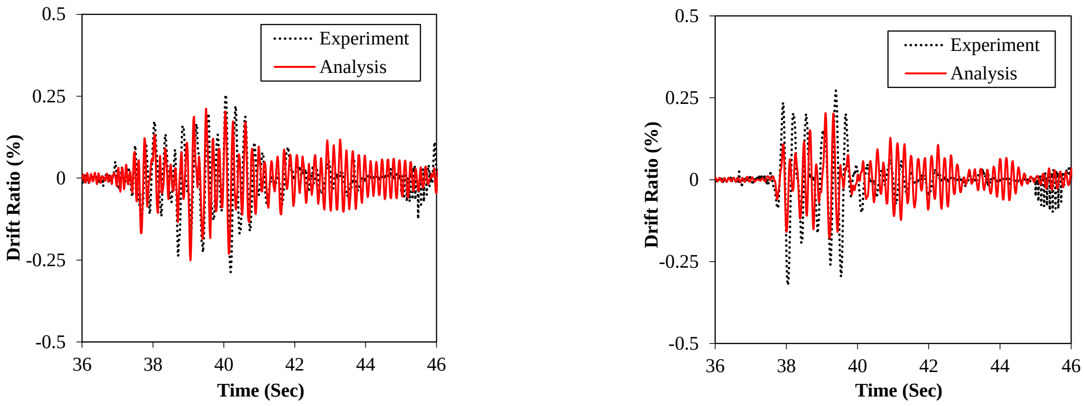

(a) Drift history in X-direction

(b) Drift history in Y-direction

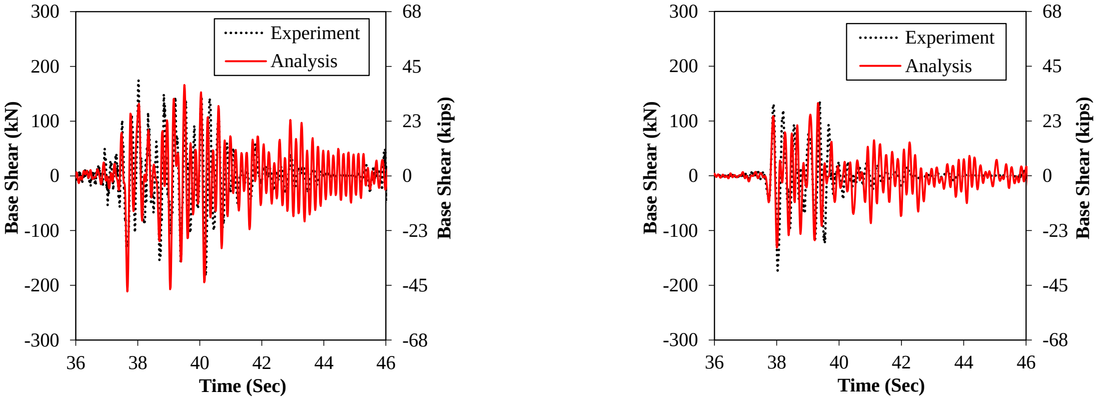

(c) Base shear history in X-direction

(d) Base shear history in Y-direction

Figure 6.11: Response time histories of the wall specimen during the 5th ground motion

The sixth ground motion had PGAs of 1.02g and 0.52g, and resulted in a maximum roof drift ratio of 0.77% and 0.60% in the X- and Y- directions, respectively. In this motion, the specimen incurred severe damage through the formation of diagonal shear cracks and rupture of transverse rebars in the web wall. No damage was observed in the coupling beams (Kante 2005). Figures 6.12a and 6.12b shows the analytical and experimental crack patterns. As can be seen from the figures, the FE analysis has predicted the formation of large diagonal shear cracks in the web of the wall specimen well. Additionally, the rupture of longitudinal and transverse rebars is visually detected in the analytical model, as depicted in Figure 6.12c.

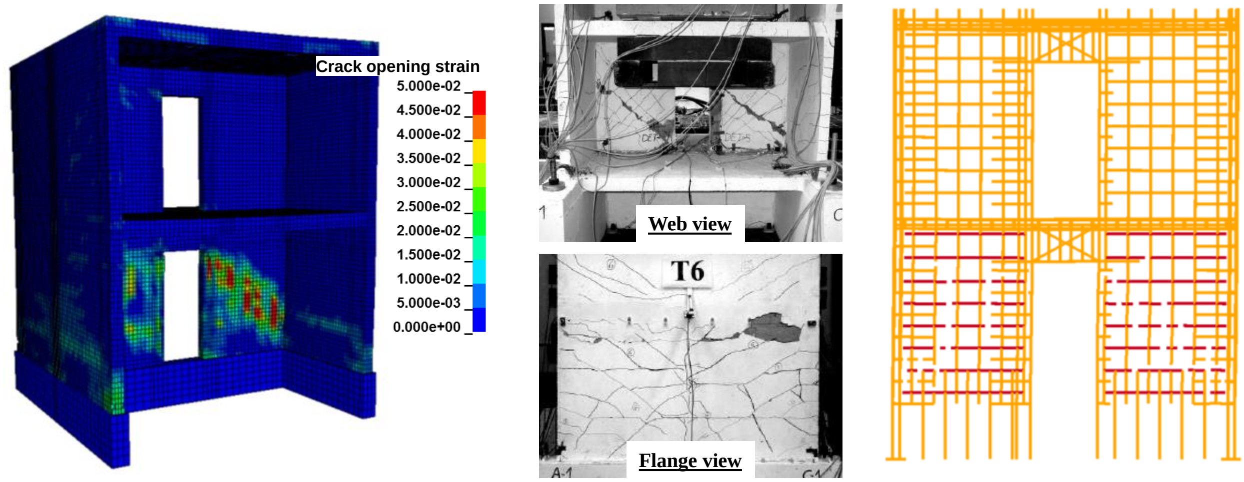

(a) Maximum crack opening strain contours during 6th motion

(b) Experimental cracking pattern after 6th motion

(c) Rebar rupture during 6th motion

Figure 6.12: Damage of the wall specimen during 6th ground motion

Figure 6.13 compares the analytically obtained drift and base shear time histories for the 6th motion, with the corresponding experimental data. Very good agreement between analysis and experiment is obtained in terms of the peak lateral strength and maximum drift values.

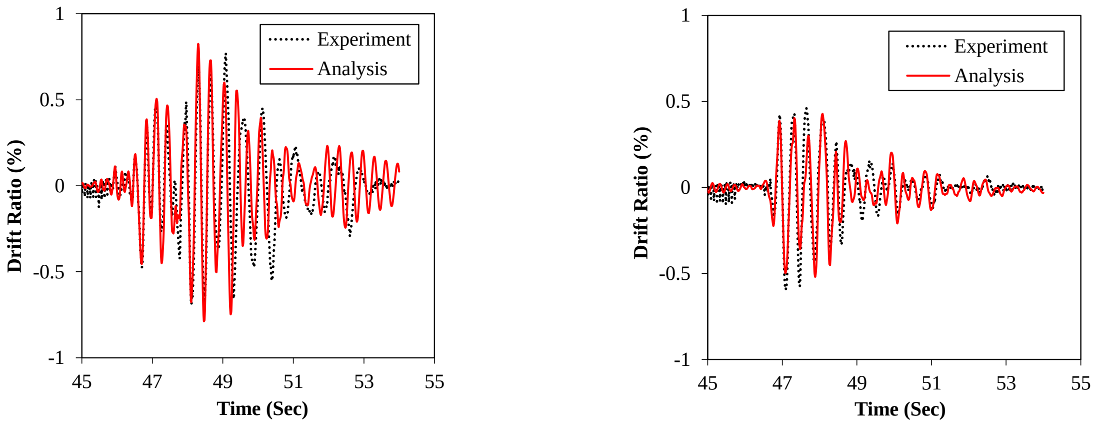

(b) Drift history in Y-direction

(a) Drift history in X-direction

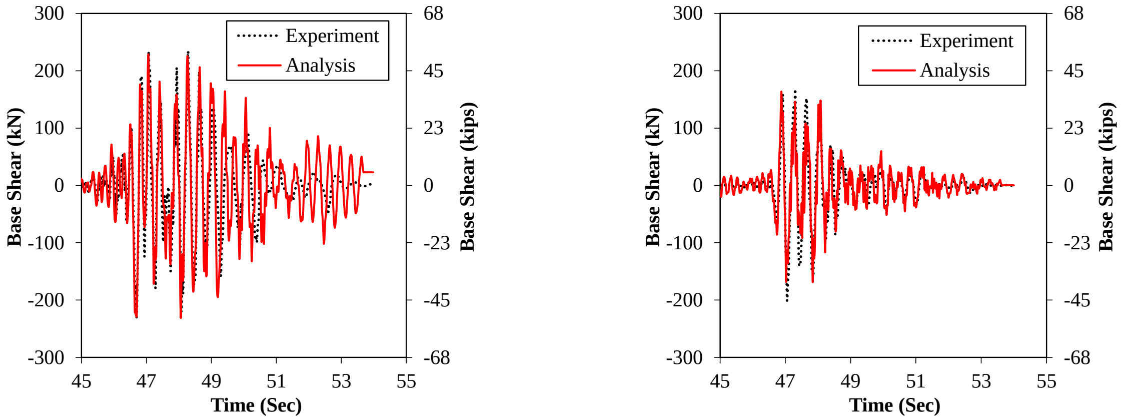

(c) Base shear history in X-direction

(d) Base shear history in Y-direction

Figure 6.13: Response time histories of the wall specimen during the 6th ground motion

6.2 Parametric analyses

The results obtained in the previous section – especially those for the two single-story walls – are not as satisfactory as those obtained for flexure-dominated members simulated in Chapter 5. For this reason, a series of parametric analyses is conducted, to investigate whether improved results can be obtained. The analyses are to elucidate the impact of the mesh size and of the value of mode-I fracture energy on the results of an analysis.

6.2.1 Effects of mesh size

To investigate the effect of the mesh size on the response, the analysis of the single-story RC wall tested by Massone (2006) is repeated, using a coarser and finer mesh than that employed in Section 6.1.1. Specifically, the size of the elements in one analysis is set equal to 50 mm, and in the other analysis it is equal to 12 mm. The analysis in Section 6.1.1 corresponds to an element size of 25 mm. A comparison of the analytically obtained and experimentally recorded hysteretic response for the two additional analyses is presented in Figure 6.14. As can be seen from the figure, the initial slope and the capacity of the wall are captured well for the first case and slightly underestimated for the case with very refined discretization. Additionally, similar to the hysteretic response presented in Figure 6.2a, the drift ratio at which the shear failure was occurred is underestimated. Figure 6.15 presents the crack opening strain contours for the two cases. The same figure demonstrates the formation of continues, diagonal, shear crack similar to that of experimental observations.

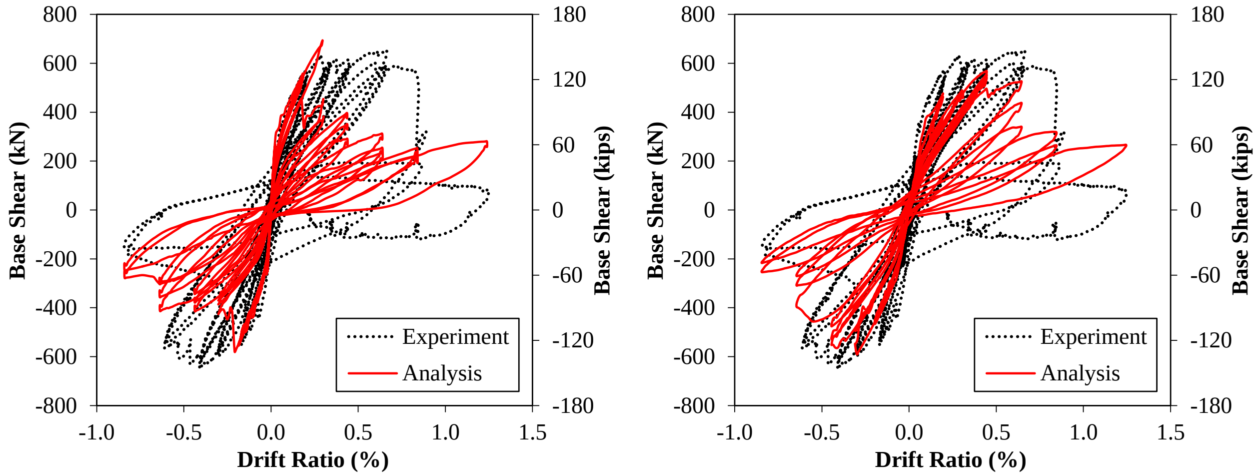

(a) Case 1: *h* = 50 mm

(b) Case 2: *h* = 12 mm

Figure 6.14: Mesh size effects on overall hysteretic response of the shear-dominated wall tested by Massone (2006).

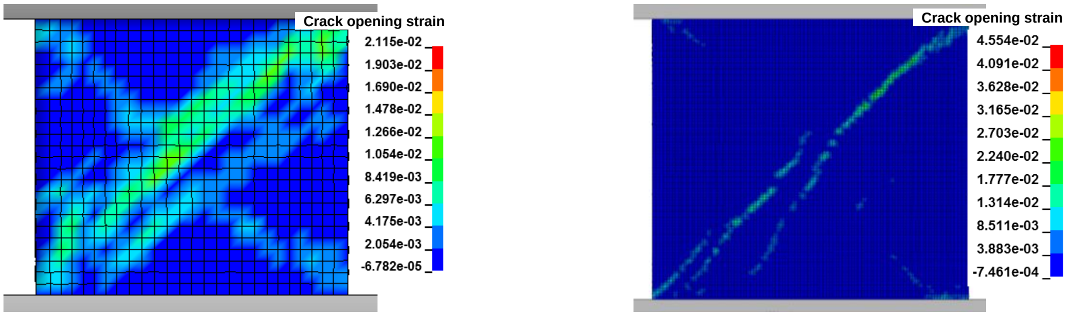

(a) Case 1: $h = 50$ mm (b) Case 2: $h = 12$ mm

Figure 6.15: Analytically obtained crack patterns for models with different element size Experimental

6.2.2 Effects of mode-I fracture energy on obtained results

To examine the effect of the mode-I fracture energy (tensile fracture energy), the analysis of the specimens by Massone (2006) and Shing et al. (1991) is repeated. In the analyses presented herein, the value of tensile fracture energy, G_t, reported in Table 6.1, is multiplied by factors of 4 and 2, for the walls tested by Massone (2006) and Shing et al. (1991), respectively. Figure 6.16 compares the analytically obtained hysteretic response with the experimentally recorded data. As can be seen from the figure, by increasing the fracture energy the analytical models capture satisfactorily both the hysteretic response and the onset of shear failure. The specific analyses, especially the one for the wall tests by Massone (2006), are found to be very sensitive to the value of fracture energy. This is expected, given the brittle nature of the response of these specimens and the fact that strength degradation is caused by the sudden formation of an inclined shear crack.

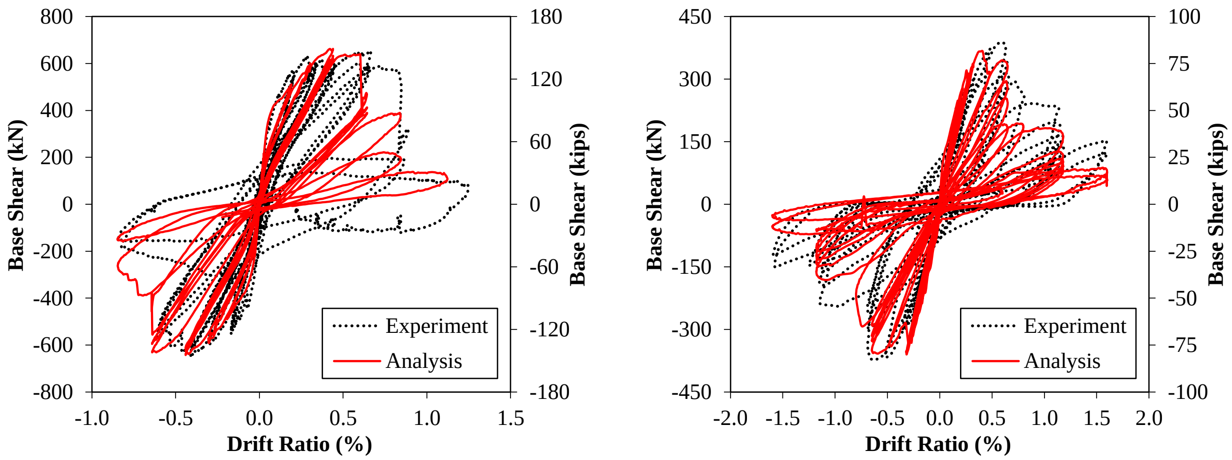

(a) Specimen tested by Massone (2006) (b) Specimen tested by Shing et al. (1991)

Figure 6.16: Analytically obtained and experimentally recorded hysteretic response of RC/RM shear-dominated wall specimens with increased tensile fracture energy.

6.3 Preliminary verification of the capability of the meshless, Smoothed Particle Hydrodynamics method to simulate the damage and failure of shear-dominated RC walls

As mentioned in the introductory sections of this chapter, the fact that stress lock-in phenomena have been attributed to the use of finite element methods which enforce the continuity of the displacement field, indicates that methods which do not enforce continuity of the displacement field, may be well-suited for simulations of components where strongly localized cracks occur. One such method is the meshless, Smoothed Particle Hydrodynamics (SPH) method. A preliminary verification of the capability of SPH for capturing the response of shear-dominated components is pursued herein.

In the SPH (Liu and Liu 2003, Li and Liu 2004), a continuous medium is replaced by an assemblage of particles, as shown in Figure 6.17a. The variation of a field function $A(\mathbf{x})$ is approximated by means of the values $A(\vec{x}_I)$ at the locations of the particles and a kernel function, $\Phi_h(\vec{x}) = \Phi(h, \vec{x})$. The following approximation is introduced for the field function (Li and Liu 2004).

$$A(\vec{x}) = \int_{\Omega} \Phi_h(\vec{x} - \vec{x}') \cdot A(\vec{x}') . d\Omega_{x'} \approx \sum_{I \in \Lambda} \Phi_h(\vec{x} - \vec{x}_I) \cdot A(\vec{x}_I) \cdot \Delta V_I \tag{6.1}$$

where h is called the support size (or smoothing length) of the kernel and it determines the zone around each particle for which the kernel function is nonzero. The summation in Equation (6.1) is conducted at all particles belonging to *Λ*, where *Λ* is the region for which the kernel function attains a nonzero value. Vector x_I is the position vector of particle *I*, and ΔV_I is the volume of the same particle, given by the following equation.

$$\Delta V_I = \frac{m_I}{\rho_I} \tag{6.2}$$

where m_I and ρ_I are the user-defined mass and density of the particle, respectively.

The SPH also establishes approximations for the values of the local gradient of any field function, *A(x,y,z)*, evaluated at the location of particle *I*. The following expression is commonly employed (Li and Liu 2004):

$$\left(\frac{\vec{\nabla} A}{\rho}\right)_I = \sum_{J \in \Lambda} \left[\left(\frac{A_I}{\rho_I^2} + \frac{A_J}{\rho_J^2} \right) \vec{\nabla}_I \Phi_{IJ} \cdot m_J \right] \tag{6.3}$$

where , for two particles *I* and *J*, $\Phi_{IJ} = \Phi(h, \vec{x}_I - \vec{x}_J)$ and $\vec{\nabla}_I \Phi_{IJ}$ is the gradient of the function $\Phi(h, \vec{x} - \vec{x}_J)$ evaluated at the location of the particle *I*. The specific gradient can be obtained from the following expression.

$$\vec{\nabla}_I \Phi_{IJ} = \frac{\vec{x}_I - \vec{x}_J}{x_{IJ}} \frac{\partial \Phi_{IJ}}{\partial x_{IJ}} \tag{6.4}$$

where x_{IJ} is the magnitude of vector $x_I - x_J$.

A major conceptual difference between the SPH and the finite element method is that the former is based on an approximation of the strong form, i.e., the differential equations of motion for solid mechanics. In the absence of body forces, these equations can be written as follows.

$$\rho\frac{\partial \vec{v}}{\partial t}+\vec{\nabla}\bullet[\sigma]=0 \text{ or } \frac{\partial \vec{v}}{\partial t}=-\frac{1}{\rho}\vec{\nabla}\bullet[\sigma] \tag{6.5}$$

where the vector field $\vec{\nabla}\bullet[\sigma]$ is the divergence of the stress tensor.

Contrary to the SPH, the finite element method is an approximation of a weak form of the differential equations of motion. This weak form corresponds to the principle of virtual displacements. The following equations define the rate of the velocity vector $\vec{v}_I$ for any particle *I* in an SPH model.

$$\frac{d\vec{v}_I}{dt}=-\sum_{J\in\Lambda}\left[\left(\frac{[\sigma]_I}{\rho_I^2}+\frac{[\sigma]_J}{\rho_J^2}\right)\vec{\nabla}_I\Phi_{IJ}\cdot m_J\right] \tag{6.6}$$

LS-DYNA includes an SPH module, which uses an explicit scheme to integrate the equations of motion in time. The program also includes capabilities to resolve several difficulties associated with the SPH, such as the well-known tensile instability problem (Li and Liu 2004) and the imposition of essential boundary conditions. The SPH implementation of LS-DYNA uses a cubic spline kernel function, given by the following expression.

$$\Phi(h,\vec{x})=\begin{cases}\dfrac{1}{4\pi\cdot h^3}\left(1-6\dfrac{\|\vec{x}\|^2}{h^2}+3\dfrac{\|\vec{x}\|^3}{h^3}\right), & 0\le\|\vec{x}\|\le h\\ \dfrac{1}{4\pi\cdot h^3}\left(2-\dfrac{\|\vec{x}\|}{h}\right)^3, & h\le\|\vec{x}\|\le 2h\\ 0, & \|\vec{x}\|>2h\end{cases} \tag{6.7}$$

where $\|\vec{x}\|$ is the magnitude of vector $\vec{x}$.

The function Φ_{IJ} is obtained by substituting $\vec{x}_I - \vec{x}_J$ for $\vec{\chi}$ in Equation (6.7). An explicit scheme is used for the integration of the particle equations in time. Once the velocities of the particles are known, the velocity gradient, containing the partial derivatives of the velocity vectors with respect to the spatial coordinates, can be obtained through an expression similar to Equation (6.6). The strain rates can be then obtained, allowing the calculation of stresses in the particles. A complete description of the method and its computational implementation is provided by Li and Liu (2004).

The SPH method has so far been used for problems involving extreme deformations and high loading rates, e.g., blast or impact load. Some applications of the SPH approach for cracking processes in concrete under static loading have been conducted, as shown in Figure 6.17b for a dam simulation by Das and Cleary (2013).

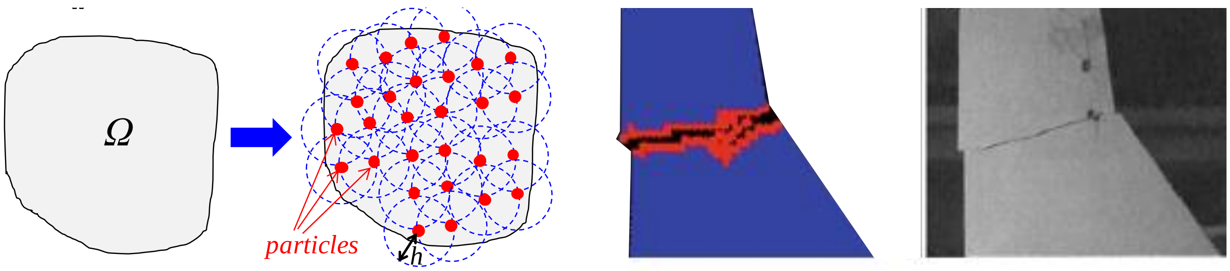

(a) SPH approach

(b) Simulation of fracture in concrete dam using SPH (Das and Cleary 2013)

Figure 6.17: Smoothed Particle Hydrodynamics for concrete structures

The preliminary verification of the capabilities of SPH for capturing shear failure is conducted by simulating the RC wall specimen by Massone (2006). In this analysis, the wall panel is represented through a meshless particle assembly instead of solid elements. The reinforcing steel bars and the top and base beams are modeled using with the same type of finite elements as those employed in Section 6.1.1. The connection between the SPH and FE parts of the model is established by coupling the displacements of the FE nodes to the displacements of the corresponding SPH particles. The calibration of the material laws is identical to that conducted for the analysis presented in Section 6.2.2. Figure 6.18 shows the analytically obtained hysteretic response and damage pattern of the specimen. It can be deduced that the SPH can give very similar results to those obtained with the finite element analysis, shown in Figure 6.16a.

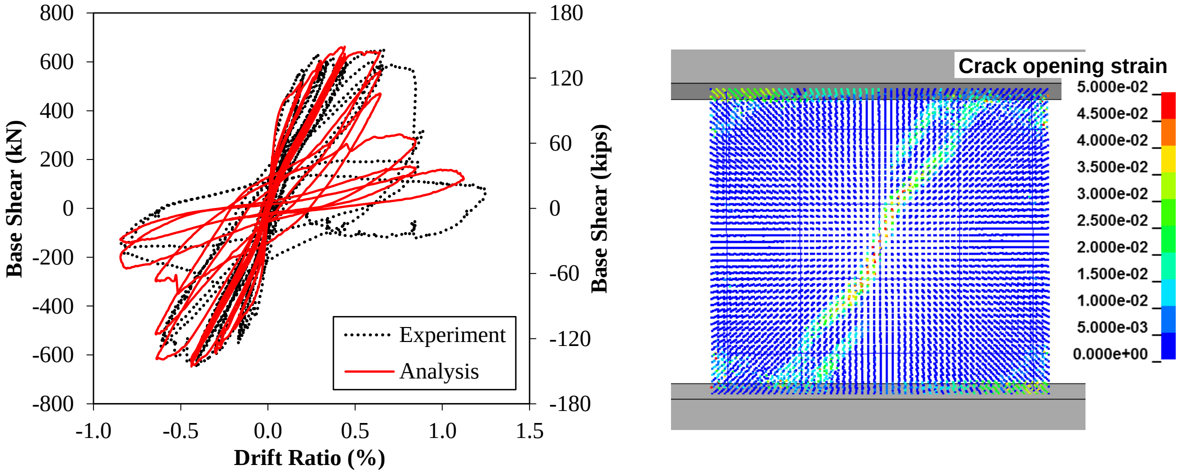

(a) Hysteretic response

(b) Crack opening strain contours at the onset of strength degradation

Figure 6.18: Results of analysis of the shear-dominated wall tested by Massone (2006) using the Smoothed Particle Hydrodynamics method.

The results of the preliminary verification analysis presented herein show that SPH may be appropriate to capture shear failure of RC/RM structural components. Furthermore, the constitutive model for concrete presented in Chapter 3 can be readily combined with SPH, without any modification in the calibration compared to that employed in finite element models.

Chapter 7 : Nonlinear Truss Analogy for the Analysis of Shear-Dominated Reinforced Concrete and Masonry Structures

Despite the accuracy of three-dimensional finite element models, the vast majority of researchers and practitioners will most probably prefer simplified analysis methods for performance assessment of reinforced concrete (RC) and reinforced masonry (RM) structures. Nonlinear truss analogy was successfully used for the analysis of RC shear walls where large diagonal crack, from top corner to the bottom opposite corner, dominated the shear failure mode. However, the method is not appropriate for the analysis of more slender structures, e.g. RC columns or RC/RM walls with door/window openings. In these type of structures, a so called aggregate interlock effect, measure of surface roughness for masonry material, plays a crucial role that affects both the failure mode and the hysteretic response.

This chapter summarizes the requirement for using nonlinear truss models. A recently established methodology (Panagiotou et al. 2012, Lu and Panagiotou 2013), developed for the analysis of RC walls, is enhanced to allow the simulation of RC columns and RM walls and wall systems. An equation is proposed to determine the inclination angle of the diagonal members in the truss models. The constitutive laws are provided with the capability to account for the effect of aggregate interlock across an inclined shear crack. Finally, the strain penetration effect is accounted for by introducing additional vertical elements at end regions of members.

7.1 Description of truss modeling approach

The nonlinear truss model idealizes a RC column or a RM wall as an assemblage of horizontal, vertical and diagonal truss elements, as shown in Figure 7.1. The vertical elements are mainly intended to capture the axial-flexural response of the wall, while the diagonal elements capture the inclined compressive field developed due to the combined effect of axial force, shear force and bending moment in the member (Vecchio and Collins 1986).

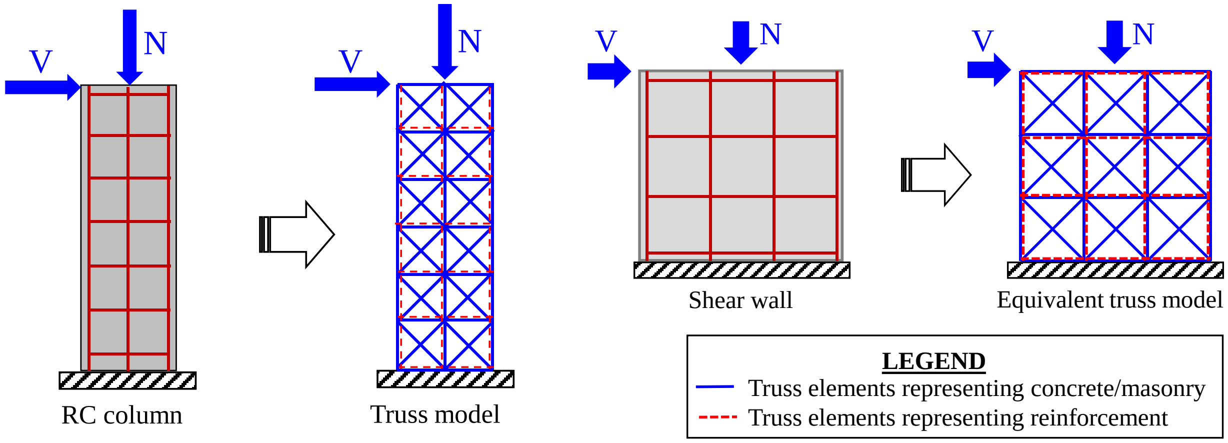

(a) Beam/column member

(b) Shear wall

Figure 7.1: Truss representation of RC/RM structural components

7.2 Determination of truss geometry

The procedure described herein for the determination of the geometry of a truss model is based on the work by Panagiotou et al. (2012) and Lu and Panagiotou (2013), who developed and employed truss models for the analysis of RC walls. This section provides guidelines to obtain the cross-sectional area of the various truss elements and to calculate the inclination angle of diagonal members.

7.2.1 Vertical elements

The first step to obtain the geometry of a truss model is the determination of the location and sectional properties of the vertical elements. Given the number of vertical elements along the length, L_h, of a structural member, e.g. wall or column, the two outermost vertical elements are placed at the centroid of the outermost vertical reinforcement. The tributary sectional depths of the various vertical elements are then determined by equally subdividing the region between neighboring elements. The cross-sectional area of each concrete/masonry vertical element is the product of the tributary depth and t, with t being the out-of-plane width of the cross section. For the vertical reinforcing steel elements, the cross-sectional area of the two outermost elements is equal to the total area of the outermost reinforcing steel, and the rest of the reinforcing steel is equally distributed to the remaining vertical elements.

An example showing the determination of the depths for the vertical concrete/masonry elements and of the cross-sectional areas for the elements representing the longitudinal reinforcement is presented in Figure 7.2. In the specific example, a total of four vertical elements are used along the member length, L_h. The vertical element spacing is equal to b, while the cover values for the longitudinal reinforcement at the two ends of the section are equal to c_1 and c_2. The cross-sectional area of each vertical concrete/masonry element is obtained by multiplying the tributary depth of the element by the cross-sectional thickness, t. The cross-sectional area for each of the outer vertical steel elements is equal to the total area of the outermost reinforcement at the same location. Thus, for the example in Figure 7.2, the steel areas for the vertical truss elements (1) and (4) will be equal to $A_{s,v1}$ and $A_{s,v3}$, respectively. The remaining vertical reinforcement, $A_{s,v2,tot}$, is equally subdivided among the intermediate vertical elements, (2) and (3).

Distribution of sectional depth to vertical concrete/masonry elements

Member	1	2	3	4
Sectional Depth	$c_1 + 0.5b$	$(0.5b + 0.5b) = b$	$(0.5b + 0.5b) = b$	$c_2 + 0.5b$

Distribution of area to vertical steel elements

Member	1	2	3	4
Steel Area	$A_{s,v1}$	$0.5A_{s,v2,tot}$	$0.5A_{s,v2,tot}$	$A_{s,v3}$

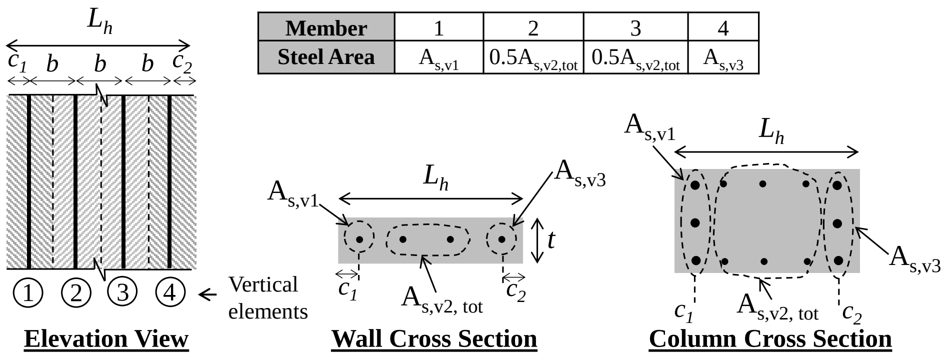

Figure 7.2: Example of determination of cross-sectional dimensions for vertical elements in a nonlinear truss model.

7.2.2 Diagonal elements

One of the most significant parameters for the determination of a truss model is the inclination angle, θ_d, of the diagonal elements. In the present study, the value of θ_d is determined differently in the truss models of RC columns and RM wall specimens. While a simple equation is proposed for calculating the inclination angle of diagonal elements in RC columns, θ_d is set approximately equal to 45^o for the analysis of RM shear walls. This value has been found to provide accurate results for shear-dominated RC walls (Panagiotou et al. 2012).

In reinforced concrete columns, the inclination angle of the diagonal elements of a truss model is established based on the assumption that the direction of the diagonal compressive field is parallel to the initial crack that occurs under the combined effect of compressive axial force and shear force. A uniform axial and shear stress distribution is assumed for the cross-section. While this assumption is not perfectly accurate, it leads to a conceptually simple procedure for the establishment of the inclination angle. The compressive stress ratio, i.e. the ratio of the uniform compressive stress over the concrete compressive strength, is taken equal to *v*. The stress state is characterized by the uniform compressive stress, σ and the uniform stress due to shear force, τ, acting on a horizontal (sectional) plane. The maximum principal stress, σ_1, is equal to the tensile strength, f_t, and given by the following equation (Gere and Timoshenko 1997):

$$\sigma_1 = f_t = \frac{\sigma}{2} + \sqrt{\frac{\sigma^2}{4} + \tau^2} \tag{7.1}$$

If both sides of Equation (7.1) are divided by f_c, the following relation is obtained:

$$\frac{f_t}{f_c} = \frac{-v}{2} + \sqrt{\frac{v^2}{4} + a^2} \tag{7.2}$$

where *a* is the ratio of the applied shear stress at cracking over the compressive strength. The direction angle, θ_p, of the maximum principal stress is given by (Gere and Timoshenko 1997):

$$\tan\left(2\theta_p\right) = \frac{2\tau}{-\sigma} \tag{7.3}$$

Division by the compressive strength of the numerator and denominator in the right-hand-side yields the following expression:

$$\tan\left(2\theta_p\right) = \frac{2a}{v} \tag{7.4}$$

The assumed stress state and the orientation of the maximum principal stress are presented in Figure 7.3. The direction of the diagonal crack is perpendicular to that of the principal stress σ_1, and thus the inclination angle θ_d of the diagonal crack and of the diagonal members is given by:

$$\theta_d = 90^o - \theta_p \tag{7.5}$$

Based on the above, the value of θ_d only depends on the axial load ratio, *v*, and the ratio f_t / f_c. Table 7.1 provides the value of θ_d for various combinations of f_t / f_c and *v*.

Table 7.1: Inclination Angle θ_d (in degrees) obtained from Equations (7.1)-(7.5).

	v = 0.00	v = 0.05	v = 0.10	v = 0.15	v = 0.20	v = 0.25	v = 0.30	v = 0.35	v = 0.40
f_t/f_c = 0.050	45	55	60	63	66	68	69	71	72
f_t/f_c = 0.075	45	52	57	60	62	64	66	67	68
f_t/f_c = 0.100	45	51	55	58	60	61	63	65	66
f_t/f_c = 0.125	45	50	53	56	58	60	62	63	64

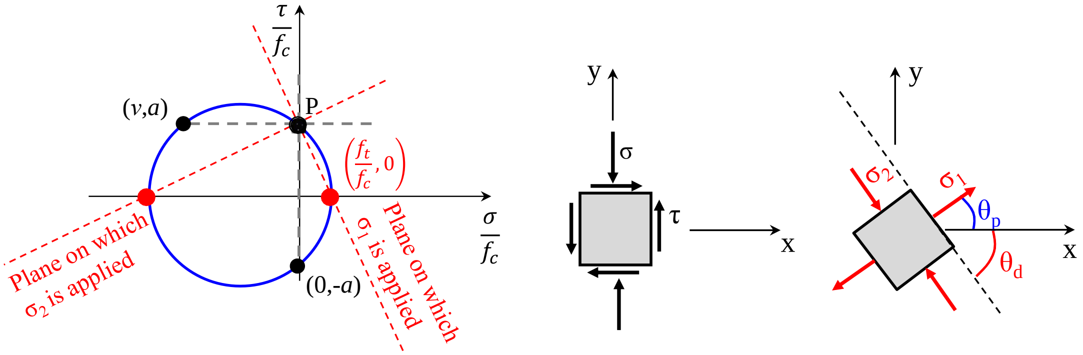

Figure 7.3: Stress state for determination of the inclination angle of diagonal elements, θ_d

A number of alternative expressions have been proposed and can be used for the determination of the crack inclination angle. For example, Kim and Mander (1999) have obtained an expression for θ_d by minimizing the external work done by a unit shear force. Lu et al. (2014) have defined the value of θ_d as the angle of the compressive strut that forms at the maximum resisted lateral load.

The equations proposed in the present study have been found to provide better estimates of the shear crack angles for the three column members examined in the validation analyses. Special considerations are required for the case of members such as perimeter frame columns whose axial force significantly changes with lateral deformations due to framing action. In such cases, which are not the object of this study, an initial analysis can be conducted to estimate the value of axial force at the occurrence of first cracking and allow the determination of the inclination angles for the diagonal elements, based on the principles described above.

Once the inclination angle of the diagonal elements has been established, their sectional depth, b_d, can be determined, as shown in Figure 7.4a, in accordance with the following equation (Panagiotou et al. 2012):

$$b_d = b \cdot sin\theta_d \tag{7.6}$$

where b is the spacing of the vertical elements in the truss model. The use of Equation (7.6) for the determination of b_d has been shown to provide good estimates of the strength and stiffness contributed by the diagonal members of the truss model.

7.2.3 Horizontal elements

After the location of the vertical elements and the inclination angle of the diagonal elements have been determined, the truss geometry is finalized by establishing the location and cross-sectional area of the horizontal elements. The intersection of vertical and diagonal elements defines the nodes of horizontal elements. The cross-sectional depth of the horizontal elements is obtained by equally dividing the height between consecutive horizontal elements. The obtained sectional depth is multiplied by t to give the cross-sectional area of each concrete/masonry horizontal truss element. If the amount and spacing of the transverse reinforcement are constant over a wall or a column segment, the cross-sectional area of the truss elements representing the horizontal steel reinforcement is obtained by dividing the total amount of transverse reinforcement in the segment by the corresponding number of horizontal truss elements. An example determination of the cross-sectional areas of the four horizontal elements of the truss model for a column or a wall segment is presented in Figure 7.4b.

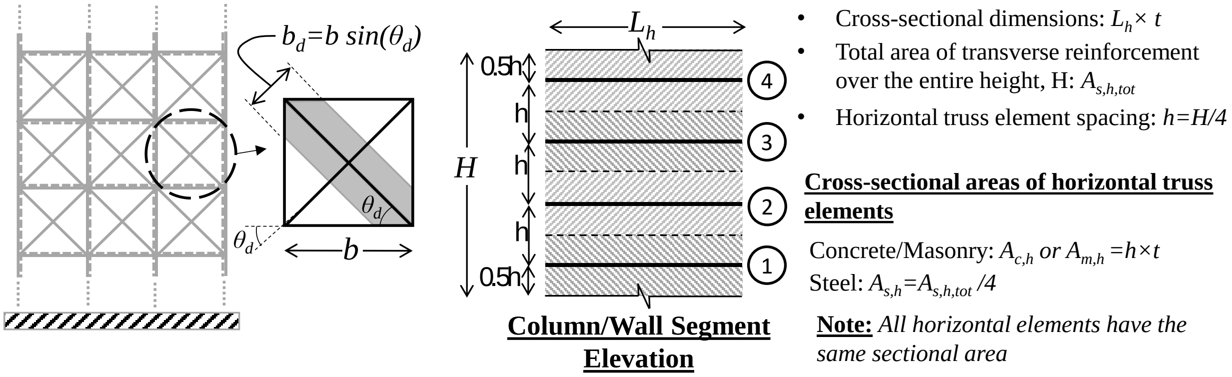

(a) Sectional depth of diagonal elements

(b) Determination of sectional areas for horizontal elements

Figure 7.4: Determination of geometry for diagonal and horizontal truss elements

7.3 Material constitutive laws

The truss modeling approach uses a set of uniaxial constitutive laws to capture the salient features affecting the hysteretic behavior of structures. This section describes the material models employed in the present study.

7.3.1 Concrete/Masonry

The uniaxial stress-strain law by Lu and Panagiotou (2013), which is shown in Figure 7.5a, is used to describe the behavior of the concrete and masonry materials. The specific law can account for strength and stiffness degradation associated with cracking and compression-induced crushing. Softening in the tensile regime can be described by either an exponential or a trilinear curve. In later, the first linear segment corresponds to the pre-cracked linearly elastic behavior, while the other two linear segments describe the softening behavior due to cracking processes. If properly calibrated, the material model can also capture the behavior of confined concrete, as shown in Figure 7.5a.

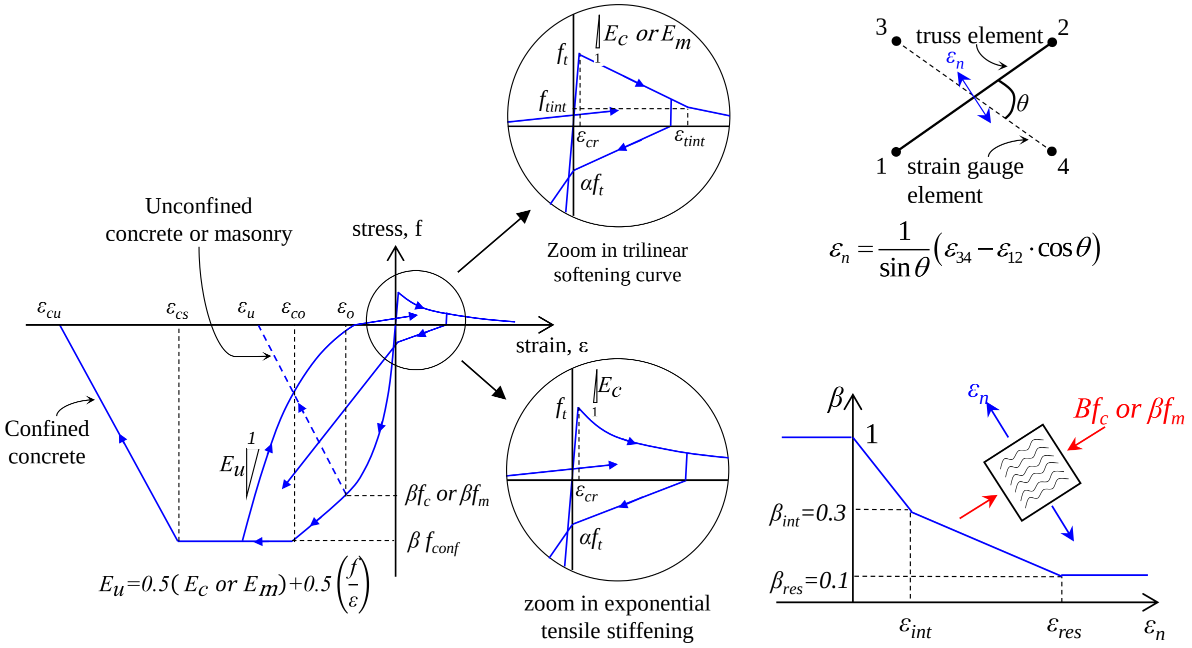

(a) Uniaxial stress-strain law

(b) Calculation of transverse strain and variation of coefficient β

Figure 7.5: Constitutive model for concrete and masonry material

The concrete/masonry constitutive law of the diagonal truss members accounts for the instantaneous effect of transverse tensile strains on the compressive resistance, in accordance with experimental observations by Vecchio and Collins (1986). To this end, at every step in an analysis, the diagonal compressive stresses are multiplied by a reduction coefficient, β, which expresses the adverse effect of transverse tension on the compressive stress of concrete. Thus, every diagonal truss element requires the definition of an additional pair of nodes to establish a fictitious "strain gauge" element which allows the calculation of the transverse strain, as shown in Figure 7.5b and explained in detail in (Panagiotou et al. 2012). To alleviate the effect of overlapping areas of diagonal, vertical and horizontal truss elements, the tensile strength in the diagonal elements is set equal to zero. This assumption has been shown (Lu and Panagiotou 2013) to lead to satisfactory stiffness estimates for reinforced concrete walls, when the width of the diagonal elements is calculated using Equation (7.6).

The constitutive model for concrete and masonry involves softening, and thus the stress-strain laws must be regularized to prevent the spurious dependence of the analysis results on the size of the mesh (Bažant and Planas 1998). The parameters pertaining to compressive inelastic strains are regularized according to Panagiotou et al. (2012). For the regularization of the constitutive model for tensile strains, a distinction is made between masonry and concrete. For lightly reinforced or unreinforced concrete and for all masonry elements, the tensile softening portion of the stress-strain curve is adjusted with the element size so that the area under this portion of the curve is related to the mode-I (tensile) fracture energy (Bažant and Planas 1998). For reinforced concrete, e.g. vertical elements in RC column, the effect of tension stiffening on the post-cracked response of concrete is accounted for, and the softening part of the stress-strain curve is determined using the equations by Stevens et al. (1991). The RC columns examined in the next chapter are characterized by low levels of transverse reinforcement and significant longitudinal reinforcement. For this reason, the equations by Stevens et al. (1991) are used only for the calibration of the stress-strain laws of the vertical truss members in RC columns, while all other concrete and masonry elements are calibrated based on the work by Bažant and Planas (1998). Panagiotou et al. (2012) have shown that the equation giving the variation of the reduction coefficient β with the transverse tensile strain must also be adjusted with element size. The regularization procedure described in (Lu and Panagiotou 2013) is used for the calibration of the constitutive equations giving the variation of β with transverse strain. Specifically, the values of ε_{int} and ε_{res} in Figure 7.5b are defined as a function of strain gage element length, L_g, and reference length, L_R, as:

$$\varepsilon_{\text{int}} = 0.01\frac{L_R}{L_g} \text{ and } \varepsilon_{res} = 0.025\frac{L_R}{L_g} \tag{7.7}$$

Using the MCFT (Vecchio and Collins 1986), the value of reference length is set equal to 600 mm in all of the analysis cases presented herein.

7.3.2 Aggregate interlock for cracked concrete and masonry

The proposed modeling approach can also capture the effect of aggregate interlock on the resistance of inclined shear cracks. This effect must be accounted for in slender members to correctly capture the structural behavior, like the column and the shear wall presented in Figure 7.6a. The specific wall includes a door opening which allows considering the system as a pair of coupled piers. Inclined diagonal cracks are assumed to have occurred in the column cross section and in the two piers of the shear wall, and the shear force transfer mechanism between two consecutive compressive diagonal struts (1-2-3) and (4-5-6) is examined. The concrete or masonry material of the horizontal and diagonal elements under tension is assumed to have completely lost their tensile strengths. Consequently, only the horizontal reinforcing steel elements can transfer tensile force across the crack planes. It can be verified from Figure 7.6a that horizontal (shear) force transfer from the strut (1-2-3) to the strut (4-5-6) can only occur through tensile forces at the horizontal steel elements, (4-2) and (5-3). In this regard, the shear capacity of the wall cannot exceed the value V_s corresponding to the contribution of the transverse reinforcement to the shear resistance. Thus, the contribution of the concrete or masonry material to the shear resistance will not be accounted for by the truss model.

The analyses by Panagiotou et al. (2012) were able to capture the response of squat, shear-dominated RC walls, despite the fact that the aggregate interlock effect was not accounted for in the models. The reason why it is not necessary to explicitly consider the aggregate interlock effect for squat walls is schematically explained in Figure 7.6b. In such a wall, after the occurrence of a diagonal crack, the truss model has a continuous diagonal strut, 1-2-3-4-5, spanning from the top corner to the opposite bottom corner. Since this diagonal strut will be capable of carrying part of the applied lateral force, there will always be a concrete/masonry contribution to the shear resistance of the truss model. In this case, the strength degradation in the wall will eventually be caused by softening of the diagonal strut, which can be captured by the model even without explicitly including the aggregate interlock effect.

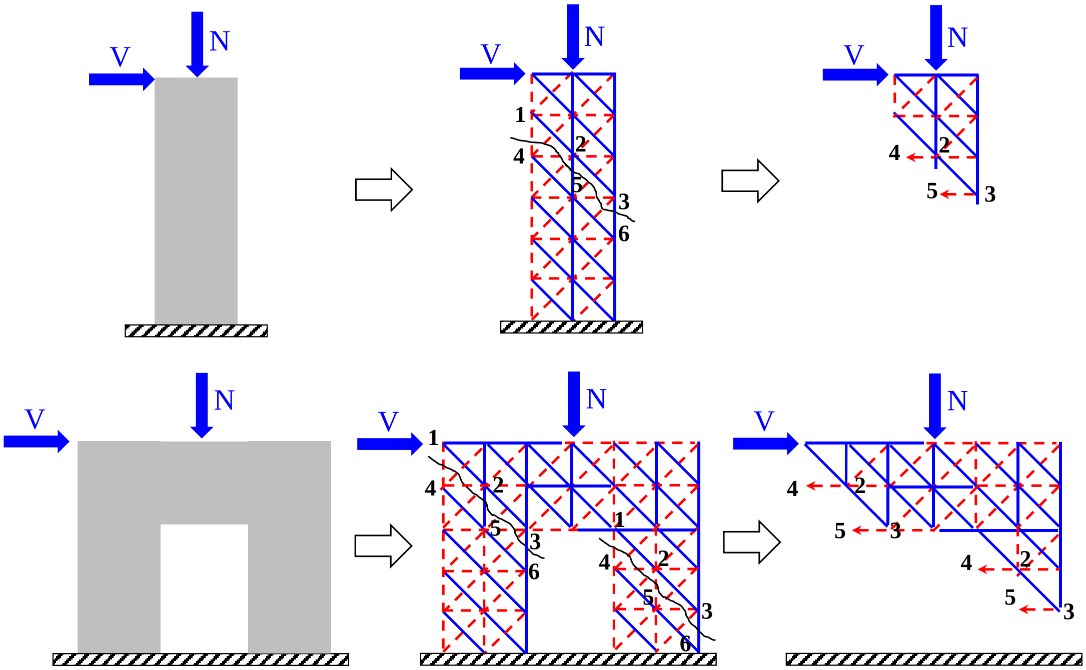

After strength degradation of horizontal and diagonal truss members under tension, horizontal (shear) force transfer from (1-2-3) to (4-5-6) occurs only through (4-2) & (5-3), i.e. horizontal steel reinforcement.

(a) Truss model for a slender member (a wall with no continuous diagonal struts from top to bottom)

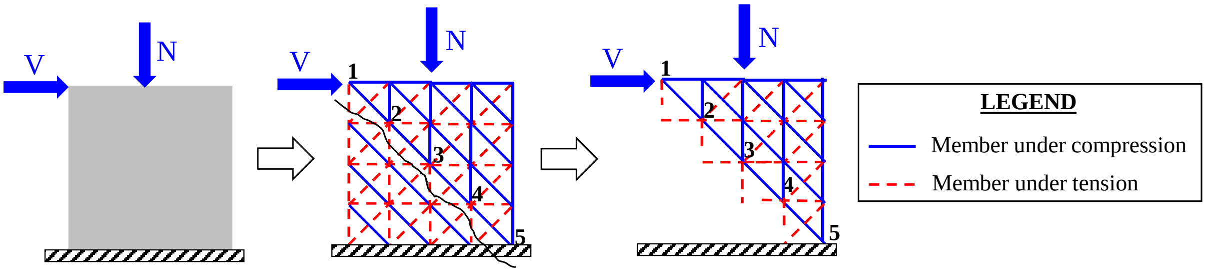

The continuous diagonal strut (1-2-3-4-5) can always transfer part of the horizontal force “V” to the ground.

(b) Truss model for a squat wall (a wall with continuous diagonal struts from top to bottom)

Figure 7.6: Force transfer mechanism after tensile cracking in horizontal elements

Based on the above, if a truss model is used for the analysis of slender members such as RC columns and RM walls with opening, the material laws of the horizontal elements need to somehow account for the contribution of the concrete, V_c, or masonry, V_m, to the shear resistance. The concrete contribution to the shear resistance is mainly attributed to aggregate interlock, since it has been argued that the contribution of the dowel action of the longitudinal reinforcement to V_c can be neglected (Elwood and Moehle 2005b). In masonry structures, the contribution of the masonry material to the shear resistance is due to friction between two sides of a crack, and not the actual interlocking between aggregates.

The aggregate interlock is accounted for through the combination of several simplifying assumptions and a previously proposed equation (Walraven 1980) for the estimation of the shear resistance across a shear crack. The basic assumption made is that the cracks form at an angle equal to that of the diagonal members, θ_d. Additionally, the overall crack displacement vector is assumed to be parallel to the horizontal direction. If the crack displacement magnitude, $u_{cr,h}$, is known, then the crack-normal displacement, w, and the crack-parallel displacement, s, can be obtained from the following expressions, in accordance with Figure 7.7a:

$$w = u_{cr,h} \cdot sin\theta_d \tag{7.8}$$

$$s = u_{cr,h} \cdot \cos\theta_d \tag{7.9}$$

Once w and s are obtained, the shear stress along the inclined crack plane can be calculated using the following equation (Walraven 1980), which has been proposed for cracks in concrete.

$$\tau = -\frac{f_{cc}}{30} + \left[1.80 w^{-0.8} + \left(0.234 w^{-0.71} - 0.20 \right) f_{cc} \right] s \tag{7.10}$$

where f_{cc} is the compressive cube strength of the material (in MPa), which can be conservatively set equal to the cylinder compressive strength of concrete or masonry, f_c or f_m. The displacement components w and s in Equation (7.10) must be expressed in mm. The shear stress along the crack is an increasing function of *s*. The equation by Walraven (1980) is used for both concrete and masonry given the absence of experimental data providing the aggregate interlock resistance of cracks in masonry under cyclic loading. For a given value of *s*, the shear stress decreases with increasing crack opening displacement, *w*. The curves shown in Figure 7.7b, which have been obtained using Equation (7.10), reflect this behavior.

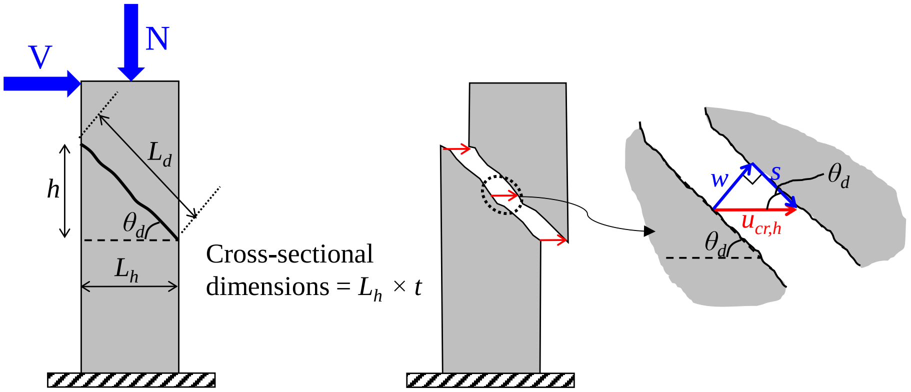

(a) Crack geometry and displacement discontinuity

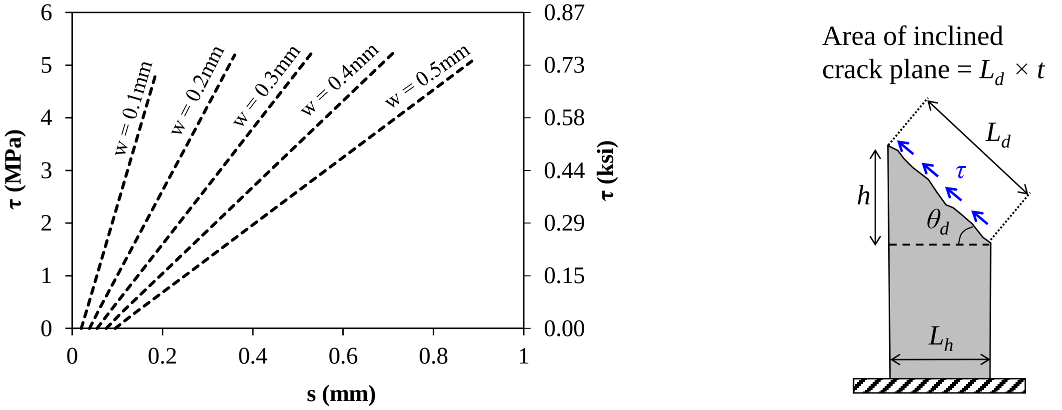

(b) Variation of shear stress as a function of crack opening displacement, *w*, and shear displacement, *s*, for *fcc* = 17.9 MPa (2.6 ksi).

(c) Shear stresses along crack plane

Figure 7.7: Accounting for aggregate interlock along the shear crack

The inclined resultant force due to the aggregate interlock is equal to the product of τ and the corresponding area of the inclined crack plane, $L_d \times t$, as shown in Figure 7.7c. The horizontal component of this force is:

$$F_{a,h} = \tau \cdot L_d \cdot \cos\theta_d \cdot t \tag{7.11}$$

The length L_d of the inclined crack plane can be obtained from the following expression:

$$L_d = \frac{h}{\sin\theta_d} \tag{7.12}$$

where the vertical distance h is equal to the spacing between horizontal truss elements.

In the truss models used here, the force $F_{a,h}$ due to aggregate interlock is carried by the horizontal members. The additional stress that each horizontal member needs to carry is obtained by dividing the force $F_{a,h}$ by the corresponding cross-sectional area of the element.

$$\sigma_{a,h} = \frac{F_{a,h}}{h \cdot t} = \frac{\tau \cdot L_d \cdot \cos\theta_d \cdot t}{L_d \cdot \sin\theta_d \cdot t} = \frac{\tau}{\tan\theta_d} \tag{7.13}$$

An example curve showing the variation of the stress $\sigma_{a,h}$ with the crack displacement magnitude $u_{cr,h}$ is presented in Figure 7.8a. Given the strain, ε_h, of a horizontal truss member, the magnitude of the crack displacement vector can be obtained by multiplying ε_h with the element length, L_h. Subsequently, the stress $\sigma_{a,h}$ can be calculated using Equations (7.8) through (7.13). This stress is added to the stress obtained using the concrete/masonry material law for the horizontal elements to give the total stress, σ_h, of these elements.

The above procedure allows the establishment of an overall stress-strain curve for the horizontal members, expressing the relation between the stress σ_h and the strain ε_h. The truss models presented herein use a trilinear approximation for the tensile total stress-strain curve of the horizontal members, as shown in Figure 7.8b, since such approximation was found to closely match the actual nonlinear curves.

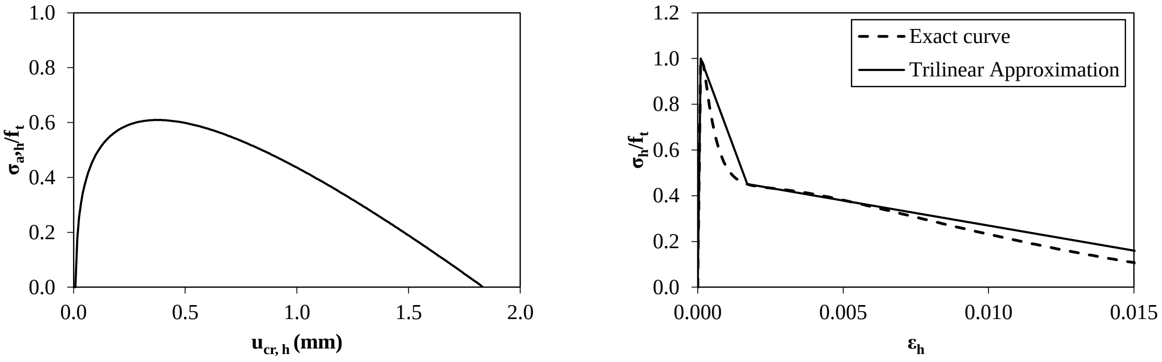

(a) Example horizontal stress-displacement curve expressing contribution of aggregate interlock

(b) Example total stress-strain curve of horizontal elements and trilinear approximation

Figure 7.8: Example constitutive model for horizontal concrete and masonry elements

Equation (7.10) in this work was established by Walraven (1980) based on the results of experimental tests in which the maximum aggregate size, D_{max}, was equal to 16 mm or 32 mm. The maximum aggregate size in the shake-table specimen tested by Elwood and Moehle (2003) was 10 mm, which is outside of the size range from which Equation (7.10) was obtained. Additionally, the aggregate interlock effect for masonry is the measure of surface roughness which is likely to be less than 16 mm. Consequently, the aggregate interlock effect is expected to be less pronounced for both smaller aggregate sizes and also masonry material. In the absence of experimental data, a theoretical model by Walraven (1980) is used to scale the aggregate interlock strength if needed.

The model is based on the following assumptions: i) the concrete is a mixture of rigid, circular aggregate particles embedded in cement paste, as shown in Figure 7.9a, ii) cracking occurs along the circumference of the aggregate particles, iii) the response of the cement matrix in compression is rigid-plastic, with a strength equal to σ_{pu}, iv) the sliding displacement results from compressive plastic strains of the matrix material due to contact with the aggregate particles, v) frictional stresses develop at contact regions between the matrix and the aggregate, and they are equal to the product of σ_{pu} times a frictional coefficient, μ.

The total shear resistance due to aggregate interlock along the crack plane is obtained from the following equation:

$$T = \sigma_{pu}\left(\sum a_y + \mu \cdot \sum a_x\right) \cdot t \tag{7.14}$$

where t is the out-of-plane width of the crack plane, and $\sum a_x$ and $\sum a_y$ are the sums of the projections of the crack contact surfaces along a horizontal and vertical plane, respectively, as shown in Figure 7.9b. The values of σ_{pu} and μ have been determined from pertinent experimental data to be equal to $5.83f_{cc}$ and 0.5, respectively (Walraven 1980).

The values of $\sum a_x$ and $\sum a_y$ are obtained from probabilistic considerations (Walraven 1980), accounting for the aggregate size distribution, and the volume fraction of aggregate in the concrete, which is assumed to be equal to 0.75. The two projections of the contact surface also depend on the crack-normal displacement, w, the crack-parallel displacement, s, and the maximum aggregate size, D_{max}.

Assuming that Equation (7.10) corresponds to D_{max} = 24mm, which is the average of 16 mm and 32 mm, the aggregate interlock resistance, τ_{10mm}, for a maximum aggregate size of 10 mm is obtained from the following equation:

$$\tau_{10mm}\left(u_{cr,h}\right) = S_F\left(u_{cr,h}\right) \cdot \tau\left(u_{cr,h}\right) \tag{7.15}$$

where τ is the aggregate interlock resistance obtained from Equation (7.10) and S_F is a scaling factor, equal to the ratio of the aggregate resistance obtained from Equation (7.14) for D_{max} = 10 mm over the resistance obtained from the same equation for D_{max} = 24 mm. The scaling factor is a function of the crack horizontal displacement, $u_{cr,h}$, since the aggregate interlock resistance obtained from Equations (7.14) and (7.15) depends on the crack-normal and crack-parallel displacements. The two displacement components can be uniquely defined from $u_{cr,h}$, based on the assumption that the overall crack displacement vector is horizontal.

The aggregate interlock resistance curve for $D_{max} = 10$ mm is obtained as a function of the horizontal crack displacement, $u_{cr,h}$, using the following algorithm:

1. Given a value of $u_{cr,h}$ and the inclination angle, θ_d, of the crack, determine the values of w and s using Equations (7.8) and (7.9).
2. For the values of w and s, use Equation (7.10) to obtain $\tau(u_{cr,h})$, which corresponds to $D_{max} = 24$ mm.
3. For the values of w and s, use Equation (7.14), as described in (Walraven 1980), to find the aggregate resistance, T_{ref} corresponding to $D_{max} = 24$ mm and the aggregate resistance, T, corresponding to $D_{max} = 10$ mm. Obtain the scaling factor, S_F, by dividing T by T_{ref}: $S_F = T/ T_{ref}$.
4. Obtain $\tau_{10mm}\left(u_{cr,h}\right)$ using Equation (7.15).
5. Establish a new value of $u_{cr,h}$ and go to step 1.

After repeating the above five-step algorithm for a range of values of $u_{cr,h}$, a curve giving the aggregate resistance, τ_{10mm}, as a function of the crack horizontal displacement, $u_{cr,h}$, is obtained. The additional strength of the horizontal elements to account for the aggregate interlock effect is then obtained using Equations (7.11) to (7.13). The curve giving the variation of the additional stress, $\sigma_{a,h}$, of the horizontal elements as a function of $u_{cr,h}$ obtained for the specimen of Elwood and Moehle (2003) is compared to the curve obtained with Equation (7.10) in Figure 7.9c.

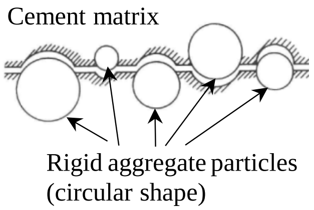

(a) Theoretical physical model

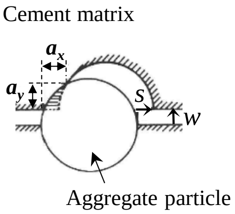

(b) Definition of contact areas between aggregate particles and cement matrix

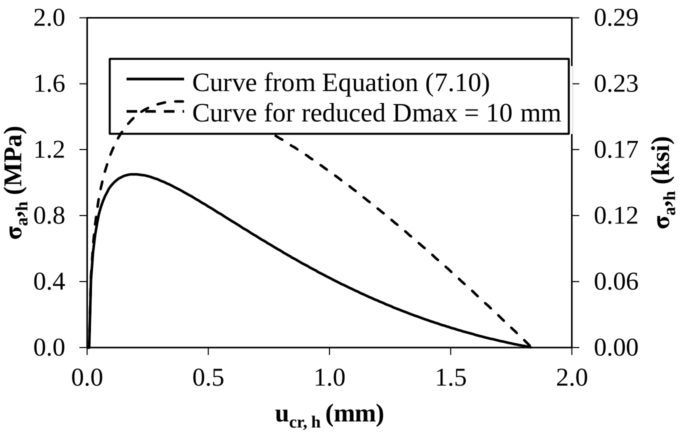

(c) Horizontal stress-displacement curve due to aggregate resistance for the concrete strength of the specimen tested by Elwood and Moehle (2003), f_c = 24.5 MPa (3.55 ksi).

Figure 7.9: Theoretical model used for scaling the aggregate interlock resistance

7.3.3 Reinforcing steel

The truss elements representing the longitudinal and transverse reinforcement use the Giuffre-Menegotto-Pinto (GMP) material model (Filippou et al. 1983). The specific material model is characterized by a monotonic envelope curve with linear hardening after yielding. In the analyses presented herein, the slope of the hardening portion of the stress-strain curve, $\beta_h .E_s$, has been calibrated using data from tensile monotonic tests on reinforcing steel. The GMP model can also account for the nonlinear hysteretic behavior of reinforcing steel, as shown in Figure 7.10. A detailed explanation of the model, including the mathematical expressions which describe the nonlinear unloading-reloading curves, is provided in the work by Filippou et al. (1983). The GMP model cannot capture the effects of bar buckling and rupture on the stress-strain response of the reinforcing steel. Such effects exist in flexure-dominated members where the longitudinal reinforcement is subjected to large inelastic deformations and they are not expected to be significant for the shear-dominated members considered here.

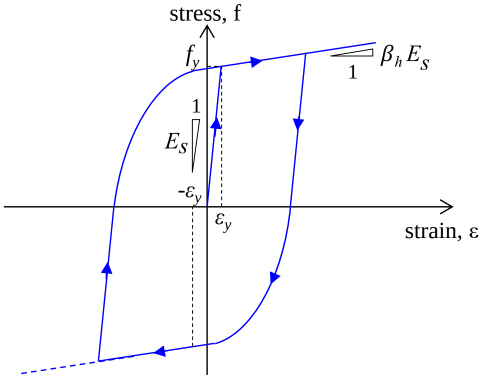

Figure 7.10: Constitutive model for reinforcing steel

The use of the tensile softening law by Stevens et al. (1991) must be accompanied by a modification of the stress-strain curve of the steel reinforcement to represent the average steel stress in cracked concrete. The most significant part of the modification is to slightly reduce the yield stress of the reinforcement. A reduction of 3% or less was obtained for the yield stress of the reinforcement in the RC columns examined in this study, and was found to have a negligible effect on the analytical results.

7.3.4 Accounting for the strain penetration effects

The hysteretic response of RC members undergoing flexural inelastic deformations is affected by the strain penetration effect in the member end regions. The slip of the reinforcement in beam-to-column joint regions and at the base of each column leads to additional rotations at the ends of each member. These additional rotations increase the total deformation for a given curvature distribution along the member length and need to be accounted for in a simulation to provide accurate predictions of the hysteretic response of a RC column.

The truss representation of RC columns studied herein accounts for the strain penetration effect at locations where flexural inelasticity is expected to occur. This is accomplished by introducing additional vertical elements at end regions, as shown in Figure 7.11a for the case of a cantilever column. The extended vertical elements are rigid in compression, so that the slip affects only rebars under tension. The length L_b of the additional elements is determined so that the total slip due to strain penetration when the rebars yield equals the value obtained with the expression proposed by Zhao and Sritharan (2007). Given the value s_y, of the total slip at yield, L_b can be obtained by stipulating that the uplift due to the additional vertical elements – which, at the onset of yield of the vertical reinforcement, will have an axial strain equal to ε_y – is equal to s_y, as explained in Figure 7.11b:

$$s_y = \varepsilon_y \cdot L_b \rightarrow L_b = \frac{s_y}{\varepsilon_y} \tag{7.16}$$

The empirical expression by Zhao and Sritharan (2007) can be rewritten as:

$$s_y = 0.54\left(\frac{d_b . f_y}{\sqrt{f_c}}\right)^{2.5} + 0.34 \tag{7.17}$$

where the total slip, s_y, is defined as a function of rebar diameter, d_b, rebar yield stress, f_y, and compressive strength of the surrounding concrete, f_c. In this equation, the values of s_y and rebar diameter are needed to be substituted in mm and the stresses should be in MPa.

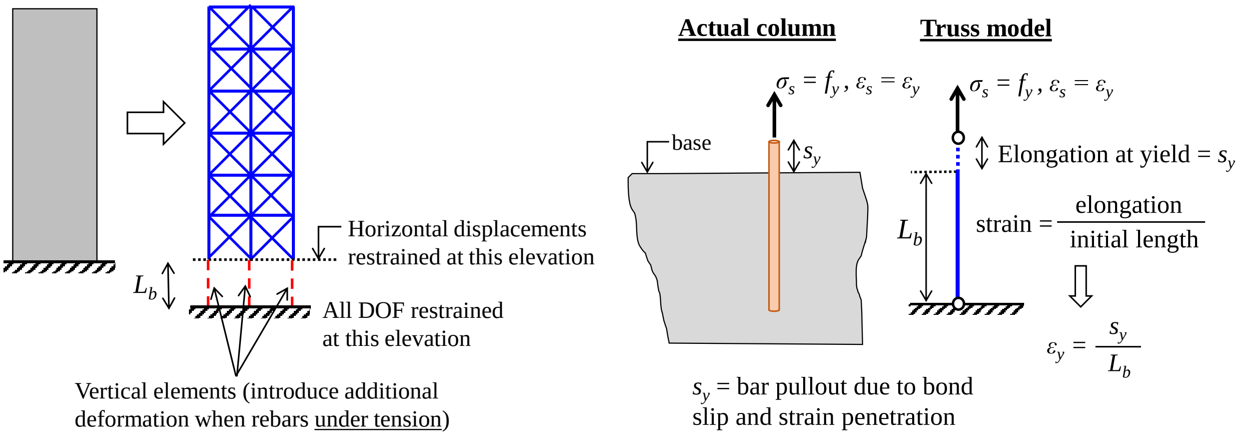

(a) Elements to account for strain penetration (b) Determination of length L_b

Figure 7.11: Methodology to account for strain penetration effect

Chapter 8 : Verification of the Capability of Nonlinear Truss Model for the Analysis of Shear-Dominated RC/RM Structural Components

The nonlinear truss methodology, described in Chapter 7, is validated through conducting nonlinear analysis for shear-dominated reinforced concrete (RC) columns and reinforced masonry (RM) walls. Specifically, two RC column specimens under quasi-static cyclic loading, a planar RC frame structure subjected to a base excitation, two RM wall specimens under cyclic loading, and a two-story RM wall system subjected to a sequence of ground motions are analyzed using the nonlinear truss models. Very good agreement is obtained between analytically obtained and experimentally recorded hysteretic response. Additionally, shear failure modes, such as formation of diagonal tensile cracks and sliding at base, are well captured. Additional parametric studies have been performed to verify the objectivity of the constitutive equations with respect to mesh size, to examine the sensitivity of the modeling technique to the inclination angle of diagonal elements, and finally to show the impact of ignoring the aggregate interlock effect on the hysteretic response and failure modes of structures examined herein. The conceptual simplicity and the numerical efficiency of the nonlinear truss models establish the method as an attractive simulation tool for systematic assessment of shear-dominated RC/RM structural components and systems.

8.1 Validation of the analysis methodology using reinforced concrete columns and frame structures

In this section, the modeling approach based on the truss analogy has been validated with the results of quasi-static and dynamic tests on RC column specimens. The analyses have been conducted using the nonlinear analysis program OpenSees (2000) which includes the element formulations and constitutive laws of the modeling approach described in Chapter 7. The material models for concrete and steel are available in OpenSees as *ConcretewBeta*, and *Steel02*, respectively, and a nonlinear truss element accounting for the transverse strain effect is available as *Truss2* element.

The material properties used in the analytical models are exactly the same as experimentally reported values. However, due the lack of experimental data, the tensile strength of concrete is assumed to be either 10% of the compressive strength or calculated using the following expression.

$$f_t = 0.33\sqrt{f_c} \tag{8.1}$$

8.1.1 Analysis of RC column specimens under quasi-static cyclic load

The first set of verification analyses is conducted for shear-dominated columns tested by Priestley et al. (1994). Two of the specimens, namely, specimens R1A and R3A, are analyzed using the truss modeling approach. The configuration and cross-sectional reinforcement for the two specimens are shown in Figure 8.1. The same figure presents the geometry of the truss models. Both specimens were restrained against rotation at both ends and were subjected to a cyclic displacement history at the top.

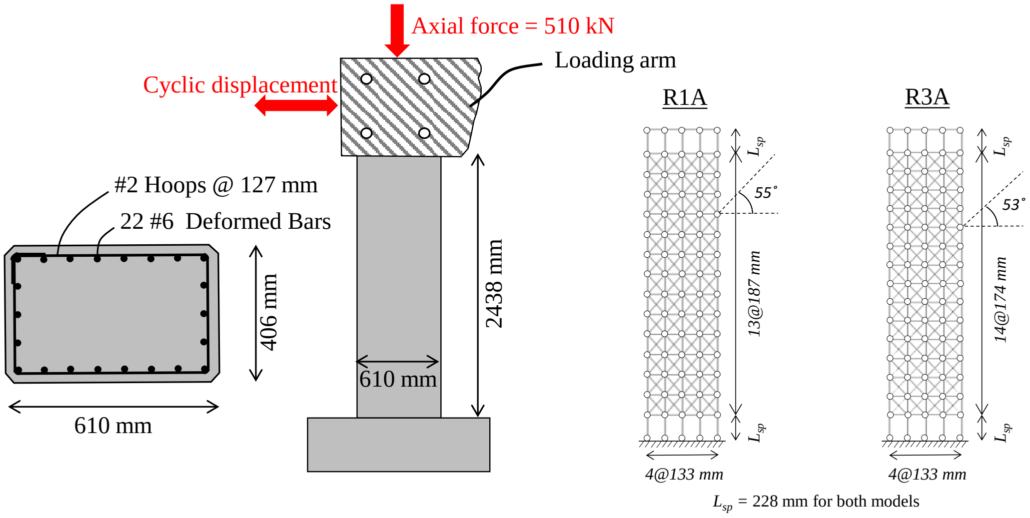

Figure 8.1: Test configuration for column specimens tested by Priestley et al. (1994).

The axial load was equal to 510 kN (114 kip) for both specimens, while the concrete compressive strength was equal to 37.8 MPa (5.5 ksi) for specimen R1A and 34.4 MPa (5.0 ksi) for specimen R3A. The axial load ratio was 0.054 for column R1A and 0.060 for column R3A. The longitudinal reinforcement consisted of 19 mm – diameter (#6) deformed bars, and the transverse reinforcement was 6 mm – diameter (#2) ties with a spacing of 127 mm (5 in.). The longitudinal and transverse reinforcement ratios were equal to 0.0254 and 0.0012, respectively, for both specimens. The main difference between the two specimens was that the yield stress of the longitudinal reinforcement was equal to 323 MPa (47 ksi) for specimen R1A and 467 MPa (68 ksi) for specimen R3A, and the yield stress of the transverse reinforcement was equal to 357 MPa (52 ksi) for specimen R1A and 323 MPa (47 ksi) for specimen R3A. The two specimens incurred strength degradation due to shear damage at drift ratios of 1.40% and 0.95%, respectively.

The parameters of the analytical models are presented in Tables 8.1, 8.2 and 8.3. Table 8.1 presents the cross-sectional areas of the various elements in the truss models. The values assigned to the concrete and steel material parameters for the truss elements of each analysis are presented in Tables 8.2 and 8.3, respectively.

Table 8.1: Cross-sectional areas for truss elements

	$A_{c,v1}$ (mm^2)	$A_{c,v2}$ (mm^2)	$A_{c,h}$ (mm^2)	$A_{c,d}$ (mm^2)	$A_{s,v1}$ (mm^2)	$A_{s,v2}$ (mm^2)	$A_{s,h}$ (mm^2)
Priestley et al. R1A	42833	53998	76202	44058	1425	1140	100
Priestley et al. R3A	42833	53998	70759	42926	1425	1140	93
Elwood & Moehle	17013	18874	26061	15286	451	395	57

Note: $A_{c,v1}$ = area of outermost vertical concrete elements, $A_{c,v2}$ = area of interior vertical concrete elements, $A_{c,h}$ = area of horizontal concrete elements, $A_{c,d}$ = area of diagonal elements, $A_{s,v1}$ = area of outermost vertical steel elements, $A_{s,v2}$ = area of interior vertical steel elements, $A_{s,h}$ = area of horizontal steel elements.

Table 8.2: Material parameters for concrete

	f_c (MPa)	E_c (MPa)	f_t (MPa)	Vertical Elements				Horizontal Elements			
				ε_{cres}	ε_{cint}	f_{cint} (MPa)	M	ε_{tres}	f_{tres} (MPa)	ε_{tint}	f_{tint} (MPa)
Priestley et. al R1A	-38.0	38000	2.03	-0.0113	-0.0066	19.00	0.131, 0.083	0.012	0.031	0.0025	1.8
Priestley et. al R3A	-34.0	34000	3.40	-0.0121	-0.0071	17.00	0.131, 0.083	0.012	0.052	0.0026	1.7
Elwood & Moehle	-24.5	24500	2.45	-0.0183	-0.010	12.25	0.144, 0124	0.022	0.001	0.0017	1.1

Note 1: ε_{cres} = strain at which the concrete completely loses compressive strength, (ε_{cint}, f_{cint}) = strain and stress values, respectively, of an intermediate point in the compressive softening regime of the uniaxial stress-strain curve, M = parameter affecting the tensile strength degradation of reinforced concrete, f_{tres} = residual tensile strength, ε_{tres} = strain at which the residual tensile strength is attained, (ε_{tint}, f_{tint}) = strain and stress values, respectively, of the intermediate point in the trilinear tensile regime of the uniaxial stress-strain curve

Note 2: Two values are reported for M in each analysis, the first corresponding to the outermost vertical elements and the other to the interior vertical elements

Note 3: ε_0 = 0.002 and ε_u = 0.004 were assumed (for a reference length of 600 mm) for the diagonal elements in all the simulations

Table 8.3: Material Parameters for reinforcing steel

		f_y (MPa)	E_s (MPa)	β_h
Priestley et. al R1A	V	324	200000	0.046
	H	358		0.020
Priestley et. al R3A	V	467	200000	0.020
	H	322		
Elwood & Moehle	V	479	200000	0.020
	H	718		0.000

Note: f_y = yield stress, E_s = elastic modulus, β_h = ratio of hardening modulus over elastic modulus

The analytically obtained hysteretic plots for the two specimens are compared to the corresponding experimental observations in Figures 8.2a and 8.2b for columns R1A and R3A, respectively. It can be seen that the truss models provide very good estimates of the load-displacement response of the two specimens, including the significant strength degradation obtained due to shear damage. As shown in Figures 8.3a and 8.3b, the strength degradation in the analyses is caused by the occurrence of inclined cracks, just like in the experimental tests.

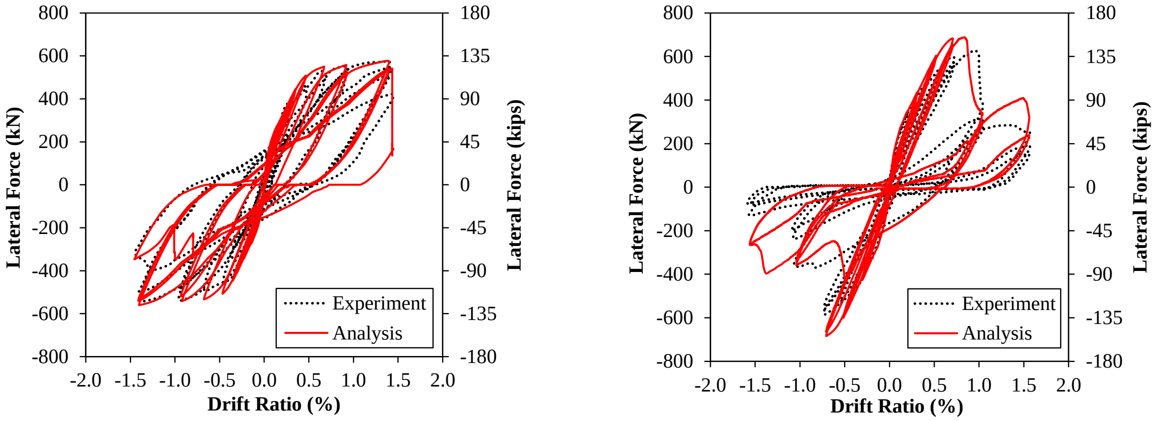

(a) Specimen R1A

(b) Specimen R3A

Figure 8.2: Comparison of analytically obtained and experimentally recorded force-displacement response for column specimens tested by Priestley et al. (1994).

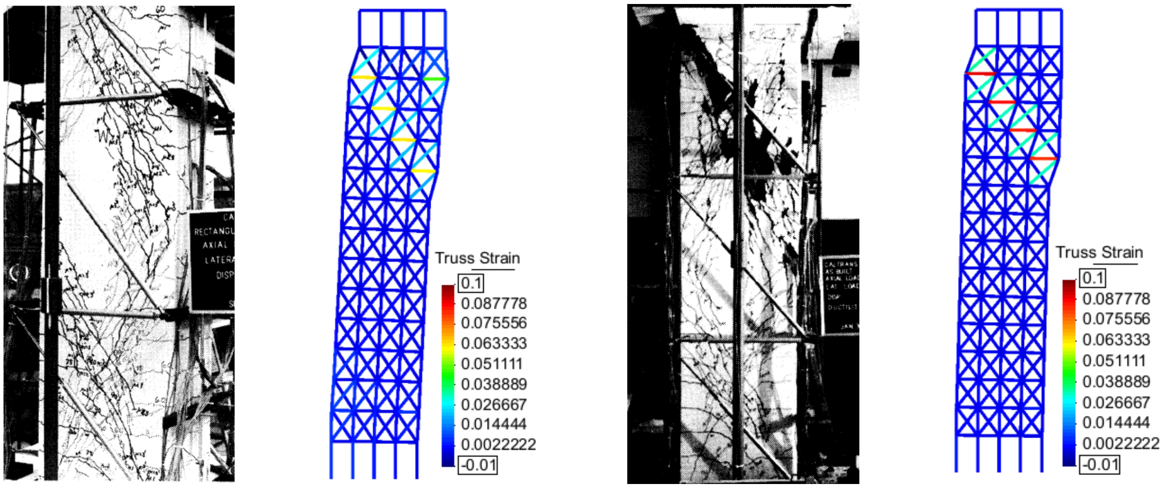

(a) Specimen R1A

(b) Specimen R3A

Figure 8.3: Comparison of analytical and experimental damage patterns for column specimens tested by Priestley et al. (1994), deformations in analytical results are magnified by a factor of 5.

To demonstrate the significance of accounting for the aggregate interlock effect in truss models of RC columns, the analysis for the R3A specimen tested by Priestley et al. (1994) has been repeated, this time without including the contribution of the aggregate interlock in the shear resistance. The analysis gives the diagonal tension failure observed in the test, but it significantly underestimates the strength of the column, as shown in Figure 8.4a, which compares the hysteretic response obtained for the analysis of column R3A without aggregate interlock to the experimentally obtained load-displacement curve.

Additionally, the effect of the inclination angle of the diagonal elements is investigated for column R3A. More specifically, the analysis of the column, which had been conducted for $\theta_d = 53^o$, was repeated for $\theta_d = 47^o$ and $\theta_d = 59^o$. The hysteretic curves obtained from the three analyses are compared in Figure 8.4b. The analysis for $\theta_d = 47^o$ predicts the same damage pattern as that shown in Figure 8.3b. On the other hand, the analysis for $\theta_d = 59^o$ gives a flexure-dominated response, and no strength degradation due to shear damage is obtained. In fact, the significant increase of the cross-sectional area of the horizontal concrete and steel truss elements does not allow the occurrence of strength degradation associated with inclined diagonal cracking.

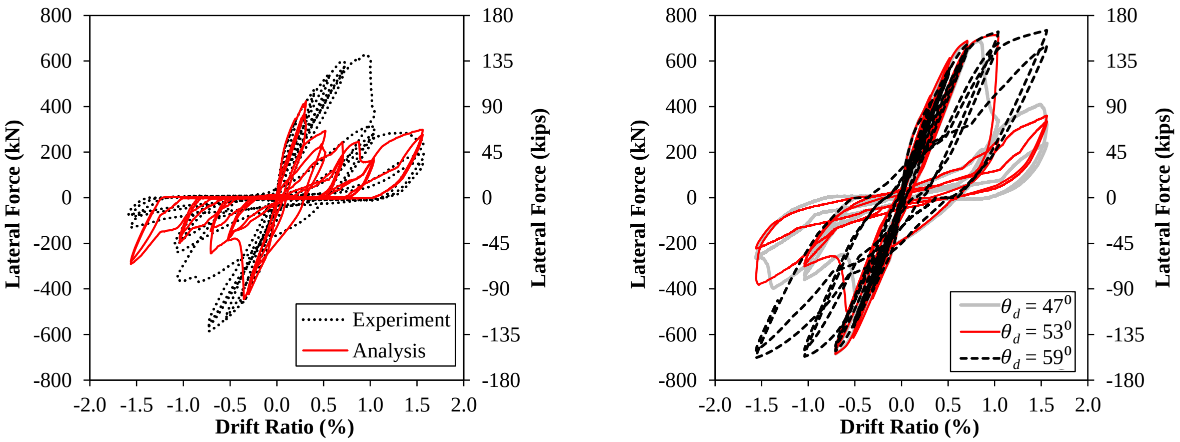

(a) Results without aggregate interlock effect

(b) Effect of angle, θ_d, of diagonal elements

Figure 8.4: Sensitivity study for column R3A tested by Priestley et al. (1994).

8.1.2 Analysis of RC frame structure subjected to dynamic loading

The proposed analysis method is also validated for dynamic loading using the results of the shake-table tests by Elwood and Moehle (2003) on a half-scale, single-story, two-bay frame specimen. The concrete compressive and tensile strength were equal to 24.5 MPa (3.6 ksi) and 2.45 MPa (0.36 ksi), respectively, while the yield stress of the longitudinal steel reinforcement was equal to 479 MPa (69.7 ksi). To satisfy the scaling requirements, steel wires were used as transverse reinforcement. The yield stress of the wire reinforcement was equal to 718 MPa (104.5 ksi). The longitudinal reinforcement ratio was equal to 0.0252, while the transverse reinforcement ratio was equal to 0.0018. The specimen was subjected to a scaled version of a ground motion record from the 1985 Chile earthquake. The seismic excitation led to severe shear damage in the middle column.

The configuration of the specimen and of the corresponding analytical model is shown in Figure 8.5. A truss assemblage is used for the middle column, while the other frame members are modeled by nonlinear beam elements having a fiber-section. The confinement effect of the transverse reinforcement on the core concrete of the circular columns is accounted for in the analyses. More specifically, the compressive strength and ductility of the material in the core concrete fibers are increased using the equations by Mander et al. (1988). Rigid end offsets are included in the connections of the beam elements. Rayleigh initial stiffness damping is used in the analysis, with a damping ratio of 2% prescribed for the first and second modes of the system. Finally, a leaning column is added in the analytical model, to capture the effect of geometric nonlinearities resulting from the relatively large drift levels reached during the tests.

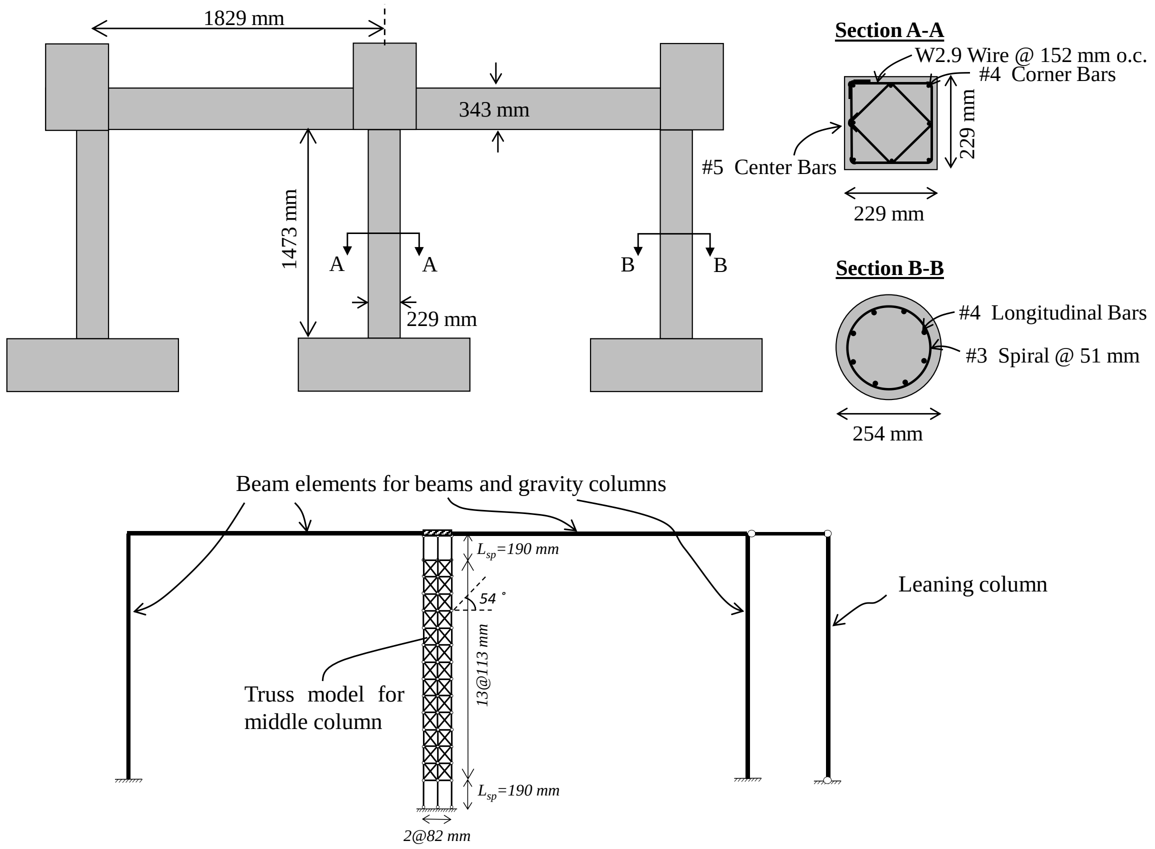

Figure 8.5: Configuration and analytical model for the shake-table specimen tested by Elwood and Moehle (2003).

Additional considerations are required for the calibration of the aggregate interlock equations in this particular analysis. More specifically, Equation (7.10) was obtained from experimental tests where the maximum size of the aggregate was equal to either 16 mm or 32 mm. The concrete in the specimen tested by Elwood and Moehle (2003) had a maximum aggregate size of 10 mm. Since the aggregate interlock effect is expected to be less pronounced for smaller aggregate sizes, the aggregate resistance across a cracked plane is reduced based on a theoretical approach by Walraven (1980), as explained in Section 7.3.2.

The analytically obtained hysteretic response and drift time histories are compared to their experimentally recorded counterparts in 8.6a and 8.6b. The major discrepancy is observed for the positive drift values, which are underestimated by the analysis after the occurrence of severe shear damage. The strength of the column is also overestimated by 19%. Still, the analytically obtained results can be considered as very satisfactory. The strength degradation in the analysis is associated with shear damage in the middle column, similar to the damage pattern observed in the experimental test, as shown in Figures 8.7a and 8.7b.

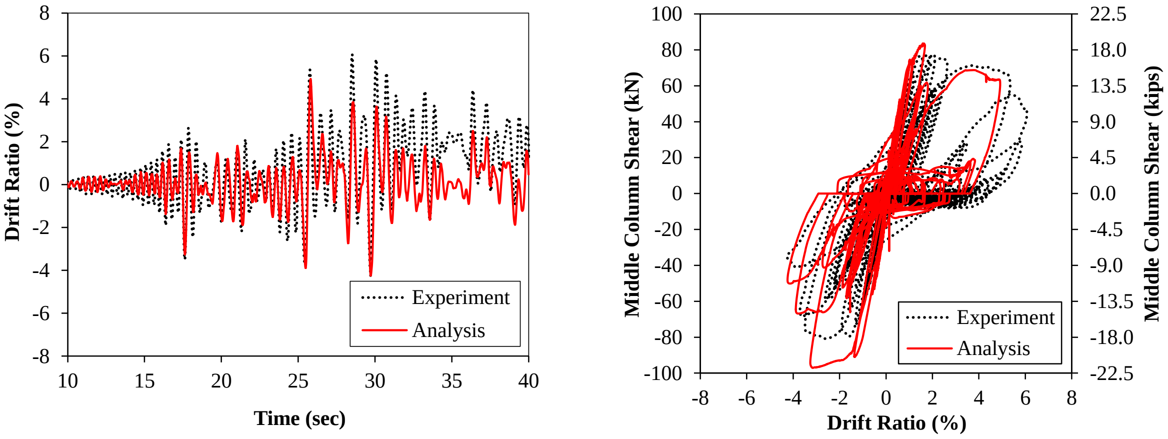

(a) Drift time history

(b) Hysteretic response

Figure 8.6: Comparison of analytical and experimental results for the shake-table specimen tested by Elwood and Moehle (2003).

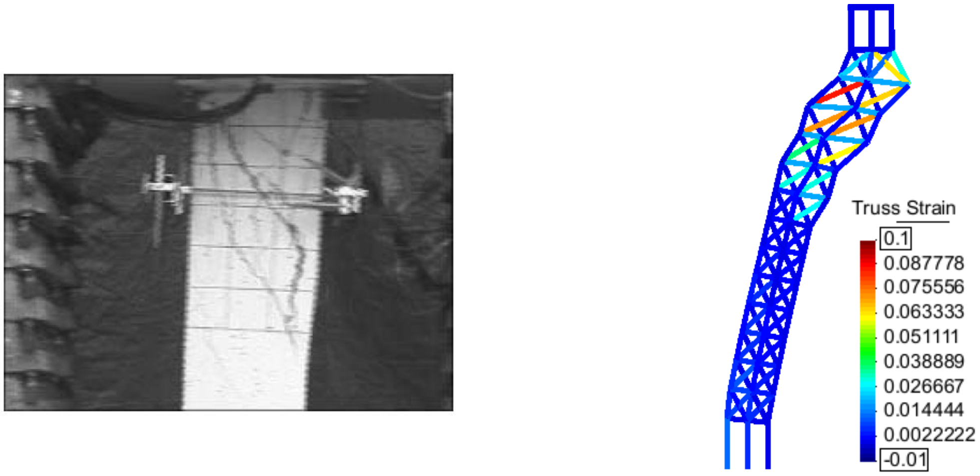

(a) Specimen damage at time t = 24.9s

(b) Deformation (magnified by a factor of 5) at peak positive displacement in analysis (t = 25.8s)

Figure 8.7: Comparison of analytically obtained and experimentally observed damage pattern for the shake-table specimen tested by Elwood and Moehle (2003).

8.2 Verification of the analysis methodology using reinforced masonry shear walls

The truss modeling approach has been further validated with experimental data from quasi-static (Shing et al. 1991) and dynamic (Ahmadi et al. 2015b) tests on RM wall specimens. As mentioned in Section 8.1, the analyses have been performed using the nonlinear analysis program OpenSees (McKenna et al. 2000) which includes the element formulations and constitutive laws of the modeling approach.

The experimental tests used for the validation of the analysis method were accompanied by material tests which provided the masonry prism compressive strength and the yield strength of the reinforcing steel. These strength values are used unaltered in the analytical models. In the absence of material test data, the masonry tensile strength is assumed to be 8% of the compressive strength for all analyses.

8.2.1 Analysis of single-story RM wall specimens under quasi-static cyclic load

The first set of validation analyses is conducted for two RM wall specimens tested by Shing et al. (1991). The first specimen, named specimen 5 in Shing et al. (1991), incurred strength degradation due to large inclined cracks. The second specimen, termed specimen 11 in Shing et al. (1991), incurred strength degradation due to the occurrence of horizontal sliding at the base. The configuration and cross-sectional reinforcement of the two specimens are shown in Figure 8.8. The same figure presents the geometry of the truss models. Both specimens were restrained against rotation only at bottoms and were subjected to a cyclic displacement history at the top.

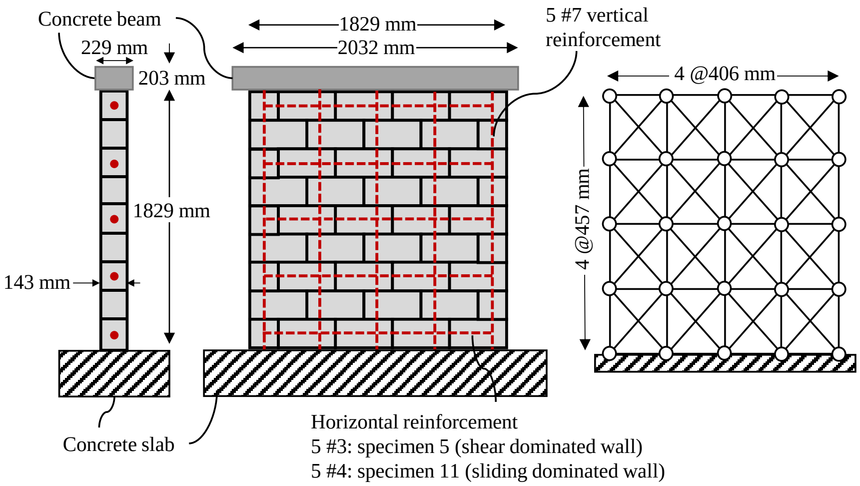

Figure 8.8: Test configuration for wall specimens tested by Shing et al. (1991).

The masonry prism compressive strength was equal to 17.9 MPa (2.6 ksi) and 22.1 MPa (3.2 ksi) for specimens 5 and 11, respectively. The wall vertical reinforcement consisted of 22 mm – diameter (#7) bars with a yield strength of 496 MPa (72 ksi). The main difference between the two specimens was in the size and yield strength of the transverse reinforcement. For specimen 5, 10 mm (#3) bars with a yield strength of 386 MPa (56 ksi) were used, while specimen 11 included 13 mm (#4) bars with a yield strength of 462 MPa (67 ksi). The longitudinal reinforcement ratio was equal to 0.74% for both specimens, and the transverse reinforcement ratio was 0.14% and 0.24% for specimens 5 and 11, respectively. A constant axial load of 178 kN (40 kip), corresponding to an axial stress of 0.69MPa (100 psi) and a compressive stress ratio of 3.8%, was applied on specimen 5, while no axial load was applied on specimen 11. Specimens 5 and 11 incurred strength degradation due to shear-induced damage at drift ratios of 0.58% and 0.92%, respectively.

The cross-sectional areas of the truss elements in the models are presented in Table 8.4. The material parameters of the analytical models are presented in Tables 8.5 and 8.6 for the masonry and reinforcing steel, respectively.

Table 8.4: Cross-sectional areas of truss elements assemblage used to model single-story walls

	$A_{m,v1}$ (mm^2)	$A_{m,v2}$ (mm^2)	$A_{m,h}$ (mm^2)	$A_{m,d}$ (mm^2)	$A_{s,v1}$ (mm^2)	$A_{s,v2}$ (mm^2)	$A_{s,h}$ (mm^2)
Specimen 5	43225	58064	65161	43225	387	387	71
Specimen 11	43225	58064	65161	43225	387	387	129

Note: $A_{m,v1}$: area of the outermost vertical masonry elements, $A_{m,v2}$: area of the intermediate vertical masonry elements, $A_{m,h}$: area of the horizontal masonry elements, $A_{m,d}$: area of the diagonal masonry elements, $A_{s,v1}$: area of the outermost vertical steel elements, $A_{s,v2}$: area of the intermediate vertical steel elements, $A_{s,h}$: area of the horizontal steel elements

Table 8.5: Masonry material parameters used to model single-story wall specimens

Element Type	f_m (MPa)	E_m (MPa)	f_t (MPa)	ε_{mres}	ε_{mint}	f_{mint} (MPa)	ε_{tres}	ε_{tint}	f_{tint} (MPa)
Vertical	-17.9^1 -22.1^2	14934^1 18381^2	1.44^1 1.72^2	-0.0055	-0.0039	-9.0^1 -11.0^2	0.0003	0.0002	0.32^1 0.39^2
Horizontal				-0.0061	-0.0042		0.0047	0.0007	1.46^1 1.62^2
Diagonal				-0.0043	-0.0034		n.a.	n.a.	n.a.

^{1}: Values for specimen 5

^{2}: Values for specimen 11

Note 1: ε_{mres} = strain at which the masonry completely loses compressive strength, (ε_{mint}, f_{mint}) = strain and stress values, respectively, of an intermediate point in the compressive softening regime of the uniaxial stress-strain curve, ε_{tres} = strain at which the masonry completely loses tensile strength, (ε_{tint}, f_{tint}) = strain and stress values, respectively, of the intermediate point in the trilinear tensile regime of the uniaxial stress-strain curve

Note 2: $\varepsilon_0 = 0.0024$ and $\varepsilon_u = 0.004$ were assumed (for a reference length of 600 mm)

Table 8.6: Reinforcing steel material parameters used to model single-story walls

Element Type	f_y (MPa)	E_s (MPa)	β_h
Vertical	496	200000	0.01
Horizontal	386^1, 462^2		

^{1}: Values for specimen 5

^{2}: Values for specimen 11

The analytically obtained hysteretic response curves for both specimens are compared to the corresponding experimental observations in Figures 8.9a and 8.9b for specimens 5 and 11, respectively. It can be seen that the truss models provide satisfactory estimates of the load-displacement response of the two specimens, particularly the peak strength and onset of strength degradation obtained due to diagonal cracking and horizontal sliding. The pre-peak stiffness of specimen 5 is overestimated by the analysis. A similar overestimation of the initial stiffness of the specific specimen has been obtained for a finite element analysis by Lotfi and Shing (1991). A possible reason for such overestimation is that the material of the specific wall had increased deformability (i.e., lower modulus of elasticity) than that indicated by the accompanying masonry prism tests.

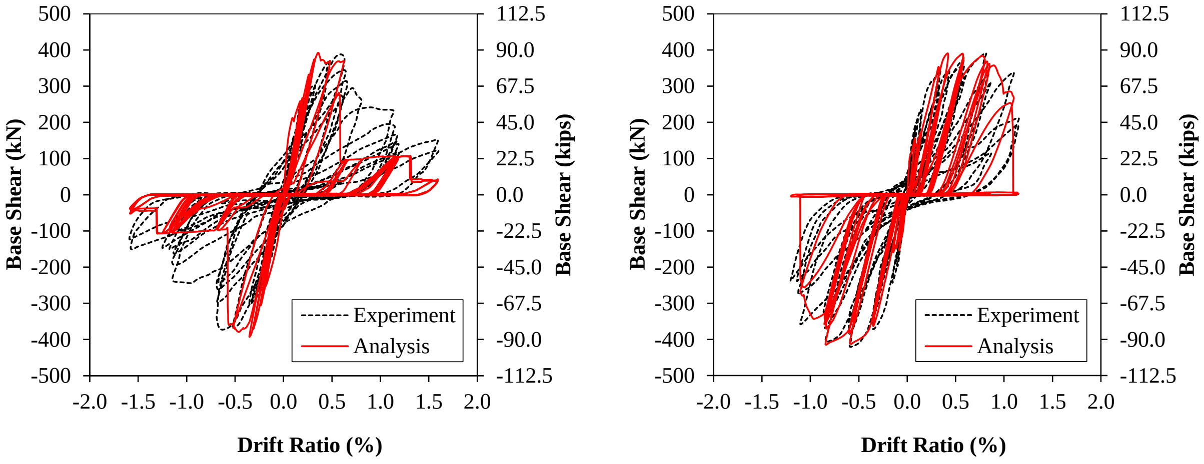

(a) Specimen 5

(b) Specimen 11

Figure 8.9: Comparison of analytically obtained and experimentally recorded force-displacement response for RM wall specimens tested by Shing et al. (1991).

The experimentally observed damage pattern of specimen 5 was dominated by diagonal cracks, as shown in Figure 8.10a. As shown in Figures 8.10b and 8.10c, the strength degradation in the analyses of specimen 5 is caused by the occurrence of inclined cracks, just like in the experimental tests. The inclined cracking adversely affects the compressive resistance of the diagonal strut. The wall incurs significant strength degradation due to loss of compressive resistance of the elements along the diagonals.

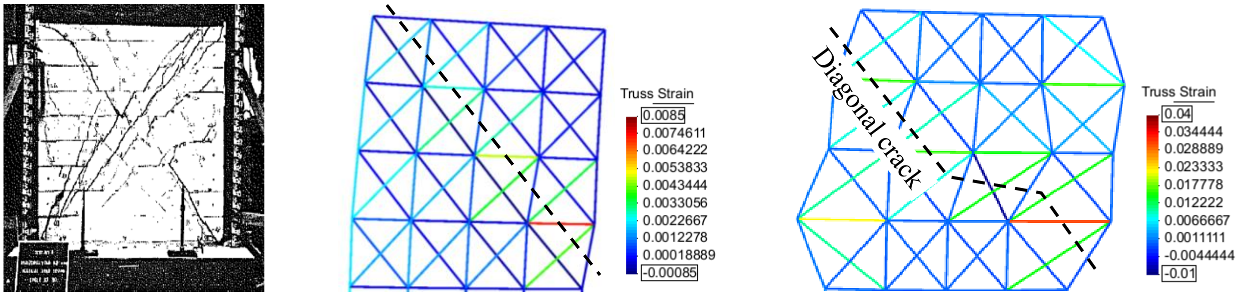

(a) Experimental cracking pattern

(b) Analytically obtained deformed shape at drift ratio of 0.4%

(c) Analytically obtained deformed shape at drift ratio of 0.61%

Figure 8.10: Comparison of damage patterns for specimen 5.

The damage pattern obtained in the experimental test of specimen 11 is shown in Figure 8.11a, while the deformed shapes obtained at different stages of the analysis are presented in Figures 8.11b and 8.11c. The deformed truss model shown in Figure 8.11b indicates that the analytical model experiences flexural cracking at an early stage of loading. The increased size of horizontal reinforcing bars and the absence of axial force (which leads to reduced flexural strength) prevent the occurrence of strongly localized diagonal cracks and the wall has a ductile hysteretic response up to a drift ratio of 0.92%. At that point, the diagonal compressive struts at the bottom row of the truss model incur strength degradation. This degradation leads to the formation of a sliding-like failure mechanism (Figure 8.11c). The sliding is accompanied by vertical bulging and lateral strength degradation. After the onset of strength degradation due to shear failure, the residual resistance in the two specimens was provided by dowel action of the vertical reinforcement. Since the dowel action of the reinforcement is not explicitly accounted for in the truss model, the strength degradation in the analyses is much more severe than that obtained in the experimental tests. Properly accounting for the dowel action and its interaction with the axial resistance of the bars would require complicated models based on, e.g., beam elements for the rebars. Such models are not employed here, given that the onset of severe strength degradation due to shear damage corresponds to wall failure.

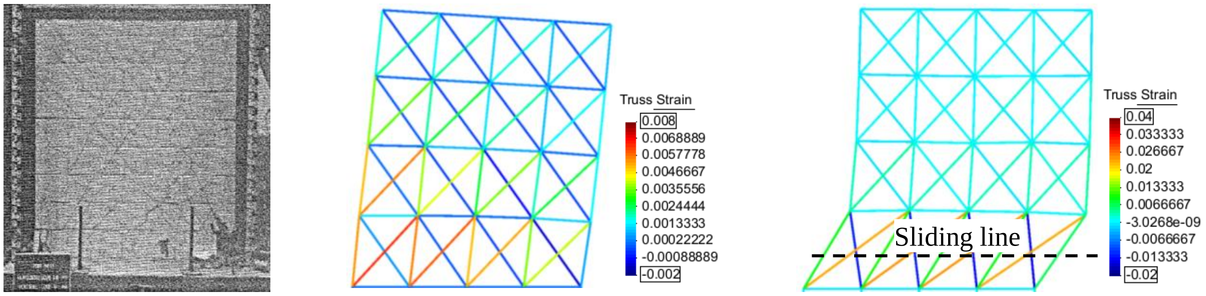

(a) Experimental cracking pattern

(b) Analytically obtained deformed shape at drift ratio of 0.58%

(c) Analytically obtained deformed shape at drift ratio of 1.1%

Figure 8.11: Comparison of cracking patterns for specimen 11.

To verify that the truss modeling approach is objective with respect to element size, the analyses for the two wall specimens have been repeated for a finer mesh. The hysteretic response and damage patterns obtained in the analyses for a finer mesh are presented in Figure 8.12. The use of a finer mesh does not spuriously affect the calculated peak strength or ductility for the specimens. A finer mesh does lead to better estimates of the hysteretic response, especially for specimen 5. This is expected, since refining a finite element mesh with objective material models should be leading to more accurate results. However, the initial stiffness overestimation and more severe strength degradation compared to the test results are still observed in the analytical models.

To determine the significance of the aggregate interlock effect in the truss models of the two wall specimens, the analyses are also conducted without including the contribution of the aggregate interlock to the shear resistance. For specimen 5, the analysis without aggregate interlock gives the same damage pattern, but it slightly underestimates the shear strength of the wall, as shown in Figure 8.13a. The figure compares the analytically obtained hysteretic response for specimen 5 with and without aggregate interlock. As shown in Figure 8.13b, similar hysteretic response diagrams are obtained for specimen 11, with and without aggregate interlock. However, the case without aggregate interlock gave a damage pattern which was dominated by inclined diagonal cracks, instead of horizontal sliding.

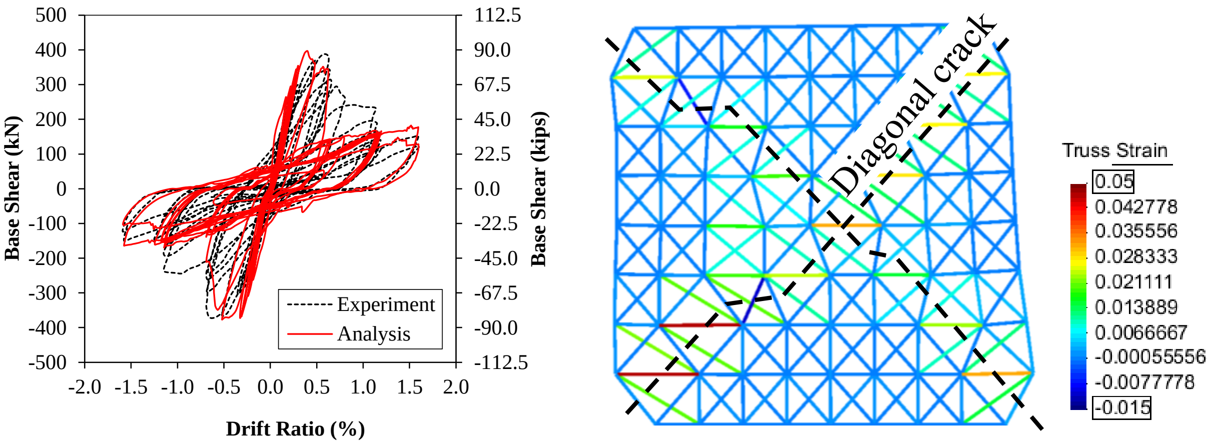

(a) Specimen 5

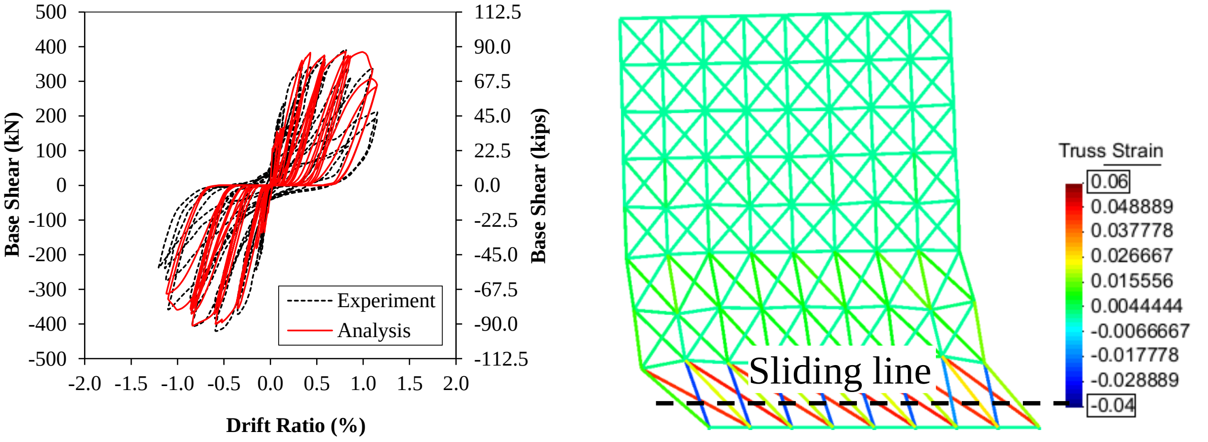

(b) Specimen 11

Figure 8.12: Analytical results for wall specimens and for a refined mesh

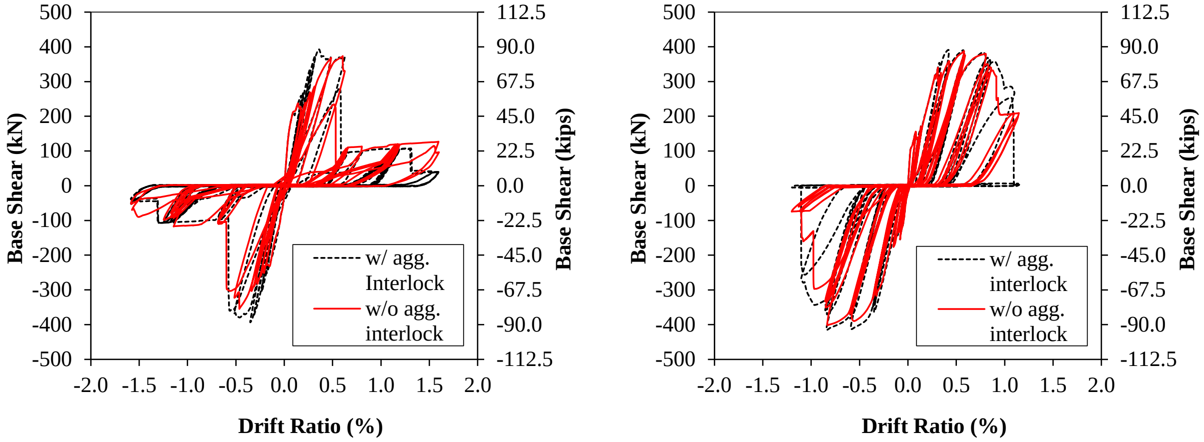

(a) Specimen 5 (b) Specimen 11

Figure 8.13: Effect of aggregate interlock on the hysteretic behavior of the single-story wall specimens.

The wall specimens had a height-to-length ratio of 1 and the truss models included a continuous diagonal compressive strut along the entire specimen height. Thus, the fact that the aggregate interlock resistance would not be significant for the strength of the walls was expected. The fact that the damage pattern for specimen 11 was different without aggregate interlock is attributed to the similar shear strength values corresponding to localized diagonal cracking and horizontal sliding. Removing the aggregate interlock effect is expected to affect the shear strength associated with diagonal cracking, while the shear strength associated with horizontal sliding remains unaltered. For this reason, a localized diagonal cracking pattern is obtained when the aggregate interlock is not accounted for in the analysis.

8.2.2 Analysis of two-story RM wall system subjected to a sequence of ground motions

The truss modeling approach has been further validated using the results of a shake-table test on a two-story, fully grouted, RM wall system (Ahmadi et al. 2015b). As shown in Figure 8.14a, the specimen had an H-shaped plan, consisting of three perforated planar walls. The direction of shaking was such that one of the three planar walls, referred to as the web wall, was subjected to in-plane loads, while the other two walls, referred to as the flange walls, were subjected to out-of-plane loads. The elevations of the web wall and flange walls are presented in Figures 8.14b and 8.14c, respectively. The masonry prism compressive strength was 15.6 MPa (2.26 ksi) for the bottom story and 11.2 MPa (1.62 ksi) for the second story, while the yield strength of the steel reinforcement was 448 MPa (65 ksi). The reinforcing steel layout of the walls is presented in Figure 8.15. The specimen floor slabs consisted of precast hollow planks with a 3-inch thick, cast-in-place concrete topping.

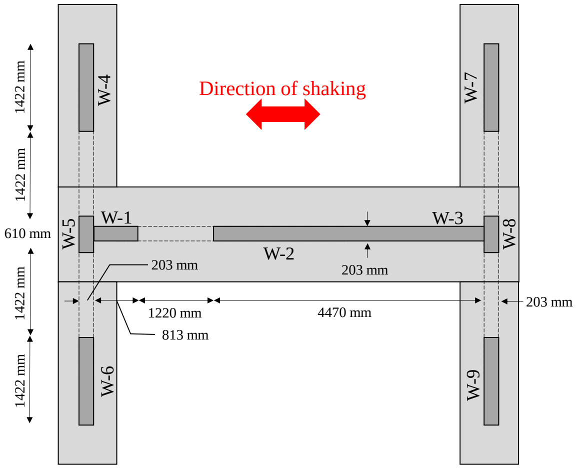

(a) Plan view

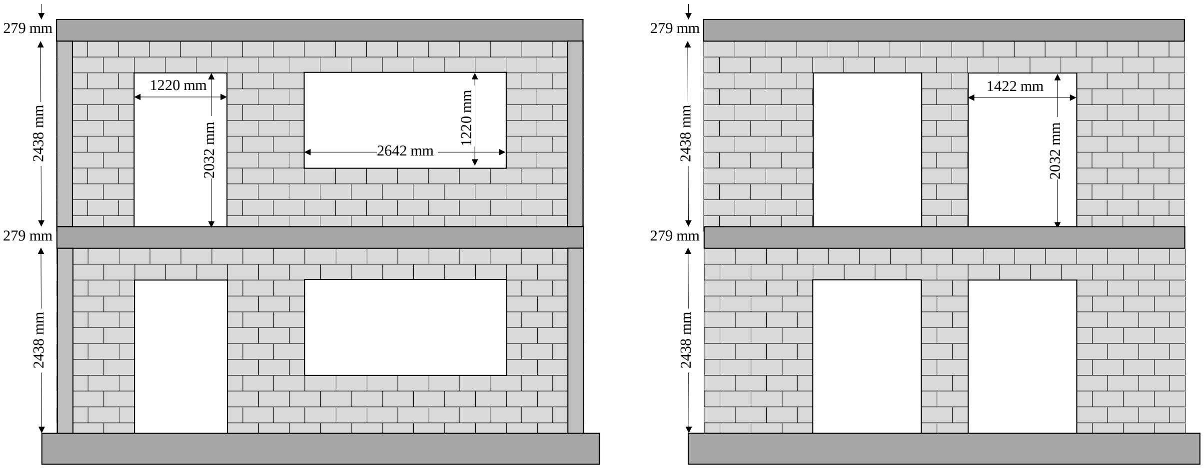

(b) Web wall elevation

(c) Flange wall elevation

Figure 8.14: Configuration of two-story shake-table specimen tested by Ahmadi et al. (2015b).

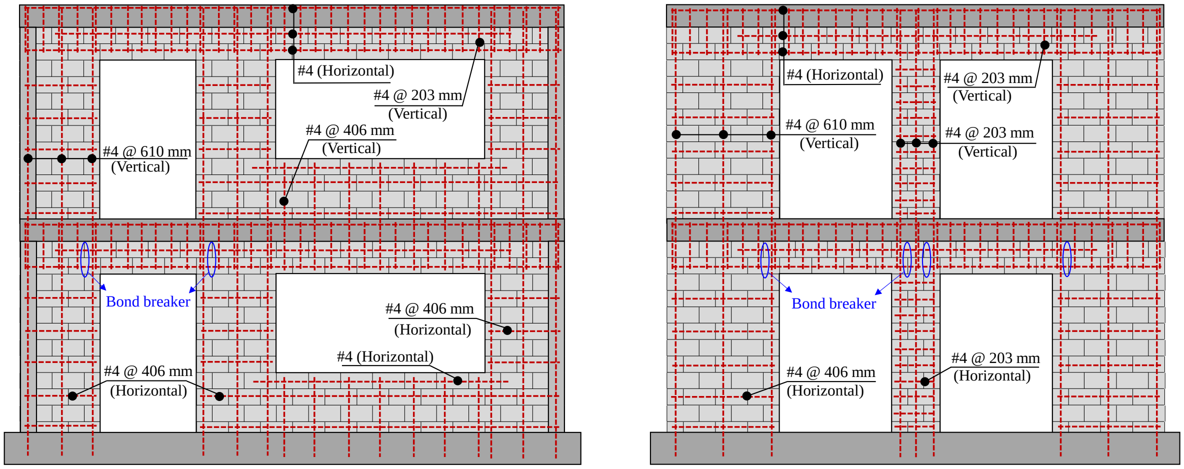

(b) Web wall

(c) Flange walls

Figure 8.15: Reinforcement details of two-story shake-table specimen tested by Ahmadi et al. (2015b).

The structure was subjected to a sequence of three ground motions with increasing intensity, until severe diagonal cracking was obtained at the bottom story of the web wall. The applied ground motions were scaled versions of the El Centro record from the 1979 Imperial Valley earthquake.

A two-dimensional truss model is created for the web wall of the specimen, as shown in Figure 8.16. The truss model includes three piers, which are termed W-1, 2 and 3 as shown in the Figure. The contribution of the flange walls W4, W6, W7 and W9 to the resistance is accounted for by truss assemblages superimposed at the left and right ends of the model. The model is fully restrained at the base, and rigid beam elements are used at the floor levels to enforce the constraint introduced by the floor slabs. The use of rigid beam elements is deemed valid, considering the fact that the entire floor slab width in each story was effective in restraining the flexural deformation of the walls.

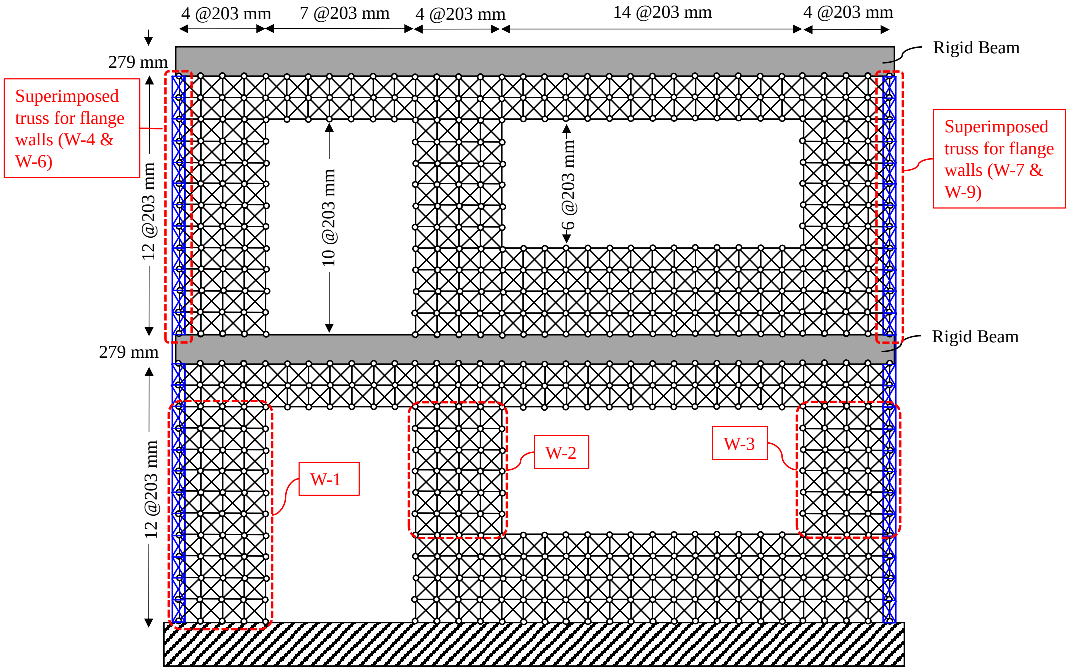

Figure 8.16: Truss model of two-story shake-table specimen tested by Ahmadi et al. (2015b).

The cross-sectional areas of the different types of elements in the truss model are presented in Tables 8.7 and 8.8. The sectional properties of the truss elements at the left and right end of the truss model account for the effect of the flanges W-5 and W-8 shown in Figure 8.14a. Tables 8.9 and 8.10 summarize the values of material parameters used in the analysis. A Rayleigh proportional damping matrix is used, with a damping ratio of 0.5% prescribed for the first and second modes of vibration. The stiffness-proportional part of the damping matrix is based on the initial stiffness matrix of the structure. The response of the structure is examined for the last three motions of the test sequence, which led to the gradual development of shear cracking in walls W-2 and W-3 of the bottom story.

Table 8.7: Cross-sectional areas of masonry truss elements used to model two-story RM wall

	$A_{m,v1}$ (mm^2)	$A_{m,v2}$ (mm^2)	$A_{m,v3}$ (mm^2)	$A_{m,h1}$ (mm^2)	$A_{m,h}$ (mm^2)	$A_{m,h3}$ (mm^2)	$A_{m,d1}$ (mm^2)	$A_{m,d}$ (mm^2)	$A_{m,d3}$ (mm^2)
W-1	123871	41290	41290	123871	41290	41290	87097	29032	29032
W-2	41290	41290	41290	41290	41290	41290	29032	29032	29032
W-3	41290	41290	192	41290	41290	192	29032	29032	87097
Masonry below the windows	41290	41290	123871	123871	41290	123871	87097	29032	87097
Masonry above the openings	123871	41290	123871	123871	41290	123871	87097	29032	87097
Flanges	n.a.	289031	n.a.	n.a.	578063	n.a.	n.a.	258064	n.a.

Note: $A_{m,v1}$ & $A_{m,v3}$: area of the left and right outermost vertical masonry elements, respectively; $A_{m,v2}$: area of the intermediate vertical masonry elements; $A_{m,h1}$ & $A_{m,\,h3}$: area of horizontal masonry elements for flanges W-5 and W-8, respectively; $A_{m,h}$: Area of the horizontal masonry elements; $A_{m,d1}$ & $A_{m,\,d3}$: area of diagonal masonry elements for flanges W-5 and W-8, respectively; $A_{m,d}$: area of the diagonal masonry elements

Table 8.8: Cross-sectional areas of steel truss elements used to model two-story RM wall

	$A_{s,v1}$ (mm^2)	$A_{s,v2}$ (mm^2)	$A_{s,v3}$ (mm^2)	A_{sh} (mm^2)
W-1	193.5	64.5	129.0	58.0
W-2	129.0	419	129.0	58.0
W-3	129.0	64.5	193.5	58.0
Wall below the windows	129.0	71.0	193.5	77.4
Wall above the openings	387.0	129	387.0	129
Flanges	n.a.	387	n.a.	n.a.

Note: $A_{s,v1}$ & $A_{s,v3}$: area of the left and right outermost vertical steel elements, respectively; $A_{s,v2}$: area of the intermediate vertical steel elements; $A_{s,h}$: area of the horizontal steel elements.

Table 8.9: Masonry material parameters used in truss model of two-story RM wall

	Element Type	f_m (MPa)	E_m (MPa)	f_t (MPa)	ε_{mres}	ε_{mint}	f_{mint} (MPa)	ε_{tres}	ε_{tint}	f_{tint} (MPa)
1st Story	Vertical	-15.6	7653	1.24	-0.0124	-0.0073	-7.80	0.0010	0.0006	0.27
	Horizontal				-0.0124	-0.0073	-7.80	0.0105	0.0012	1.83
	Diagonal				-0.0088	-0.0056	-7.86	n.a.	n.a.	n.a.
2nd Story	Vertical	-11.2	7550	0.89	-0.0108	-0.0063	-5.60	0.0007	0.0004	0.20
	Horizontal				-0.0108	-0.0063	-5.60	0.0110	0.0012	1.55
	Diagonal				-0.0077	-0.0048	-5.65	n.a.	n.a.	n.a.

Note 1: ε_0 = 0.0023 and ε_u = 0.004 were assumed for the first story (for a reference length of 600mm)

Note 2: ε_0 = 0.0018 and ε_u = 0.004 were assumed for the second story (for a reference length of 600mm)

Table 8.10: Reinforcing steel material parameters used in truss model of shake-table specimen

Element Type	f_y (MPa)	E_s (MPa)	β_h
Vertical Horizontal	448	197200	0.02

The analytically obtained drift time histories of the bottom story for the last three motions of the test sequence are compared to the experimentally recorded histories in Figure 8.17. The scaling applied to the amplitude of the El Centro motion during these tests was 108%, 145% and 160%, respectively. The analytical results closely match the experimental observations for the first two motions. The agreement for the last motion is very good up to the point where the maximum drift is attained at the bottom story. After this point, the analysis underestimates the drift values. It is improbable that the experimentally recorded response during the last stage of 160% El Centro can be well captured even by more refined models.

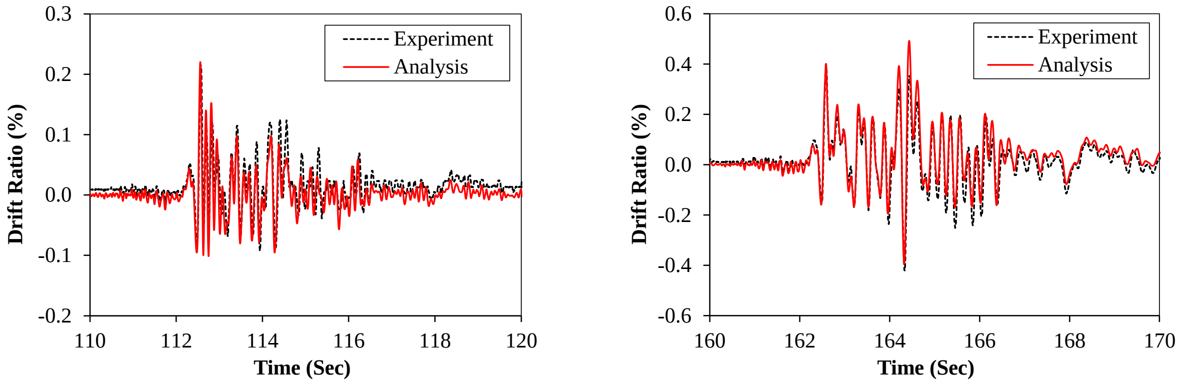

(a) 108% El Centro

(b) 145% El Centro

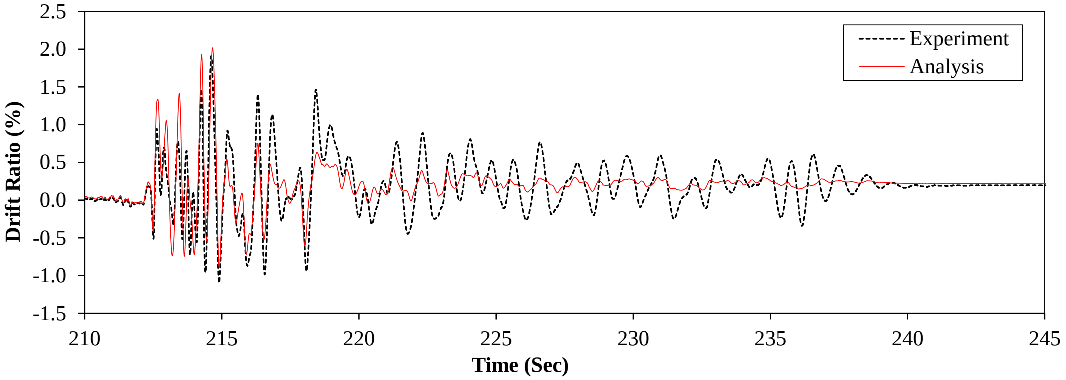

(c) 160% El Centro

Figure 8.17: Comparison of analytically obtained and experimentally recorded bottom story drift history for two-story shake-table specimen.

The analytically obtained hysteretic response of the bottom story for 145% El Centro and 160% El Centro is compared to its experimental counterparts in Figure 8.18. The analysis satisfactorily captures the stiffness and strength degradation as well as the hysteretic energy dissipation of the wall. Additionally, the damage pattern of the structure is well captured by the analysis, as shown in Figure 8.19. The strength degradation in both the experiment and the analysis is caused by severe shear cracking in wall piers W-2 and W-3, as shown in 8.20a and 8.20b. It is worth mentioning that a three-dimensional finite element model in Ahmadi et al. (2015b) could not capture the strength degradation during the 160% El Centro test and significantly underestimated the drift values for this test.

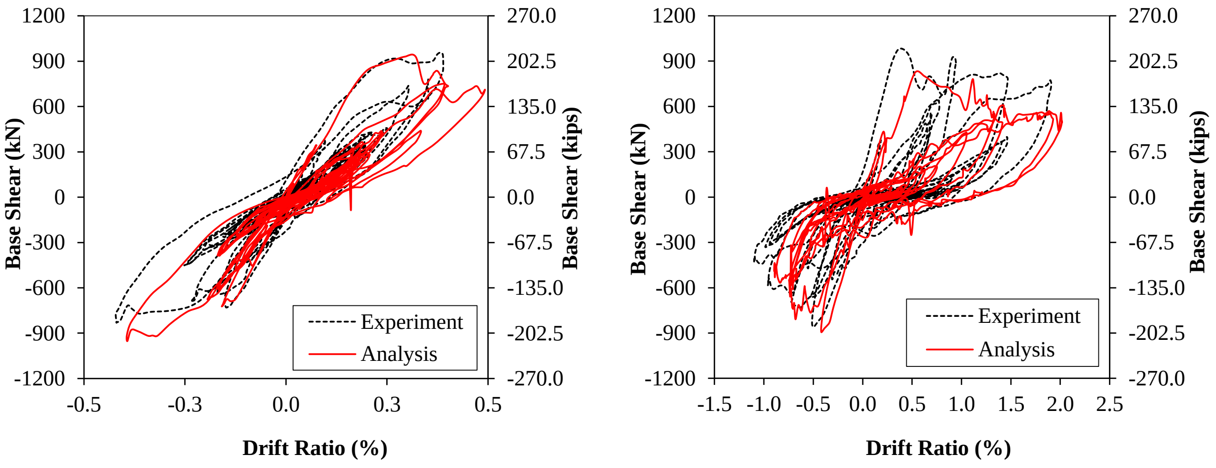

(a) 145% El Centro earthquake

(b) 160% El Centro earthquake

Figure 8.18: Comparison of analytically obtained and experimentally recorded force-displacement response for two-story shake-table specimen.

(a) Crack patterns at the end of the experiment

b) Deformed shape for drift ratio of 1.33% during the El Centro 160% test

Figure 8.19: Comparison of analytical and experimental damage patterns for two-story wall (deformations in analytical model have been magnified by a factor of 20).

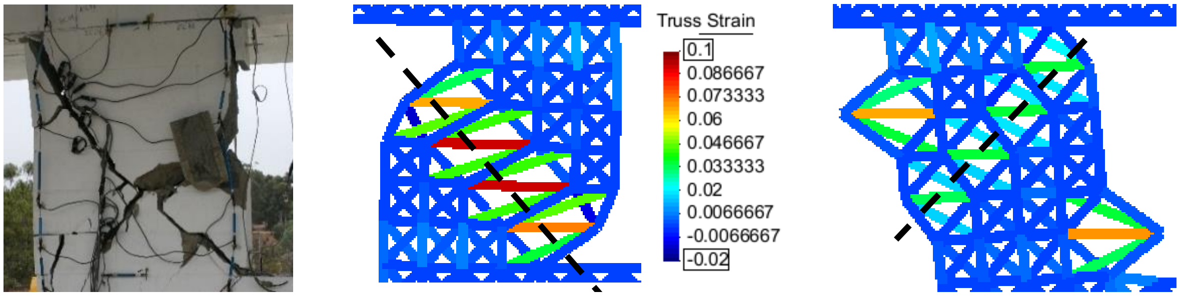

Experiment Analysis, positive drift Analysis, negative drift

(a) Damage in W-2 (middle pier)

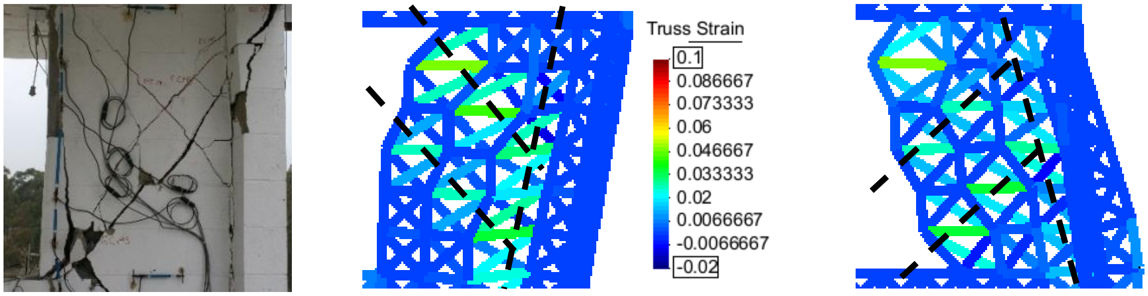

Experiment Analysis, positive drift Analysis, negative drift

(b) Damage in W-3

Figure 8.20: Experimentally observed and analytically obtained damage at the bottom story of the shake-table specimen.

To determine the significance of the aggregate interlock effect in the model of the two-story wall specimen, the analysis is repeated without including the aggregate interlock effect. The analytically obtained hysteretic response of the model without aggregate interlock for the 108% El Centro motion is compared with the corresponding experimental data in Figure 8.21a. The absence of the aggregate interlock from the model leads to significant underestimation of the resistance of the structure, which in turn leads to premature severe damage in the analysis (Figure 8.21b) and overestimation of the obtained drift values. As described in Section 7.3.2, the lack of a continuous diagonal strut along the height of the wall piers prevents the analytical model from properly accounting for the masonry contribution to the shear strength.

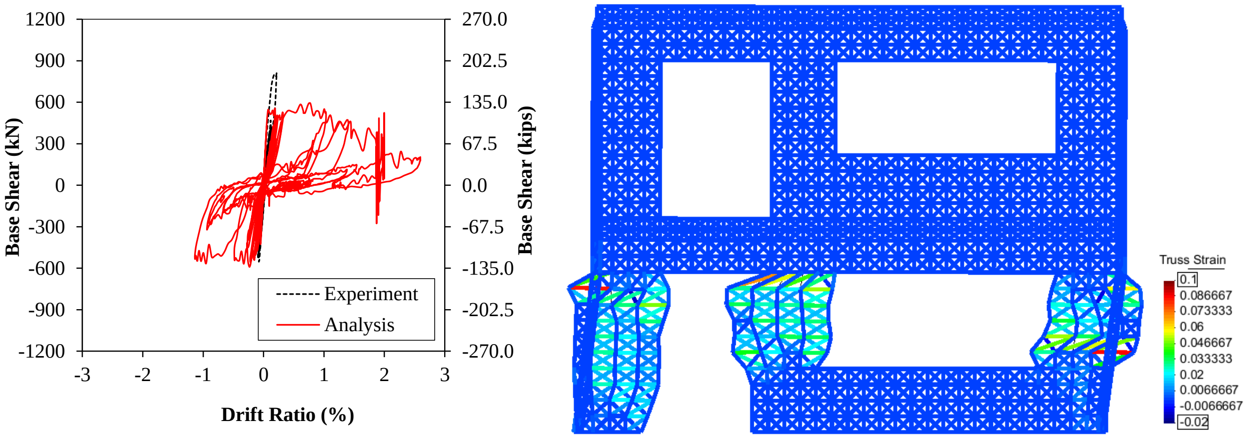

(a) Base shear versus drift ratio

(b) Damage pattern after motion

Figure 8.21: Comparison of analytically obtained response without aggregate interlock and experimentally recorded response for two-story RM wall during the 108% El Centro motion.

As mentioned in Section 7.3.2, the aggregate interlock resistance obtained in accordance with Walraven (1980) depends on the maximum aggregate size, D_{max}, and a value of D_{max} = 10 mm is assumed as representative of masonry. To examine the validity of this assumption and the sensitivity of the analysis results on the aggregate size, the dynamic analysis for the shake table specimen is also conducted for D_{max} = 24 mm and D_{max} = 5 mm. The value of D_{max} = 24 mm is the average value of aggregate size for the concrete specimens by Walraven (1980) which led to the formulation of Equation (7.10). For D_{max} = 5 mm, the analysis underestimates the resistance of the structure, leading to premature strength degradation during the 108% El Centro, as shown in Figure 8.22a. On the other hand, a value of D_{max} = 24 mm leads to an overestimation of the shear resistance of the wall piers, which delays the occurrence of severe shear cracking and leads to an underestimation of drift values, as deduced from Figures 8.22b and 8.22c which present results for the 145% El Centro and 160% El Centro, respectively.

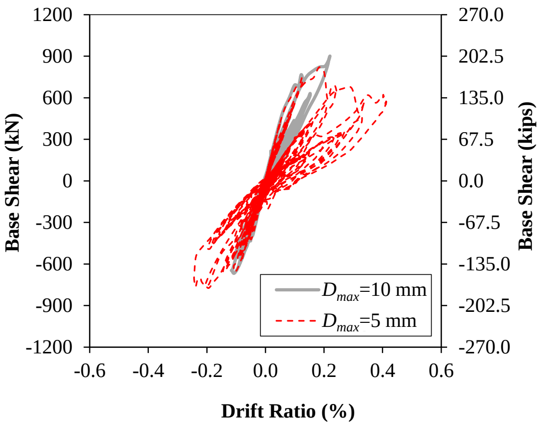

(a) 108% El Centro

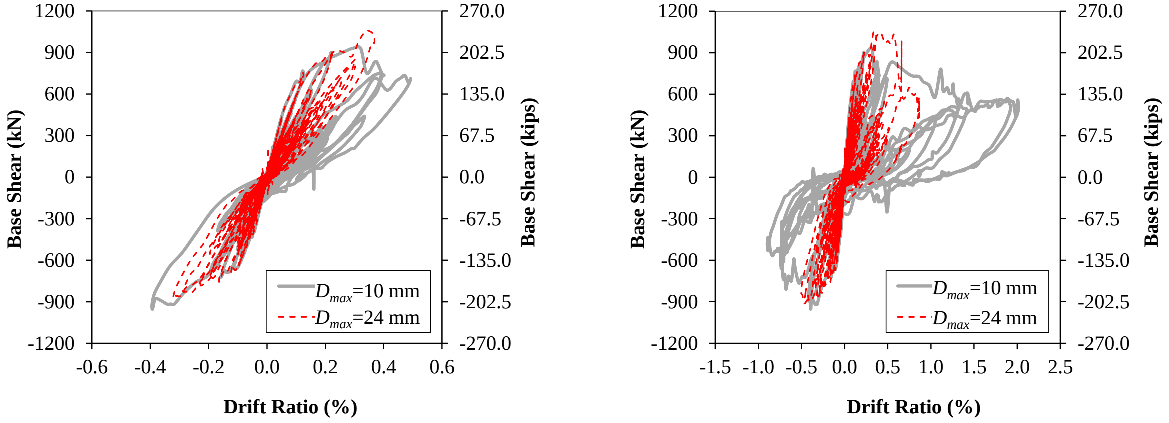

(b) 145% El Centro

(c) 160% El Centro

Figure 8.22: Effect of assumed maximum aggregate size on the hysteretic response of two-story shake-table specimen.

Chapter 9 : Concluding Remarks and Recommendations

The present study has been focused on developing simulation tools for the analysis of damage and failure of reinforced concrete (RC) and reinforced masonry (RM) structures under cyclic loads such as those caused by earthquakes. Two methods with different levels of sophistication have been used, namely, three-dimensional finite element (FE) models and nonlinear truss models. Other existing methods have been overviewed in the literature review section and the limitations of each method have been discussed.

A novel constitutive model has been formulated for concrete to allow the simulation of RC structures subjected to cyclic loading. The specific formulation resolves issues associated with the description of cyclic crack opening/closing behavior that exist in many available material models. The model combines an elastoplastic formulation to describe the behavior under compressive stress states and a rotating smeared-crack model to capture the effect of tensile cracking. The stress update algorithm has been established to satisfy the compatibility between the elastoplastic and the cracking parts of the model. Validation analyses have demonstrated the capability of the material model to capture the hysteretic response of RC components subjected to cyclic loading. Parametric analyses have been performed to verify the objectivity of the model with respect to mesh size effect and the need to account for the confinement effect on the ductility of the material. Issues associated with the overestimation of the lateral strength related to the use of another yield surface have been identified and a potential remedy to these issues has been proposed. The accuracy and robustness of the proposed model render it suitable for the systematic performance assessment of reinforced concrete structures.

The developed constitutive model for concrete has been combined with a recently developed uniaxial material law for reinforcing steel that can capture rebar rupture due to low-cycle fatigue. Consequently, a three-dimensional, continuum-based, finite element analysis framework has been developed for the simulation of reinforced concrete structures subjected to lateral cyclic loads. The modeling scheme has been validated with experimental tests for flexure-dominated components including two post-tensioned wall specimens, a U-shaped shear wall, and a bridge pier. The proposed method has been found capable of reproducing the global response and damage accumulation for the experimentally tested components. The salient phenomena associated with damage, such as rebar buckling and rupture and concrete cover spalling have been satisfactorily captured. Further analyses have been performed for two single-story walls and a five-story wall system to validate the capability of the modeling scheme to capture severe strength and stiffness degradation due to shear damage. Additional parametric studies have shown that viscous damping has a significant effect on the response before the development of inelastic deformations and that the strain penetration effect is not significant for RC walls.

Although collapse did not occur in the experimental tests considered, the capability of the modeling scheme to capture full collapse, without failure in the stress update process of the material laws or in the global solution scheme, has been demonstrated. The study has also shown the sensitivity of the results of analysis of shear-dominated members to the value of tensile fracture energy. A preliminary verification of the capability of the meshless, Smoothed Particle

Hydrodynamics (SPH) method to capture the response of shear-dominated RC members, has been conducted. Given that the SPH method does not enforce continuity of the displacement field in a solution, it can be an efficient means to avoid inaccuracies due to stress lock-in, without a need to resort to complicated formulations such as discrete-cohesive crack models.

Furthermore, the nonlinear truss analogy has been used for the analysis of shear-dominated RC columns and fully-grouted, RM wall structures subjected to cyclic lateral loading. A previously established analysis methodology has been enhanced to account for the contribution of the aggregate interlock effect to the shear resistance of structures. While this contribution is shown to be minor for squat, single-story walls, it must be accounted for in truss models of more slender walls and columns, i.e. for cases where a continuous diagonal strut from the top corner to the opposite bottom corner of the member cannot be developed. A simple equation has been proposed for the determination of the inclination angle of the diagonal members in the truss models of columns. The analysis method has been validated using the results of quasi-static and dynamic tests on RC columns and RM walls. The conceptual simplicity and good predictive capabilities establish nonlinear truss models as an attractive analytical tool for the systematic analysis of shear-dominated RC and RM structures.

9.1 Major contributions

The major contributions of the present study are the following.

- Develop a novel triaxial constitutive model for concrete material subjected to cyclic loading.
- Establish a robust and numerically efficient stress-update algorithm to satisfy the consistency condition between cracking and elastoplastic material laws.

- Validate the concrete material model for different loading scenarios.
- Validate the capability of the material model to capture the response of RC components, including columns and beam-to-column joint.
- Develop an accurate and robust analytical scheme to capture failure of RC and RM structures subjected to extreme loading.
- Accounting for the loss of cover concrete and rebar rupture with element removal techniques.
- Using continuum-based beam elements to account for rebar buckling.
- Capture the damage pattern of flexure- and shear-dominated components.
- Demonstrate the capability of the modeling scheme to capture full collapse, without failure in the stress update algorithm.
- Provide a comparative assessment of implicit and explicit global solution methods.
- Examine the possibility of using meshless methods in the analysis of shear-dominated structures.
- Validate the applicability of the nonlinear truss analogy to the analysis of shear-dominated RC columns and frames.
- Use nonlinear truss models in the analysis of shear-dominated, fully grouted, RM structural walls and systems.
- Establish a simple method to define the geometry of truss models uniquely.
- Propose a simple equation for finding the inclination angle of diagonal truss elements.
- Modify the constitutive law of horizontal concrete elements of truss models to account for the effect of aggregate interlock.

9.2 Recommendations for future research

In this study, analyses were conducted using the continuum-based three-dimensional finite element models. The proposed refined FE models can be used to calibrate simplified analysis methods, and to quantify the impact of inaccuracies associated with existing simulation tools, such as beam-based models, on the performance metrics of RC and RM structures.

The proposed constitutive model for concrete was formulated for solid elements and/or plane-strain shell elements, while development of plane-stress formulation can be also pursued.

The material model does not include the long-term effects, e.g. creep and shrinkage. Additionally, the constitutive model is rate-independent, and therefore, is not suitable for impact simulation. These features can be added by future research to the material model described herein.

The constitutive models of concrete and reinforcing steel can be enhanced to allow multi-physics simulations (e.g., moisture transport, carbonation, chloride transport and corrosion of reinforcement).

The proposed analytical framework used a simple elastoplastic constitutive law to express the effect of strain penetration. More refined bond-slip laws are necessary for simulations of components such as beam-to-column joints.

Calibration of the steel material parameters, such as the value of critical damage parameter, requires experimental testing. At present, there are few experimental studies to characterize the low-cycle fatigue and fracture behavior of reinforcing steel. Thus, experimental tests are necessary to provide data for the calibration of the low-cycle fatigue criterion in the constitutive model for steel and to further validate the capability of the three-dimensional finite element analysis scheme to capture inelastic rebar buckling.

Given the capabilities for parallel computation which are available in research institutions, the modeling scheme described herein can be used in the future for the simulation of full-scale, multi-story, three-dimensional prototype structures under earthquake loading. Such simulations will elucidate system effects which are not present in experimental tests of structural components. Such effects include the effect of diaphragm action and the flexural coupling action of beams or floor slabs connecting parts of the lateral load-resisting system.

The nonlinear truss analogy has been shown to be capable of capturing the response of shear-dominated walls, including a two-story RM wall system. Given the conceptual simplicity and algorithmic efficiency of the method, it can be used by future research for the quantitative performance assessment of prototype RM wall systems whose response may be affected by shear failures.

References

ACI (2011). *Building Code Requirements for Masonry Structures*, ACI 530-11/ASCE 5-11/TMS 402-11, Masonry Standards Joint Committee of the American Concrete Institute, Farmington Hills, Michigan; Structural Engineering Institute of the American Society of Civil Engineers, Reston, Virginia; and The Masonry Society, Boulder, Colorado.

ACI (2014), *Building Code Requirements for Structural* Concrete, ACI 318-14, American Concrete Institute, Farmington Hills, Michigan.

Ahmadi, F., Mavros, M., Klingner, R. E., Shing, P. B., and McLean, D. (2015a). "Displacement-based seismic design for reinforced masonry shear-wall structures, part 1: Background and trial application." *Earthquake Spectra*, 31(2), 969-998.

Ahmadi, F., Mavros, M., Klingner, R. E., Shing, P. B., and McLean, D. (2015b). "Displacement-based seismic design for reinforced masonry shear-wall structures, part 2: Validation with shake-table tests." *Earthquake Spectra*, 31(2), 999-1019.

Anderson, M., Lehman, D., and Stanton, J. (2008). "A cyclic shear stress–strain model for joints without transverse reinforcement." *Engineering Structures*, 30(4), 941-954.

Ang, B. G. (1981). *Ductility of reinforced concrete bridge piers under seismic loading*. University of Canterbury, Christchurch, New Zealand.

ASCE (2010). *Minimum Design Loads for Buildings and Other Structures*, ASCE/SEI 7-10, American Society of Civil Engineers, Reston, Virginia.

ASCE-ACI committee 445 on shear and torsion. (1998). “Recent approaches to shear design of structural concrete.” *Journal of Structural Engineering*, 124, 1375-1417.

Bao, Y., Lew, H. S., and Kunnath, S. K. (2012). “Modeling of reinforced concrete assemblies under column-removal scenario.” *Journal of Structural Engineering*, 140(1), 04013026:1-13.

Bao, Y., Kunnath, S. K., El-Tawil, S., and Lew, H. S. (2008). “Macromodel-based simulation of progressive collapse: RC frame structures.” *Journal of Structural Engineering*, 134(7), 1079-1091.

Barth, K. E., and Wu, H. (2006). “Efficient nonlinear finite element modeling of slab on steel stringer bridges.” *Finite elements in analysis and design*, 42(14), 1304-1313.

Bažant, Z. P. (2002). “Concrete fracture models: testing and practice.” *Engineering Fracture Mechanics*, 69(2), 165-205.

Bažant, Z. P., Caner, F. C., Carol, I., Adley, M. D., and Akers, S. A. (2000). “Microplane model M4 for concrete. I: Formulation with work-conjugate deviatoric stress.” *Journal of Engineering Mechanics*, 126(9), 944-953.

Bažant, Z. P., and Gambarova, P. G. (1984). “Crack shear in concrete: Crack band microplane model.” *Journal of Structural Engineering*, 110(9), 2015-2035.

Bažant, Z. P., and Lin, F. B. (1988). “Nonlocal smeared cracking model for concrete fracture.” *Journal of Structural Engineering*, 114(11), 2493–2510.

Bažant, Z. P., and Oh, B. H. (1983). “Crack band theory for fracture of concrete.” *Matériaux et construction*, 16(3), 155-177.

Bažant, Z. P., and Oh, B. H. (1984). “Rock fracture via strain-softening finite elements.” *Journal of engineering mechanics*, 110(7), 1015-1035.

Bažant, Z. P., and Planas, J. (1998). *Fracture and size effect in concrete and other quasibrittle materials*, CRC Press, Boca Ratton, FL.

Beckingsale, C. W. (1980). *Post elastic behavior of reinforced concrete beam-column joints*. University of Canterbury, Christchurch, New Zealand.

Belytschko, T., and Bindeman, L. P. (1993). "Assumed strain stabilization of the eight node hexahedral element." *Computer Methods in Applied Mechanics and Engineering*, 105(2), 225-260.

Beres, A., White, R.N., and Gergely, P. (1992), "Seismic behavior of reinforced concrete frame structures with nonductile details: Part I - summary of experimental findings of full scale beam-column joint tests," *Report NCEER-92-0024,* National Center for Earthquake Engineering Research, State University of New York at Buffalo, Buffalo, NY.

Beyer, K., Dazio, A., and Priestley, M. J. N. (2008). "Quasi-static cyclic tests of two U-shaped reinforced concrete walls." *Journal of earthquake engineering*, 12(7), 1023-1053.

Brancaleoni, F., Ciampi, V., and Di Antonio, R. (1983). "Rate-Type models for nonlinear hysteretic structural behavior." *In EUROMECH colloquium*, Palermo, Italy.

Caliò, I., Marletta, M., and Pantò, B. (2012). "A new discrete element model for the evaluation of the seismic behavior of unreinforced masonry buildings." *Engineering Structures*, 40, 327-338.

Caner, F. C., and Bažant, Z. P. (2012a). "Microplane model M7 for plain concrete. I: Formulation." *Journal of Engineering Mechanics*, 139(12), 1714-1723.

Caner, F. C., and Bažant, Z. P. (2012b). "Microplane model M7 for plain concrete. II: Calibration and verification." *Journal of Engineering Mechanics,* 139(12), 1724-1735.

Červenka, J., and Papanikolaou, V. (2008). "Three dimensional combined fracture–plastic material model for concrete." *International Journal of Plasticity*, 24, 2192-2220.

Červenka Counsulting *s.r.o* (2016) *ATENA Program Documentation*, Prague, Czech Republic.

Chandrasekaran, S., Nunziante, L., Serino, G., and Carannante, F. (2011). “Curvature ductility of RC sections based on Eurocode: Analytical procedure.” *KSCE Journal of Civil Engineering*, 15(1), 131-144.

Chen, Q., and Qian, J. (2002). “Static inelastic analysis of RC shear walls.” *Earthquake Engineering and Engineering Vibration*, 1(1), 94-99.

Chung, W., and Sotelino, E. D. (2006). “Three-dimensional finite element modeling of composite girder bridges.” *Engineering Structures*, 28(1), 63-71.

Clough, R., Benuska, K., and Wilson, E. (1965). “Inelastic earthquake response of tall buildings.” *In Proceedings of Third World Conference on Earthquake Engineering*, New Zealand.

Coelho E., Fischinger M., Campos Costa A., Falcao Silva M. J., Kante, P. (2006). “Shaking table tests on think lightly reinforced H-shaped structural wall.” *In Proceedings of First European Conference on Earthquake Engineering and Seismology*, Geneva, Switzerland.

Crawford, J. E., Wu, Y., Choi, H-J., Magallanes, J. M., Lan, S. (2012). “Use and validation of the release III K&C concrete material model in LS-DYNA.” *Report No. TR-11-36.5*, Karagozian and Case, Glendale, CA.

CSC (2009). *ANSYS User’s Manuals*, Computer Software Corporation, Canonsburg, PA, USA.

CSC (2009). *ANSYS AUTODYN User’s Manuals*, Computer Software Corporation, Canonsburg, PA, USA.

CSI (2006a). *Perform-Collapse User’s Manuals*, Computer and Structures Incorporation, Berkeley, CA, USA.

CSI (2006b). *Perform-3D User’s Manuals*, Computer and Structures Incorporation, Berkeley, CA, USA.

CSI (2000). *SAP2000 User’s Manuals*, Computer and Structures Incorporation, Berkeley, CA, USA.

Das, R., and Cleary, P.W. (2013), “A mesh-free approach for fracture modeling of gravity dams under earthquake.” *International Journal of Fracture*, 179(1-2), 9-33.

Deaton, J. (2013). *Nonlinear finite element analysis of reinforced concrete exterior beam-column joints with non-seismic detailing*. Ph.D. Dissertation, Georgia Institute of Technology, Atlanta, GA.

De Borst, R., and Nauta, P. (1985), "Non-orthogonal cracks in a smeared finite element model." *Engineering Computations* 2(1), 35-46.

Dodd, L. L., and Restrepo-Posada, J. I. (1995). "Model for predicting cyclic behavior of reinforcing steel." *Journal of Structural Engineering*, 121(3), 433-445.

Drysdale, R. G., Hamid, A. A., and Baker, L. R. (1994). *Masonry structures: behavior and design*. 2nd Edition, The Masonry Society.

Eligehausen, R., Ožbolt, J., Genesio, G., Hoehler, M. S., and Pampanin, S. (2006). "Three-dimensional modelling of poorly detailed RC frame joints". *NZSEE Conference*, 23.

Elwood, K., and Moehle, J. (2003). "Shake table tests and analytical studies on the gravity load collapse of reinforced concrete frames." *PEER Report No. 2003/01*, Berkeley, CA.

Elwood, K.J. (2004). "Modelling failures in existing reinforced concrete columns." *Canadian Journal of Civil Engineering*, 31(5), 846–859.

Elwood, K., and Moehle, J. (2005a). "Drift capacity of reinforced concrete columns with light transverse reinforcement." *Earthquake Spectra*, 21(1), 71-89.

Elwood, K., and Moehle, J. (2005b). "Axial capacity model for shear-damaged columns." *ACI Structural Journal*, 102(4), 578-587.

Elwood, K., and Moehle, J. (2008). "Dynamic collapse analysis for a reinforced concrete frame sustaining shear and axial failures." *Earthquake Engineering and Structural Dynamics*, 37(7), 991-1012.

Etse, G., and Willam, K. (1994). "Fracture energy formulation for inelastic behavior of plain concrete." *Journal of Engineering Mechanics*, 120(9), 1983-2011.

Faria, R., Oliver, J., and Cervera, M. (1998). “A strain-based plastic viscous-damage model for massive concrete structures.” *International Journal of Solids and Structures*, 35(14), 1533-1558.

Faria, R., Oliver, J., and Cervera, M. (2004). “Modeling material failure in concrete structures under cyclic actions.” *Journal of Structural Engineering*, 130(12), 1997-2005.

Taylor, R. L. (2013). *FEAP User’s Manual, A Nonlinear Finite Element Analysis Program*, University of California, Berkley, CA, USA.

Filippou, F., Popov, E., and Bertero, V. (1983). “Effects of bond deterioration on hysteretic behavior of reinforced concrete joints.” *Report No. UCB/EERC-83/19*, Berkeley, CA.

Flanagan, D. P., and Belytschko, T. (1981). “A uniform strain hexahedron and quadrilateral with orthogonal hourglass control.” *International Journal for Numerical Methods in Engineering*, 17(5), 679-706.

Gangi, M. J. (2015). “Analytical Modeling of the Repair Impact-Damaged Prestressed Concrete Bridge Girders.” Master Thesis, Virginia Tech.

Gere, J., and Timoshenko, S. (1997). *Mechanics of materials*. 4th Edition, PWS Publishing, Boston, MA.

Ghobarah, A., and Youssef, M. (1999). “Modelling of reinforced concrete structural walls.” *Engineering Structures*, 21(10), 912-923.

Giberson, M. F. (1967). *The response of nonlinear multi-story structures subjected to earthquake excitation.* Ph.D. Dissertation, California Institute of Technology.

Gill, W. D. (1979). *Ductility of rectangular reinforced concrete columns with axial load*. University of Canterbury, Christchurch, New Zealand.

Gopalaratnam, V. S., and Shah, S. P. (1985). “Softening response of plain concrete in direct tension.” *ACI Journal proceedings*, 82(3), 310-323.

Grassl, P., and Jirásek, M. (2006a). “Damage-plastic model for concrete failure.” *International Journal of Solids and Structures*, 43(22), 7166-7196.

Grassl, P., and Jirasek, M. (2006b). “Plastic model with non-local damage applied to concrete.” *International Journal for Numerical and Analytical Methods in Geomechanics,* 30(1), 71-90.

GSA, U. (2000). *Progressive collapse analysis and design guidelines for new federal office buildings and major modernization projects*. Washington, DC.

Gu, X., Wang, X., Yin, X., Lin, F., and Hou, J. (2014). “Collapse simulation of reinforced concrete moment frames considering impact actions among blocks.” *Engineering Structures,* 65, 30-41.

Guedes, J., Pegon, P., and Pinto, A. (1994). “A fibre/Timoshenko beam element in CASTEM 2000.” *JRC-Special Publication No. I 94.31*, Ispra, Italy.

Hallquist, J. (2007). *LS-DYNA keyword user’s manual,* Livermore Software Technology Corporation, Livermore, CA.

Haselton, C.B., and Deierlein, G.G., (2007). “Assessing seismic collapse safety of modern reinforced concrete frame buildings.” *John A. Blume Earthquake Engineering Center Technical Report No. 156,* Stanford University, Stanford, California.

Hawileh, R. A., Rahman, A., and Tabatabai, H. (2010). “Nonlinear finite element analysis and modeling of a precast hybrid beam–column connection subjected to cyclic loads.” *Applied Mathematical Modelling*, 34(9), 2562-2583.

Hiraishi, H. (1984). “Evaluation of shear and flexural deformations of flexural type shear walls.” *In Proceeding of 8th WCEE*, 5.

Hoffmann, G.W., Kunnath, S.K., Reinhorn, A.M., and Mander, J.B. (1992), “Gravity-load-designed reinforced concrete buildings: Seismic evaluation of existing construction and detailing strategies for improved seismic resistance,” *Report NCEER-92-0016,* National Center for Earthquake Engineering Research, State University of New York at Buffalo, Buffalo, NY.

Hrennikoff, A. (1941). “Solution of Problems of Elasticity by the Framework Method.” *Journal of Applied Mechanics*, 8 (4), 169-175.

Hsieh, S., Ting, E., and Chen, W.F. (1982), “A plastic fracture model for concrete.” *International Journal of Solids and Structures*, 18(3), 181-197.

Hsu, T. T. (1996). “Toward a unified nomenclature for reinforced-concrete theory.” *Journal of Structural Engineering*, 122(3), 275-283.

Hughes, T. J., and Liu, W. K. (1981a). “Nonlinear finite element analysis of shells: Part I. Three-dimensional shells.” *Computer Methods in Applied Mechanics and Engineering*, 26(3), 331-362.

Hughes, T. J., and Liu, W. K. (1981b). “Nonlinear finite element analysis of shells-part II. Two-dimensional shells.” *Computer Methods in Applied Mechanics and Engineering*, 27(2), 167-181.

Ibarra, L.F., Medina, R.A., and Krawinkler, H., (2005). “Hysteretic models that incorporate strength and stiffness deterioration.” *International Journal for Earthquake Engineering and Structural Dynamics*, 34(12), 1489-1511.

Imran, I., and Pantazopoulou, S. J. (2001). “Plasticity model for concrete under triaxial compression.” *Journal of Engineering Mechanics*, 127(3), 281-290.

Inel, M., and Ozmen, H. B. (2006). “Effects of plastic hinge properties in nonlinear analysis of reinforced concrete buildings.” *Engineering Structures*, 28(11), 1494-1502.

Iribarren, B. S., Berke, P., Bouillard, P., Vantomme, J., Massart, T. (2011). “Investigation of the influence of design and material parameters in the progressive collapse analysis of RC structures. Engineering Structures.” *Engineering Structures*, 33, 2805-2820.

Jiang, J. J., Lu, X. Z., and Ye, L. P. (2005). *Finite element analysis of concrete structures*. Tsinghua University Press, Beijing, China.

Kaba, S. A., and Mahin, S. A. (1984). “Refined modeling of reinforced concrete columns of seismic analysis.” *Earthquake Engineering Research Inst*., Berkeley, *NASA STI/Recon Technical Report N 03/1984; 85:13089*.

Kabeyasawa, T., Shiohara, H., Otani, S., and Aoyama, H. (1983). “Analysis of the full-scale seven-story reinforced concrete test structure.” *Journal of the Faculty of Engineering*, 37(2), 431-478.

Kang, H. D., Willam, K., Shing, P. B., and Spacone, E. (2000). “Failure analysis of R/C columns using a triaxial concrete model.” *Computers and Structures*, 77(5), 423-440.

Kante P. (2005). *Potresna Ranljivost Armiranobetonskih Sten*, Ph.D. Dissertation, University of Ljubljana, Slovenia.

Karsan, I. D., and Jirsa, J. O. (1969). “Behavior of concrete under compressive loadings.” *Journal of the Structural Division*, 95(12), 2543-2564.

Kaya, M., and Arslan, A. S. (2009). “Analytical modeling of post-tensioned precast beam-to-column connections.” *Materials and Design*, 30(9), 3802-3811.

Keshavarzian, M., and Schnobrich, W. C. (1985). “Analytical models for the nonlinear seismic analysis of reinforced concrete structures.” *Engineering Structures*, 7(2), 131-142.

Kim, J. H., and Mander, J. B. (1999), “Truss modeling of reinforced concrete shear-flexure behavior,” *Report MCEER-99-0005,* Multidisciplinary Center for Earthquake Engineering Research, Buffalo, N.Y.

Kim, S. H., Koutromanos, I. (2016). “Constitutive model for reinforcing steel under cyclic loading.” *ASCE Journal of Structural Engineering*, accepted for publication.

Kim, T. H., Lee, K. M., Chung, Y. S., and Shin, H. M. (2005). “Seismic damage assessment of reinforced concrete bridge columns.” *Engineering Structures*, 27(4), 576-592.

Kokot, S., Anthoine, A., Negro, P., and Solomos, G. (2012). “Static and dynamic analysis of a reinforced concrete flat slab frame building for progressive collapse.” *Engineering Structures*, 40, 205-217.

Kotsovos, M. D., and Spiliopoulos, K. V. (1998). “Modelling of crack closure for finite-element analysis of structural concrete.” *Computers and structures*, 69(3), 383-398.

Koutromanos, I., and Shing, P. B. (2010). “Trial application: reinforced masonry shear wall structures.” *Chapter 1: In evaluation of the FEMA P-695 methodology for quantification of building seismic performance factors*. National Institute of Standards and Technology, USA.

Koutromanos, I., and Shing, P. B. (2012). “Cohesive crack model to simulate cyclic response of concrete and masonry structures.” *ACI Structural Journal*, 109(3), 349-358.

Koutromanos, I., Stavridis, A., Shing, P. B., and Willam, K. (2011). “Numerical modeling of masonry-infilled RC frames subjected to seismic loads.” *Computers and Structures,* 89(11), 1026-1037.

Kwan, W. P., and Billington, S. L. (2001). “Simulation of structural concrete under cyclic load.” *Journal of Structural Engineering*, 127(12), 1391-1401.

Kwasniewski, L. (2010). “Nonlinear dynamic simulations of progressive collapse for a multistory building.” *Engineering Structures*, 32(5), 1223-1235.

Leborgne, M. R. (2012). *Modeling the post-shear failure behavior of reinforced concrete columns*. Ph.D. Dissertation, University of Texas, Austin, TX.

Leborgne, M. R., and Ghannoum, W. M. (2013). “Analytical element for simulating lateral-strength degradation in reinforced concrete columns and other frame members.” *Journal of Structural Engineering*, 140(7), 04014038:1-12.

Lee, J., and Fenves, G.L. (1998). “Plastic-Damage model for cyclic loading of concrete structures.” *ASCE Journal of Engineering Mechanics*, 124(8), 892-900.

Lee, J., and Fenves, G. L. (2001). “A return-mapping algorithm for plastic-damage models: 3-D and plane stress formulation.” *International Journal for Numerical Methods in Engineering*, 50(2), 487-506.

Légeron, F., Paultre, P., and Mazars, J. (2005). “Damage mechanics modeling of nonlinear seismic behavior of concrete structures.” *Journal of Structural Engineering*, 131(6), 946-955.

Leibengood, L., Darwin, D., and Dodds, R. (1986). “Parameters Affecting FE Analysis of Concrete Structures.” *Journal of Structural Engineering*, 112(2), 326–341.

Leon R. S. (1983). *The influence of floor members on the behavior of reinforced beam-column joints subjected to severe cyclic loading*. Ph.D. Dissertation, University of Texas, Austin, TX.

Li, H., and Li, B. (2004). “Experimental study on seismic restoring performance of reinforced concrete shear walls.” *Journal of Building Structures*, 25(5), 35-42.

Li, S., and Liu, W. K. (2007). *Meshfree particle methods*. Springer, New York.

Li, Y.-J., and Ožbolt, J. (2002). “Three-dimensional cyclic analysis of compressive diagonal shear failure.” *ACI Special Publication SP-205*, 61-80.

Liu, G.R., and Liu, M.B. (2003), *Smoothed Particle Hydrodynamics: A Meshfree Particle Method*, World Scientific, Hong-Kong.

Lin, X., Zhang, Y. X., and Hazell, P. J. (2014). “Modelling the response of reinforced concrete panels under blast loading.” *Materials and Design*, 56, 620-628.

Linde, P. (1993). *Numerical modelling and capacity design of earthquake-resistant reinforced concrete walls*. Birkhäuser. Diss. Techn. Wiss. ETH Zürich, Nr. 10124.

Lotfi, H. R., and Shing, P. B. (1991). “An appraisal of smeared crack models for masonry shear wall analysis.” *Computers and Structures*, 41(3), 413-425.

Lotfi, H. R., and Shing, P. B. (1994). “Interface model applied to fracture of masonry structures.” *Journal of Structural Engineering*, 120(1), 63-80.

Lourenço P. B. (2002). “Computations on historic masonry structures.” *Progress in Structural Engineering and Material*, 4(3), 301–319.

Lourenço, P. B., Rots, J. G., and Blaauwendraad, J. (1998). “Continuum model for masonry: parameter estimation and validation.” *Journal of Structural Engineering*, 124(6), 642-652.

Lowes, L. N., and Altoontash, A. (2003). “Modeling reinforced concrete beam-column joints subjected to cyclic loading.” *Journal of Structural Engineering*, 129(12), 1686-1697.

LSTC (2007). *LS-DYNA User’s Manuals*, Livermore Software and Technology Corporation, Livermore, CA, USA.

Lu, X., Lu, X., Guan, H., and Ye, L. (2013). “Collapse simulation of reinforced concrete high-rise building induced by extreme earthquakes.” *Earthquake Engineering and Structural Dynamics*, 42(5), 705-723.

Lu, Y., and Panagiotou, M. (2013). “Three-dimensional cyclic beam-truss model for non-planar reinforced concrete walls.” *ASCE Journal of Structural Engineering*, 140(3), 04013071:1-11.

Lu, Y., Panagiotou, M., and Koutromanos, I. (2014). “Three-dimensional beam-truss model for reinforced-concrete walls and slabs subjected to static or dynamic loading.” *PEER Report No. 2014/18*, University of California, Berkeley, CA.

Lubliner, J., Oliver, J., Oller, S., and Onate, E. (1989). “A plastic-damage model for concrete.” *International Journal of Solids and Structures*, 25(3), 299-326.

Luccioni, B. M., Ambrosini, R. D., and Danesi, R. F. (2004). “Analysis of building collapse under blast loads.” *Engineering Structures*, 26(1), 63-71.

Lybas, J. and Sozen, M. (1977). “Effect of beam strength and stiffness on dynamic behavior of reinforced concrete coupled walls.” *Report No. UILU-ENG-77-2016*, University of Illinois at Urbana-Champaign.

Maekawa, K., Pinanmas, A., Okamura, H. (2003). *Nonlinear mechanics of reinforced concrete*, Spon Press, New York, NY.

Magallanes, J. M., Wu, Y., Malvar, L. J., and Crawford, J. E. (2010). “Recent improvements to release III of the K&C concrete model.” *In Proceeding of 11th International LS-DYNA Users Conference*, Michigan, USA, 3-37.

Mahin, S. A., and Bertero, V. V. (1975). “An evaluation of some methods for predicting seismic behavior of reinforced concrete buildings.” *Earthquake Engineering Research Center*, University of California, Berkeley.

Malvar, L. J., Crawford, J. E., Wesevich, J. W., and Simons, D. (1997). “A plasticity concrete material model for DYNA3D.” *International Journal of Impact Engineering*, 19(9), 847-873.

Mander, J. B., Priestley, M. J., and Park, R. (1988). “Theoretical stress-strain model for confined concrete.” *Journal of Structural Engineering*, 114(8), 1804-1826.

Martinelli, L., (2008). “Modeling shear-flexure interaction in reinforced concrete elements subjected to cyclic lateral loading.” *ACI Structural Journal*, 105(6), 675-684.

Massone, L. M. (2006). *RC wall shear–flexure interaction: Analytical and experimental responses,* Ph.D. Dissertation, Unversity of Califorinia, Los Angeles.

Mazars J., Kotronis, P., and Davenne, L. (2002). “A new modeling strategy for the behavior of shear walls under dynamic loading.” *Earthquake Engineering and Structural Dynamics*, 31(4), 937-954.

McKenna, F., Fenves, G.L., Scott, M.H., and Jeremic, B. (2000), “Open System for Earthquake Engineering Simulation.” *Pacific Earthquake Engineering Research Center*, University of California, Berkeley, CA.

Mehrabi, A. B., and Shing, P. B. (1997). “Finite element modeling of masonry-infilled RC frames.” *Journal of Structural Engineering*, 123(5), 604-613.

Menetrey, P., and Willam, K. J. (1995). “Triaxial failure criterion for concrete and its generalization.” *ACI Structural Journal*, 92(3), 311-318.

Miki, T., and Niwa, J. (2004). “Nonlinear analysis of RC structural members using 3D lattice model.” *Journal of Advanced Concrete Technology*, 2 (3), 343-358.

Mitra, N., and Lowes, L.N. (2004). “Evaluation, calibration, and verification of a reinforced concrete beam–column joint model.” *ASCE Journal of Structural Engineering*, 133(1), 105–120.

Mohamad-Hussein, A., and Shao, J. F. (2007). “Modelling of elastoplastic behaviour with non-local damage in concrete under compression.” *Computers and Structures*, 85(23), 1757-1768.

Moharrami, M., and Koutromanos, I. (2016). “Triaxial Constitutive Model for Concrete under Cyclic Loading.” *Journal of Structural Engineering*, 04016039:1-15.

Moharrami, M., Koutromanos, I., Panagiotou, M., and Girgin, S. C. (2015a). “Analysis of shear-dominated RC columns using the nonlinear truss analogy.” *Earthquake Engineering and Structural Dynamics*, 44(5), 677-694.

Moharrami, M., Koutromanos, I., Williams, S. A. (2015b). “Analysis of Shear-Dominated Reinforced Masonry Walls Using Truss Models.” *The Masonry Society Journal*, 33(1), 27-48.

Moretti, M. L., and Tassios, T. P. (2006). “Behavior and ductility of reinforced concrete short columns using global truss model in concrete beams.” *ACI Structural Journal*, 103(3), 319-327.

Mostafaei, H., and Kabeyasawa, T. (2007). “Axial-shear-flexure interaction approach for reinforced concrete columns.” *ACI Structural Journal*, 104(2), 218-226.

MSC (2005). *MSC.Marc User’s Manuals*, MSC. Software Corporation, Newport Beach, CA, USA.

Mullapudi, T. R. S., and Ayoub, A. (2010). “Modeling of the seismic behavior of shear-critical reinforced concrete columns.” *Engineering Structures*, 32(11), 3601-15.

Murcia-Delso, J. (2013). *Bond-Slip behavior and development of bridge column longitudinal reinforcing bars in enlarged pile shafts*. Ph.D. Dissertation, University of California, San Diego, La Jolla, CA.

Murcia-Delso, J., and Benson Shing, P. B. (2014). "Bond-Slip model for detailed finite-element analysis of reinforced concrete structures." *Journal of Structural Engineering*, 141(4), 04014125:1-10.

Murcia-Delso, J., Stavridis, A., and Shing, P. B. (2013). "Bond strength and cyclic bond deterioration of large-diameter bars." *ACI Structural Journal*, 110(4), 659-670.

Murray, Y. (2007). "User's manual for LS-DYNA material model 159." *Report No. FHWA-HRT-05-062*, Federal Highway Administration, McLean, VA.

Murray, Y. D., Abu-Odeh, A. Y., and Bligh, R. P. (2007). "Evaluation of LS-DYNA concrete material model 159." *Report No. FHWA-HRT-05-063*, Federal Highway Administration, McLean, VA.

Neuenhofer, A., and Filippou, F. C. (1997), "Evaluation of nonlinear frame finite-element models." *ASCE Journal of Structural Engineering*, 123(7), 958–966.

Nguyen, G. D., and Korsunsky, A. M. (2008). "Development of an approach to constitutive modelling of concrete: isotropic damage coupled with plasticity." *International Journal of Solids and Structures*, 45(20), 5483-5501.

Noguchi, H., and Uchida, K. (2004). "Finite element method analysis of hybrid structural frames with reinforced concrete columns and steel beams." *Journal of Structural Engineering*, 130(2), 328-335.

Oliver, J. (1996). "Modelling strong discontinuities in solid mechanics via strain softening constitutive equations. Part 1: Fundamentals." *International journal for numerical methods in engineering,* 39(21), 3575-3600.

Otani, S. and Sozen, M. A. (1972). "Behavior of multistory reinforced concrete frames during earthquakes." *Technical Report,* University of Illinois at Urbana-Champaign.

Ottosen, N. S. (1977). “A failure criterion for concrete.” *Journal of Engineering Mechanics*, (103), 527-535.

Ožbolt, J., Li, Y., and Kožar, I. (2001). “Microplane model for concrete with relaxed kinematic constraint.” *International Journal of Solids and Structures*, 38(16), 2683-2711.

Pakiding, L., Pessiki, S., Sause, R., Rivera, M. (2014). “Experimental testing of cast-in-place seismic resistant unbonded post-tensioned special reinforced concrete walls.” *ATLSS Report No. 14-07*.

Palermo, D., and Vecchio, F. J. (2004). “Compression field modeling of reinforced concrete subjected to reversed loading: Verification.” *ACI Structural Journal*, 101(2), 155-164.

Panagiotou, M., Restrepo, J., Shoettler, M., and Kim, G. (2012). “Nonlinear cyclic truss model for reinforced concrete walls.” *ACI Structural Journal*, 109(2), 205-214.

Papanikolaou, V. K., and Kappos, A. J. (2007). Confinement-sensitive plasticity constitutive model for concrete in triaxial compression. International Journal of Solids and Structures, 44(21), 7021-7048.

Park, H., and Eom, T. (2007). “Truss model for nonlinear analysis of RC members subject to cyclic loading.” *ASCE Journal of Structural Engineering*, 133(10), 1351-1363.

Petrangeli, M., Pinto, P., and Ciampi, V. (1999). “Fiber element for cyclic bending and shear of RC structures. I: Theory.” *Journal of Engineering Mechanics*, 125(9), 994-1001.

Pivonka, P. (2001). *Constitutive modeling of triaxially loaded concrete considering large compressive stresses: application to pull-out tests of anchor bolts*. Ph.D. Dissertation, Technische Universität Wien, Austria.

Priestley, M. J. N., Seible, F., Xiao, Y., and Verma, R. (1994). “Steel jacket retrofitting of reinforced concrete bridge columns for enhanced shear strength - Part 2: Test results and comparison with theory.” *ACI Structural Journal*, 91(5), 537–551.

Ramirez, J. A., French, C. W., Adebar, P. E., Bonacci, J. F., and Collins, M. P. (1998). “Recent approaches to shear design of structural concrete.” *Journal of Structural Engineering*, 124(12), 1374.

Ranzo, G., and Petrangeli. M. (1988). “A fibre finite beam element with section shear modelling for seismic analysis of RC structures.” *Journal of Earthquake Engineering*, 2(3), 443-473.

Rashid, Y. R. (1968). “Ultimate strength analysis of prestressed concrete pressure vessels.” *Nuclear Engineering and Design*, 7(4), 334-344.

Rots, J. G. (1988). *Computational modeling of concrete fracture,* Ph.D. Dissertation, TU Delft.

Rots, J. G., and Blaauwendraad, J. (1989). “Crack models for concrete, discrete or smeared? Fixed, multi-directional or rotating?” *HERON*, 34 (1).

Roufaiel, M. S., and Meyer, C. (1987). “Analytical modeling of hysteretic behavior of R/C frames.” *Journal of Structural Engineering*, 113(3), 429-444.

Saatcioglu, M., Derecho, A. T., and Corley, W. G. (1987). “Parametric study of earthquake-resistant coupled walls.” *Journal of Structural Engineering*, 113(1), 141-157.

Sagiroglu, S., and Sasani, M. (2013). “Progressive collapse-resisting mechanisms of reinforced concrete Structures and Effects of Initial Damage Locations.” *Journal of Structural Engineering*, 140(3), 04013073:1-12.

Sasani, M., and Kropelnicki, J. (2008). “Progressive collapse analysis of an RC structure.” *The Structural Design of Tall and Special Buildings*, 17(4), 757-771.

Sasani, M., Werner, A., and Kazemi, A. (2011). “Bar fracture modeling in progressive collapse analysis of reinforced concrete structures.” *Engineering Structures*, 33(2), 401-409.

Schoettler, M. J., Restrepo, J. I., Guerrini, G., Duck, D. E., and Carrea, F. (2012). “A full-scale, single-column bridge bent tested by shake-table excitation.” *Center for Civil Engineering Earthquake Research, Dept. of Civil Engineering*, Univ. of Nevada, Reno, NV.

Schwer, L. E., and Malvar, L. J. (2005). “Simplified concrete modeling with* mat_concrete_damage_rel3.” *JRI LS-Dyna User Week*, 49-60.

Schlaich, J., SchRafer, I., Jennewein, M. (1987). “Towards a consistent design of structural concrete.” *Journal of Prestressed Concrete Institute*, 32, 74 –150.

Scordelis, A. C., and Ngo, D. (1967). “Finite element analysis of reinforced concrete beams.” *ACI Journal*, 64(3), 152-163.

Scott, M.H., and Fenves, G.L. (2006), “Plastic hinge integration methods for force-based beam-column elements,” *ASCE Journal of Structural Engineering*, 132(2), 244-252.

Seible, F., LaRovere, H. L., and Kingsley, G. R. (1990a). “Nonlinear analysis of reinforced concrete masonry shear wall structures - monotonic loading.” *TMS Journal*, 9(1), 70-77.

Seible, F., LaRovere, H. L., and Kingsley, G. R. (1990b). “Nonlinear analysis of reinforced concrete masonry shear wall structures - cyclic loading”. *TMS Journal*, 9(1), 60-69.

Selby, R.G., and Vecchio, F.J. (1997). “A constitutive model for analysis of reinforced concrete solids.” *Canadian Journal of Civil Engineering*, 24(3), 460-470.

Shing P. B., Noland, J., Spaeh, H., Klamerus. E., and Schuller, M. (1991). “Response of single-story reinforced masonry shear walls to in-plane lateral loads.” *National Science Foundation*.

Shirai, K., Matsumori, T., and Kabeyasawa, T. (2007). “3-D Dynamic Collapse Test of a Six-Story Full-Scale RC Wall-Frame Building.” *Structural Engineering Research Frontiers*, 1-10.

Simo, J., and Hughes, T.J.R. (1998), *Computational Inelasticity*, Springer, New York.

Simo, J. C., Kennedy, J. G., and Govindjee, S. (1988). “Non-smooth multisurface plasticity and viscoplasticity. Loading/unloading conditions and numerical algorithms.” *International Journal for Numerical Methods in Engineering*, 26(10), 2161-2185.

Spencer, B., and Shing, P. B. (2002). “Stress Hybrid Embedded Crack Element Analysis for Concrete Fracture.” *Special Publication*, 205, 323-346.

Spiliopoulos, K. V., and Lykidis, G. C. (2006). “An efficient three-dimensional solid finite element dynamic analysis of reinforced concrete structures.” *Earthquake Engineering and Structural dynamics*, 35(2), 137-157.

Stevens, N. J., Uzumeri, S. M., Collins, M. P., and Will, T. G. (1991), “Constitutive model for reinforced concrete finite element analysis.” *ACI Structural Journal*, 88(1), 49–59.

Suidan, M., and Schnobrich, W. C. (1973). “Finite element analysis of reinforced concrete.” *Journal of the Structural Division*, 99(10), 2109-2122.

Taghdi, M., Bruneau, M., and Saatcioglu, M. (2000). “Analysis and design of low-rise masonry and concrete walls retrofitted using steel strips.” *Journal of Structural Engineering*, 126(9), 1026-1032.

Takayanagi, T., and Schnobrich, W. C. (1977). “Computed behavior of coupled shear walls.” *Proceeding of 6th WCEE*, New Delhi, India, IH, 3069-3074.

Talaat, M. M., and Mosalam m. K. (2007). “Computational modeling of progressive collapse in reinforced concrete frame structures.” *PEER Report 2007/10*, University of California, Berkeley, CA.

Teng, J. G., Xiao, Q. G., Yu, T., and Lam, L. (2015). “Three-dimensional finite element analysis of reinforced concrete columns with FRP and/or steel confinement.” *Engineering Structures*, 97, 15-28.

Thiagarajan, G., Kadambi, A. V., Robert, S., and Johnson, C. F. (2015). “Experimental and finite element analysis of doubly reinforced concrete slabs subjected to blast loads.” *International Journal of Impact Engineering*, 75, 162-173.

TNO DIANA $_{\text{BV}}$. (2011). *User’s Manual DIANA*. TNO Company, Delft, the Netherlands.

Tsai, M. H., and Lin, B. H. (2008). “Investigation of progressive collapse resistance and inelastic response for an earthquake-resistant RC building subjected to column failure.” *Engineering Structures*, 30(12), 3619-3628.

Valentini, B., and Hofstetter, G. (2013). “Review and enhancement of 3D concrete models for large-scale numerical simulations of concrete structures.” *International Journal for Numerical and Analytical Methods in Geomechanics,* 37(3), 221-246.

Vallenas, J. M., Bertero, V. V., and Popov, E. P. (1979). “Hysteric behavior of reinforced concrete structural walls.” *NASA STI/Recon Technical Report N, 80, 27533*.

Vecchio, F. J. (1989). “Nonlinear finite element analysis of reinforced concrete membranes.” *ACI Structural Journal*, 86(1), 26-35.

Vecchio, F. J., and Collins, M. P. (1986). “The modified compression-field theory for reinforced concrete elements subjected to shear.” *ACI Journal*, 83(2), 219-231.

Vulcano, A., Bertero, V. V., and Colotti, V. (1988). “Analytical modeling of R/C structural walls.” *In 9th World Conference on Earthquake Engineering*, 6, 41-6.

Walraven, J.C. (1980). *Aggregate interlock: a theoretical and experimental analysis*. Ph.D. Dissertation, TU Delft.

Wight, J. K. and MacGregor, J. G. (2012). *Reinforced concrete: Mechanics and design*. Pearson Education, Inc., Upper Saddle River, NJ: Prentice Hall.

Willam, K., and Warnke, E. (1974), “Constitutive model for the triaxial behavior of concrete.” *IABSE Report,* International Association of Bridge and Structural Engineers, 19, 1-30.

Willam, K. J. and Warnke, E. P. (1975). “Constitutive models for the triaxial behavior of concrete.” *In Proceedings of the International Association for Bridge and Structural Engineering*, ISMES, Bergamo, Italy, 19, 1-30.

Wolf, J. (2008). *A plasticity model to predict the effects of confinement on concrete*. Ph.D. Dissertation, California Institute of Technology, Pasadena, CA.

Wu, J.Y., Li, J., and Faria, R. (2006). “An energy release rate-based plastic-damage model for concrete.” *International Journal for Solids and Structures*, 43, 583-612.

Yu, T., Teng, J. G., Wong, Y. L., and Dong, S. L. (2010). “Finite element modeling of confined concrete-I: Drucker-Prager type plasticity model.” *Engineering Structures*, 32(3), 665-679.

Yuzugullu, O., and Schnobrich, W. (1972). “Finite element approach for the prediction of inelastic behavior of shear wall-frame systems”. *University of Illinois at Urbana-Champaign*.

Zeris, C.A., and Mahin, S.A. (1988), “Analysis of reinforced concrete beam-columns under uniaxial excitation.” *ASCE Journal of Structural Engineering*, 114(4), 804–820.

Zhao, J., and Sritharan, S. (2007). “Modeling of strain penetration effects in fiber-based analysis of reinforced concrete structures.” *ACI Structural Journal*, 104(2), 133-141.

Zheng, Y., Robinson, D., Taylor, S., and Cleland, D. (2009). “Finite element investigation of the structural behaviour of deck slabs in composite bridges.” *Engineering Structures*, 31(8), 1762-1776.